NASA-CP-2271 19830026080

SA Conference Publication 2271

Nonlinear Constitutive Relations for High Temperature Applications

Proceedings of a symposium held at
the University of Akron
Akron, Ohio
May 19-20, 1982

3 1176 01316 1998

Disclaimer

Use of trade names or names of manufacturers in this report does not constitute an official endorsement of such products or manufacturers, either expressed or implied, by the National Aeronautics and Space Administration

NASA Conference Publication 2271

Nonlinear Constitutive Relations for High Temperature Applications

Proceedings of a symposium sponsored by
the University of Akron and
NASA Lewis Research Center and held at
the University of Akron, Akron, Ohio
May 19-20, 1982

National Aeronautics
and Space Administration

**Scientific and Technical
Information Office**

1983

PREFACE

A Symposium on Nonlinear Constitutive Relations for High Temperature Applications, under the joint sponsorship of the NASA Lewis Research Center and the University of Akron, was held at the University of Akron on May 19-20, 1982. Some seventy-five attendees and participants representing NASA, other Government agencies, universities and industries were at the Symposium. The purpose of this Symposium was to review the state-of-the-art in nonlinear constitutive modeling of high temperature materials and to identify the needs for future research and development efforts in this area.

One of the specific goals of the NASA Lewis Research Center is to foster technological development of gas turbine engine structures. In this connection, it was recognized that considerable research efforts are urgently needed in the development of nonlinear constitutive relations for high-temperature applications. This need is stimulated by recent advances in high-temperature materials technology and new demands on material and component performance. The demands for better material performance have come from not only the aerospace industry but also the stationary power and automotive industries. Therefore, the intent of this Symposium was to bring together both the developers and users of nonlinear constitutive relations for exchange and quick dissemination of recent research progress and new technology in this area.

The Symposium was organized into the following five sessions:

I. Material Behavior
II. Constitutive Modeling I
III. Constitutive Modeling II
IV. Numerical Methods
V. Panel Discussion and Recommendations

There were a total of twenty-one papers presented in the first four sessions. The papers (extended abstracts or abstracts where papers were not available) and the authors are grouped by session and identified in the Table of Contents. Following the technical papers is a summary of the panelists' remarks focusing on the identification of required future research and development in nonlinear constitutive relations for high temperature applications.

We, the Organizing Committee, wish to express our appreciation to the session chairmen, authors and speakers, and panelists whose efforts have contributed to the technical excellence and success of the Symposium. We are also grateful to the staff and Mrs. Mary E. Chesrown, Assistant Director of the Institute of Civic Education at the University of Akron, for their relentless help before and during the Symposium.

D. A. Ross
T. Y. Chang
R. L. Thompson

TABLE OF CONTENTS

CORRELATION OF RUPTURE LIFE, CREEP RATE, AND MICROSTRUCTURE FOR TYPE 304 STAINLESS STEEL*

R. W. Swindeman
Oak Ridge National Laboratory
Oak Ridge, Tennessee 37830

and

J. Moteff
University of Cincinnati
Cincinnati, Ohio 45221

ABSTRACT

The stress and temperature sensitivities of the rupture life (t_R) and secondary creep rate ($\dot{e}_s$) were examined in detail for a single heat of type 304 stainless steel (9T2796). Assuming that the rupture life (t_R) has a power law stress dependency, we observed relatively small differences in the stress exponent (n_R) over a broad range of stress and temperature. In contrast, large changes were observed for equivalent parameter (n_s) for secondary creep rate ($\dot{e}_s$). As a result of these differences, the Monkman-Grant correlation was sensitive to stress and temperature below 650°C. Metallurgical studies based on light and transmission electron microscopy suggested that the temperature and stress sensitivities of $\dot{e}_s$ at temperatures below 650°C were related to features of the substructure not present at higher temperature. Specifically, the presence of a fine dislocation network stabilized by precipitates altered the stress and temperature sensitivities relative to what might be expected from high-temperature studies.

INTRODUCTION

Structural components in high-temperature service usually experience variable loading conditions. Hence to assure that premature failure will not occur, the design analyst must use some parameter for summing damage. For nonreversing stresses time-under-stress,[1,2] creep strain,[3] and strain rate[4] are sometimes used to sum damage; for fatigue loadings, cycles-to-failure related to stress,[5] strain,[6] and work energy[7] are sometimes used; and for creep-fatigue two or more damage parameters are sometimes used.[8]

One of the difficulties in developing damage concepts for time-dependent failure is the need to verify that methods are valid for 10^9 s (3×10^5 h). Since fracture by creep or fatigue can be measured only once in a test, there is no direct way to measure damage without destroying the test specimen. Verification of a damage accumulation model therefore requires a large commitment of time and testing equipment. Crack growth rates can be measured under varying conditions, but the existence of cracks and the control of their growth in pressure boundary materials are not consistent with design to prevent crack initiation. In contrast, strain rate can be measured, does not require the preexistence of a crack, and on the basis of

*Work performed under DOE/RRT 189a 0H048, *High-Temperature Structural Design Methods*.

the Monkman-Grant[9] correlation between minimum creep rate and rupture life seems to be related to fracture. Consequently, several cumulative damage models as proposed by Majumdar,[10] Ostergren,[11] and Manjoine[4] use the strain-rate response to estimate damage and predict fracture.

To place confidence in predictions that are based on strain rate as a measure of damage, it is necessary to establish that the stress and temperature dependences of the secondary creep rate ($\dot{e}_s$) and the rupture life (t_R) are similar. Further, it should also be demonstrated that this similarly persists for conditions for which fracture data are meager.

This paper examines the stress and temperature dependences of $\dot{e}_s$ and t_R for a heat of type 304 stainless steel on which a very large data base exists. We also examine the validity of the Monkman-Grant correlation and show how stress and temperature influences this correlation. Finally, metallurgical factors that influence creep rate and rupture life are discussed.

DATA BASE AND ANALYSIS METHODS

The data base consisted of several hundred tensile and creep-rupture tests, which covered times in the range 1 to 1.4×10^8 s and temperatures from 427 to 871°C. Data included 25-mm plate and 16-mm bar of a reference heat of type 304 stainless steel (9T2796). Although not used directly in the correlations, data on 51-mm plate extending to 2.2×10^8 s were of considerable value in estimating the behavioral trends at long times.

Most of the data on which calculations were based have been published elsewhere.[12-14] In some instances engineering stresses were reported, while in others true stresses were reported. Our tensile stress data represent the saturation flow stresses obtained from a fit of the Voce equation to the true stress vs true strain data.[14] The "rupture life" in tensile tests represents the time between the ultimate strength and fracture.[12] The creep stress data represent true stresses obtained by multiplying engineering creep stress by the factor $1 + e_p$ where e_p is the inelastic strain about halfway through the test.[12] Below 650°C e_p was dominated by the plastic loading strain, and the stress changed by less than 10% during the creep test. Above 650°C e_p was dominated by the creep strain, which was in the 30–60% range.

The stress sensitivities of $\dot{e}_s$ and t_R were evaluated with the assumption that power relations existed between both $\dot{e}_s$ and σ/E and t_R and σ/E. Thus, for any isothermal pair of points at $(\sigma_1/E, \dot{e}_{s_1})$ and $(\sigma_2/E, \dot{e}_{s_2})$, the stress exponent for creep rate, n_s, was calculated:[1]

$$n_s = \frac{ln(\dot{e}_{s_1}/\dot{e}_{s_2})}{ln(\sigma_2/\sigma_1)} \quad \ldots\ldots\ldots\ldots\ldots \quad (1)$$

Similarly, the stress exponent for rupture, n_R, was calculated:

$$n_R = \left| \frac{ln(t_{R_2}/t_{R_1})}{ln(\sigma_2/\sigma_1)} \right| \quad \ldots\ldots\ldots\ldots\ldots \quad (2)$$

Data pairs were read from visually smoothed curves through the experimental points. The two stresses, σ_1/E and σ_2/E, were generally spaced about 0.15 log cycles apart.

RESULTS

Contour Maps

Figure 1 shows a contour map of the variation in the stress exponent for rupture (n_R) with the modulus-compensated stress (σ/E) and the temperature (T). Over most of the range where data are available n_R falls between 6 and 8. A region also exists around 600°C for σ/E less than 10^{-3} where n_R appears to increase above 8. The stress exponent for creep rate, n_ε, exhibits a more complicated pattern as σ/E and T are varied. This pattern is shown in Fig. 2. At temperatures above 600°C n_ε usually falls in the range 6 to 8. Thus, n_ε and n_ε agree. Higher n_ε values are observed for high σ/E, and this pattern is also consistant with the trend for n_R. Below 650°C the n_ε values differ from the n_R values. For example, between 540 and 600°C the n_ε values are in the range 8 to 10 compared to n_ε values in the range 6 to 8. Below 540°C and at low stresses the n_ε values seem to decrease, but no data exist for n_R; hence, no comparison is possible.

Correlations Between Strain Rate and Rupture Life

Comparison of data in Figs. 1 and 2 leads us to conclude that the stress and temperature dependencies of $\dot{e}_\varepsilon$ and t_R are similar above 650°C, at least over the range where data are available. Thus, it should be possible to use $\dot{e}_\varepsilon$ as a parameter to sum damage for varying stresses. It is equally apparent that the stress and temperature dependencies of $\dot{e}_\varepsilon$ and t_R are dissimilar below 650°C. Even so, it might be possible to sum damage with $\dot{e}_\varepsilon$ if we can understand the functional relationship between $\dot{e}_\varepsilon$ and t_R. If we assume that both $\dot{e}_\varepsilon$ and $1/t_R$ can be represented by power law expressions, then we can eliminate stress and show that for isothermal conditions:

$$t_R \propto \dot{e}_\varepsilon^{-m} \quad \ldots\ldots\ldots\ldots\ldots\ldots \quad (3)$$

where m is the slope of the Monkman-Grant plot and is equal to the ratio n_R/n_ε. In Fig. 3 we plot log t_R vs log $\dot{e}_\varepsilon$ for temperatures of 816, 760, 704, 649, 593, 538, and 482°C. Data at the two highest temperatures plot as a straight line with a slope close to −1.0 (Fig. 3, Curve A). This trend covers six decades of $\dot{e}_\varepsilon$ and t_R. Data for 704°C more-or-less follow a trend similar to data at higher temperatures (Fig. 3, Curve B).

Data for 649°C fall near Curve C in Fig. 3. Here the data at high $\dot{e}_\varepsilon$ follow the m = 1.0 trend, but for rates below 10^{-5}/s the slope decreases slightly and is closer to −0.97. The data base at 593°C is very extensive and covers approximately ten decades of $\dot{e}_\varepsilon$ (Fig. 3, Curve D). The curve starts out with a slope near −1.0 then shifts to a slope of near −0.88 until $\dot{e}_\varepsilon$ is 10^{-8}/s. Below this $\dot{e}_\varepsilon$ the slope decreases precipitously and around 10^{-10}/s the value of m is 0.5 or less. The large scatter in the data is attributable to grain size variations in the material. Finer grain sizes

(80 μm) lead to greater rupture lives than coarser grain sizes (180 μm). Relative to the high-temperature Monkman-Grant Curve A, Curve D at 593°C has shifted downward by a factor of two at high strain rates and considerable more at very low strain rates.

Data for 538°C are plotted in Fig. 3 and fall near Curve E. Here we see that m = 1.0 for high $\dot{e}_s$ and 0.83 for lower strain rates. If the trend continued the Monkman-Grant curve for 538°C would intersect the curve for 593°C at a strain rate around 10^{-10}/s. No data are available to verify this. Difficulties occur in defining the $\dot{e}_s$ values at 482°C because the creep curves have tertiary creep character. Hence, the data plotted along Curve F in Fig. 3 for 482°C should be considered as tenuous. Over much of the data range m is near 0.75 at 482°C. Compared to the high-temperature Monkman-Grant Curve A, the curve at 482°C is displaced toward lower t_R by more than a decade at low strain rates.

In summary, at high strain rates (10^{-4} to 10^{-1}/s) the log t_R vs log $\dot{e}_s$ plots follow the m = 1.0 trend for all temperatures, but there is a small decrease in t_R with decreasing temperature for the same $\dot{e}_s$. Assuming that $n_R = n_s$ at high $\dot{e}_s$ values, it follows that the decrease in t_R is associated with a decrease in the post-uniform strain in the tensile tests with decreasing temperature. At intermediate strain rates (10^{-9} to 10^{-4}/s the log t_R vs log $\dot{e}_s$ plots fan out, with m decreasing and t_R decreasing with decreasing temperature for the same $\dot{e}_s$. This implies that n_R is less than n_s, which is consistent with the contour maps shown in Figs. 1 and 2. Very low-strain-rate data at 593°C exhibit low n values, but we do not know whether the other curves bend over. This is important from an engineering viewpoint since most of the creep-rupture damage is accumulated at strain rates in the range 10^{-11} to 10^{-8}/s, while most fatigue damage is accumulated at rates in the range 10^{-6} to 10^{-5}/s. Thus, service conditions often enter into the region of poorly defined behavior.

An alternative approach to the use of strain rate as a parameter in damage accumulation is the linear strain parameter. This is defined as the product $\dot{e}_s t_R$ and is sometimes called the "plasticity resource."[15,16] Whereas the Monkman-Grant approach attempts to "predict" rupture from the "known" strain rate, the linear strain parameter is not predictive since both the $\dot{e}_s$ and t_R must be known to evaluate the parameter. The parameter $\dot{e}_s t_R$ is highly sensitive to differences in the stress and temperature sensitivities of $\dot{e}_s$ and t_R. Assuming power law behavior:

$$\dot{e}_s t_R \propto (\sigma/E)^{n_s - n_R} \quad \ldots\ldots\ldots\ldots (4)$$

Hence, a plot of log $\dot{e}_s t_R$ vs log σ/E will define a curve with a slope that reflects the difference $n_s - n_R$. Data are plotted in Fig. 4. Here we see that at high temperatures the isothermal data fall on horizontal lines. This implies that $n_s = n_R$. At lower temperatures data fall on lines that exhibit slopes between 1 and 2. At low stresses the data trend is not well defined, but there is some evidence at 593°C of a very steep slope. The linear strain parameter is highly variable with stress and temperature, and its "predictive" capabilities for very low stresses are questionable.

Metallurgical Features

The features of the metallurgical substructure (Figs. 5–8) are more-or-less consistent with the observed mechanical behavior. In the region of stress and temperature where $n_s = n_R$, subgrains form (Fig. 5) and precipitate when present consists of large and blocky particles. Matrix carbide particles exceed 0.1 μm (Fig. 6), and grain boundary carbide particles are 0.5 μm in size (Fig. 7). Failure is always intergranular and initiated at triple points and twin grain boundary intersections. At the lowest stresses we suspect that microvoid formation and coalescence are active, but we have not studied them quantitatively. Below 650°C the evolution of substructure is complex, and this complexity probably produces the variation of n_s with stress and temperature. At high stresses cells generally form and grain boundary carbides are often present. These carbide particles quickly grow to a size in the range 0.1 to 0.2 μm. Matrix carbides may be absent or relatively fine (<0.05 μm). Failure is predominantly intergranular with wedge-type cracks nucleating at grain boundary triple points. When σ/E values fall below 0.001 no cells or subgrains form. Rather, the substructure consists of a fine network of dislocations perhaps stabilized by the fine distribution of carbide, as suggested by Hopkin and Taylor.[17] The change in dislocation density appears to be about 50% higher than for comparable σ/E values at higher temperatures (Fig. 8). Large grain boundary carbide particles (0.1 ato 0.4 μm) are present, and failure is intergranular with wedge-type cracking. At stresses below the range where rupture data are available, the substructure consists of coarse dislocation networks decorated by a fine precipitate. This is essentially the same substructure that developed in simply aged material.[18] Below 510°C matrix carbides are not observed to 36 Ms, and even grain boundaries are relatively free of precipitates. Again, failure is initiated by wedge cracks at grain boundaries, but often these cracks are blunted by additional plastic deformation in the final stages of creep rupture. Thus, the transgranular creep rupture described by Ashby and coworkers[19,20] dominates.

Cracking patterns were studied in approximately 50 specimens. Data were obtained in several categories including crack density, ratio of the number of triple point cracks to total cracks, ratio of crack length to grain boundary length, and the orientation angle between the crack and the stress axis. Most of the data were obtained by Bhargava, who used procedures developed by Nahm, Michel, and Moteff.[21,22]

No cracks were observed in specimens with less than 3% total strain, and when cracks were present both the crack density and the crack length increased with creep strain. The orientation angle between the cracks and the stress axis increased with decreasing strain rate and was usually in the range 50 to 80°. Grain boundary migration was sometimes observed above 593°C, while recrystallization was sometimes observed above 704°C. These observations are consistent with literature data.[22,23]

DISCUSSION

The strong stress and temperature dependencies of log t_R vs log $\dot{e}_s$ and log $\dot{e}_s t_R$ vs log σ/E are not unique to heat 9T2796. Indeed, we have analyzed data on two other heats of type 304 stainless steel and find similar trends at 593 and 649°C. To some extent the rupture life is influenced by the pre-

cipitation of the $M_{23}C_6$ carbide, and this influence shows up as a slight cusp in the log t_R vs log σ curve.[12] However, the variations in the stress and temperature dependencies of t_R are not nearly as severe as the variations for $\dot{e}_s$. The reasons for high n_s values around 600°C are not altogether clear. One possibility is that the precipitation-stabilized dislocation network acts in much the same way as precipitation hardening. If so, we could speak of an internal stress, σ_i, which is relatively constant for a given temperature. Then $\dot{e}_s$ in terms of an effective stress is

$$\dot{e}_s = f\left\{T,\ [(\sigma-\sigma_i)/E]\right\} \quad \ldots\ldots\ldots\ldots\ldots (5)$$

where $[(\sigma-\sigma_i)/E]$ is the effective stress (Lagneborg,[24] Wilshire,[25] and Nix and coworkers[26]). As the carbide particles grow in size and particle spacing increases, σ_i could change. If it does not, then when the applied stress is below σ_i, the secondary creep rate would be zero (if we ignore the contribution of grain boundary sliding, diffusional flow, and climb over the particles). Creep would then consist of only transient and tertiary components. However, at 649°C subgrains sometimes form and the matrix carbide particle size is large. Thus, diffusion and thermal recovery proceed rapidly, and the possibility of hardening as outlined above is questionable. Tanaka and Shinoda[27] link the creep strength at 650°C to the carbide particle size and spacing, which suggests that the carbide continues to influence σ_i. Our data on carbide particle sizes agree well with weak heats of 18-8 stainless steel studied by Tanaka and Shinoda[27] and Étienne, Dortland, and Zeedijk.[28] However, we emphasize that it is not the precipitate alone that produces the hardening. We say this because, as pointed out by Barnby[29] and Sikka et al.,[18] the results from creep tests on aged materials that develop precipitates show either a loss or no change in creep strength relative to the nonaged condition. Thus, dynamic precipitation gives rise to the strengthening effect of σ_i. Precipitation kinetics with or without strain is qualitatively understood in type 304 stainless steel. We know, for example, that the matrix carbide develops more rapidly under monotonic and cyclic strains than under simple aging. We do not know whether the dislocation substructure produced by dynamic precipitation is different from the substructure developed by creep testing aged material. This would be of considerable interest.

An alternative explanation for high n_s values could be solid-solution strengthening, as proposed recently by Miller and Sherby.[30] Here the solid solution is produced by a Cottrell atmosphere drag force on dislocations. The magnitude of the effect is a function of a temperature-compensated strain rate $\dot{e}_s/\theta$, where θ is given by $exp(-Q/RT)$ and Q is the activation energy associated with the species that produces the Cottell atmosphere. Miller and Sherby[30] propose a "drag" rather than a "friction" strengthening effect. Hence, instead of Eq. (5) we have

$$\dot{e}_s = f\left\{T,\ \frac{\sigma}{\sigma_D(T,\dot{e}_s)}\right\} \quad \ldots\ldots\ldots\ldots\ldots (6)$$

where σ_D is the strengthening effect due to drag. This is a very powerful modification, since it is possible to let $\sigma_D(T,\dot{e}_s)$ reflect interstitial,

substitutional, and interaction solid-solution hardening effects. It is also possible to introduce a dependence of $\sigma_D(T,\dot{\varepsilon}_s)$ on the total deformation as well. With this much flexibility the complex variation of n_s could be modeled to any degree of accuracy. If we restrict ourselves to only one solution strengthening mechanism, then by use of the treatment outlined by Miller and Sherby,[30] n_s should be a unique function of σ/E and not vary with temperature for constant σ/E. If we assume that more than one solution hardening mechanism is present and that Eq. (6) could be used to represent $\dot{\varepsilon}_s$, then we would expect that the slope of log t_R vs $\dot{\varepsilon}_s$ might return to -1 at sufficiently low stresses. Similarly, the linear creep component $\dot{\varepsilon}_s t_R$ should always exhibit nonzero values and perhaps even increase at low stresses. Eventually, new deformation mechanisms and failure mechanisms may enter the picture, as suggested by Ashby and coworkers.[19,20] However, it is beyond the scope of our experimental data to assess these new problems. Nevertheless, Morris and Harris[31] recently suggest that a deformation "mechanism based on dislocation locking by solute atom complexes" occurs in type 316 stainless steel around 525°C. Hence, apparently more data are being obtained for this temperature range.

CONCLUSIONS

1. Above 650°C the stress and temperature dependences of the secondary creep rate ($\dot{\varepsilon}_s$) and the rupture life (t_R) are similar. The product $\dot{\varepsilon}_s t_R$ is relatively constant, and the exponent in the Monkman-Grant relation is close to 1.0. These observations apply to at least 4×10^6 s.

2. Below 650°C the stress and temperature dependences of $\dot{\varepsilon}_s$ and t_R often differ. The product $\dot{\varepsilon}_s t_R$ decreases stress and decreasing temperature. The exponent in the Monkman-Grant changes from 1.0 toward zero as temperature and $\dot{\varepsilon}_s$ decrease. These observations apply in the range 10^4 to 10^8 s.

3. The fact that $\dot{\varepsilon}_s$-t_R correlations are stress and temperature sensitive below 650°C is due primarily to changes in the $\dot{\varepsilon}_s$ behavior rather than in the rupture mechanism. Changes in the $\dot{\varepsilon}_s$ behavior could be attributed to either a high internal stress, σ_i, produced by the development or precipitation-stabilization dislocation network or to a somewhat complex solute hardening mechanism.

4. Although grain boundary carbide particle sizes and crack densities change over our range of stress and temperature, there was no evidence to indicate that these features of microstructure greatly influence the stress and temperature dependence of the rupture life.

5. Above 650°C $\dot{\varepsilon}_s$ can be a parameter for a damage accumulation model. Below 650°C $\dot{\varepsilon}_s$ can be used to sum damage over the range of stress and times where the relation between $\dot{\varepsilon}_s$ and t_R is known.

REFERENCES

1. E. L. Robinson, *Trans. ASME*, 1952, vol. 74, pp. 777–80.

2. S. Taira, *Creep in Structures*, pp. 96–124, Academic Press, New York, 1962.

3. D. A. Spera, Report No. NASA TN D-5489, NASA-Lewis Laboratories, Cleveland, Ohio, 1969.

4. M. J. Manjoine, *J. Eng. Mater. Technol.*, 1975, vol. 97, pp. 156–61.

5. M. A. Minor, *J. Appl. Mech.*, 1945, vol. 12, pp. 159–65.

6. L. F. Coffin, Jr., *Trans. ASME*, 1954, vol. 76, pp. 931–50.

7. J. D. Morrow, *Internal Friction, Damping, and Cyclic Plasticity STP 378*, pp. 45–87, American Society for Testing and Materials, Philadelphia, 1965.

8. R. D. Campbell, *Advances in Design for Elevated Temperature Environment*, pp. 45–56, American Society of Mechanical Engineer, New York, 1975.

9. F. C. Monkman and N. J. Grant, *Proc. Am. Soc. Test. Mater.*, 1956, vol. 56 pp. 593–605.

10. S. Majumdar and P. S. Maiya, *Symposium on Creep-Fatigue Interaction*, pp. 323–44, American Society of Mechanical Engineers, 1976.

11. W. J. Ostergren and E. Krempl, General Electric Company, Schenectady, and Rennsalear Polytechnic Institute, Troy, paper 78-PVP-63, ASME/CSME Pressure Vessel and Piping Conference, Montreal, Canada, June 25–30, 1978.

12. R. W. Swindeman, *Structural Materials for Service at Elevated Temperatures in Nuclear Power Generation*, pp. 1–30, American Society of Mechnical Engineers, New York, 1975.

13. R. V. Bhargava, J. Moteff, and R. W. Swindeman, *Structural Materials for Service at Elevated Temperatures in Nuclear Power Generation*, pp. 31–54, American Society of Mechanical Engineers, New York, 1975.

14. R. W. Swindeman, *J. Eng. Mater. Technol.*, 1975, vol. 98, pp. 98–106.

15. V. S. Ivanova, *Zavod. Lab*, 1955, vol. 21, pp. 212–16.

16. M. K. Booker, C. R. Brinkman, and V. K. Sikka, *Structural Materials for Service at Elevated Temperatures in Nuclear Power Generation*, pp 108–45, American Society for Mechanical Engineers, New York, 1975.

17. L.M.T. Hopkin and L. H. Taylor, *J. Iron Steel Inst. London*, 1967, vol. 205 pp. 17–27.

18. V. K. Sikka, C. R. Brinkman, and H. E. McCoy, Jr., *Structural Materials for Service at Elevated Temperatures in Nuclear Power Generation*, pp. 316–50, American Society of Mechanical Engineers, New York, 1975.

19. M. F. Ashby, Report No. CUED/C/MATA/TR.34, Cambridge University, Cambridge, England (undated).

20. M. F. Ashby, R. J. Fields, and T. Weerasooiya, Report No. CUED/C/MATS/TR.47, Cambridge University, Cambridge, England (undated).

21. D. J. Michel, H. Nahm, and J. Moteff, *Mater. Sci.*, 1973, vol. 11, pp. 97–102.

22. H. Nahm, D. J. Michel, and J. Moteff, *J. Mater. Sci.*, 1968, vol. 3, pp. 596–602.

23. F. Garofalo, *Fundamentals of Creep and Creep-Rupture in Metals*, pp. 221–26, MacMillan Company, New York, 1968.

24. R. Lagneborg, *J. Mater. Sci.*, 1968, vol. 3, pp. 596–602.

25. J. D. Parker and B. Wilshire, *Met. Sci.*, 1975, vol. 9, pp. 249–52.

26. R. W. Lund and W. D. Nix, *Acta. Metall.*, 1976, vol. 24, pp. 469–81.

27. T. Shinoda and R. Tanaka, *Nippon Kinzoku Gakkai Kaiho*, 1962, vol. 11, pp. 180–91.

28. C. F. Etienne, W. Dortland, and H. B. Zeedijk, *Creep and Fatigue in Elevated Temperature Applications*, pp. 225.1–225.9, The Institute of Mechanical Engineers, London, England, 1975.

29. J. T. Barnby, *J. Iron and Steel Inst. London*, 1966, vol. 204, pp. 23–27.

30. A. K. Miller and O. D. Sherby, *Acta. Metall.*, 1978, vol. 26, pp. 298–304.

31. D. G. Morris and D. R. Harries, *Met. Sci.*, 1978, vol. 12, pp. 525–31.

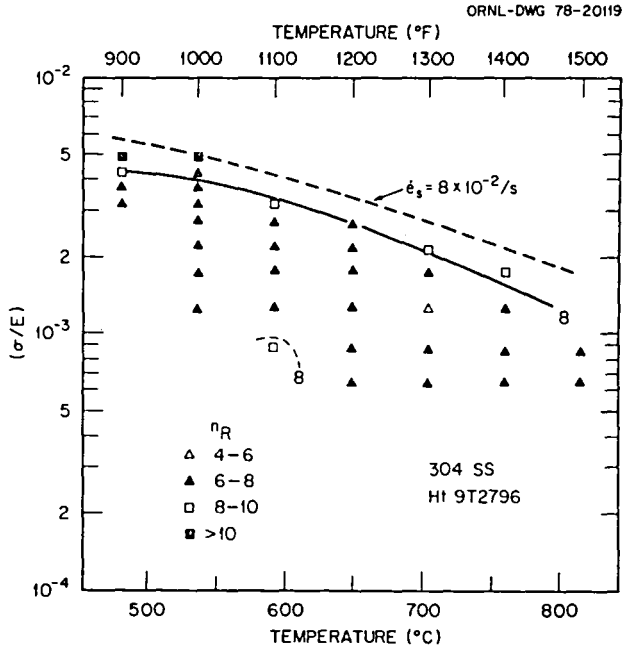

Fig. 1. Variation of the Stress Exponent for Rupture (n_R) with Modulus-Compensated Stress and Temperature.

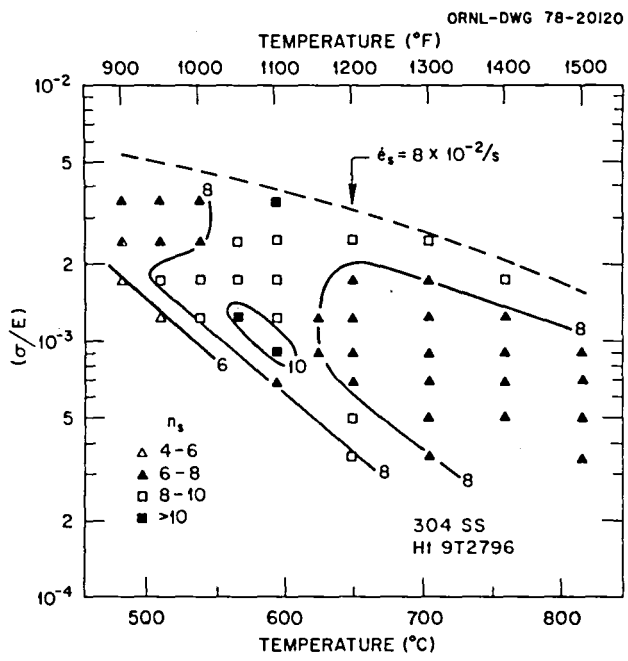

Fig. 2. Variation of the Stress Exponent for Secondary Creep Rate ($\dot{e}_s$) with Modulus-Compensated Stress and Temperature.

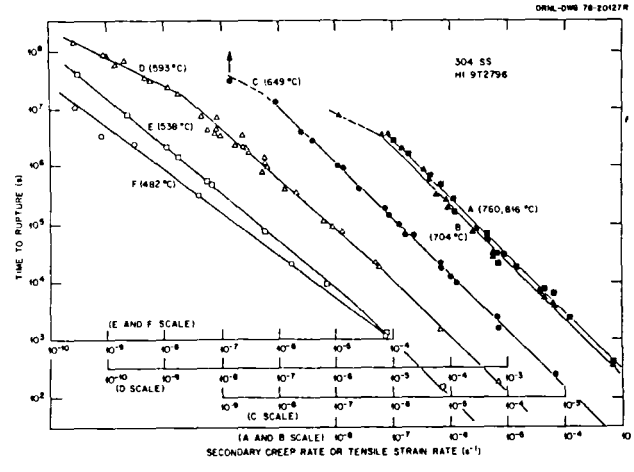

Fig. 3. Monkman-Grant Plots for Type 304 Stainless Steel at Temperatures from 482 to 816°C.

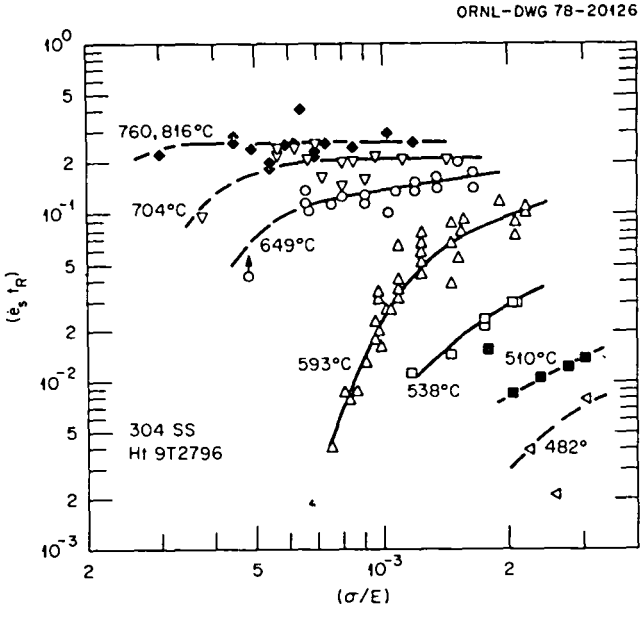

Fig. 4. Effects of Temperature on Linear Strain Parameter vs Modulus-Compensated Stress for Type 304 SS.

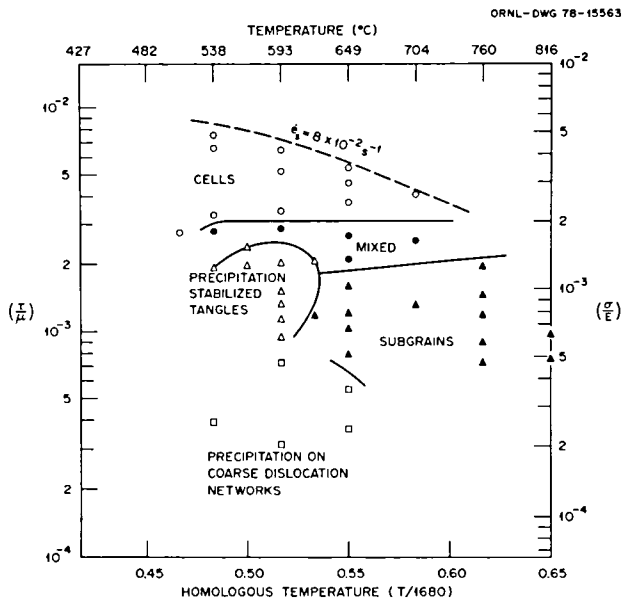

Fig. 5. Metallurgical Substructure Map for Type 304 Stainless Steel Heat 9T2796.

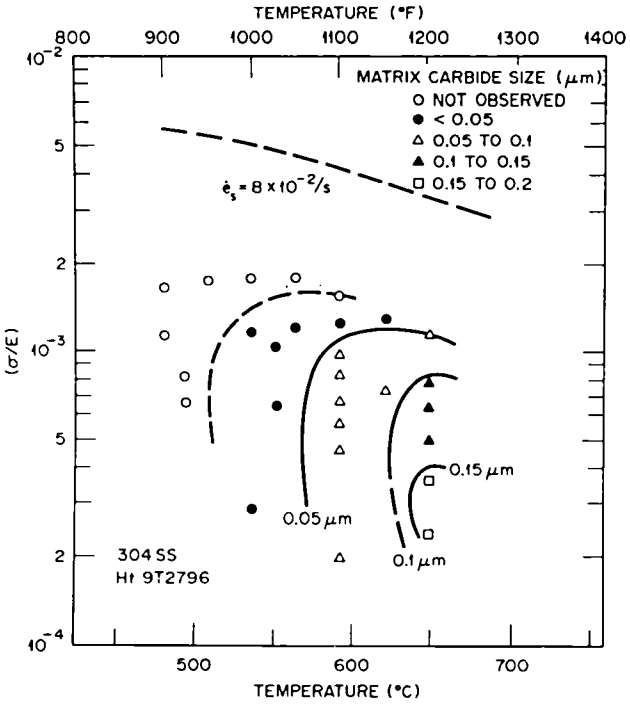

Fig. 6. Variation of Matrix Carbide Particle Size with Modulus-Compensated Stress and Temperature in Creep Tested Specimens

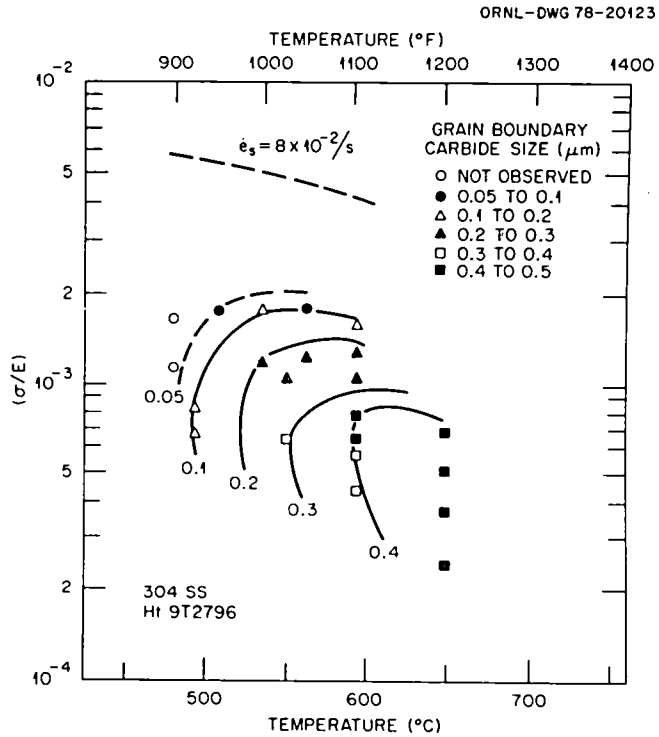

Fig. 7. Variation of Grain Boundary Carbide Particle Size with Modulus-Compensated Stress and Temperature in Creep Tested Specimens.

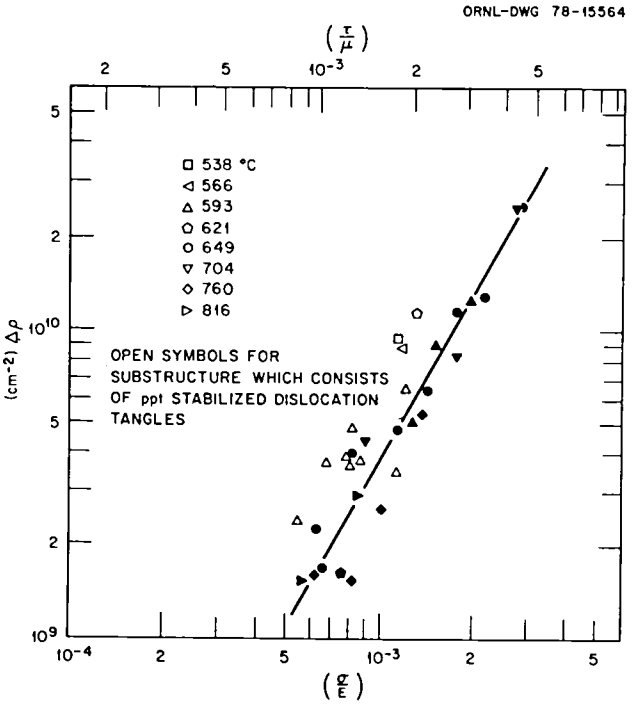

Fig. 8. Change in Dislocation Density vs Modulus-Compensated Stress for Creep and Tensile Specimens.

TENSILE AND COMPRESSIVE CONSTITUTIVE RESPONSE OF 316 STAINLESS STEEL AT ELEVATED TEMPERATURES*

S. S. Manson and U. Muralidharan
Case Western Reserve University
Cleveland, Ohio 44106

G. R. Halford
National Aeronautics and Space Administration
Cleveland, Ohio 44135

ABSTRACT

It is demonstrated that creep rate in compression is lower by factors of 2 to 10 than in tension if the microstructure of the two specimens is the same and they are tested at equal temperatures and equal but opposite stresses. Such behavior is characteristic for monotonic creep and conditions involving cyclic creep. In the latter case creep rate in both tension and compression progressively increases from cycle to cycle, rendering questionable the possibility of expressing a time-stabilized constitutive relationship.

The difference in creep rates in tension and compression is considerably reduced if the tension specimen is first subjected to cycles of tensile creep (reversed by compressive plasticity), while the compression specimen is first subjected to cycles of compressive creep (reversed by tensile plasticity). In both cases, the test temperature is the same and the stresses are equal and opposite. Such reduction is a reflection of differences in microstructure of the specimens resulting from different prior mechanical history. If specimens of identical microstructure are tested in tension and in compression, large differences in creep rate are again evident, whether that microstructure was developed by prior loading in tensile creep/compressive plasticity or by tensile plasticity/compressive creep. The significance of the differences in creep rate under tension vs. compression, as related to the development of constitutive relationships for creep-fatigue problems, requires further study.

Little research has been conducted to explain the physical basis for this behavior. Several speculative reasons are offered, but require verification.

*This work was performed under NASA Grant NAG3-46.

INTRODUCTION

It is common to assume that the creep characteristics of metals in compression are similar to those in tension. Such an assumption derives from the fact that the time-independent deformation characteristics in tension and compression are similar. Very few experimental programs have, however, been conducted to determine the validity of presupposing similarity of creep characteristics.

In the course of our studies of Strainrange Partitioning over the past decade it has become clear to us that the differences between tensile and compressive creep rates at the same stress level can be appreciable, at least for 316 stainless steel, which we have investigated most extensively. The early tests in 1971 [1] on cyclic creep were very revealing in this respect. These tests will be discussed later in this report. Loading was first in tension, allowing creep to develop a pre-specified strain. The stress was then reversed to a compression of equal magnitude, and this stress was maintained until the compressive creep strain completely reversed the tensile strain. In many cases the time required to produce the compressive creep strain was as much as a factor of three or more higher than that to develop the tensile creep strain. This long time was, in fact, the basis for conducting what turned out to be the first cp test (in Strainrange Partitioning terminology [2]) when an attempt was made to reduce the unacceptably long times required to reverse the tensile creep by imposing much higher compressive stress which reduced the reversal time essentially to zero.

In addition to the experience with the cyclic creep tests, we have observed in a number of other test programs that the compressive creep rate at a given stress level is lower than the corresponding creep rate at an equal tensile stress. It is the purpose of this paper to outline the results of some of these experiments. Though the difference between tensile and compressive creep strain rates is not necessarily of great importance in many aspects of formulation of the constitutive relations discussed in this Conference, it may be of significance in some cases, as will be illustrated later.

The micromechanistic reasons for the differences in creep rates have not been extensively investigated; in this report we offer several speculations which, of course, require verification.

ACKNOWLEDGMENTS

The authors are indebted to Mr. Aydin Seren and Mr. Donald Roulette, graduate students at CWRU, whose experimental results have been freely used in our discussion. We are also grateful to Mr. R. W. Uhinck of NASA Lewis who prepared some of the figures, and to Ms. Tilda Paltza of CWRU for typing the manuscript.

EXPERIMENTS INVOLVING DIFFERENCES BETWEEN TENSILE AND COMPRESSIVE CREEP RATES

The following discussion relates to observations wherein appreciable difference was observed between tension and compression creep rates. Although most of the results shown involve AISI 316 stainless steel, we have also observed the effect in a limited number of other materials, which leads us to speculate the phenomenon is a general one, the magnitude of the effect varying, of course, among materials.

A. CYCLIC CREEP RUPTURE TESTS

a) Background

Reference to these tests has already been made in the introduction. They were initiated in an effort to improve the time-and-cycle approach for treating creep-fatigue, as discussed in Ref. 1. In this approach creep damage is taken as the ratio of time at which a given stress and temperature is imposed divided by the creep-rupture time at the same stress and temperature. Because the use of monotonic creep-rupture tests often gives poor results when so applied, and in recognition that creep-fatigue tests involve cyclic variations of stress, our hypothesis was that cyclic creep rupture tests would produce improvements in predictions made by this method. Reference 1, in fact, demonstrates the validity of this hypothesis.

The type of test adopted for obtaining cyclic creep rupture tests is shown schematically in Fig. 1. The loading was generally started in compression to insure that the stress level chosen would not immediately produce a run-away creep strain. As shown in Fig. 1(a) the selected stress was held constant until a specified total strain was reached, usually of the order of 1 to 2%. The time required is shown as AB in Fig. 1(a), and the strain pattern is shown by the curve OAB. At point B the stress was reversed to tension, and this stress was held constant until an equal tensile strain was reached. The stress and strain pattern during this period are shown as BCD in Figs. 1(a) and 1(b), respectively. The pattern of reversal of equal stresses and strains in tension and compression was repeated successively as shown in Figs. 1(a) and 1(b) for as many cycles as were required to rupture. The hysteresis loop followed in all cycles was essentially OABCDA of Fig. 1(c).

The results of these tests are shown in Fig. 2, representing a plot of stress versus rupture time, as in conventional creep-rupture plots. Monotonic creep-rupture is shown by curve M. When only the tension time of the test is used (neglecting the reversal time in compression), the results are shown by curve N. In the analyses of Ref. 1 we found good agreement between predictions and experiments when several types of creep-fatigue tests were analyzed using the creep rupture curve N in the "time-fraction" terms. The total time curve P, which includes the compression time, did not prove as useful as curve N in the analysis, and its development required excessively long times.

As can be seen from Fig. 2, factors as high as 5 or more existed between P and N. In order to minimize the test time a type of loop shown in Fig. 3 was developed. The compressive stress pattern BCE was introduced, reversing the creep strain AB by only essentially instantaneous plasticity. Thus the loop ABCDA (essentially what was later termed a cc loop in SRP terminology) was replaced by ABCEDA, later recognized as a cp loop (in the same terminology). While a small effect was produced on the tensile time creep-rupture curve N in Fig. 2, the curve so obtained for the cyclic creep rupture representation of the material was about equally suitable for creep-fatigue analysis by the time and cycle fraction method. Test time was, however, appreciably reduced.

b) Comparison of tension and compression creep rates

Since the tensile and compressive stresses were the same in the cc loops, and since the temperature was held constant, the results of these tests provide direct data for comparison of creep rates under the two loading conditions. Some of the data used are shown in Fig. 4 which is a scale plot analogous to the schematic of Figs. 1(a) and 1(b). Fig. 4 shows two effects on creep rate.

First, it is noted that both tension and compression creep rates vary as a function of time (or applied cycles). The time required to complete the first cycle is nearly a factor of 10 longer than the time required to complete the 90th cycle in this test which ran 98 cycles to cause rupture. In each cycle the time required to complete the tension creep is considerably shorter than the time required to complete the compressive creep of equal magnitude. Thus there are two major effects: the relation between the tensile and compressive creep rates in any single cycle, and the relations among the tensile and compressive creep rates in successive cycles.

The complete analysis of results shown in Fig. 4 is given in Fig. 5. Here both the tension and compression creep rates are plotted as a function of cycle ratio. It is clear from this figure that both the tensile and compressive creep rates increase as cycle ratio increases, varying by as much as a factor of 10 from the first cycle to the last few cycles. Similarly, it is clear that the tensile creep rate is higher than the compressive creep rate in each cycle. The compressive creep rate is, on average, about 1/3 as high as the tensile creep rate.

An addititonal test which shows similar results is shown in Fig. 6. This figure also clarifies how creep rates were determined without introducing error associated with cross-sectional changes that are different in tension and in compression. Figure 6(a) shows the hysteresis loop. By measuring the tensile creep rate at point E where the strain is zero, and the compressive creep rate at point F where the strain is also zero, true creep rates are determined, since the cross-sectional areas were exactly the same at the two points in the cycle. The creep rates are shown in Fig. 6(b). The tensile creep rate is

again seen to be two to three times as high as compression. Although the steepness of rise in creep rate in the later cycles gives the illusion that the two curves are approaching each other, the difference by a factor of two to three persists until near-failure, as can be determined by measuring vertical distance between the two curves. Since the vertical scale is logarithmic, this constancy of vertical displacement implies a constant ratio between the two values.

c) Significance of results

These results show not only that creep rate in tension differs from that in compression, but that both rates vary significantly during the lifetime, even for this simple repetitive loading pattern. Attempts to develop constitutive equations that will be applicable throughout the life should be in harmony with this simple observation.

On the other hand, it should be pointed out that stabilization has readily been achieved in many SRP strain cycling tests involving creep in only one direction. Thus while some caution is required in seeking constitutive relations involving reversed creep, the more practical applications in which the major creep component occurs only in one half of the cycle (tension or compression) does not seem to involve this complication.

B. CONSTANT LOAD TESTS

Another series of tests we have conducted in which differences in tensile and compressive creep rates have been observed relate to ordinary static creep under constant load. The results are described below.

a) Specimen Stabilization

In these tests the specimens were first stabilized relative to cyclic plastic strain by the scheme shown in Fig. 7. The strain amplitude was first gradually increased to 1% while cycling at a frequency of 0.20 Hz. Then 30-40 cycles of the 1% strain amplitude was applied, after which the strain amplitude was reduced during cycling in a manner symmetrical to the forward-loading. The cycles at constant $\pm$ 1% strain stabilized the material and established a repetitive hysteresis loop, similar to the manner a material is normally stabilized in room temperature fatigue to establish a cyclic stress strain curve. Such curves do not significantly reflect the hardening or softening characteristic of the early loading cycles. The stabilization was initially introduced because the intended purpose was to develop a constitutive creep model for the material for later use in creep-fatigue analysis. Thus it was thought appropriate to decouple the cyclic creep effects from the cyclic plasticity effects. In the present discussion we are concerned only with the static creep behavior of the stabilized material.

Fig. 7(b) shows the hysteresis loops developed during the increasing amplitude straining (continuous lines), the stabilized hysteresis loop (heavy line), and the decreasing amplitude straining (dotted lines). It is clear that in the final state the net stress and strain are both zero. Thus the creep tests which follow are on specimens which have neither residual stress nor residual strain nor do they have a memory of prior straining in one particular direction. Since the stabilization cycling is very rapid, there is essentially no creep damage on the test specimens. Also, since the specimen can withstand about 15 such blocks as shown in Fig. 7(a), the amount of fatigue damage is

also small.

b) Correction for cross-sectional area changes

Typical creep curves obtained are shown in Fig. 8 which are for a nominal 18 ksi stress in tension and compression at 1300F. While the creep curve OAB in tension is clearly higher than that in compression, part of the difference is due to cross-sectional area changes rather than inherent differences in creep characteristics at the two stress states. In tension the cross-sectional area continuously decreases as the strain decreases. Thus, for the constant load (nominally 18 ksi for the original cross-sectional area) the true tensile stress is continuously increasing.

The compression creep curve OA'B' involves an increasing cross-sectional area which reduces the true compressive stress.

If we assume that creep rate at constant temperature is proportional to a power law of stress m we can correct the tensile creep rate at a strain ε by dividing by $(1+\varepsilon)^m$ to obtain the rate that would have been observed if the stress had been kept constant by reducing the load progressively. Similarly, for the compressive strain the creep rate must be divided by $(1-\varepsilon)^m$ to obtain the appropriate strain-independent creep rate.

c) Test results

Figure 9 shows the results for tension and compression for a number of creep tests conducted at several stress levels in both tension and compression. Approximate straight lines can be drawn through the test results when steady state creep rate is plotted against stress on logarithmic scales. Thus a power law exists between the two variables. As seen in the figure strain rate for

both tension and compression vary as approximately the 11th power of stress, the multipliers being different depending on whether the loading is tension or compression, and whether the cross-sectional area correction is applied or not. However, even when the correction is applied, the creep rate in tension is about a factor of 5 higher than in compression. The "engineering" values, for which no correction is made, show differences of about a factor of 7.

d) Significance of results

These results show that, at least for 316 stainless steel at 1300F, it is inappropriate to develop constitutive relations based on the assumption that tensile creep rate and compressive creep rate are equal at the same stress and temperature. However, they also show that creep rate varies as the 11th power of stress. Thus, to maintain a creep rate in compression equal to that in tension it is necessary to increase the compressive stress by only a small amount. If, for example, the creep rate at a tensile stress of 40 ksi is to be reproduced as an equal value under compression, the compressive stress need only be increased to 46.40 ksi. When tests are conducted which are strain-controlled, forcing equal tensile and compressive creep rates will cause the compressive stress to be higher than the tensile stress (16% in the present illustration).

No reversed creep was involved in these tests. How the results would be affected by the presence of such creep requires further study. But from the results of Section A it is speculated that a significant effect could develop. Constitutive relationships for application to cyclic creep and plasticity might require appropriate recognition of this phenomenon.

C. THERMOMECHANICAL LOADING TESTS

Applications involving simultaneous variation in stress, strain, and temperature, commonly called thermomechanical loading, are among the most important cases for which constitutive modeling is required. Because a cooperative program between Case Western Reserve University and NASA-Lewis is currently underway, it is appropriate to include here some of the results which are pertinent to the question of the relation between tensile and compression creep characteristics.

a) Tests in progress

Figure 10 shows some of the control patterns of tests that are in progress. These tests use AISI 316 stainless steel specimens, not, however, stabilized according to the pattern of Fig. 7. In one type of test, Fig. 10a, the strain and temperature are cycled in-phase, high temperature and tensile stress being achieved simultaneously. Such a loading usually develops cp type of strain because the highest tensile stresses occur while the temperature is high, causing creep, while the highest compressive stresses occur when the temperature is low so that no compressive creep occurs. In the second type of loading the strain and temperature are out of phase, producing net compressive creep because the temperature is high only when stress is compressive.

b) Creep rates during actual cycling

Ideally, it would be desirable to compare the creep rates of the specimens at the same temperatures and at equal but opposite stresses at appropriate points in the in-phase and out-of-phase cycling where such conditions develop. Unfortunately, such conditions do not develop for the very reason that compres-

sive creep response differs from the tensile creep response. This fact can be seen in Fig. 11 which shows the stresses developed at each temperature during the in-phase and out-of-phase tests. If tensile and compressive creep response were similar, the two curves would be mirror images of each other with respect to the horizontal axis. The fact that the compressive stresses reached are higher than the tensile values, verifies that creep rates at a given stress and temperature are lower in compression than in tension. Thus, to maintain the equal strain rates imposed, a slightly higher stress develops during the out-of-phase loading tests, as is clear from Fig. 11. From this figure it can be seen, then, that it is not possible to compare directly specimens taken from each of these tests when they are at the same temperature and at stresses which are equal but of opposite sign.

By writing analytical relations for creep rates in the two tests in terms of stress and temperature, it is possible, however, to calculate the creep rates at the same stress in tension and compression. Several forms of constitutive relationships have been studied; we consider here only the simplest type taken in the form of the Arhenius equation

$$\dot{\varepsilon} = A\,\sigma^{m}\,e^{-\frac{\Delta H}{RT}} \qquad (1)$$

Analyses were made using the in-phase data only, the out-of-phase data only, and combining all the data into one correlation. A complete discussion of all the results will be published when the program is completed; the tentative results pertinent to the current subject will be discussed only briefly.

Using the common formulation of all the data, including both the in-phase and out-of-phase results, the equation becomes:

$$\dot{\varepsilon}_{ss} = (123.832)\sigma^{10} \exp\left(\frac{-180633}{T}\right) \qquad (2)$$

where σ = stress, ksi

T = temperature, degrees R

$\dot{\varepsilon}_{ss}$ = creep rate per sec.

Fig. 12 shows the correlation between the experimental creep rates measured in both the in-phase and out-of-phase tests and the computations based on Eq. (2). The agreement is quite good, suggesting a common constitutive relationship for both tension and compression creep rates as a function of stress and temperature. While this result is very satisfying from the analyst's view of desiring to neglect differences between tensile and compressive constitutive behavior, it seems to negate the findings about the differences discussed. In order to clarify the apparent discrepancy additional tests were conducted as discussed in the next section.

c) Creep rates at approximately constant microstructure

The microstructure of a specimen sampled at a point of tension during the in-phase loading can be considerably different from the microstructure of a specimen sampled from an out-of-phase test at the same temperature (and approximately equal and opposite stress). Thus, although it is fortuitous that the same equation can be used to determine the strain rate of both specimens, the equality of tensile and compressive creep rates does not negate our general

finding that compressive creep rate is lower than the tensile creep rate at the same temperature and equal but opposite stress. To determine if this finding is general, and still valid for material in thermomechanical loading, it is necessary to conduct tests in tension and compression of material in the same microstructural state. Ideally, a scheme such as shown in Fig. 13(a) would be suitable for this purpose. The hysteresis loop represents the path, for example, of in-phase loading. At point A the thermomechanical loading is discontinued, and temperature and stress are "frozen" and maintained constant at the value achieved at this point. By holding the stress constant, creep strain occurs along AB as a function of time as shown in Inset I of Fig. 13(a). The steady state creep rate which develops is then characteristic of the tensile creep behavior of the material in its microstructural condition at A. To obtain the compressive creep characteristic we should, ideally, use a second specimen, stabilize the loading loop by applying the same number of cycles, stop again at point A, and then reverse the stress to an equal but opposite value, maintaining the temperature. The path A'B', both on the stress-strain diagram, and the strain-time diagram of Insert II then represents the compressive characteristic of the material in its microstructure of point A. The creep curves of Inserts I and II provide the needed comparison of tension and compression for a material in the same microstructural condition.

The scheme actually used in this program is shown in Fig. 13(b). A single specimen was first crept along AB, after which the load was reversed to an equal but opposite value, and the compressive creep characteristic A'B' was obtained. This procedure was used for two reasons: conservation of specimens, and avoiding the possibility of scatter resulting from using separate speci-

mens. Actually, then, a small change in microstructure was introduced by the tensile creep AB for the material subsequently tested along A'B'. However, the economy and efficiency of using a single specimen was deemed sufficient to justify the alternate approach in the preliminary tests. Furthermore, our expectation was that the compressive creep rate would be lower than the tensile creep rate. Since it is reasonable to assume that the prior tensile creep AB would, if it had any effect, accelerate the compressive creep rate (in accordance with the results of Figs. 1-3), any observed lower creep rate in compression would in fact be accentuated were the prior tensile creep not imposed.

A number of tests of the type described above were conducted, stopping at various points in the in-phase loading loop. Similarly, analogous tests were conducted by stopping at selected points of compressive stress in the out-of-phase loading, and conducting tests in both compression and tension for microstructures developed in these tests. Typical results shown in Fig. 14(a) relate to one of the tests for in-phase loading; Fig. 14(b) displays results for out-of-phase loading. It is clear that in both cases the creep rates in compression are significantly lower than these in tension. The other tests corroborated these observations.

We can conclude from this study that the generality holds for material in thermomechanical tests, namely that if material is sampled from any point in its path and tested both in tension and in compression, the tensile creep rate will be considerably higher than the compressive creep rate. The two tests must, however, be conducted on material in the same microstructural state.

D. CYCLIC LOADING OF HASTELLOY X

It is interesting to study the results of Walker [3] on Hastelloy-X to ascertain whether the general behavior observed on 316 SS also applies to his material. Some of his test results are shown in Fig. 15. Discussion of the results of his calculations based on the Functional Theory are beyond the scope of this paper. However, the experiments are amenable to analysis for the present purpose.

Walker's tests were conducted on a specimen which was continuously cycled at a constant strain rate, stopping at various points to establish the creep rate for the material in its current metallurgical state. After each creep loading at constant stress, the loop was re-stabilized before proceeding to the next point. Thus the creep tests were on materials in different metallurgical states, and direct comparison of tension and compression involves the difficulties already discussed in connection with Fig. 2. However, it is still instructive to make the comparison because the careful experiments do reveal differences in the two creep rates.

The continuous curves of this figure show experimental creep curves at various stresses. Some are tension creep curves, others compression. While the comparison can be made by direct examination of the curves of Fig. 15, the cross-plots of Figs. 16 and 17 are more convenient for quantitative comparison.

Fig. 16 shows the cross-plot of stress versus strain after 40 seconds. OA shows the strain developed after this time for tensile loading, OB the strain for compression loading, for each of the stress levels studied. The dotted curve OB' is a replot of OB, changing signs of both stress and strain. By comparing OA to OB' it is clear that at any stress level the amount of strain in

tension is more than that in compression after the 40 sec. used as a parameter. The cross-plot of Fig. 17 shows the ratio of strain developed in tension to that developed in compression after various times for the 21.5 ksi tests. While these results are not as dramatic as those we have obtained for 316 SS, it is quite clear that tensile creep rate is higher than compression creep rate at the same temperature but equal and opposite stress.

PARAMETERS THAT CAN AFFECT CREEP RATE AS A FUNCTION OF STRESS DIRECTION

The reason for the differences in creep rate at equal tensile and compressive stress has not received much attention. In fact, the phenomenon is not sufficiently well recognized to have stimulated study. We can only speculate at this time why the phenomenon exists. Following are some possibilities.

I. Effective Friction at the Grain Boundary

One way of viewing the problem is by analogy to friction of masses in contact moving relative to each other. Since creep frequently involves grains sliding along their boundaries we can regard the individual grain motion and the "friction" between them. The treatment is complicated, of course, by the fact that there are numerous grains oriented at numerous directions relative to each other. A simplified analysis is shown in Fig. 18 which assumes an average orientation of 45 degrees. Drawing the analogy with the movement of a weight on a frictional surface, shown in Fig. 18(a), we can see in Fig. 18(b) that the net frictional force is larger when two grains are in compression than they are when in tension. If we choose R as the ratio of the two forces, and assume

that the relative creep rate varies as some power law of R, we get the results shown in Fig. 18(c). The plot shows the relationship for different choices of μ and m. It is seen that reasonable choices of μ and m produce R values agreeing with our experimental results.

II. Change of Lattice Parameter

The size of the lattice increases in tension and decreases in compression. An effect can thus be produced on the creep rate according to the explanation given in Ref. 5:

> "For close-packed crystals like fcc, hcp, the partial molar volume of vacancies is an appreciable fraction of molar volume of the metal. Under hydrostatic pressure in tension, the specimen will lose vacancies in an effort to relieve the pressure increase. This decrease in the concentration of vacancies will in turn decrease the self diffusion."

If creep rate is influenced by self-diffusion, as is commonly accepted, the hydrostatic compression should reduce creep rates and hydrostatic tension should increase creep rates.

III. Grain Boundary Cavitation:

At high temperature, cavities are generated in the grain boundaries which are in tension, facilitating the movement of one atom over the other, increasing in creep rate. In compression, however, the cavities are absent or collapsed even if activated previously in tension. This phenomenon is shown schematically in Fig. 19. Accordingly we can expect higher grain boundary creep when the net force across the grain boundaries is tensile than when it is compressive.

IV. Defects Other Than Grain Boundary Cavitation

Any defects developed in the microstructure of the material would tend to be open in tension and closed in compression, Fig. 20. Hence there would be greater tendency for reduction of cross sectional area in tension. Therefore the creep rate would be higher in tension than in compression.

CONCLUDING REMARKS

In all of the various types of tests that we have studied, tensile creep rate has always been higher than compressive creep rate if the loading is on specimens that have the same microstructure. This similarity of microstructure may be the result of absence of significant prior straining history, or it may be the result of a complex history of thermomechanical loading. Differences in creep rate from 2 to 10 have been observed. However, if the microstructure of the specimen to be tested in tension is different from that used in compression, the general pattern of behavior can be altered, although in the limited cases we have examined, there is still a bias toward lower creep rate in compression. Some of the effect is geometrical, -- tension producing a higher true stress because of decreases in cross-sectional area, while the area of a compression specimen increases. However, even when appropriate corrections are made for cross-sectional variations, the qualitative comparisons are not altered, although quantitatively the effect is somewhat smaller.

Of special interest is that the microstructure that develops during hysteresis cycling -- whether at constant strain rate and constant temperature, or whether the temperature variation is cycled in- or out-of-phase with the strain -- seems to be such as to bring closer together creep rates in the two direc-

tions when the tension specimen is taken at a point in the tensile part of the hysteresis loop and the compression specimen is taken at a point in the compression part of the loop. Whether there is a natural tendency for microstructure to develop to produce such a bias remains to be determined by studying additional loading patterns. From an engineering point of view, the effect is fortuitous because it makes more accurate the assumption usually made that the two creep rates are equal.

Even when there is an appreciable difference between the two creep rates at equal but opposite stresses, the error of engineering calculations based on the assumption of rate equality is mitigated by the fact that creep rate bears a high-exponent power law relationship to stress, so that only moderate changes in stress are needed to bring the actual creep rates to equality. Also, it is fortunate that in most of the important engineering problems involving stress and strain reversal, particularly thermal fatigue problems, the loadings are governed by imposed strains and strain rates. Thus the assumption that the stresses developed follow the same stress / strain / strainrate relationships in both tension and compression produces small error in the stress determinations. Were the loads specified, the errors in stress and strain rates would be much higher. The effect is further mitigated by the metallurgical tendency of microstructural development to more closely justify the usual engineering assumption.

Thus, while the effect of the phenomenon is somewhat suppressed in some practical engineering problems, its presence cannot be negated. As illustrated in this report at least some applications can better be understood in terms of the characteristic differences between creep rates in tension and compression.

Further experience may reveal other important applications. In any case it is an interesting phenomenon, both from mechanistic and analytical viewpoints, and it merits recognition, if not further study.

Finally, this study has led to a closer focus on a long-held observation that a combination of tensile and compressive creep produces an anomalous effect, at least on 316 SS. When creep is either absent or monotonic -- i.e. in pp, pc, or cp loading, we have usually found that after a few cycles of loading a stable hysteresis loop develops. Stress, strain become repetitive with respect to time as measured from some arbitrary point on the hysteresis loop. When reversed creep is present, i.e. involving cc loading, the temporal aspects of the loop are not repetitive. In the cases we have studied, extreme softening takes place, and an attempt to apply a single constitutive relationship to characterize all cycles could lead to significant error. The mechanistic effect here, as well as the mechanisms that cause creep rate in tension to be much higher than that in compression justify further study. Such study should lead to an improved understanding of the nature of creep in engineering materials and provide a useful input toward determination of appropriate time-dependent constitutive relations for handling reversed creep.

REFERENCES

1. Manson, S.S., Halford, G.R., Spera, D.A., "The Role of Creep in High Temperature Low Cycle Fatigue," Advances in Creep Design, The A. E. Johnson Memorial Volume, edited by A. I. Smith and A. M. Nicolson, Applied Science Publishers Ltd., London, 1971, pp. 229-249.

2. Manson, S.S., Halford, G.R., and Hirschberg, M.H., "Creep Fatigue Analysis by Strainrange Partitioning," Design for Elevated Temperature Environment, ASME, 1971, pp. 12-24, DISC, pp. 25-28.

3. Walker, P.K., "Research and Development program for non-linear structural modeling with advanced time-temperature dependent constitutive relationships," NASA CR-165533 and PWA-5700-50.

4. Manson, S.S., "Some Useful Concepts for the Designer in Treating Cumulative Fatigue Damage at Elevated Temperatures," in Mechanical Behavior of Materials, Proceedings of the Third International Conference Held in Cambridge, England, Aug. 22-24, 1979, Vol. I, pp. 13-45.

5. Shewman, P.G., "Diffusion in Solids," McGraw-Hill Book Co., 1963.

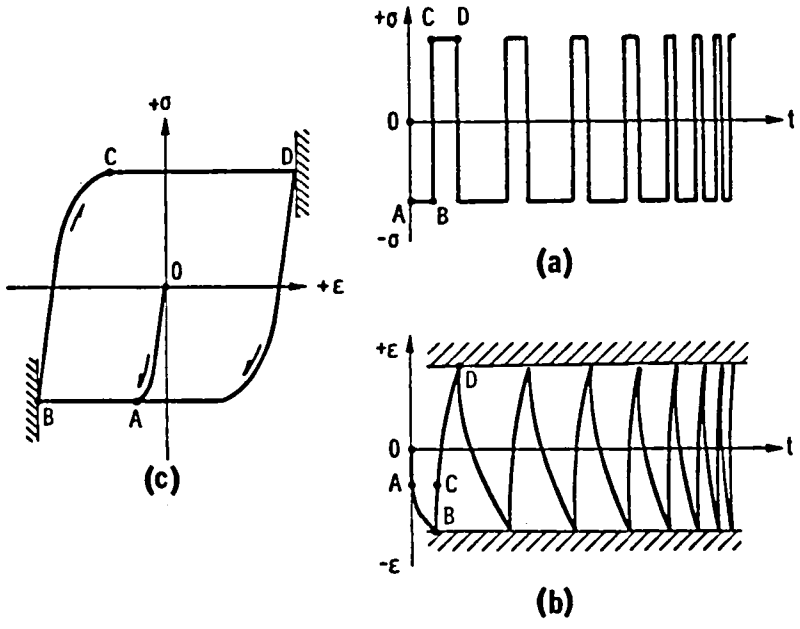

Figure 1. Schematic diagram of the cyclic creep experiment.

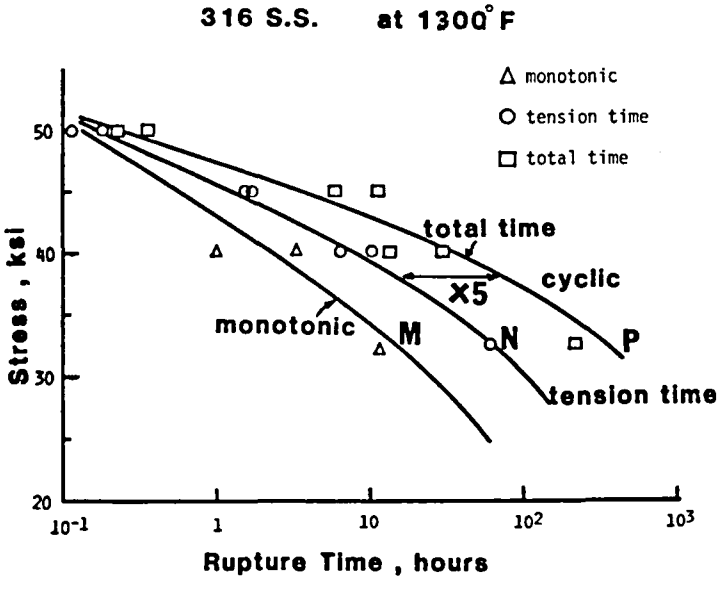

Figure 2. Tension time and total time to rupture from the cyclic creep rupture tests and time to rupture under monotonic creep plotted as a function of stress (Ref. 1).

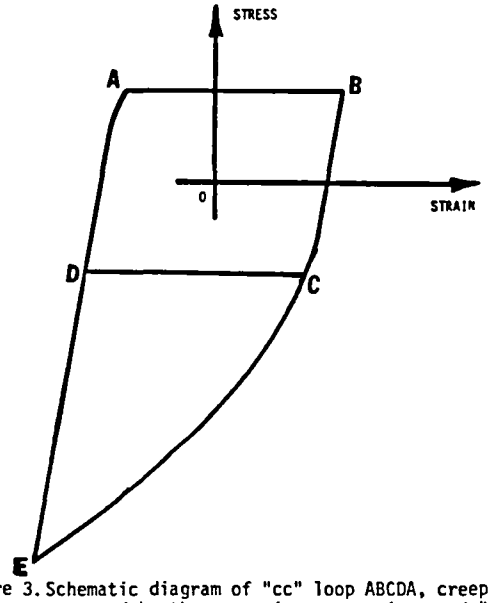

Figure 3. Schematic diagram of "cc" loop ABCDA, creep in tension reversed by the creep in compression, and "cp" loop ABCEDA, creep in tension reversed by the plasticity in compression.

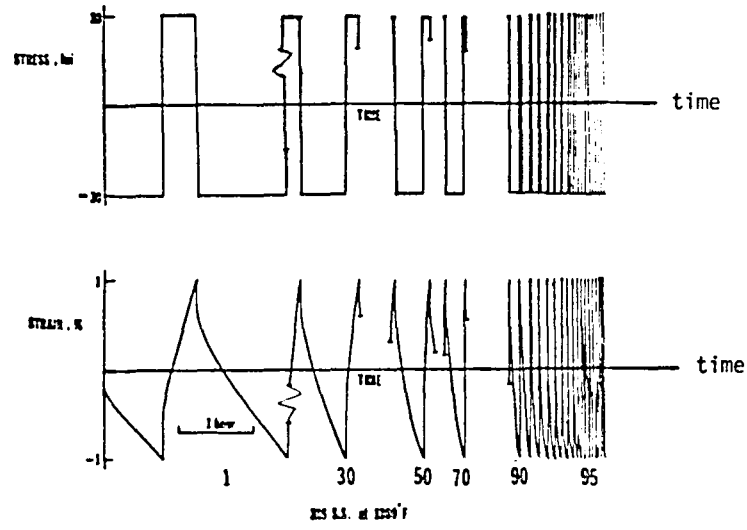

Figure 4. Stress and strain response of a typical cyclic creep-rupture test conducted on AISI 316 stainless steel at 1300°F.

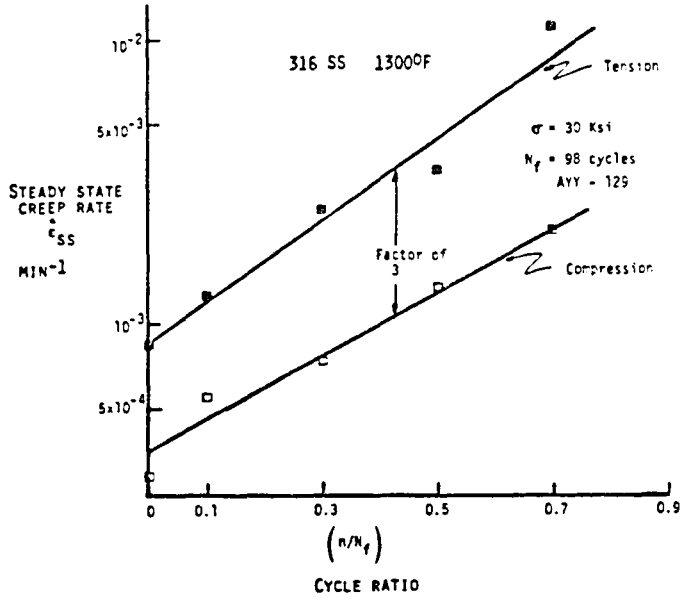

Figure 5. Tensile and compressive creep rates as a function of applied cycles for the cyclic creep rupture test shown above.

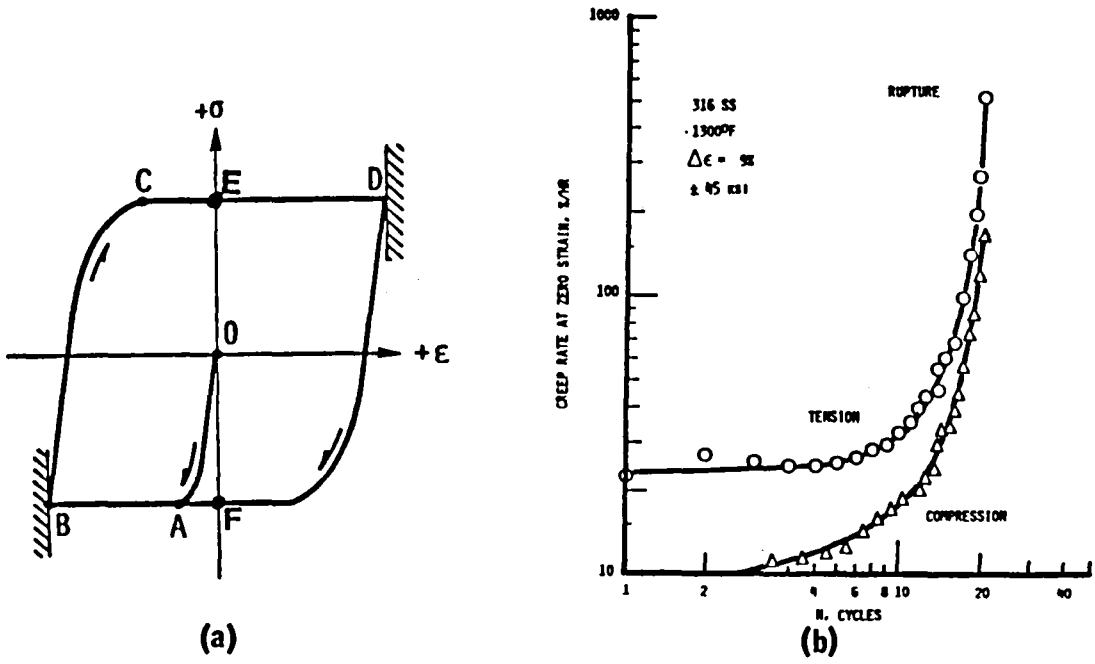

Figure 6. Tensile and compressive creep rates measured at points of zero strain (E and F) plotted as a function of applied cycles for a cyclic creep rupture test.

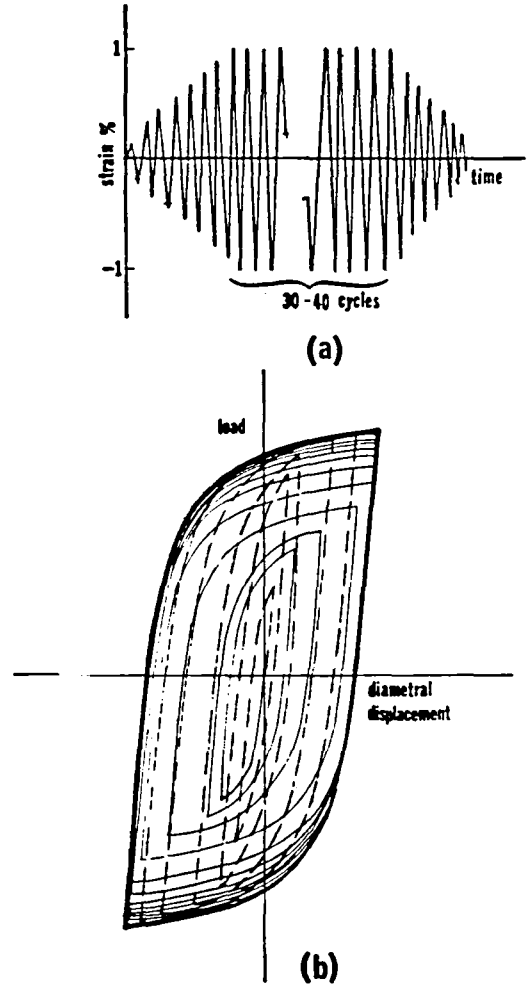

Figure 7. Stabilization of AISI 316 stainless steel at 1300°F by the rapid strain cycling.

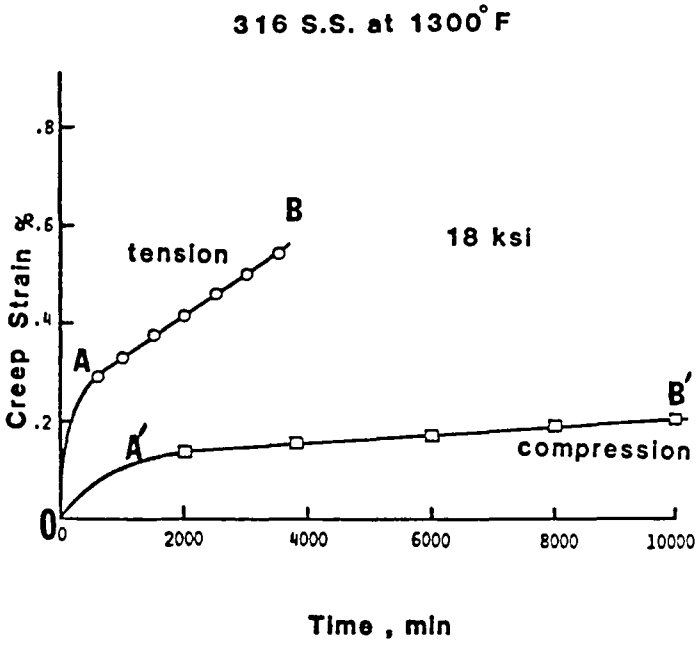

Figure 8. Creep responses in tension and compression for typical tests conducted at ± 18 ksi

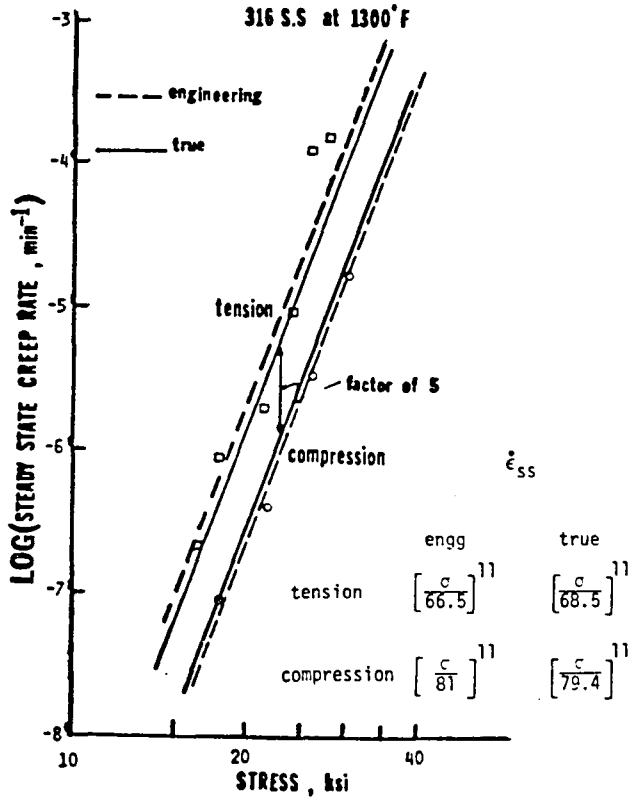

Figure 9. Engineering (observed) and true (corrected for the change in cross-sectional area) creep rates plotted as a function of applied stress on log-log coordinates

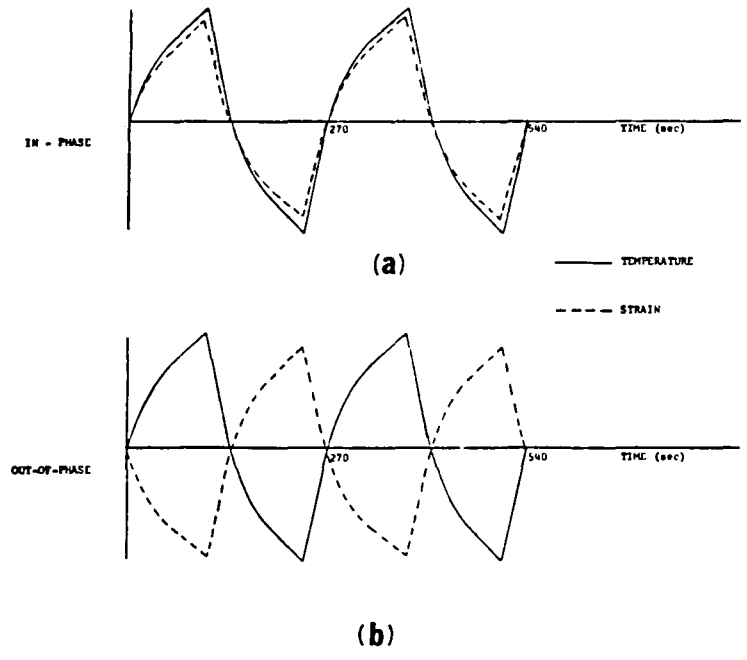

Figure 10. Temperature and strain variations with respect to time in in-phase and out-of-phase thermomechanical tests.

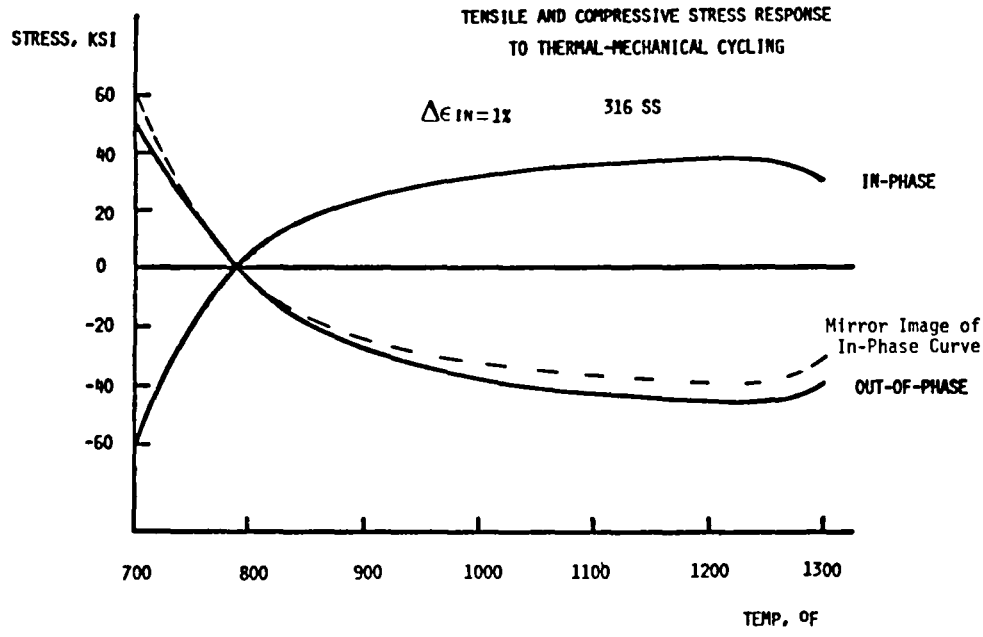

Figure 11. Stress-temperature responses for the in-phase and out-of-phase tests.

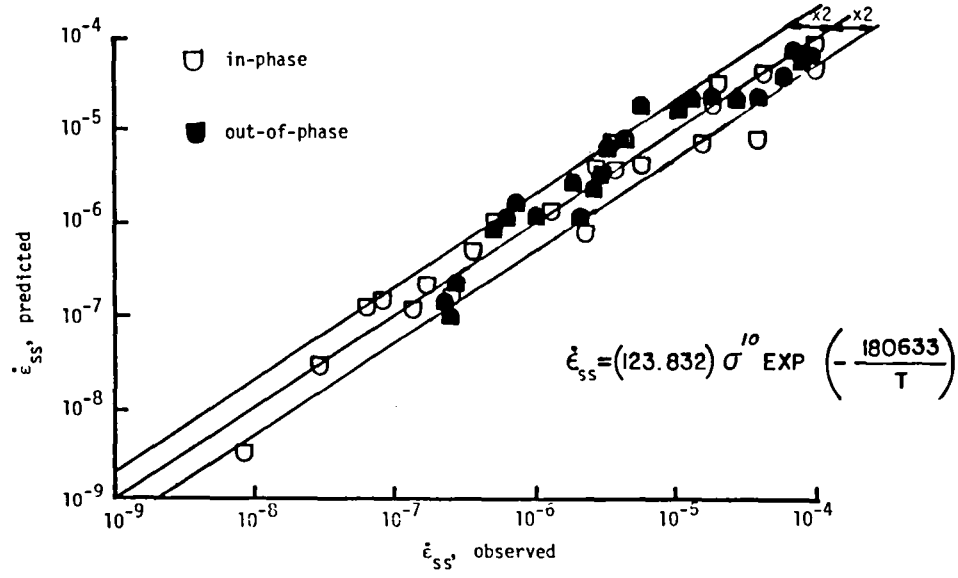

Figure 12. Comparison of the observed steady state creep rates with the ones predicted by the formula given above.

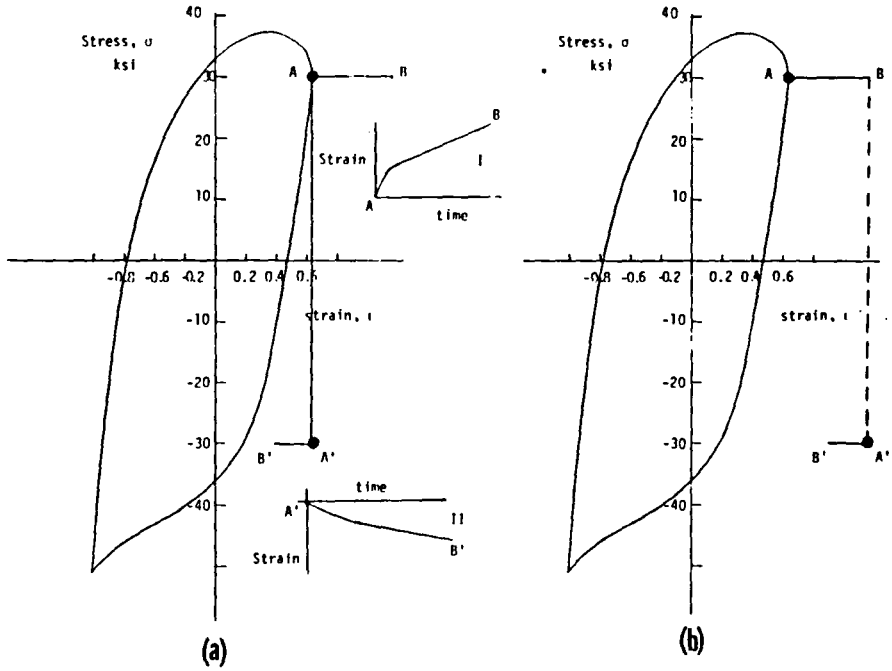

Figure 13. Stress-strain response of a typical in-phase thermomechanical test.

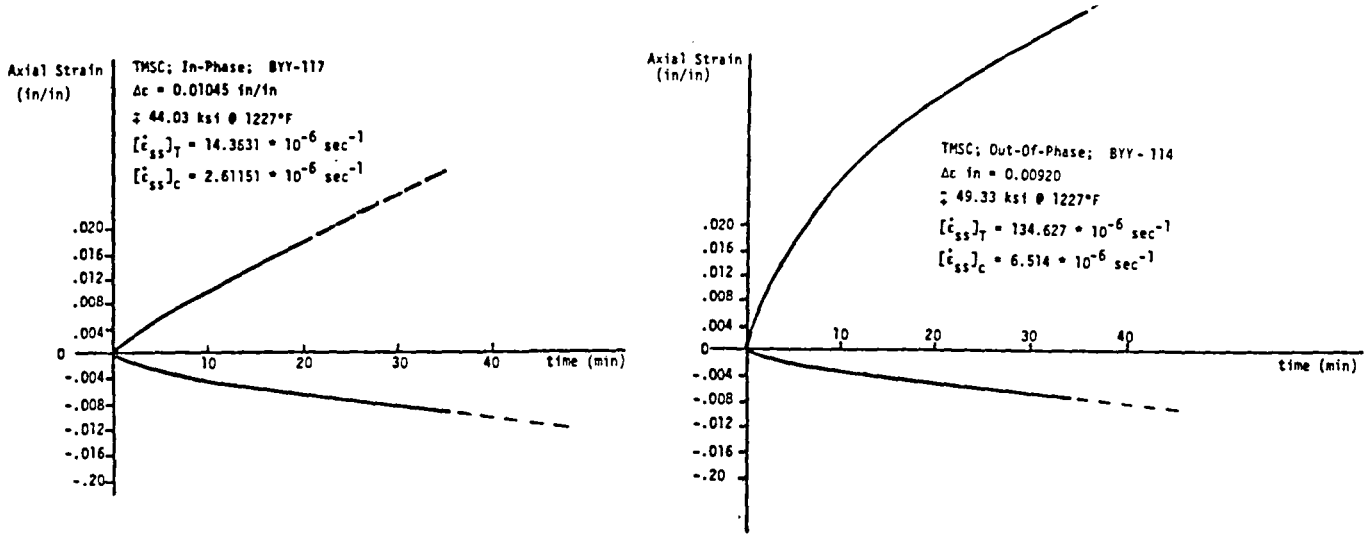

Figure 14. Creep responses in tension and compression at the stress levels shown for the in-phase and out-of-phase thermomechanical tests.

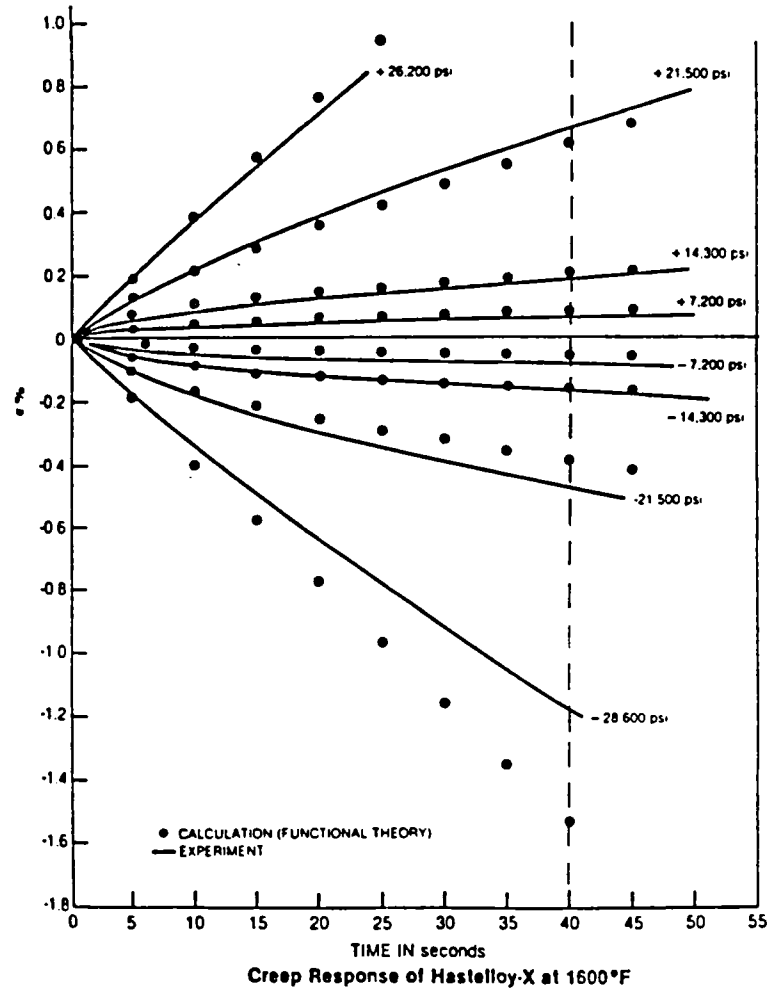

Figure 15. Creep responses in tension and compression of Hastelloy-X at 1600°F for stress levels shown (from Ref. 3).

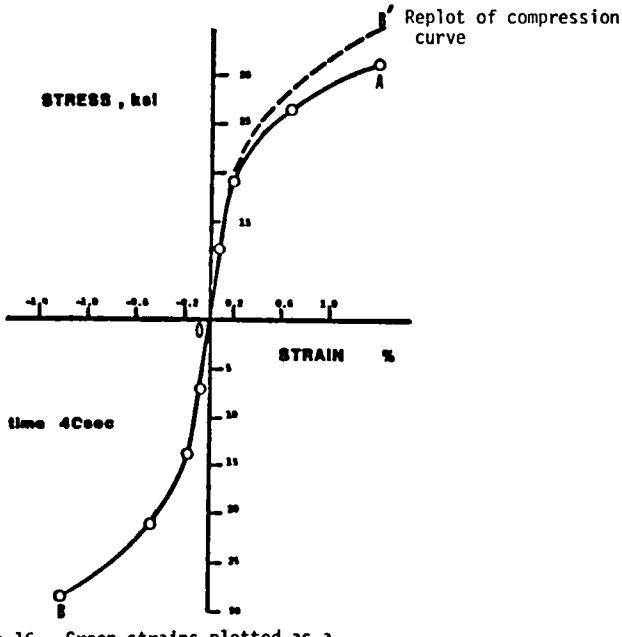

Figure 16. Creep strains plotted as a function of stress at a given time of 40 sec.

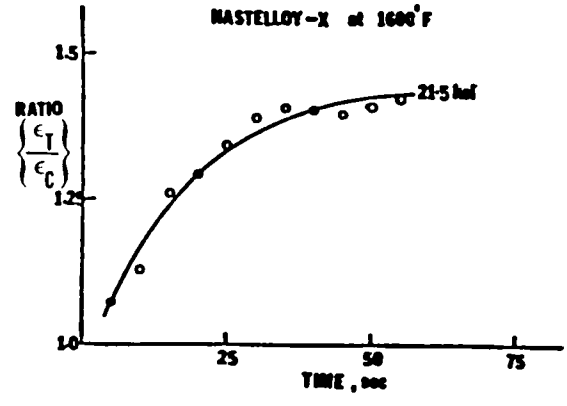

Figure 17. Variation of the ratio of tensile to compressive creep strains shown as a function of time.

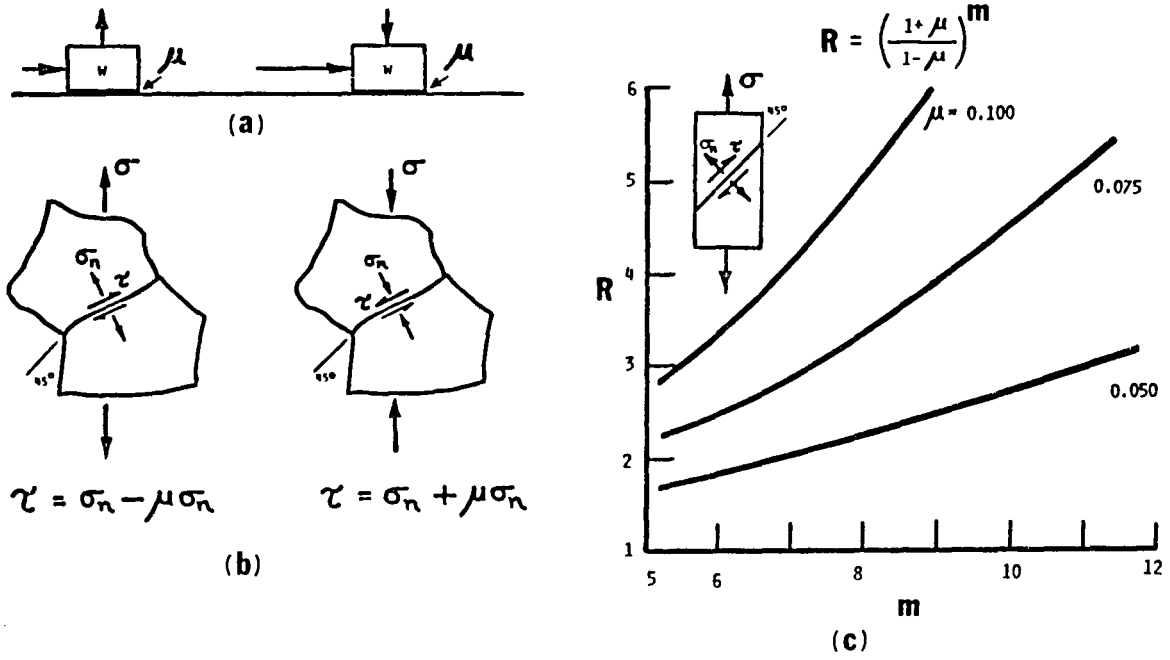

Figure 18. Ratio of the creep rates in tension to that in compression due to effective friction at the grain boundary shown as a function of exponent 'm'.

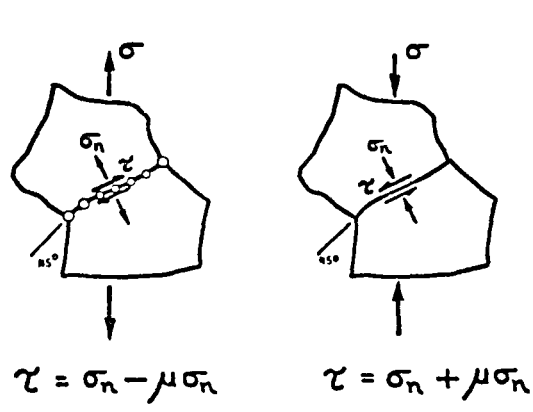

Figure 19. Grain boundary cavitation activated by net tensile stress and absent or collapsed in compression.

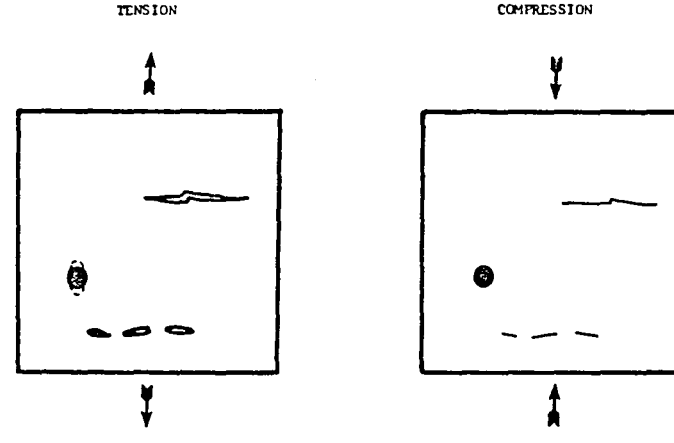

Figure 20. Reduced cross-sectional area in tension due to opening of the defects other than grain boundary cavitation in tension and not affected in compression.

EVALUATION OF THREE CONSTITUTIVE MODELS FOR THE PREDICTION OF HASTELLOY X ELEVATED TEMPERATURE CYCLIC RESPONSE

Vito Moreno
Pratt & Whitney Aircraft Group
United Technologies Corp.
East Hartford, Connecticut 06108

An evaluation of material constitutive models for the prediction of elevated temperature cyclic stress and strain response is presented. This activity is being conducted under an ongoing NASA Contract (Ref. 1) to identify a procedure for predicting structural response (stress / strain) without the need for expensive and time consuming non-linear finite element analysis.

The approach for the method development assumes that, for a thermally loaded structure, the overall strain history can be defined by linear elastic analysis. The local stress history at a fatigue critical location is then determined from a one-dimensional material behavior model and the local strain and temperature conditions. Three material models are currently being evaluated to assess their ability to predict relevant high temperature cyclic material response characteristics. They are: (1) a time independent classical plasticity and creep representation, (2) a time dependent viscoplastic model capable of predicting combined creep and plasticity effects, and (3) an approximate elastic analysis approach that uses a series of stress-strain curves and a cyclic hardening model to determine reverse plasticity.

Previous structural analyses and life prediction activity conducted on a representative gas turbine high temperature component, i.e., combustor liner (Ref. 2), has indicated that the local stress-strain response reflects several high temperature material cyclic response characteristics. They include: (1) strain rate dependence, (2) creep-plasticity interaction and (3) the interaction of properties associated with variable temperature (thermomechanical) loading. In the current program, these characteristics are being systematically investigated to aid in the material model evaluation. Hastelloy X specimen constitutive test data developed in References 2 and 3, and under the present program, is being used to establish a cyclic response data base. Representative stress-strain data for continuous fully reversed cycling, fully reversed with creep and relaxation hold periods, and various thermomechanical loading histories comprise the data base.

Preliminary results comparing two of the material models with the data base are shown below. Figure 1 compares the predictions of the time-independent classical plasticity model and the viscoplastic model with 1600°F continuous cycle testing. The classical plasticity model shows a slightly greater stress amplitude, due primarily to the differences in strain rates between the data used to generate the model and the test (.008 min^{-1} vs. .0024 min^{-1}). The prediction using the classical model also shows the characteristic square corners associated with a distinct single yield surface. The viscoplastic model predicts a more accurate stress amplitude for the test strain rate of .0024 min^{-1} and displays a smoother transition between elastic and plastic response. A comparison of the two models for the combustor louver lip thermomechanical loading cycle (Ref. 2) is shown in Figure 2. Simulation of the combustor lip with a uniaxial test specimen produced the stationary stress-strain response shown in the figure. Prediction with the classical plasticity and creep models resulted in a continuous ratchetting of the response in the positive stress direction. Shown is the 15th loading cycle. The prediction using the viscoplastic model does not display the same degree of stress ratchetting and more closely predicts the experimental data. Shown is the 2nd loading cycle.

References:

1. Development of a Simplified Analytical Method for Representing Material Cyclic Response, NAS3-22821.

2. Moreno, V.: Combustor Liner Durability Analysis. NASA CR 165250, 1981.

3. Walker, K.P.: Research and Development Program for Non-Linear Structural Modeling with Advanced Time-Temperature Dependent Constitutive Relationships, NASA CR 165533, 1981.

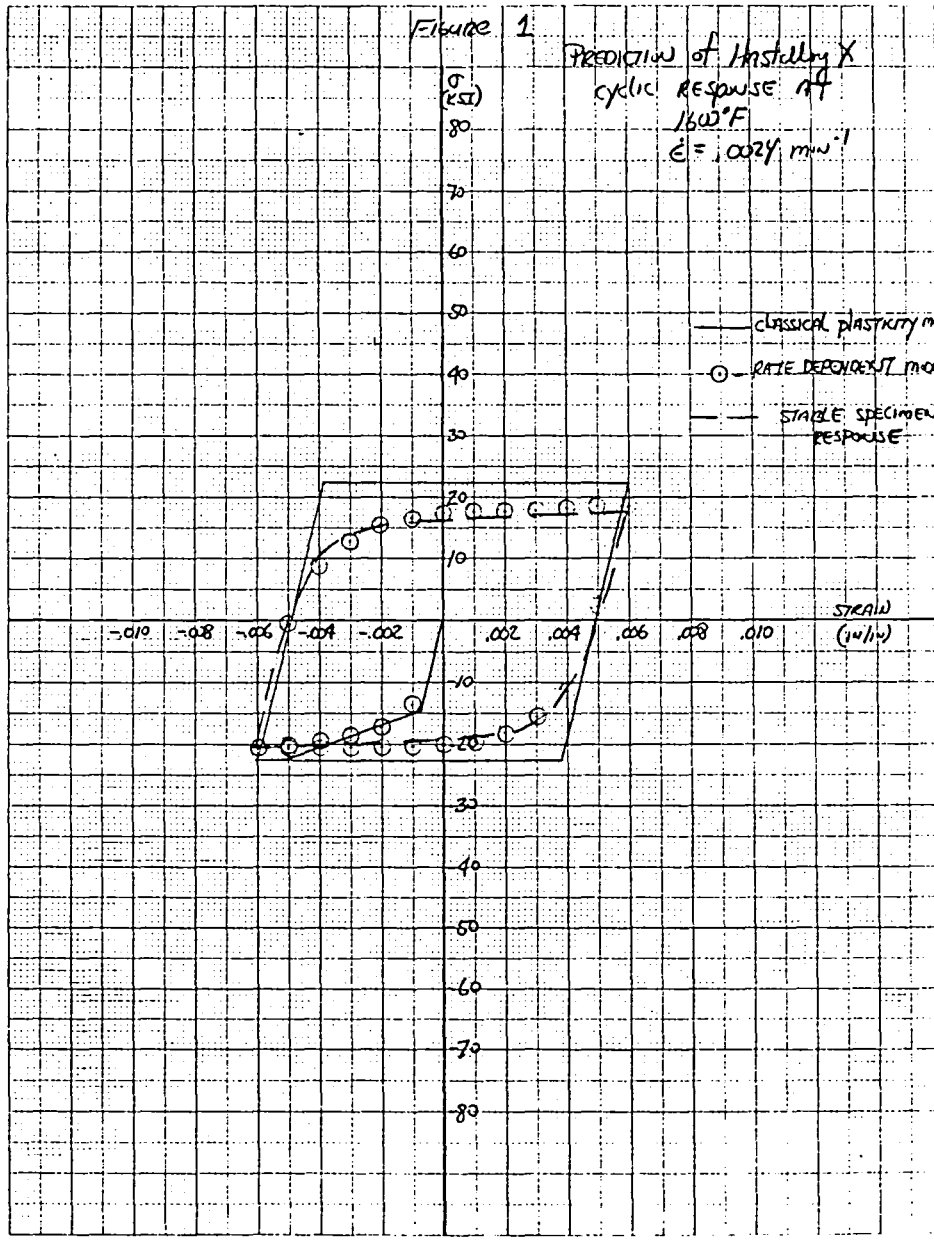
FIGURE 1
PREDICTION of INSTABILITY IN
CYCLIC RESPONSE AT
1600°F
$\dot{\varepsilon} = .0024\ min^{-1}$
σ (KSI)
80
70
60
50
40
30
20
10
CLASSICAL PLASTICITY MO
RATE DEPENDENT MODE
STABLE SPECIMEN
RESPONSE
-.010
-.008
-.006
-.004
-.002
.002
.004
.006
.008
.010
STRAIN (in/in)
-10
-20
-30
-40
-50
-60
-70
-80

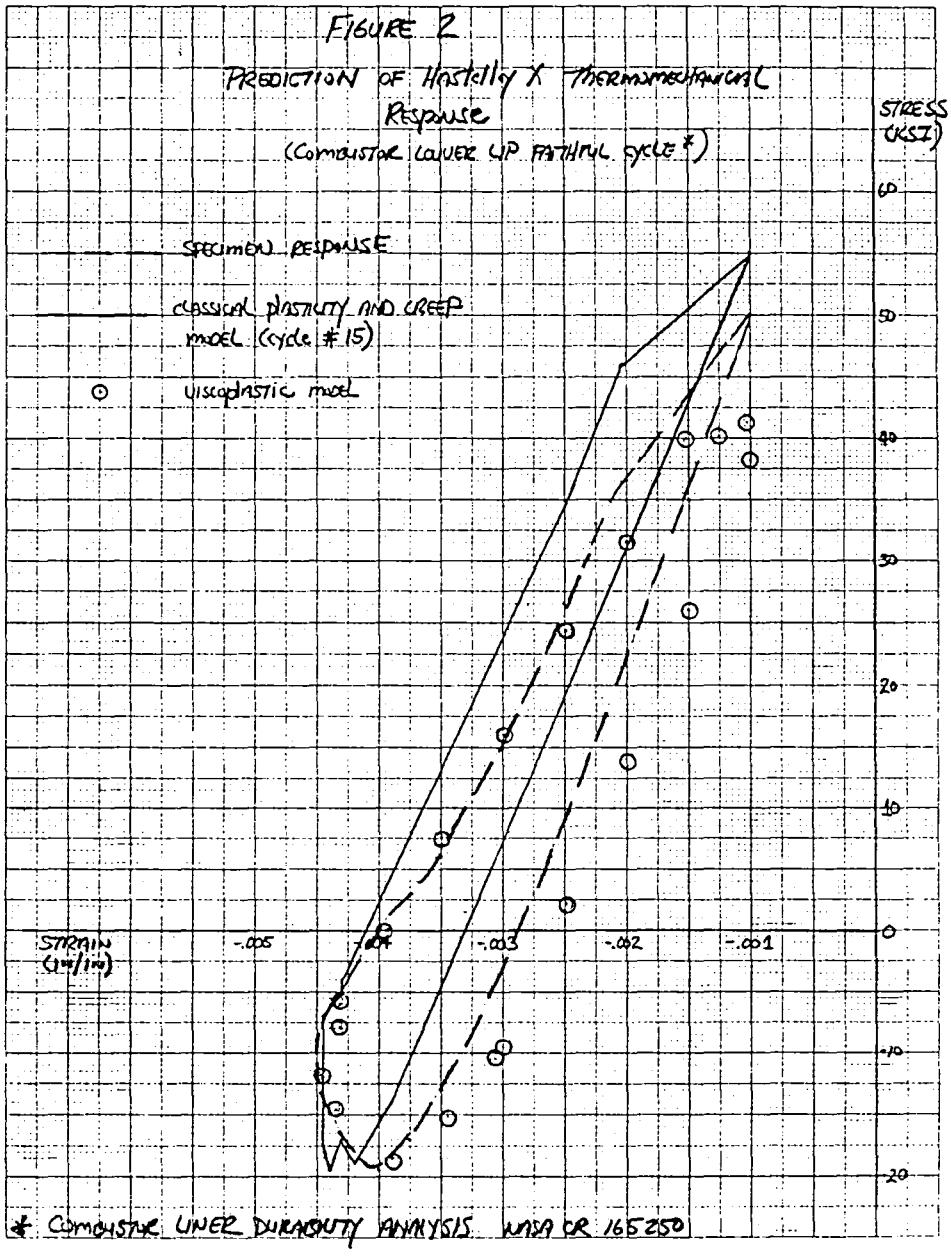
FIGURE 2
PREDICTION OF HASTELLOY X THERMOMECHANICAL RESPONSE
(COMBUSTOR LOWER LIP FATIGUE CYCLE *)
SPECIMEN RESPONSE
CLASSICAL PLASTICITY AND CREEP MODEL (CYCLE # 15)
VISCOPLASTIC MODEL
STRESS (KSI)
STRAIN (in/in)
-.005
-.004
-.003
-.002
-.001
60
50
40
30
20
10
0
-10
-20
* COMBUSTOR LINER DURABILITY ANALYSIS NASA CR 165250

EXPERIMENTAL VERIFICATION OF THE NUMBER RELATION AT ROOM AND ELEVATED TEMPERATURES*

Lonnie J. Lucas and John F. Martin
Michigan State University
East Lansing, Michigan 48823

ABSTRACT

The accuracy of the Neuber equation for predicting notch root stress-strain behavior at room temperature and at 650°C was experimentally investigated. Strains on notched specimens were measured with a non-contacting, interferometric technique and stresses were simulated with smooth specimens. Predictions of notch root stress-strain response were made from the Neuber Equation and smooth specimen behavior. Neuber predictions gave very accurate results at room temperature. However, the predicted interaction of creep and stress relaxation differed from experimentally measured behavior at 650°C.

INTRODUCTION

There has been a demand in recent years for the aircraft industry to provide a more energy efficient turbine propulsion system. Part of this task involves trying to understand the limitations of the current materials and structures being used, especially in the "hot section" of the engine [1]. The hot section components include the turbine blades, vanes, and combustors which operate under

*This work was performed under NASA Grant NAG 3-51.

severe stresses and temperatures. To make improvements in these parts it is first necessary to compile test data which describe the events leading up to failure. Theoretical models can then be developed and compared with experimental data until the failure modes and component lives may be predicted.

The combustor, fabricated from the alloy Hastelloy X, is one component which has gone through the initial testing phase and is now being examined from a theoretical stand-point. Failures in the combustor liner have been attributed to thermal-mechanical fatigue which causes cracking and buckling [2]. A number of constitutive theories have been proposed for predicting the nonlinear stress-strain behavior near holes which serve as cracking sites in the liner [3]. When these theories are incorporated into finite element codes, the final package becomes very complex and requires a large computer facility.

The purpose of this study is to examine a more basic theory, namely the Neuber relation, to see how well it can predict local stress-strain behavior in notched specimens of Hastelloy X. For cyclic loading the Neuber equation is written,

$$(\Delta\sigma)(\Delta\varepsilon) = (K_t')^2 (\Delta S)(\Delta e) \qquad (1)$$

where: $\Delta\sigma$ and $\Delta\varepsilon$ are the notch root stress and strain ranges, respectively;

ΔS and Δe are the remote stress and strain ranges, respectively;

K_t' is the elastic stress concentration factor.

Much of the work involving Neuber's relation has focused on stress redistribution near a notch [4] and the accompanying variation in the stress and strain concentration factors throughout fatigue life [5,6,7]. One of these researchers, Guillot [6], evaluated Neuber's equation at moderately elevated temperatures (260°C) and found that conservative results were obtained for life predictions in 1018 steel and 7475 aluminum. Both Bofferding [5] and Guillot [6] used an Interferometric Strain Gage (I.S.G.) [8-11] to measure notch root strains.

Equation (1) by itself is indeterminate. Knowing the remote stress or strain range leaves three unknowns. The The relationship between stress and strain at both the remote and local locations is needed. Crews and Hardrath [12] assumed that the notch stress could be found by reproducing measured notch strains in smooth samples. This assumption was upheld by Stadnick [13] and other researchers [14,15] who showed that the smooth specimen simulation gave good results in predicting fatigue lives of notched specimens. For this study it was assumed that smooth specimens could be used to supply the needed stress-strain relationship.

Stadnick and Morrow [16] worked on automating the techniques for performing tests on smooth specimens that were controlled according to the Neuber Equation. They evaluated various approaches for subjecting a smooth

specimen to the same stresses and strains that theoretically exist at a notch. This theoretical testing technique has been called "Neuber Control". These methods consisted of manual control, and analog or digital computer control.

Separate research efforts have been devoted to using smooth specimens to simulate notch root response, developing laser based measurement devices and estblishing high temperature testing techniques. This study utilized all of these tools to determine the accuracy of Neuber's equation for cyclic loading of notches specimens at temperatures up to 650°C.

EXPERIMENTAL METHODS

1. Interferometric Strain Measurement Technique

The Interferometric Strain Gage (I.S.G.) is described in detail in References [8-11]. This device was used to measure strains both at the local and remote locations in notched specimens. The I.S.G. is a non-contacting laser based device capable of measuring strains over a very short gage length, typically 50-200 microns. The gage length is formed by making two small pyramidal shaped indentations on a sample with a Vicker's hardness tester. These indentations form the actual gage on the specimen and the distance between them constitutes the gage length. Laser light which reflects off the two indentations interacts to form two interference patterns. Each pattern is composed of bright and dark bands of light. The position of each

bright fringe is a function of the wavelength of the laser light, the distance between indentations, and the reflecting angle of the indentations.

The I.S.G. functions by using scanning mirrors to reflect the interference bands onto photomultiplier tubes. When a load is applied to the specimen, the distance between the indentations changes, thereby causing the position of each bright fringe to move. Since the change in position of the fringes is proportional to the change in distance between the indentations, a computer can be used to calculate the strain in the specimen.

Two basic requirements must be met in order to utilize this strain measurement technique. First of all, the path of the incoming laser beam and the reflected fringe patterns must not be obstructed. To accomplish this, specimens were heated by an induction method for the elevated temperature tests. Heating coils which surrounded the specimen were designed so that they would not interfere with the laser beam. Another problem was that the specimen surface had to remain smooth and free of excess oxidation during high temperature testing. This problem was solved by depositing a 0.14 micron layer of 40% gold-60% palladium onto the specimen after the indentations had been made.

The I.S.G. was used to measure strains at both the local and the remote region of the notched specimen shown in Figure 1. The local indentations for creating fringe patterns were placed 50 microns from the edge of the notch. This was as near to the edge of the notch as the indentations could

be consistently made with the Vicker's hardness tester. The remote indentations were made at a distance of 6.025 mm from the notch edge.

When evaluating the Neuber equation, other investigators [5,6] have restricted loading levels to insure that the remote region remained linearly elastic. This allowed the remote strain to be calculated by knowing the stress in the net section and the modulus of elasticity. During these experiments, the complications of defining a net section stress were avoided by measuring the remote strains directly. There were also no limitations on plasticity in the remote region. This allowed the Neuber relation to be evaluated for a greater range of loading conditions.

The loading pattern for this experiment consisted of completely reversed loading with 100 second hold times in both tension and compression. A servo controlled, electro-hydraulic, closed-loop testing machine was used to perform the tests. Many of the details concerning the experimental procedure have not been included in this paper so that the results and conclusions could be emphasized.

2. Stress Simulation

To determine the stresses that existed in notched specimens, smooth specimens were subjected to the strain histories which had been measured at the local and remote locations. Strains that had been measured with the I.S.G. were recorded in real time so that they could be played back on a smooth specimen at the same strain rate that

existed on the notched specimen. From this technique, stress-strain hysterisis loops at different locations on a notched specimen were produced.

This method of simulating stresses worked very well from an experimental point of view. All parameters such as strain rate, creep, and total strain were reproduced in the smooth specimen just as they had occurred in the notched plate. The plots of local notch root stress versus strain were considered direct experimental data to which the Neuber predictions could be compared.

3. Neuber Prediction

The Neuber equation, (Eqn. 1), allows local behavior in a notched specimen to be determined as a function of remote stress and strain. In these experiments, a smooth specimen was manually controlled in real time according to Eqn. 1 with remote stress and strain as input parameters.

The measured remote strains and simulated stresses had been recorded on a time scale. These stress and strain values were multiplied together at various points in time and their product was then multiplied by the stress concentration factor squared. These values were replotted on the same time scale and constituted the Neuber prediction curves.

The Neuber relation is evaluated on a reversal by reversal basis. Therefore, the Neuber prediction curves were actually the product of the changes in stress and strain which occurred starting from the beginning of each

reversal. By following this procedure, a plot such as the one shown in Figure 2 could be constructed. This plot would allow six reversals of local behavior to be predicted. The time scale was set at 5 sec/cm when the loads were applied and then slowed to 50 sec/cm for the 100 second hold periods. During each test, the values of stress and strain from a smooth specimen were multiplied together on-line with an analog computer to represent the quantity $(\Delta\sigma)(\Delta\varepsilon)$. The specimen was manually controlled in the MTS system so that the product of stress and strain would follow the Neuber prediction curve for each reversal. The illustration in Figure 2 shows how closely the original plot was followed during such a test. An additional analog circuit was designed so that the changes in stress and strain could be multiplied together starting from zero at the beginning of each reversal.

By plotting $(K_t')^2(\Delta s)(\Delta e)$ and imposing the product $(\Delta\sigma)(\Delta\varepsilon)$, the Neuber equation was satisfied for each reversal. The resulting stress and strain values constituted the predicted notch root behavior. The Neuber predictions were then compared to the measured strain vs. simulated stress data for local response.

RESULTS AND DISCUSSION

1. Determination of Stress Concentration Factor

An elastic stress concentration factor for the circular notched specimens was found experimentally using the ISG.

From Peterson (17), the stress concentration factor, K_t was given as 2.37. The experimentally determined stress concentration factor which is defined here as K_t' was found to be equal to 2.27. Figure 3 shows where five sets of indentations for the ISG were placed across the width of a notched specimen. Room temperature strain measurements were recorded at each of these locations while the specimen was cycled well below the proportional limit. The actual strain data and the calculated strain profile are both shown in the figure. By taking the ratio of strains at location #5 and location #1, the strain concentration factor was determined. For elastic strains, the stress and strain concentration factors are equal, therefore, K_t' was also determined ($K_t' = 2.27$). This experimentally determined value of K_t' as well as the designation for the local and remote areas (locations #1 and #5) were used throughout the test program.

2. Interferometric Strain Measurements

At room temperature, strains for a notched specimen were recorded for the initial behavior and also for a cyclically stable condition, i.e. when the material at notch root was stable. Figure 4 shows I.S.G measurements of strain vs. applied load for a notched specimen during the first three cycles of constant amplitude completely reversed loading between $\pm$ 14 KN. The most noticeable effects in notch root behavior were caused by cyclic hardening. The tensile peaks showed a large decrease in

strain for each successive cycle due to strain hardening. The compressive strains experienced much less variation during the three cycle period. Creep effects were also present in the room temperature data. The largest amount of creep took place during the first 100 second hold time and then diminished with each successive reversal.

For remote behavior, which is also shown in Fig. 4, cyclic hardening again caused the total strain to decrease for each plotted loop. The effects of creep were minimal for the remote location. The amount of creep at both locations in the specimen decreased as the material stabilized.

When a sufficient number of cycles had been applied to stabilize the material, the I.S.G. was used to record data at the four cyclic load levels which are listed:

LEVEL #	LOAD (KN)
1	$\pm$ 14.0
2	$\pm$ 14.5
3	$\pm$ 15.5
4	$\pm$ 16.0

Strain measurements were obtained at each of five locations across the notched specimen as indicated in Figure 3. Figures 5 and 6 show results for the lowest load amplitude (Load Level 1) and the highest amplitude (Load Level 4). These figures illustrate the effects of cyclic loading at various distances from the notch. The plastic strain diminished significantly as the distance from the notch increased. Also, when the load was raised from Level 1 to

Level 4, the strain at the remote location (#5) increased by 21% while the local strain (#1) experienced a 50% increase. This gives an indication of the strain concentration near the notch.

Notch root and remote strains were also measured at 650°C in a specimen which had been cyclically stabilized. Four load levels were again used which are as follows:

LEVEL #	LOAD (KN)
1	± 10.5
2	± 11.3
3	± 12.3
4	± 13.3

Hysteresis loops showing applied load vs. local notch root strain at four different load levels are shown in Figures 7 and 8. At this temperature, small increases in load produced large strains, especially strain due to creep. During the 100 second hold time, the amount of creep strain at each level of loading was as follows:

Level 1: 0.05% creep strain
Level 2: 0.10% creep strain
Level 3: 0.13% creep strain
Level 4: 0.18% creep strain

These values were approximately equal for tension and compression.

3. Stress Simulation & Neuber Predictions

Smooth specimen stress simulations produced the experimental stress-strain behavior at both the remote and local regions. Neuber predictions were also made. The first three cycles of notch root stress-strain behavior at

room temperature were plotted in Figure 9. Included in this figure are both the experimental results and the Neuber predictions. During the first cycle, the Neuber prediction was slightly high on stress which caused lower strain peaks. Actually, the tensile and compressive strains were only 9% low for the first cycle. The predicted tensile strain on the second cycle was low by 8% while the compressive strain was 13% lower than the stress simulation.

The Neuber relation was also used to predict the notch root response after the material had reached the cyclically stable condition. In Figure 10, the room temperature results from tne Neuber prediction and the stress simulation have been superimposed for comparison. For the stabilized notch root response at Load Levels 1 and 2, the Neuber method was approximately 6% high in predicting tensile and compressive strain. Load Levels 3 and 4 show nearly a perfect correlation between the two sets of curves.

Neuber's rule was also studied at 650°C for the cyclically stable condition. Figure 11 and 12 show these stable results. The most noticeable trend at all four levels was the amount of stress relaxation predicted by the Neuber relation. For Load Levels 1 and 2, the stresses at the end of the 100 second hold times were low by 23% and 27%, respectively. The stresses were predicted more accurately at the higher load levels. At Load Level 3 the stresses were 22% low and at Level 4 the stresses were 15% lower than the stress simulation. In terms of strain range,

the error in predicting Level 1 strains was 20% low while the Level 4 strains were predicted within 10%.

The tendency of the Neuber relation to predict stress relaxation rather than predominant creep during the hold times was caused by the remote information which was used to construct the Neuber plots. The remote location had experienced almost no creep for the Load Levels 1 thru 3. At Load Level 4, the creep accounted for about 12% of the total strain. This caused the Neuber prediction to become more accurate at the highest load level.

CONCLUSIONS

Neuber control of a smooth specimen predicted the notch root stress-strain behavior of a circular center notched plate that was made of Hastelloy X with excellent agreement to direct experimentally measured notch root strains and simulated stresses at room temperature. The agreeement was good for initial behavior during cyclic hardening and for the stable condition at four different load levels. At 650°C and for the stable condition, agreement with experimental data were acceptable with the maximum error at 20%. At this higher temperature, the direct experimental data showed primarily creep strain during hold times. The Neuber prediction showed both creep and stress relaxation. This difference in the general behavior resulted in significantly larger errors at this elevated temperature than those for room temperature.

REFERENCES

1. Signorelly, R. A., Glasgow, T. K., Halford, G. R., and Levine S. R., "Materials and Structures Technology," NASA Conference Publication #2092, May 1979, pp. 150-162.

2. Avery, L. R., Carayanis, G. S. and Michky, G. L., "Thermal Fatigue Tests of Restrained Combustor Cooling Tubes," Experimental Mechanics, Vol. 7, No. 6, June 1967, pp. 256-264.

3. Walker, K. P., "Research and Development Program for Nonlinear Structural Modeling with Advanced Time-Temperature Dependent Constitutive Relationships," NASA Report No. CR-165533, Nov. 1981.

4. Blatherwick, A. A., and Olson, B. K., "Stress Redistribution in Notched Specimens Under Cyclic Stress," ASD Technical Report 61-451, Aeronautical Systems Division, Wright-Patterson Air Force Base, Dayton, Ohio, 1961.

5. Bofferding, C. H., "a Study of Cyclic Stress and Strain Concentration Factors at Notch Roots Throughout Fatigue Life," Master's Thesis, Michigan State University, 1980.

6. Guillot, M. W., "An Experimental Evaluation of Neuber's Cyclic Relation at Room and Elevated Temperatures," Ph.D. Thesis, Louisiana State University, May 1981.

7. Leis, B. N., Gowda, C. V. B., and Topper, T. H., "Some Studies of the Influence of Localized and Gross Plasticity on the Monotonic and Cyclic Concentration Factors," Journal of Testing and Evaluation, Vol. 1, No. 4, July 1973, pp. 341-348.

8. Sharpe, W. N., Jr., "The Interferometric Strain Gage," Experimental Mechanics, Vol. 8, No. 4, April 1968, pp. 164-170.

9. Sharpe, W. N., Jr., "Interferometric Surface Strain Measurement," International Journal of Non-Destructive Testing," Vol. 3, 1971, pp. 51-76.

10. Sharpe, W. N., Jr., "A Short Gage Length Optical Gage for Small Strain," Experimental Mechanics, Vol. 14, No. 9, 1974, pp. 373-377.

11. Sharpe, W. N., Jr., "Development and Application of an Interferometric System for Measuring Crack Displacements," Final Report on Grant NSG 1148, June 1976.

12. Crews, J. H., Jr., and Hardrath, H. F., "A Study of Cyclic Plastic Stresses at a Notch Root," Experimental Mechanics, Vol. 6, No. 6, June 1966, pp. 313-320.

13. Stadnick, S. J., "Simulation of Overload Effects in Fatigue Based on Neuber's Analysis," Department of Theoretical and Applied Mechanics, University of Illinois, Urbana, Report No. 325, 1969.

14. Leis, B. N., Gowda, C. V. B., and Topper, T. H., "Cyclic Inelastic Deformation and the Fatigue Notch Factor," ASTM STP 519, 1973, pp. 133-150.

15. Wetzel, R. M., "Smooth Specimen Simulation of Fatigue Behavior of Notches," Department of Theoretical and Applied Mechanics, Report No. 295, University of Illinois, Urbana, May 1967.

16. Stadnick, S. J., and Morrow, Jo Dean, "Techniques for Smooth Specimen Simulation of the Fatigue Behavior of Notched Members," ASTM STP 515, American Society for Testing and Materials, 1972, pp. 229-252.

17. Peterson, R. E., "Stress Concentration Factors," John Wiley and Sons, Inc., 1974,, pp. 150-196.

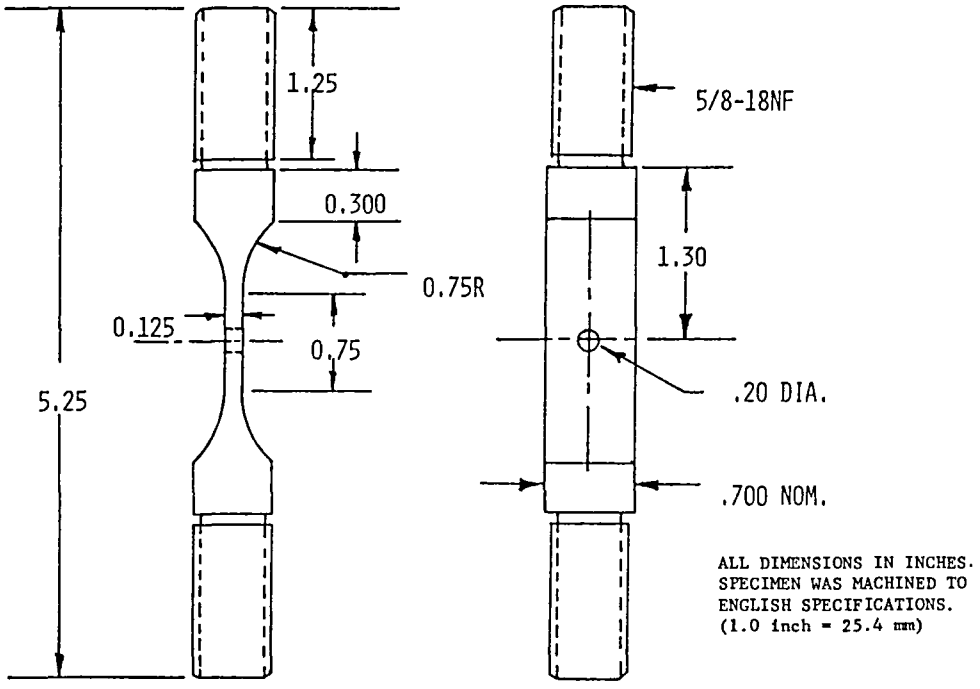

FIGURE 1 NOTCHED SPECIMEN GEOMETRY

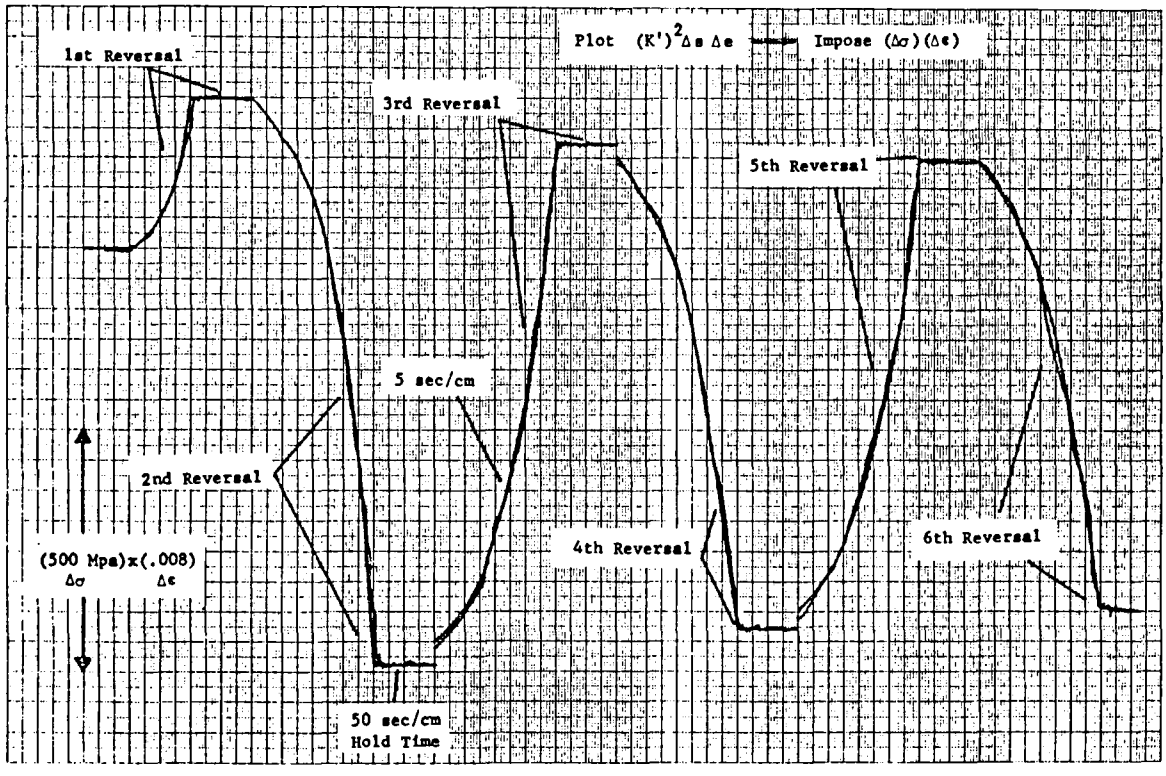

FIGURE 2 NEUBER PREDICTION CURVES

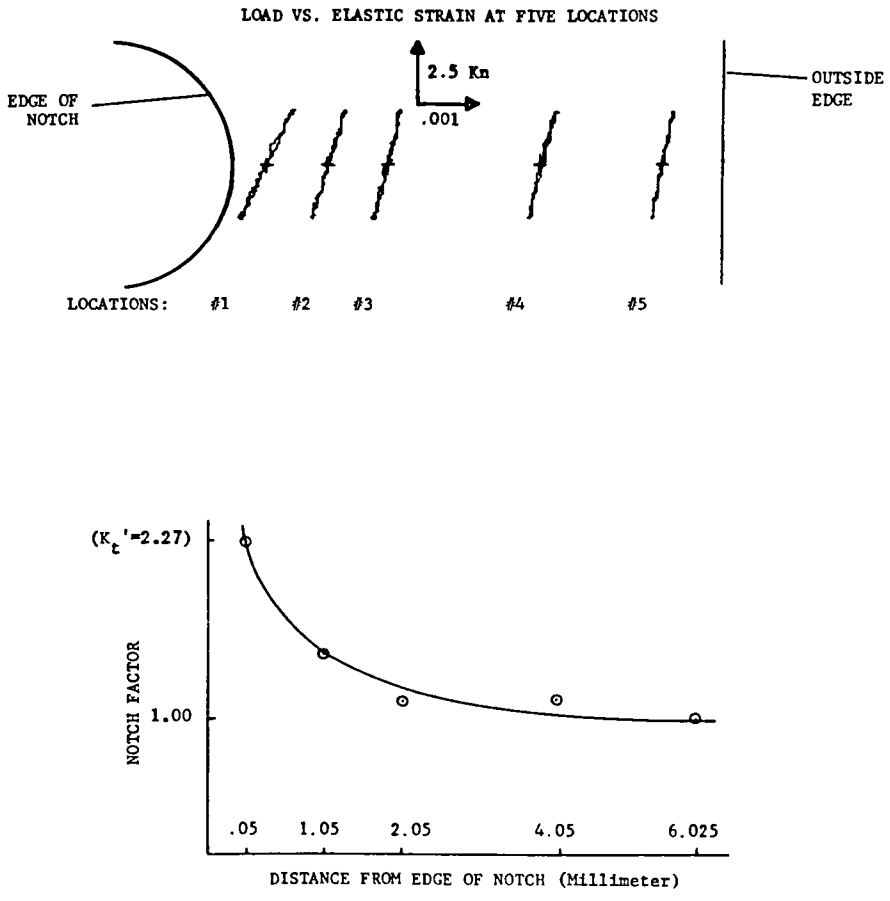

FIGURE 3 DETERMINATION OF STRAIN PROFILE

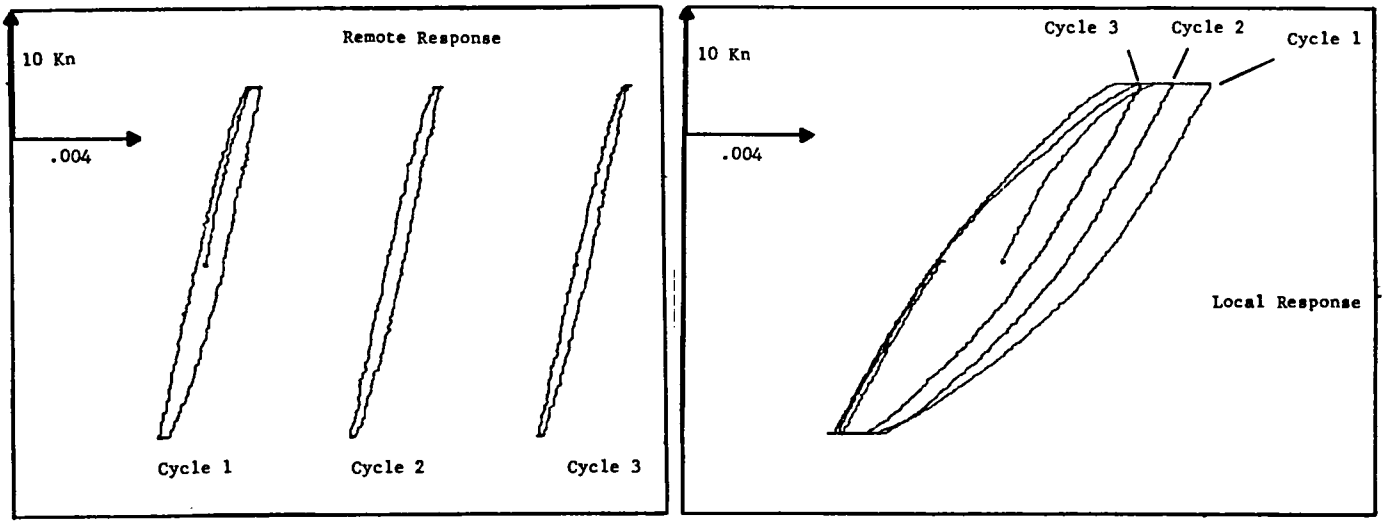

FIGURE 4 INITIAL ROOM TEMPERATURE DATA AT THE LOCAL AND REMOTE LOCATIONS

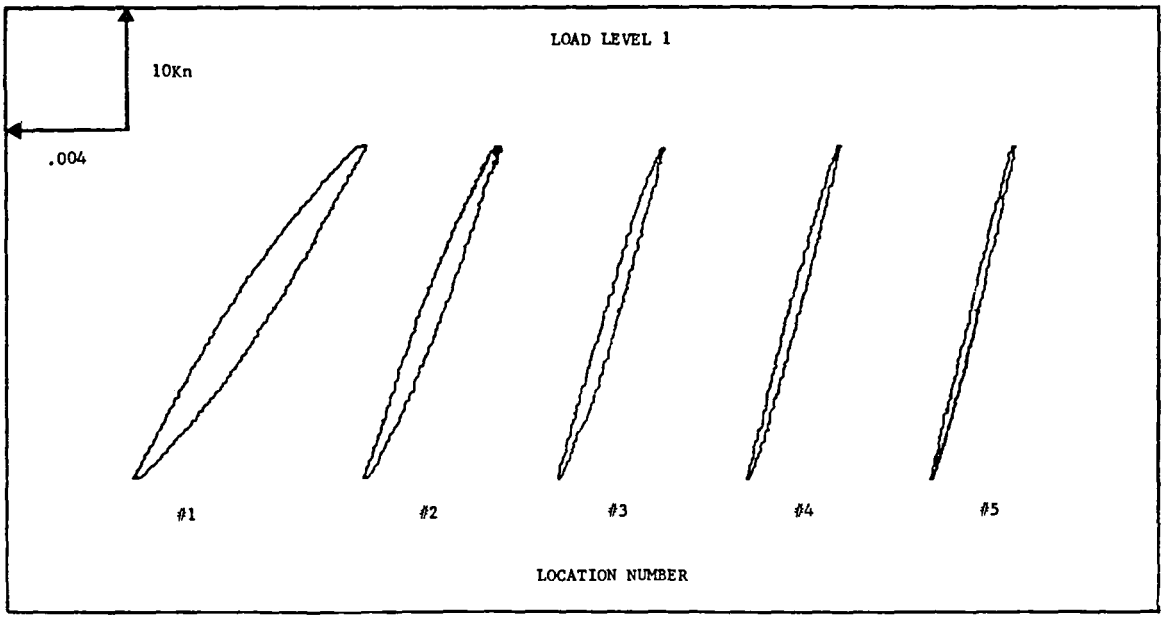

FIGURE 5 STRAIN VS. LOAD AT ROOM TEMPERATURE FOR A STABLE CONDITION

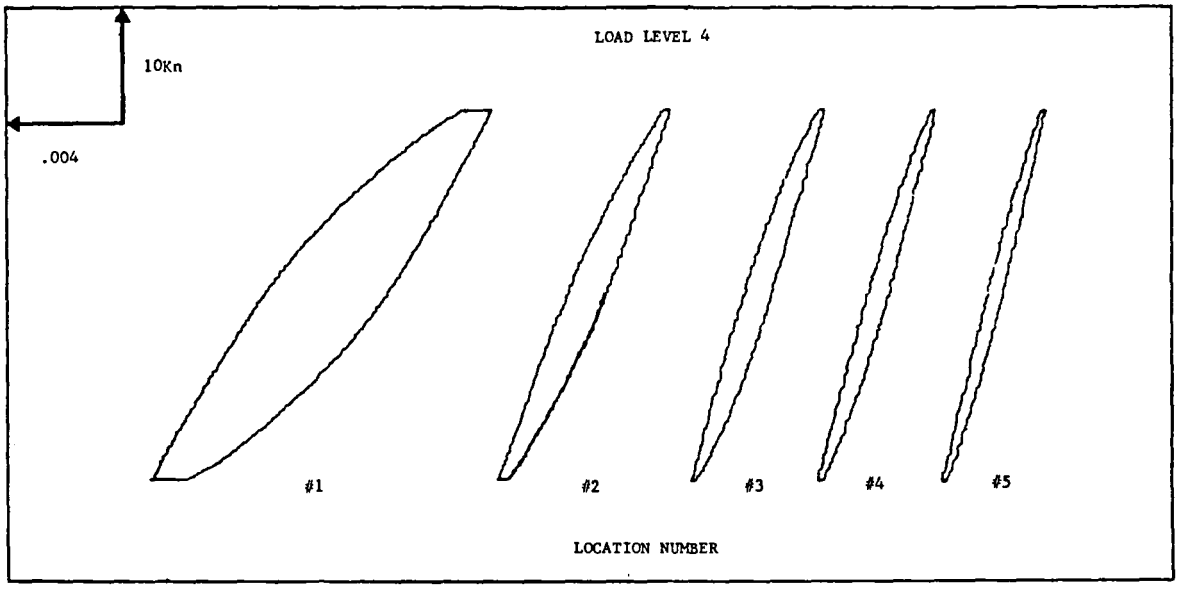

FIGURE 6 STRAIN VS. LOAD AT ROOM TEMPERATURE FOR A STABLE CONDITION

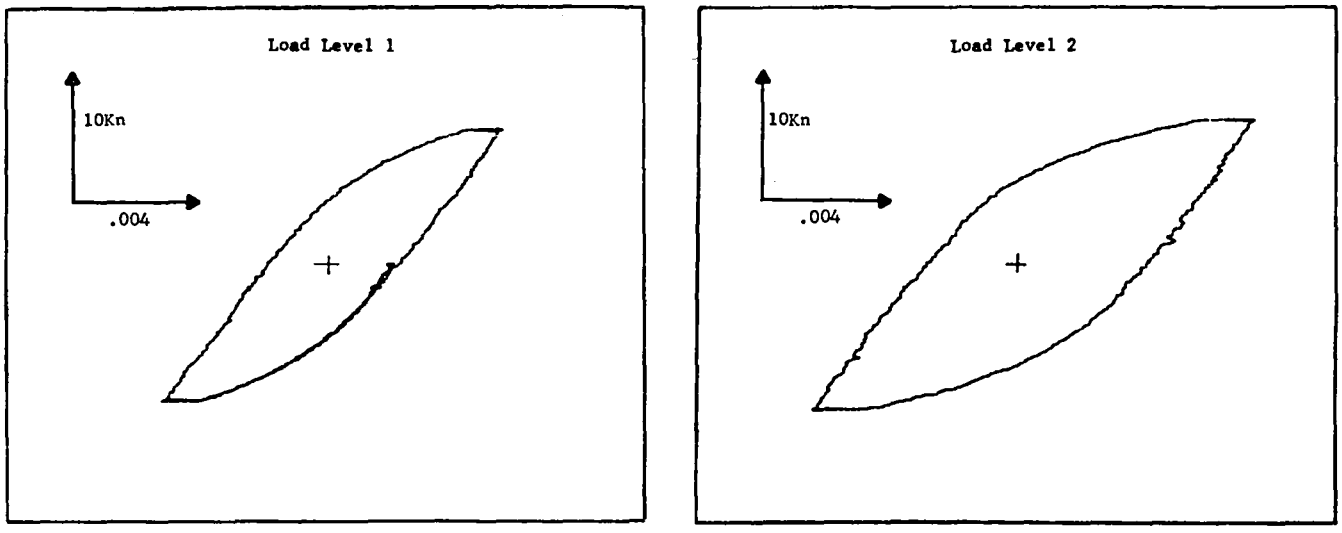

FIGURE 7 LOCALLY MEASURED STRAIN VS. LOAD AT 650°C

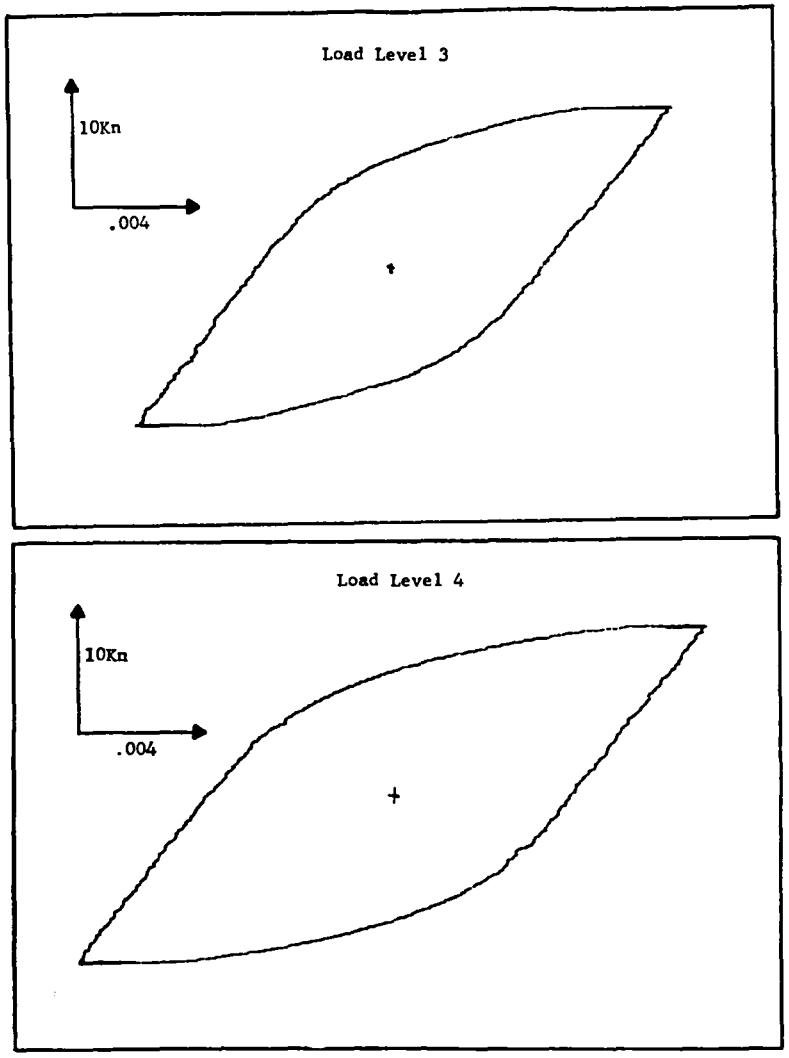

FIGURE 8 LOCALLY MEASURED STRAIN VS. LOAD AT 650°C

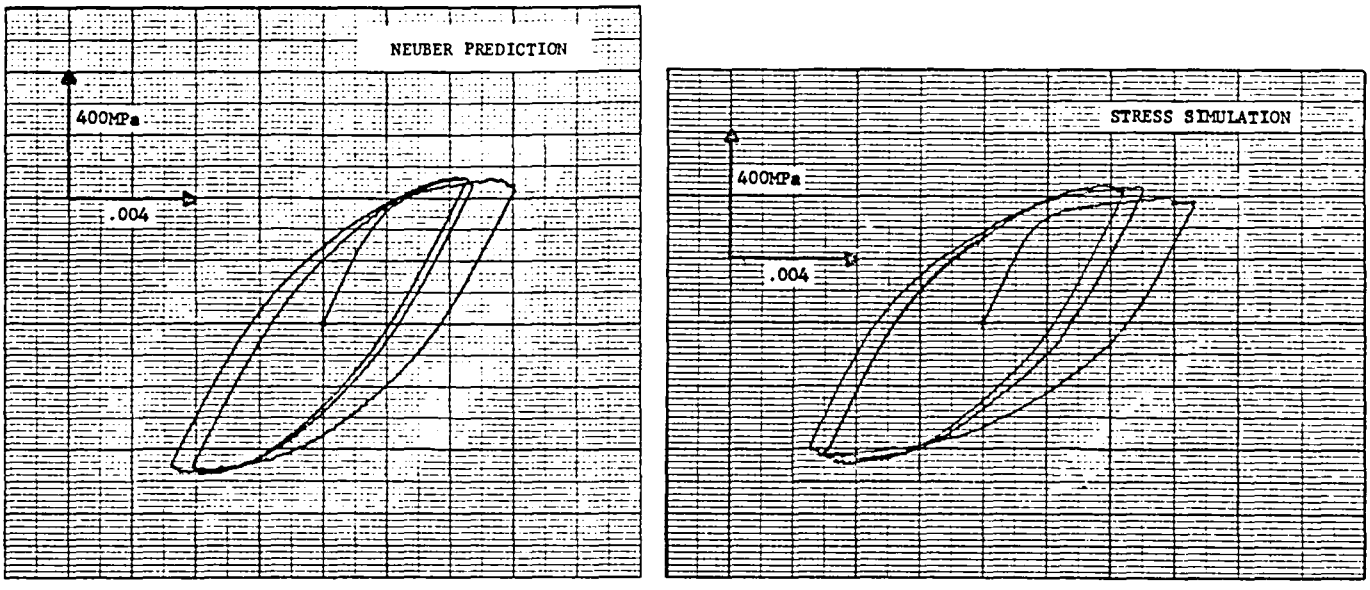

FIGURE 9 EXPERIMENTAL AND PREDICTED LOCAL RESPONSE AT ROOM TEMPERATURE

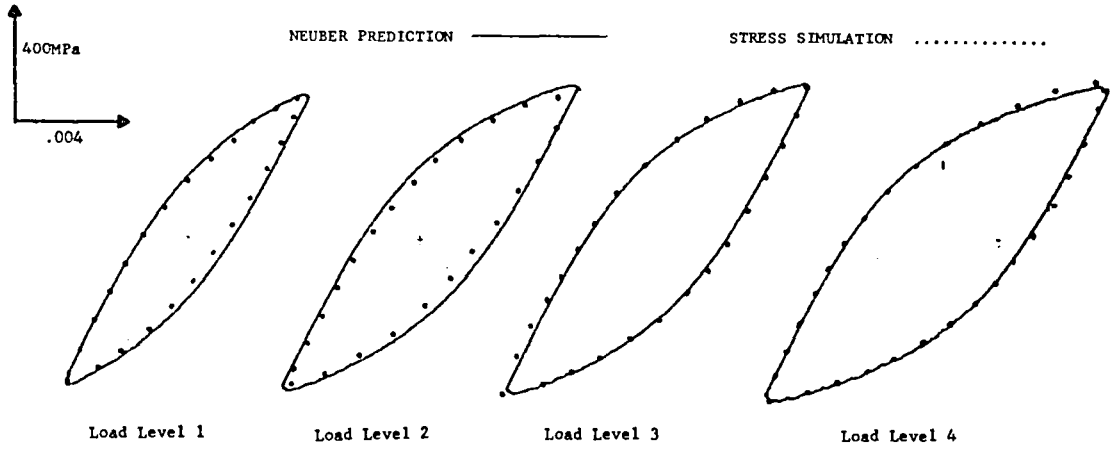

FIGURE 10 EXPERIMENTAL AND PREDICTED LOCAL RESPONSE AT ROOM TEMPERATURE

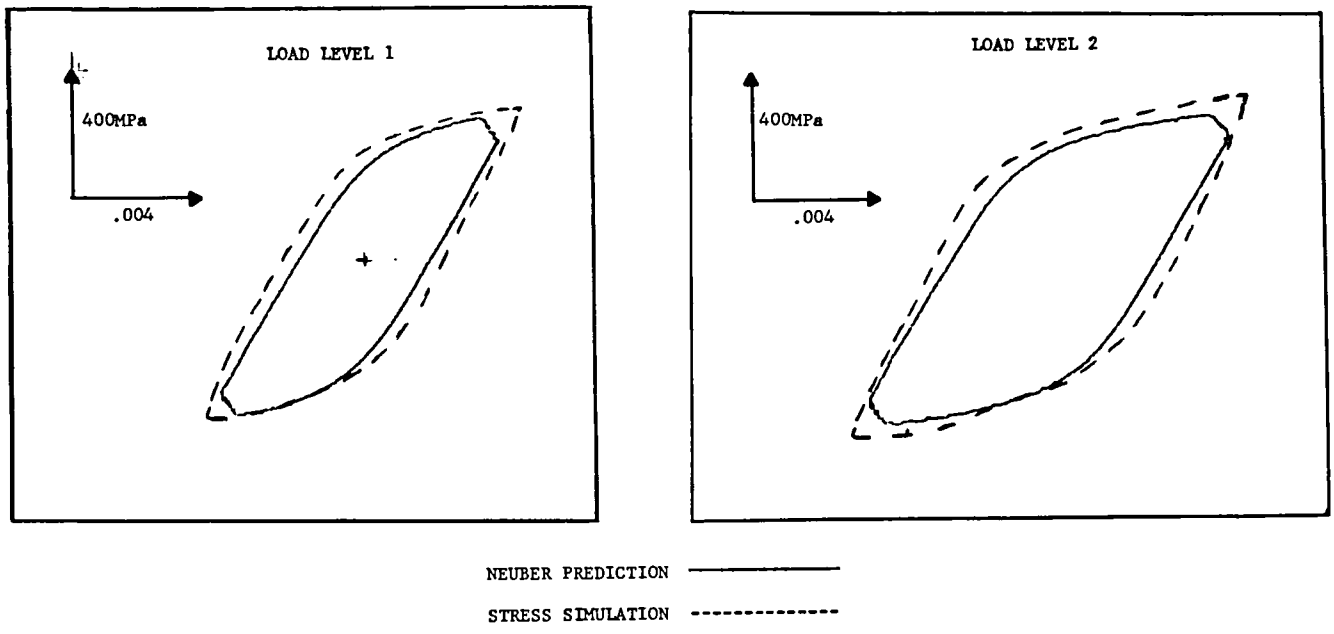

FIGURE 11 EXPERIMENTAL AND PREDICTED LOCAL RESPONSE AT 650°C

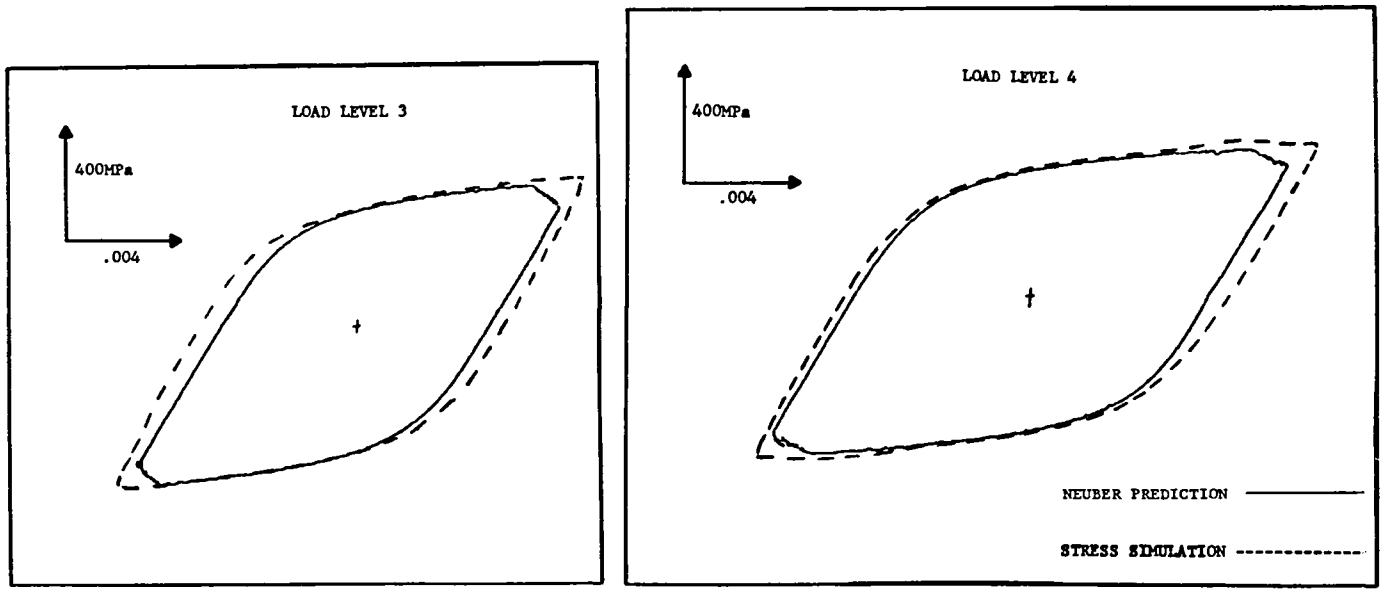

FIGURE 12 EXPERIMENTAL AND PREDICTED LOCAL RESPONSE AT 650°C

MULTIAXIAL CYCLIC THERMOPLASTICITY ANALYSIS WITH BESSELING'S SUBVOLUME METHOD

R. L. McKnight
General Electric Co.
Cincinnati, Ohio 45215

Abstract

In 1975, a modification was formulated to Besseling's Subvolume Method to allow it to use multilinear stress-strain curves which are temperature dependent to perform cyclic thermoplasticity analyses. This method automotically reproduces certain aspects of real material behavior important in the analysis of Aircraft Gas Turbine Engine (AGTE) components. These include the Bauschinger effect, cross-hardening, and memory. This constitutive equation has been implemented in a finite element computer program called CYANIDE which has been in production usage since 1977. Subsequently, classical time dependent plasticity (creep) was added to the program. Since its inception, this program has been assessed against laboratory and component testing and engine experience. The ability of this program to simulate AGTE material response characteristics has been verified by this experience and its utility in providing data for life analyses has been demonstrated. In this area of life analysis, the multiaxial thermoplasticity capabilities of the method have proved a match for the actual AGTE life experience. This paper will explore the multiaxial, variable-temperature nature of the method and show examples demonstrating its utility.

BESSELING'S MATHEMATICAL MODEL

The relation between the deviatoric stresses and the deviatoric strains is given by

$$S_{ij} = 2G(e_{ij} - e''_{ij}) \tag{1}$$

where

S_{ij} is the deviatoric stress tensor

e_{ij} is the total deviatoric strain tensor

e''_{ij} is the plastic strain tensor

G is the shear modulus

The yield strain, P, is given by the plastic potential function

$$g = (e_{ij} - e''_{ij})(e_{ij} - e''_{ij}) - P^2 = 0 \tag{2}$$

The incremental plastic strains are given by

$$\delta e''_{ij} = \frac{(e_{ij} - e''_{ij})(e_{hk} - e''_{hk})}{P^2} \delta e_{hk} \tag{3}$$

provided that

$$(e_{hk} - e''_{hk})\delta e_{hk} > 0 \tag{4}$$

The incremental stress-strain relation is

$$\delta S_{ij} = 2G\left[\delta e_{ij} - \frac{(e_{ij} - e''_{ij})(e_{hk} - e''_{hk})}{p^2}\,\delta e_{hk}\right] \tag{5}$$

The new yield strain, $e_{ij} + \delta e_{ij}$, is determined from

$$\delta g = 2(e_{ij} - e''_{ij})(\delta e_{ij} - \delta e''_{ij}) = 0 \tag{6}$$

Besseling then introduced the concept of elastic-perfectly plastic subvolumes. The elastic potential, ϕ_1, of the subvolume of density ρ after prior plastic flow is given by

$$\rho\,\phi_1 = G(e_{ij} - \bar{e}_{ij1})(e_{ij} - \bar{e}_{ij1}) \tag{7}$$

where the $\bar{e}_{ij1}$ are the plastic strains due to ideal plastic yielding. If this subvolume constitutes the fraction ψ of the volume element dV, its contribution to the total elastic potential of dV is

$$\psi G(e_{ij} - \bar{e}_{ij1})(e_{ij} - \bar{e}_{ij1})dV \tag{8}$$

If k subvolumes of the volume dV have exceeded their critical value of elastic potential and undergone plastic flow, the total elastic potential is given by

$$\rho\phi dV = \left[Ge_{ij}e_{ij}\left(1 - \sum_1^k \psi_n\right) + G\sum_1^k \psi_n(e_{ij} - \bar{e}_{ijn})(e_{ij} - \bar{e}_{ijn})\right]dV \tag{9}$$

Now, the deviatoric stress tensor is given by

$$S_{ij} = 2G\left[\left(1 - \sum_1^k \psi_n\right)e_{ij} + \sum_1^k \psi_n(e_{ij} - \bar{e}_{ijn})\right] \tag{10}$$

After yielding, the elasticity limit of subvolume k is given by

$$g_k = (e_{ij} - \bar{e}_{ijk})(e_{ij} - \bar{e}_{ijk}) - p_k^2 = 0 \tag{11}$$

The subvolume incremental plastic strains are given by

$$\delta\bar{e}_{ijk} = \frac{(e_{ij} - \bar{e}_{ijk})(e_{\alpha\beta} - \bar{e}_{\alpha\beta k})}{p_k^2}\,\delta e_{\alpha\beta k} \tag{12}$$

provided that

$$(e_{\alpha\beta k} - \bar{e}_{\alpha\beta k})\delta e_{\alpha\beta k} > 0 \tag{13}$$

The incremental stress-strain relations are

$$\delta S_{ij} = 2G\left[\delta e_{ij} - \sum_1^k \psi_n \frac{(e_{ij} - \bar{e}_{ijn})(e_{\alpha\beta} - \bar{e}_{\alpha\beta n})}{p_n^2}\,\delta e_{\alpha\beta}\right] \tag{14}$$

DEVELOPMENT OF NONISOTHERMAL CAPABILITY

The equation relating the stresses and the subvolume strains, Equation (10), can be rewritten to give

$$S_{ij} = 2G[e_{ij} - \Sigma\psi_n \bar{e}_{ijn}] \tag{15}$$

Now these stresses must be the same as the stresses given by Equation (1). Therefore, the two right-hand sides can be equated. When this is done, we get

$$\sum_{1}^{k} \psi_n \bar{e}_{ijn} = e''_{ij} \tag{16}$$

which gives a relationship between the subvolume plastic strains and the total plastic strains.

Squaring both sides of Equation (16) and multiplying by 2/3, we get

$$\frac{2}{3}\left(\sum_{1}^{k} \psi_n\right)^2 \bar{e}_{ijn}\, \bar{e}_{ijn} = \frac{2}{3}\, e''_{ij}\, e''_{ij} \tag{17}$$

Now

$$\varepsilon_p = \sqrt{\frac{2}{3}\, e''_{ij}\, e''_{ij}} \tag{18}$$

Therefore

$$\varepsilon_p = \psi_1 \varepsilon_{p1} + \psi_2 \varepsilon_{p2} + \psi_3 \varepsilon_{p3} + \ldots + \psi_n \varepsilon_{pn} \tag{19}$$

This gives a relationship between the total effective plastic strain and the subvolume effective plastic strains.

The following ratio can be formed between a subvolume effective plastic strain and the total effective plastic strain:

$$\left(\frac{\varepsilon_{pn}}{\varepsilon_p}\right)^2 = \frac{\frac{2}{3}\, \bar{e}_{ijn}\, \bar{e}_{ijn}}{\frac{2}{3}\, e''_{ij}\, e''_{ij}} \tag{20}$$

or

$$\bar{e}_{ijn}\, \bar{e}_{ijn} = \left(\frac{\varepsilon_{pn}}{\varepsilon_p}\right)^2 e''_{ij}\, e''_{ij} \tag{21}$$

By taking the square root of both sides, we obtain

$$\bar{e}_{ijn} = \frac{\epsilon_{pn}}{\epsilon_p} e''_{ij} \tag{22}$$

This gives a means of determining the subvolume plastic strains from the total plastic strains if the effective plastic strains are known.

This then provides the tools to convert Besseling's isothermal theory into a nonisothermal theory. We note that for variable temperature problems g and g_k will be functions of both strain and temperature.

$$g = g\ (e_{ij}, T) \tag{23}$$

$$g_k = g_k(e_{ij}, T) \tag{24}$$

These functions can be specified by defining temperature dependent stress-strain curves.

For incremental loading including temperature changes, the change in the plastic potential function is given by

$$dg = \frac{\partial g}{\partial e_{ij}} de_{ij} + \frac{\partial g}{\partial T} dT \tag{25}$$

There are three possible conditions that can occur due to this load increment and these are determined by the value of this differential.

For loading beyond the present yield surface

$$dg > 0 \tag{26}$$

$$\frac{\partial g}{\partial e_{ij}} de_{ij} + \frac{\partial g}{\partial T} dT > 0 \tag{27}$$

For the loading to place the point on the new yield surface

$$dg = 0 \tag{28}$$

$$\frac{\partial g}{\partial e_{ij}} de_{ij} + \frac{\partial g}{\partial T} dT = 0 \tag{29}$$

For the point to unload back into the elastic range

$$dg < 0 \tag{30}$$

$$\frac{\partial g}{\partial e_{ij}} de_{ij} + \frac{\partial g}{\partial T} dT < 0 \tag{31}$$

These last two conditions are used to accomodate temperature variations. The solution to any load condition, (N-1), is arrived at when

$$dg_{n-1} = \frac{\partial g}{\partial e_{ij}} de_{ij/T = \text{Constant}} \leq 0 \tag{32}$$

In proceeding to the next load step, (N), the temperature effects on the stress-strain curve are incorporated so as not to vialate this condition while holding the strains constant.

$$dg_{(n-1),(N)} = \frac{\partial g}{\partial T} dT = 0 \tag{33}$$

Thus, we are requiring that the change of temperature alone not effect the inelastic condition of the material. We accomplish this by realizing that

$$\frac{\partial g}{\partial T} dT = - \frac{2G}{\lambda} de^{e}_{ij} de^{p}_{ij} \tag{34}$$

Therefore, by requiring that

$$de^{p}_{ij} = 0 \tag{35}$$

We force

$$\frac{\partial g}{\partial T} dT = 0 \tag{36}$$

This then gives us the mechanism for positioning our new yield surfaces in step, N. The step, N, solution then proceeds by applying the loads and boundary conditions and iterating to obtain

$$dg = \frac{\partial g}{e_{ij}} de_{ij} \leq 0 \tag{37}$$

within your specified convergence tolerance.

CREEP ANALYSIS

The creep analysis utilizes one of two possible creep representations. When tertiary creep is not considered to be of importance, the equation used is

$$\epsilon_c = k\bar{\sigma}_e^n t^m + q\bar{\sigma}_e^r t \tag{38}$$

where

$\bar{\sigma}_e = \sigma_e/100000$, σ_e = effective stress

k, m, n, q, r = material-dependent and temperature-dependent creep coefficients.

When the material exhibits a significant amount of tertiary creep capability, an alternate representation is used. Primary creep is represented by the Bailey-Norton law.

$$\epsilon_c^P = A_1 \bar{\sigma}_e^{A_2} t^{A_3} \tag{39}$$

Secondary creep is modeled with the expression proposed by Marin, Pao, and Cuff (Reference 19)

$$\epsilon_c^S = A_4\bar{\sigma}_e^{A_5} t + A_6 \bar{\sigma}_e^{A_7} \tag{40}$$

Tertiary creep is represented with an equation of the form

$$\varepsilon_c^T = A_8 e^{A_9 \frac{}{\sigma_e}} {}^{A_{10}} t \tag{41}$$

=

A_1, A_2, ... A_{10} = material-dependent and temperature dependent creep coefficients.

CYANIDE also contains an orthotropic creep formulation. The creep strain rate is assumed to be given by

$$\dot{\varepsilon}_{ij} = g_{ijkl}\sigma_{kl} \tag{42}$$

where

$\dot{\varepsilon}_{ij}$ = strain rate tensor

σ_{kl} = stress tensor

g_{ijkl} = Tensor whose components are functions of temperature, σ_e, and hardening rule and are derivable from input creep curves.

The user can select from time hardening, strain hardening, or life fraction creep rule, depending upon the actual material characteristics. Strain hardening is ordinarily adequate for describing hardening behavior, providing that stress reversals do not occur. A stress reversal is considered to occur when

$$\varepsilon_{ij}^c \dot{\sigma}_{ij} < 0 \tag{43}$$

Where ε_{ij}^c is creep strain measured from its current origin. When a reversal occurs, the origin is changed and the analysis proceeds (Reference 20) .

The combination of general creep equations and creep rule makes the program very general in its application to structures which undergo time-dependent plastic flow in which transient effects are not significant.

CYANIDE COMPUTER PROGRAM

Many of the steps in the CYANIDE nonlinear finite element computer program are the same as those for a linear finite element analysis. The nonlinear effects are introduced into the system of finite element equations by adding vectors of pseudoforces to the right hand side.

$$|K| \{\delta\} = \{F\} + \{F_p\} + \{F_c\} \tag{44}$$

where

- $|K|$ is the elastic stiffness matrix.
- $\{\delta\}$ is the vector of nodal displacements.
- $\{F\}$ is the force vector including thermal terms.
- $\{F_p\}$ is the plastic pseudoforce vector.
- $\{F_c\}$ is the creep pseudoforce vector.

For each increment of loading, the nonlinear pseudoforces are iterated upon until the requirements of equilibrium, compatability, and the constitutive equations are met within user specified tolerances. Since this method does not require modification of the stiffness matrix during iterations it is very economical. This economy is magnified during cyclic analysis. The stiffness matrix need only be regenerated if the material properties are revised by thermal variation or if elements have been added or removed.

MULTIAXIAL, VARIABLE TEMPERATURE EXAMPLE

In a previous NASA contract, we investigated one of the common thermal stress problems in AGTE's: turbine blade tip cracking. In that case, the critical region was shown by analysis and confirmatory testing to have the cyclic stress-strain behavior noted in Figure 1. High temperature, time dependent flow rapidly relaxes the compressive stress such that on cool-down high tensile stresses are genrated. This process shakes down very rapidly to an almost elastic hysteresis loop based on modulus changes. In that case the problem was almost totally uniaxial in nature.

A second type of thermal stress problem prevalent in AGTE's is the hot spot. In this case, the stress strain response is definitely multiaxial. We will investigate a hot spot on a combustor shingle as being typical of these problems. Figure 2 shows a shingle segment. Taking advantage of its large radius of curvature and thinness, it was modeled as a flat plate in a condition of plane stress. The model is shown in Figure 3. Figures 4, 5 and 6 show the nature of the hot spot at peak temperature and Figure 7 shows the heat-up cool-down temperature cycle at the center of the hot spot. This cycle was analyzed assuming no time dependent effects occcurred during heat-up and cool-down but that a one hour hold time was associated with the peak of the hot spot.

The stress-strain results of the first cycle are shown in Figures 8, 9 and 10 for the center of the hot spot. Figure 8 shows effective stress versus effective strain and Figures 9 and 10 show the biaxial stresses versus strains. Once again the effect of plasticity and creep is to generate tensile stresses during the cool-down portion of the cycle. The next series of figures shows the shakedown stress-strain results for the center of the hot spot. Figure 11 shows the effective stress versus effective strain shakedown values and Figures 12 and 13 show the shakedown biaxial stress cycle at the center of the hot spot. Thus this multiaxial thermal stress case, just as the uniaxial case, shakes down to almost elastic cycling with a high tensile mean stress. In addition, the stresses are almost proportional. These types of analyses are important in indicating the types of response and life tests needed.

REFERENCES

1. Besseling, J. F., "A Theory of Plastic Flow for Anisotropic Hardening in Plastic Deformation of an Initially Isotropic Material", Report S.410, National Aeronautical Research Institute, Amsterdam, 1953.
2. Besseling, J. F., "A Theory of Elastic, Plastic, and Creep Deformations of an Initially Isotropic Material", SUDAER No. 78, Stanford University, April, 1958.
3. Besseling, J. F., "A Theory of Elastic, Plastic, and Creep Deformations of an Initially Isotropic Material Showing Anisotropic Strain-Hardening, Creep Recovery, and Secondary Creep", J. of Applied Mechanics, pp. 529-536, December, 1958.
4. Duwez, P., "On the Plasticity of Crystals", Physical Review, Vol. 47, p. 494, 1935.
5. White, G. N., Jr., "Application of the Theory of Perfectly Plastic Solids to Stress Analysis of Strain Hardening Solids", Graduate Division of Applied Mathematics, Brown University, Tech. Rpt. 51, 1950.
6. Turner, J. J., Clough, R. W., Martin, H. C., and Topp, L. J., "Stiffness and Deflection Analysis of Complex Structures, Journal of the Aeronautical Sciences, Vol. 23, No. 9, p. 805, Sept., 1956.
7. Armen, H. Jr., "Plastic Analysis", Structural Mechanics Computer Programs, edited by Pilkey, W., Saczalski, K., and Schaeffer, H., University Press of Virginia, 1974, pp. 37-79.
8. Armen, H., Jr., Pifko, A., and Levine, H. S., "Finite Element Analysis of Structures in the Plastic Range", NASA CR-1649, February, 1971.
9. Armen, H., Jr., Levine, H. S., and Pifko, A. B., "Plasticity - Theory and Finite Element Applications", Proc. of 2nd U.S.-Japan Seminar on Matrix Methods of Structural Analysis and Design, pp. 393-437, August 1972.
10. Witmer, E. A., Kotanchik, J. J., "Progress Report on Discrete-Element Elastic and Elastic-Plastic Analyses of Shells of Revolution Subjected to Axisymmetric and Asymmetric Loading", Proc. of the Second Conference on Matrix Methods in Structural Mechanics, WPAFB, pp. 1341-1453, December, 1969.
11. Wilson, E. L., "Finite Element Analysis of Two-Dimensional Structures", University of California, Structures and Materials Research Department of Civil Engineering, Report No. 63-2, June, 1963.
12. Salmon, M., Berke, L., and Sandhu, R., "An Application of the Finite Element Method to Elastic-Plastic Problems of Plane Stress", Air Force Flight Dynamics Laboratory, Tech. Rpt. AFFDL-TR-68-39, May, 1970.
13. Zienkiewicz, D. C., The Finite Element Method in Engineering Science, McGraw-Hill, New York, 1971.
14. Marin, J., Ulrich, B. H., and Hughes, W. P., "Plastic Stress-Strain Relations for 75S-T6 Aluminum Alloy Subjected to Biaxial Tensile Stresses", NACA TN2425, National Advisory Committee for Aeronautics, Washington, D.C., August, 1951.
15. Ueda, Y., and Yamakawa, T., "Thermal Stress Analysis of Metals with Temperature Dependent Mechanical Properties", Mechanical Behavior of Materials Vol. 3, edited by Taira, S., and Kunugi, M., The Society of Materials Science, Japan, pp. 10-20, 1972.
16. Hunsaker, B., Jr., Vaughn, D. K., Stricklin, J. A., and Haisler, W. E., "A Comparison of Current Work Hardening Models Used in the Analysis of Plastic Deformations", Texas A&M University, Texas Engineering Experiment Station, TEES-RPT-2926-73-3, October, 1973.

17. McKnight, R. L., "Finite Element Cyclic Thermoplasticity Analysis by the Method of Subvolumes", Ph.D. dissertation, University of Cincinnati, 1975.
18. McKnight, R. L. and Sobel, L. H., "Finite Element Cyclic Thermoplasticity Analysis by the Method of Subvolumes," Comput. Structures, Vol. 7, No. 3, 1977.
19. Marin, J., Pao, Y. H., and Cuff, G., "Creep Properties of Lucite and Plexiglass for Tension, Compression, Bending, and Torsion," Trans. ASME 73, 705, 1951.
20. Pugh, C. E., "Constitutive Equations for Creep Analysis of Liquid Moderated Fast Breeder Reactor (LMFBR) Components," in Advances in Design for Elevated Temperature Environment, S. Y. Zamrik and N. I. Jetter, Eds. ASME, 1975.

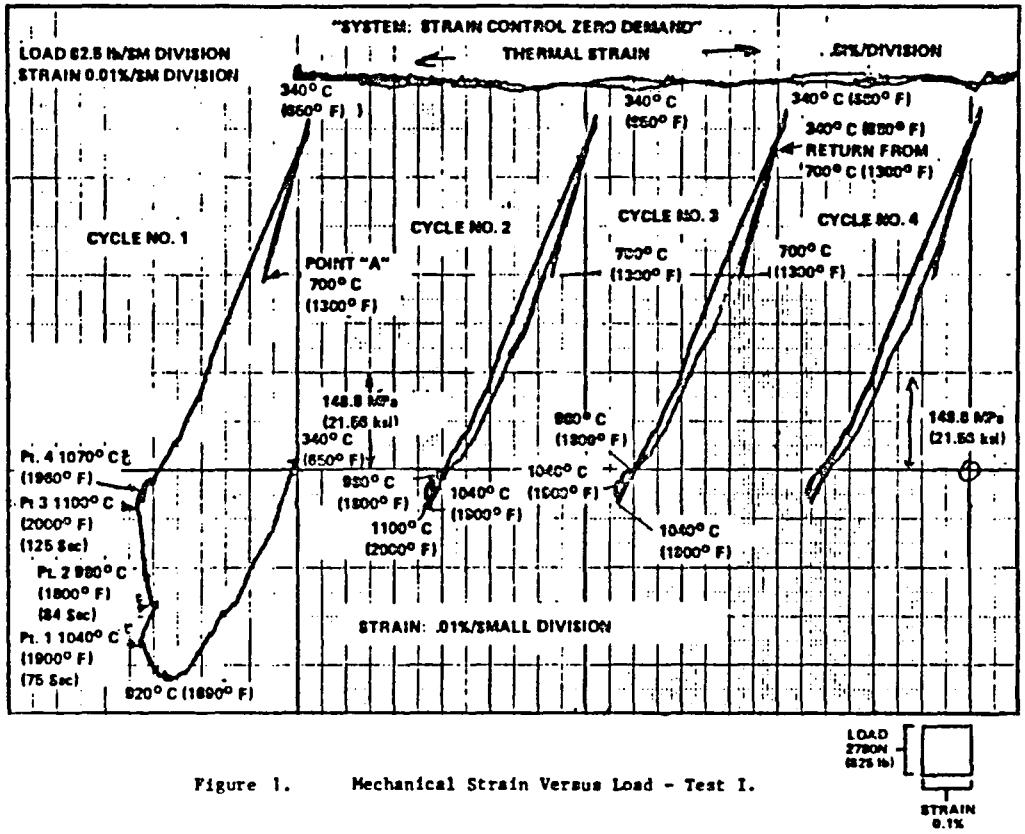

Figure 1. Mechanical Strain Versus Load - Test I.

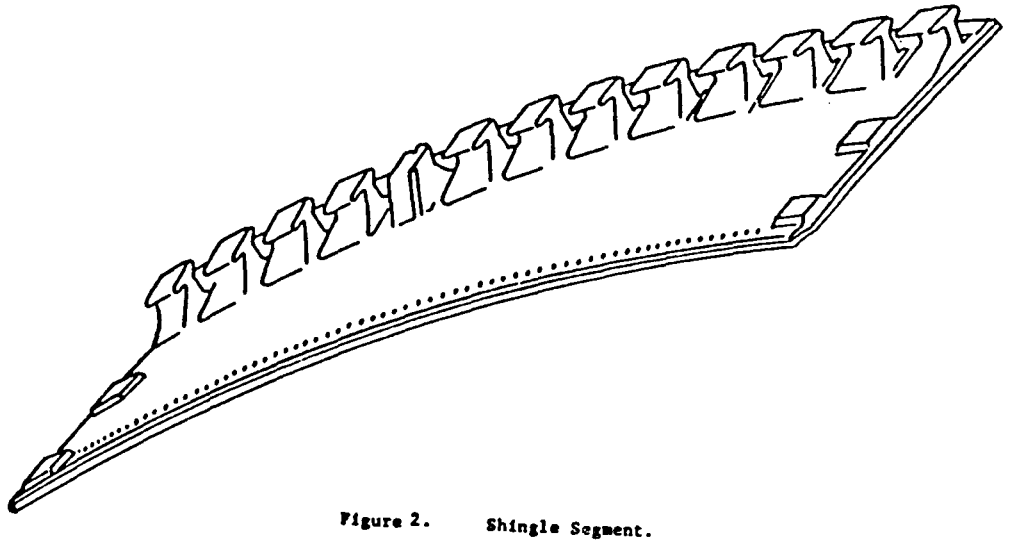

Figure 2. Shingle Segment.

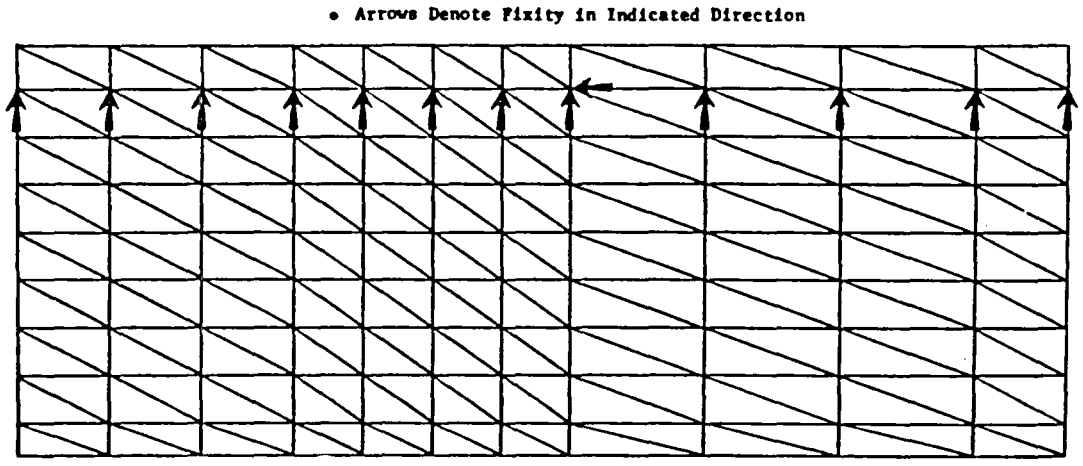

Figure 3. Boundary Conditions.

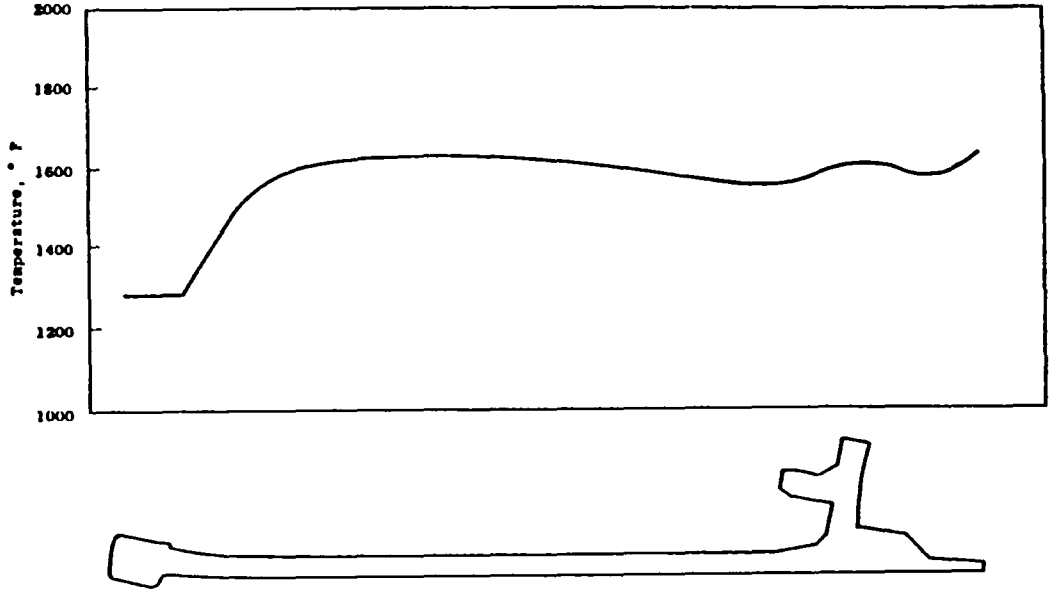

Figure 4. Axial Temperature Distribution W/O Hot Spot.

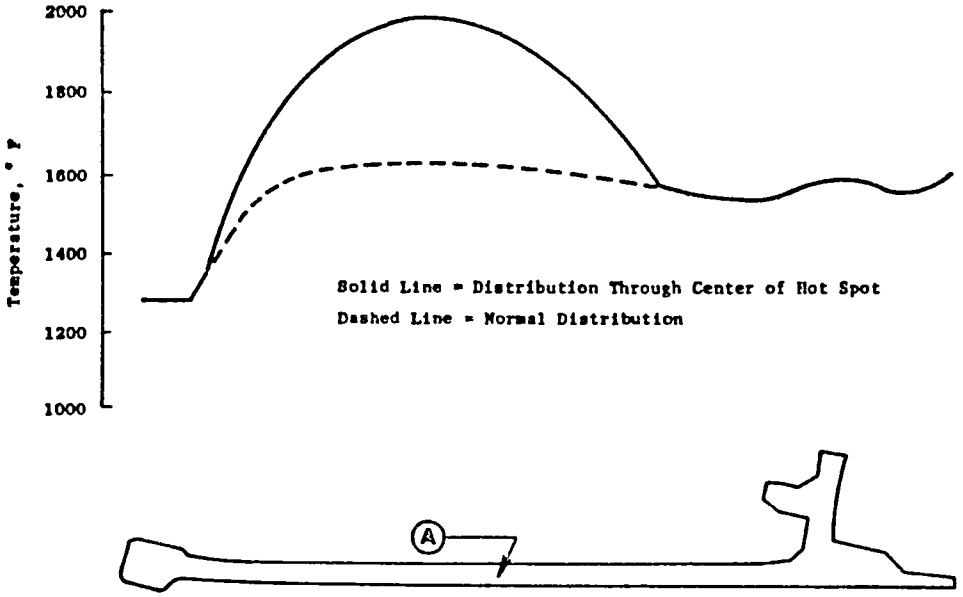

Figure 5. Axial Temperature Distribution Through Hot Spot.

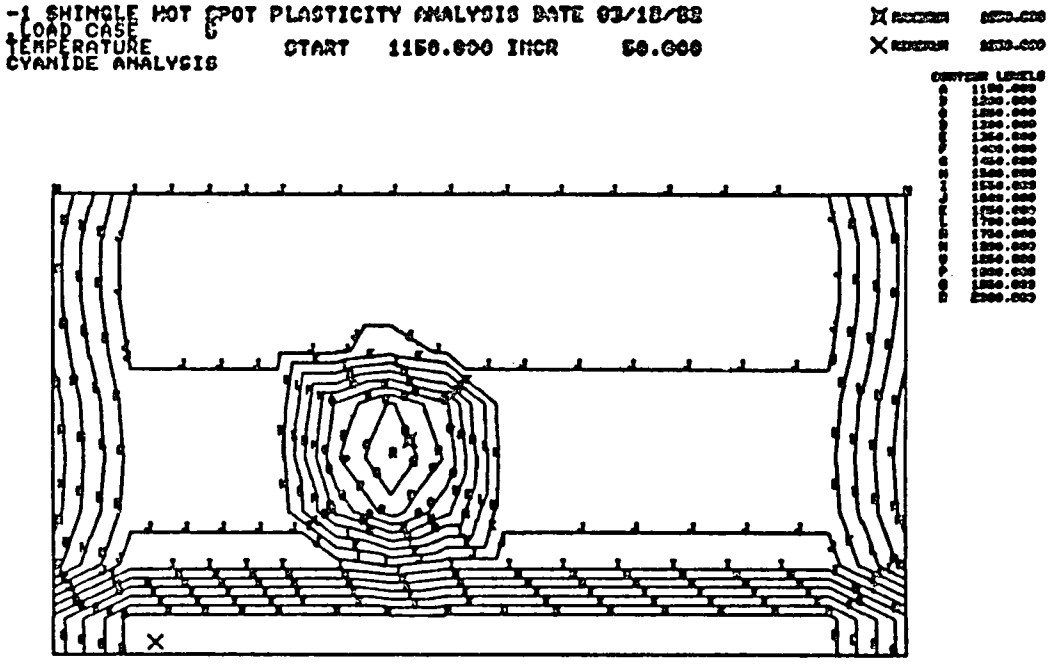

Figure 6. Temperature Contours At Peak Of Hot Spot

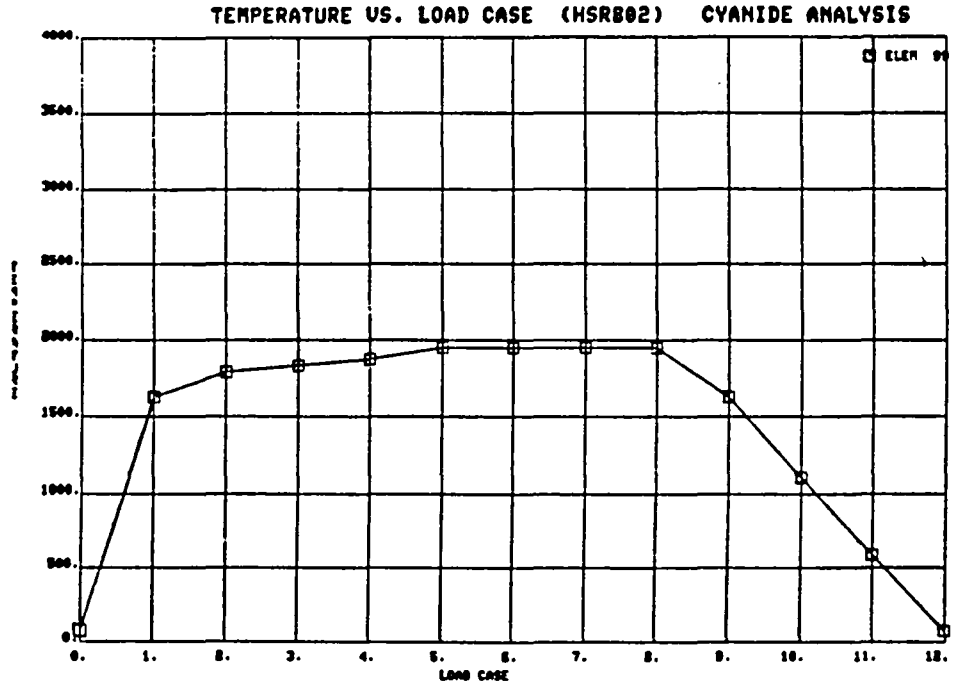

Figure 7. Heat-Up Cool-Down Cycle For Center Of Hot Spot

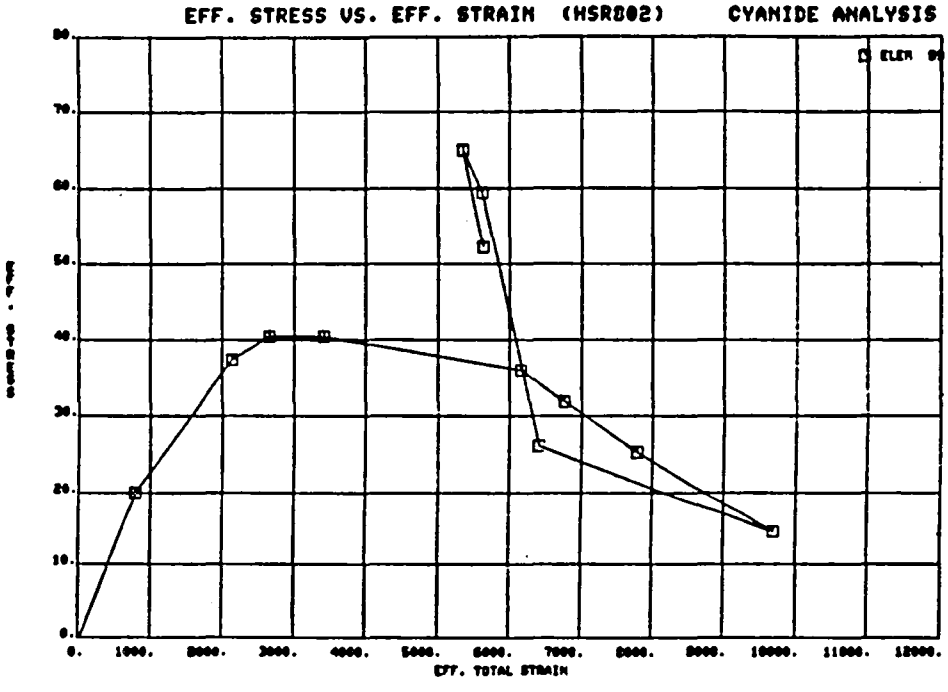

Figure 8. Effective Stress Versus Effective Strain At The Center of the Hot Spot For the First Cycle

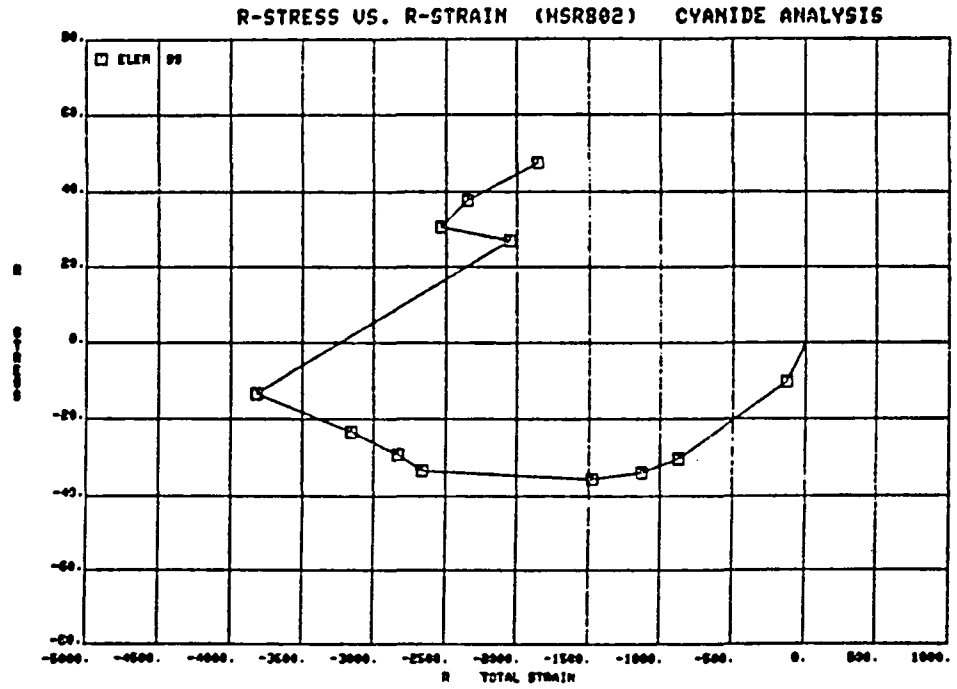

Figure 9. Transverse Stress Versus Strain At The Center of the Hot Spot For the First Cycle

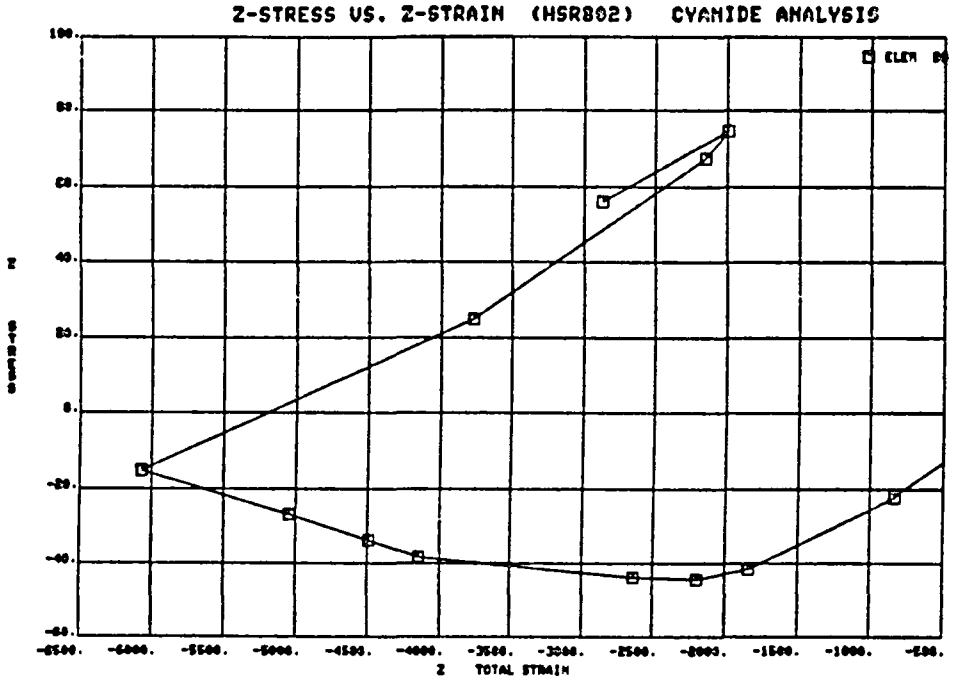

Figure 10. Longitudinal Stress Versus Strain At the Center of The Hot Spot For the First Cycle

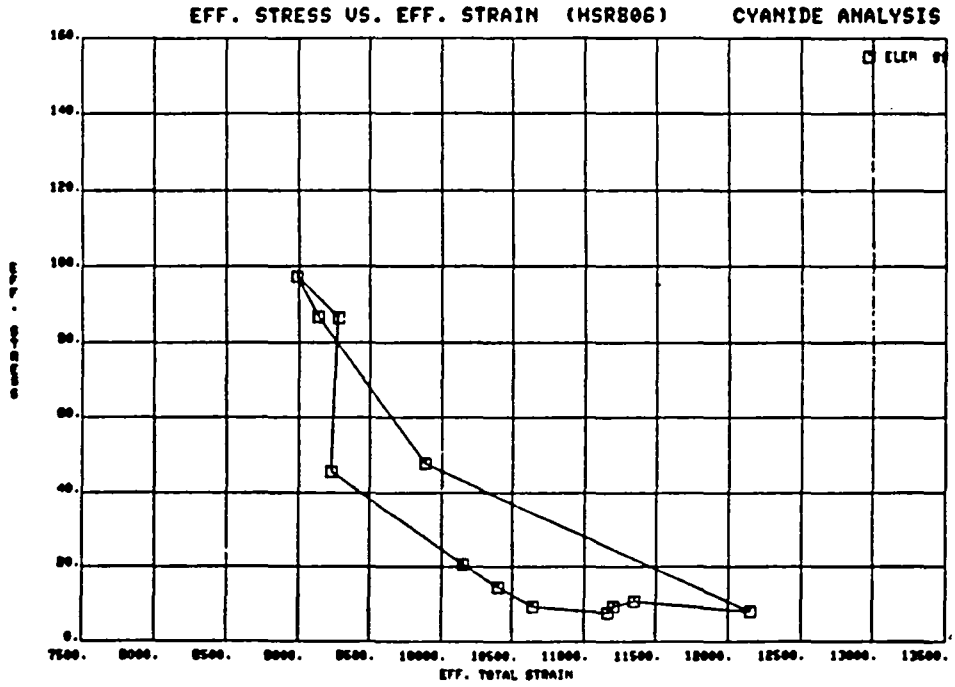

Figure 11. Shakedown Cycle of Effective Stress Versus Effective Strain At the Center of the Hot Spot

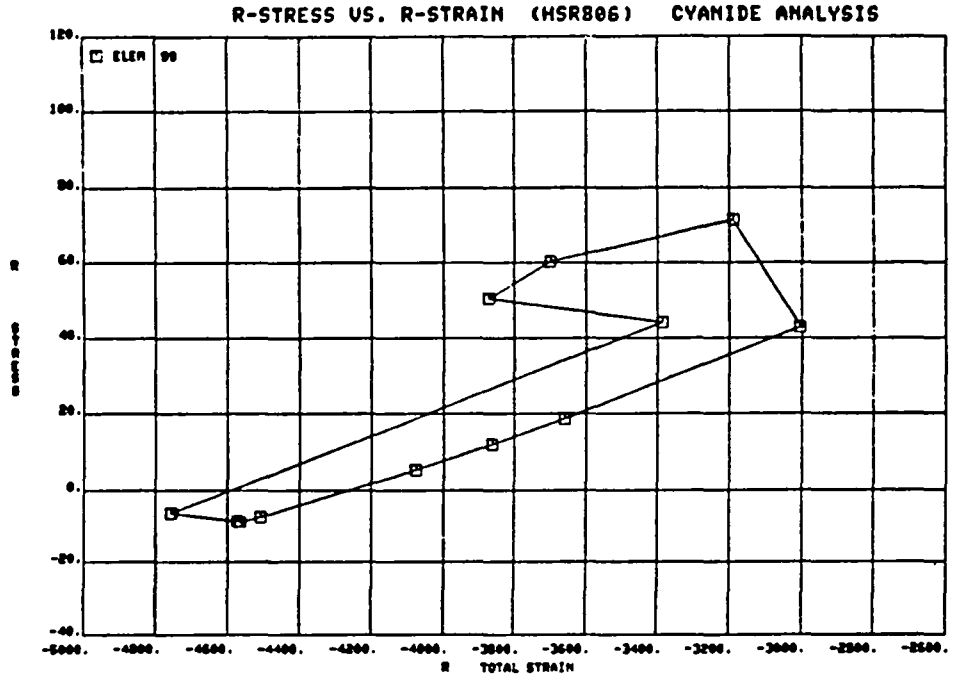

Figure 12. Shakedown Cycle For Transverse Stress Versus Strain At the Center of the Hot Spot

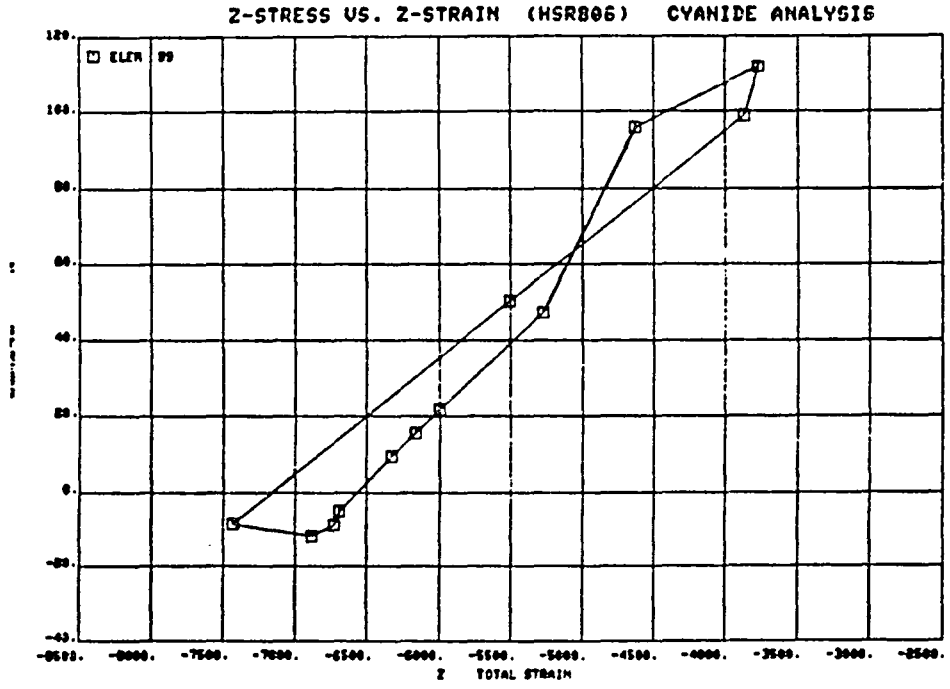

Figure 13. Shakedown Cycle For Longitudinal Stress Versus Strain at the Center of the Hot Spot

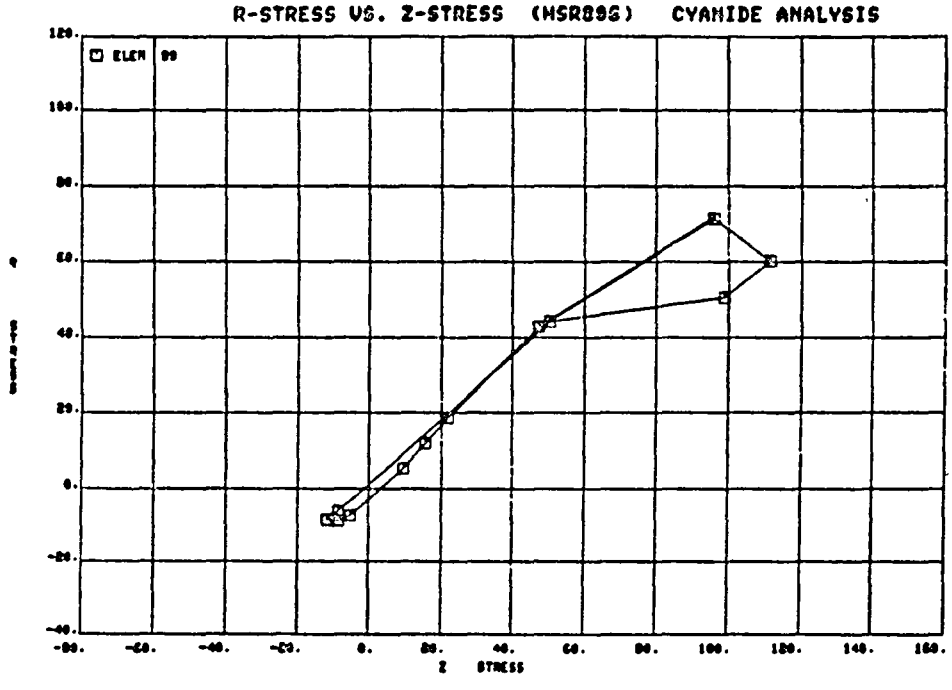

Figure 14. Shakedown Biaxial Stress Cycle At the Center Of the Hot Spot

EVALUATION OF INELASTIC CONSTITUTIVE MODELS FOR NONLINEAR STRUCTURAL ANALYSIS

Albert Kaufman

National Aeronautics and Space Administration
Lewis Research Center
Cleveland, Ohio 44135

ABSTRACT

The influence of inelastic material models on computed stress-strain states, and therefore predicted lives, was studied for thermomechanically loaded structures. Nonlinear structural analyses were performed on a fatigue specimen which had been subjected to thermal cycling in fluidized beds and on a mechanically load-cycled benchmark notch specimen. Four incremental plasticity-creep models (isotropic, kinematic, combined isotropic-kinematic, combined plus transient creep) were exercised using the MARC program. Of the plasticity models, kinematic hardening gave results most consistent with experimental observations. Life predictions using the computed strain histories at the critical location with a Strainrange Partitioning approach considerably overpredicted the crack initiation life of the thermal fatigue specimen.

INTRODUCTION

Hot section components of aircraft gas turbine engines, such as combustor liners and turbine blades and vanes, are subject to progressive creep-fatigue damage resulting from cyclic thermomechanical loading under extreme gas pressure and temperature environments. A Strainrange Partitioning approach (ref. 1) to assess the durability of these components has been under development at the NASA Lewis Research Center. In order to apply this or similar methods, it is first necessary to determine the stress-strain-

temperature history of the part at the critical location where cracks will initiate.

As part of the life prediction studies at Lewis, wedge specimens have been thermally cycled in fluidized beds as described in reference 2. In these tests, two fluidized beds were used to rapidly heat and cool prismatic bar specimens of single or double edge wedge cross-section. Nonlinear structural analyses were performed for these specimens using the MARC program (ref. 3); the results are reported in references 4 and 5. These nonlinear analyses were for specimens of several alloys and used a combined isotropic-kinematic hardening model in MARC in conjunction with monotonic stress-strain properties taken from the literature.

Finite-element nonlinear analysis methods are becoming of increasing interest for computing the cyclic stress-strain response of hot section components (refs. 6 to 10). A major disadvantage of these methods, excessive computing costs, is being alleviated by advances in computer technology. Another deficiency is that current nonlinear analysis computer codes utilize classical constitutive material models whose accuracies vary with the type of material and the cyclic conditions involved. Furthermore, these classical models simplify the analyses by uncoupling time independent (plasticity) and time dependent (creep) effects, neglecting strain rate effects on plastic flow, and defining specific yield surfaces. The NASA Lewis Research Center has instituted programs to develop constitutive models which would more realistically represent the inelastic material behavior and be computationally practical for finite-element structural analysis. To verify the nonlinear structural analysis methodologies, Lewis is also sponsoring controlled cyclic experiments to provide strain data for benchmark notch specimens (ref. 11).

In this study existing constitutive models in the MARC computer program were exercised in inelastic analyses of an IN 100 wedge specimen subjected to thermal cycling and an Inconel 718 benchmark notch specimen subjected to mechanical load cycling. The objective of the study was to evaluate the effects on calculated hysteretic response, and therefore predicted life, of different inelastic constitutive models available in nonlinear analysis computer codes.

Three dimensional elastic and nonlinear structural analyses were performed on a thermally cycled double-edge wedge specimen. The nonlinear analyses were conducted using isotropic, kinematic and combined isotropic-kinematic hardening models and a combined hardening model in conjunction with a strain hardening creep law to account for cyclic time-dependent effects. Strain histories computed at the critical location from the different constitutive models were used in conjunction with the Strainrange Partitioning method to compare predicted lives against the observed crack initiation life. Two dimensional nonlinear analyses were performed for a mechanically load-cycled benchmark notch specimen; computed strain histories at the notch root using various material models were compared against measured notch strains.

PROBLEM DESCRIPTION

The primary structure considered in this study was an IN 100 alloy double-edge wedge specimen as illustrated in figure 1. Cracking was observed at the 1/4 span position on the leading edge after 38 cycles of testing in the fluidized bed facility (ref. 2).

The physical properties of the cast IN 100 alloy are presented in table I. Mean thermal coefficient of expansion data were converted to in-

stantaneous coefficients of thermal expansion for input into the MARC program. The modulus of elasticity was determined from monotonic stress-strain tests of tensile specimens. Cyclic stress-strain curves were obtained using the single specimen incremental step procedure and equipment described in reference 12. A typical cyclic stress-strain curve, with the loci of the curve tips represented by an exponential equation, is illustrated in figure 2. Also shown for comparison in figure 2 is a monotonic stress-strain curve represented by an exponential equation. Short-time cyclic creep tests were conducted on IN 100 specimens using the procedures and facilities described in reference 13. Preprocessor programs expressed both the cyclic stress-strain and creep data as functional relations in exponential form. These equations were incorporated into MARC by means of user subroutines. The constants of the cyclic and monotonic stress-strain equations are given in table II for various temperatures. In table III the constants of the cyclic creep equations are given for various temperatures.

The specimen was thermally cycled in fluidized beds maintained at 316° and 1088° C with an immersion time of 3 minutes in each bed. Transient temperature loading on the specimens was determined from thermocouple data as described in reference 2. Curve fits of thermocouple data along the midchord at the midspan at various increments after immersion into the fluidized beds are presented in figure 3. The temperature gradient through the thickness of the wedge was assumed to be negligible. Another set of thermocouple data was taken with thermocouples mounted along the leading edge over half the span to obtain the longitudinal (along the span of the specimen) temperature gradient for the different time increments.

Supplemental analyses to evaluate the constitutive material models were

also performed for a benchmark notch specimen of Inconel 718 alloy which was load cycled at a frequency of 0.167 Hz and a temperature maintained at 649° C. The material properties given in reference 11 were correlated in the same way as the IN 100 alloy properties.

ANALYTICAL PROCEDURE

Stress and total-plastic-creep strain distributions in the wedge specimens were calculated from the MARC nonlinear, finite-element computer program. Computations were performed for 34 time increments (17 heating, 17 cooling) into which the thermal cycle was subdivided, as shown in figure 3. The analyses were terminated when stable stress-strain hysteresis loops were obtained or after three cycles if the hysteresis loops remained unstable.

Plasticity computations were based on incremental plasticity theory using the von Mises yield criterion and normality flow rule. The yield surface under reversed loading was determined from the stress-strain properties and the selected hardening model. Three hardening models available in MARC (isotropic, kinematic and combined isotropic-kinematic) were selected for evaluation. Monotonic stress-strain properties were used in conjunction with the isotropic and combined models because of their initial instability. Saturated cyclic stress-strain properties were used for the stable kinematic model. A bilinear representation of the cyclic stress-strain curve, as shown in figure 2, was applied to the kinematic hardening model. The slope of the kinematic model was determined from energy considerations so that the strain energy, as indicated by the enclosed area, would be identical with that of the actual cyclic stress-strain curve. Creep effects during the cycle were considered for one case involving the combined model

by imposing four 30 second hold times during heating and two 6 second hold times at the start of the cooling part of the cycle. These intervals were selected because the combination of temperatures and stresses indicated a possibility of the occurrence of significant creep at these times in the thermal transient. The creep computations utilized the cyclic creep data in conjunction with a strain-hardening rule. A subroutine which was inserted into the MARC program in the form of yield strengths and work hardening slopes as functions of temperature, was used to determine the stress-strain properties for the local temperatures at the Gaussian integration points. Similarly the creep properties and laws were coded into another user subroutine which was used to obtain the creep strains at the integration points.

A preprocessor program converted the thermal loading data from the wedge specimen into the form of sixth-order polynomial equations. A subroutine, which was inserted into MARC, interpolated from these equations for the local temperatures at the Gaussian integration points.

The finite element model for the wedge specimen is illustrated in figure 4. Because of symmetry only one-fourth of the specimen needed to be modelled; this model was bounded by the surface and intersecting midchord and midspan planes of symmetry. The element used was a 20 node, isoparametric, three dimensional block with 8 corner nodes and 12 edge midpoint nodes. This element had 27 Gaussian integration points. The model consisted of 36 elements with a total of 315 nodes and 778 unsuppressed degrees of freedom.

All nodes initially on the midspan and midchord faces of the model were constrained to lie on the midspan and midchord planes respectively. In addition, one node at the leading edge was constrained chordwise (leading to trailing edge) in order to prevent rigid body motion in that direction.

The analytical procedure used for the benchmark notch specimen was basically the same as for the wedge specimen. Each cycle was subdivided into 30 load steps. One fourth of the specimen was modelled as shown in figure 5 using 592 plane strain, triangular elements with a total of 335 nodes.

RESULTS AND DISCUSSION

The critical location for crack initiation in the thermally cycled double-edge wedge specimen is at the leading edge at a quarter of the specimen span from either end. Results of both elastic and inelastic structural analyses determined that the critical location based on the region of the finite element model with the largest total strain range during the cycle was coincident with the observed crack initiation site. In the following discussion, the stress-strain results for the critical location were actually computed at the closest Gaussian integration point which was 0.056 centimeter from the surface at the quarter span.

The stress-total strain solutions at the critical location from the MARC elastic and nonlinear analyses of the wedge specimen are shown in figure 6. All stresses and strains in this figure were effective or equivalent values which were originally computed as positive numbers. However, in order to construct stress-strain hysteresis loops for life prediction purposes, the stresses and total strains were assigned positive or negative signs depending on the signs of the highest magnitude principal stresses or strains. Nonlinear stress-strain hysteresis loops are presented for the second cycle of the analyses. During heating the metal temperature at the critical location increased from 343° C at the start of the cycle to 1077° C at the end of heating. In all analytical cases, the minimum total strain occurred after 30 seconds of heating when the temperature at the critical location

was 888° C and the maximum total strain after 9 seconds of cooling or a total elapsed time of 189 seconds when the temperature was 749° C.

Predicted stress-strain hysteresis loops from the elastic analysis and the nonlinear analyses using combined and kinematic hardening models are compared in figure 6(a). These results indicate that the total strain range was not appreciably affected by the choice of constitutive model or type of stress-strain data and that an elastic analysis was adequate for the computation of the total strain range. The major differences between the elastic and nonlinear hysteresis loops were in the stress levels, which shifted in the tensile direction under inelastic straining with the largest peak and mean stresses obtained with the combined hardening model. A measure of the strain energy or plastic work is the area of the hysteresis loop. The widest hysteresis loop and, therefore, the most plastic work is shown by the kinematic hardening model in figure 6. There was no further plastic straining or work during or after the second cycle using the combined hardening model and, therefore the area and shape of the combined and elastic hysteresis loops in figure 6 remained about the same.

The nonlinear analysis using the isotropic hardening model gave essentially the same stress-strain solutions as were obtained with the combined model in figure 6(a) due to the use of the same monotonic stress-strain properties and the absence of plastic strain reversal during cycling. Therefore, the discussion of results for the combined hardening model is also applicable to isotropic hardening and the latter will not be discussed separately.

Figure 6(b) compares the stress-strain hysteresis loops from the nonlinear analyses using the combined hardening models with and without creep.

Inclusion of creep effects during the thermal transients had only a small effect on the peak and mean stresses with combined hardening, but resulted in substantially more strain energy per cycle as represented by the enclosed areas of the stress-strain hysteresis loops. Although the hysteresis loops for the combined-creep and kinematic models in figure 6 are shown as closed, there was some inelastic strain ratchetting which was relatively minor and therefore ignored in plotting the loops.

Stabilization of the stress-strain solution using the combined hardening model is shown in figure 7(a) where it is seen that there was no further plastic flow after the first 60 seconds of heating; this is an impossibility since the specimen could not fail in 38 cycles without undergoing substantial plastic strain cycling. In contrast the kinematic hardening results in figure 7(a) exhibit plastic strain reversal and ratchetting with a relatively constant plastic strain range per cycle. Figure 7(b) shows the inelastic strain response for the combined-creep case. Accounting for transient creep effects resulted in creep strain ratchetting on every cycle and smaller plastic strain changes with the combined hardening model. Only slight changes in the maximum equivalent creep strain were obtained with further cycling. However, the minimum equivalent creep strain increased, and therefore the creep strain range decreased, although at diminishing rates during cycling.

The computed strain histories at the critical location were used to predict crack initiation life based on the Strainrange Partitioning Life Prediction Method. The material life relationships for this method are defined in reference 14 for cast IN 100 alloy from isothermal fatigue and creep rupture tests. For these analyses the response from the kinematic model con-

tained only pp(tensile plasticity reversed by compressive plasticity) and from the combined-creep model was conservatively assumed to contain cc(tensile creep reversed by compressive creep) damage cycles. Crack initiation lives of approximately 1400 cycles were predicted in both cases compared to the observed life of 38 cycles. The overpredictions in life are not necessarily proof of the inadequacy of the structural analysis method since there is evidence that thermal cycling produces damage at a faster rate than comparable isothermal, strain-controlled test data used in the life prediction method.

In figure 8 analytical results using both combined and kinematic hardening models are compared against the experimental load-notch strain cycle from the benchmark notch test. Creep was not a significant factor under the continuous cycling, isothermal conditions of this test. The experimental results demonstrated that a stable load strain response occurred on the first cycle with only minor strain changes due to subsequent cycling. A plasticity analysis using the combined hardening model did not accurately represent the experimental results; it predicted, after initial loading, an elastic response with further cycling (fig. 8(a)). Another plasticity analysis using the kinematic hardening model demonstrated good agreement with the experimental results. Kinematic hardening predicted ratchetting between the first and second cycles and a stable notch strain cyclic response thereafter (fig 8(b)); except for slightly overpredicting the ratchetting, these results are consistent with the experimental notch cyclic response.

SUMMARY OF RESULTS

The results of the evaluation of inelastic constitutive models available in nonlinear, structural analysis computer programs can be summarized as follows:

1. Of the plasticity hardening models which were evaluated, the kinematic model gave a predicted stress-strain response most consistent with experimental observations. The combined (as well as the isotropic) model predicted elastic response during cycling which obviously did not agree with experimental results from both the thermal fatigue wedge and benchmark notch specimen tests. Creep effects were shown to be significant during thermal transients and failure to take them into account can affect the predicted stress-strain response.

2. Of the structural analysis parameters used in low-cycle fatigue damage models only the total strain range was relatively insensitive to the choice of inelastic constitutive model. Other parameters such as inelastic strain range, mean stress, and inelastic work were significantly affected by the constitutive model. The elastically computed maximum total strain range agreed well with that computed from the inelastic analyses. The elastic analysis was also able to determine the critical location for crack initiation and the cycle times when the total strain was maximum or minimum.

3. The life prediction analyses based on the structural analysis results using the kinematic and combined-creep models in conjunction with isothermal, strain controlled fatigue test data overpredicted the observed crack initiation life of the thermally-cycled wedge specimen.

REFERENCES

1. Hirschberg, M. H. and Halford, G. R., "Use of Strainrange Partitioning to Predict High-Temperature Low-Cycle Fatigue Life," NASA TN D-8072, 1976.
2. Bizon, P. T. and Spera, D. A., "Comparative Thermal Fatigue Resistances of Twenty-Six Nickel and Cobalt-Base Alloys," NASA TN D-8071, 1975.

3. MARC General Purpose Finite Element Analysis Program, User Manual, Vols. A and B, MARC Analysis Research Corpor., 1979.

4. Kaufman, A.," Elastic-Plastic Finite-Element Analyses of Thermally Cycled Single-Edge Wedge Specimens," NASA TP-1982, 1982.

5. Kaufman, A. and Hunt, L. E., "Elastic-Plastic Finite-Element Analyses of Thermally Cycled Double-Edge Wedge Specimens," NASA TP-1973, 1982.

6. Kaufman, A. and Gaugler, R. E., "Cyclic Structural Analyses of Air-Cooled Gas Turbine Blades and Vanes," SAE Paper No. 760918, 1976.

7. Kaufman, A. and Gaugler, R. E., Nonlinear, Three-Dimensional Finite-Element Analysis of Air-Cooled Gas Turbine Blades," NASA TP-1669, 1980.

8. Kaufman, A., "Comparison of Elastic and Elastic-Plastic Structural Analyses for Cooled Turbine Blade Airfoils," NASA TP-1679, 1980.

9. Moreno, V., "Combustor Liner Durability Analysis, " PWA-5684-19, Pratt and Whitney Aircraft Group, East Hartford, Conn., Feb. 1981. (NASA CR-165250.)

10. McKnight, R. L., Laflen J. H. and Spamer, G. T., "Turbine Blade Tip Durability Analysis, General Electric Company, Cincinnati, Ohio, Feb. 1981. (NASA*CR-165268.)

11. Domas, P. A., et al., "Benchmark Notch Test for Life Prediction," NASA CR-165571, NAS3-22522, 1981.

12. Nachtigall, A. J., "Cyclic Stress-Strain Curve Determination for D6AC Steel by Three Methods," NASA TM-73815, 1977.

13. Halford, G. R., "Cyclic Creep-Rupture Behavior of Three HighTemperature Alloys," Metallurgical Transactions, Vol.3, No. 8, Aug. 1972, pp. 2247-2256

14. Halford, G. R. and Nachtigall, A. J., "Strainrange Partitioning Behavior of the Nickel-Base Superalloys, Rene' 80 and IN 100, "Characterization of Low Cycle High Temperature Fatigue by the Strain Range Partitioning Method,* AGARD-CP-243, Technical Editing and Reproduction Ltd., London, England, Apr. 1978, pp. 2-1, 2-14.

TABLE 1. IN 100 ALLOY PHYSICAL PROPERTIES

Temperature, °C	Modulus of Elasticity, MN/m^2	Mean Coefficient of Thermal Expansion, $m/m/^oC$
316	$193X10^3$	$13.1X10^{-6}$
371	190	13.3
427	186	13.5
482	183	13.7
538	179	13.9
593	176	14.0
649	172	14.4
704	168	14.6
760	163	14.9
816	157	15.4
871	152	15.8
927	145	16.4
982	139	16.7
1038	133	17.5
1093	127	18.2

TABLE II. IN100 ALLOY STRESS-STRAIN PROPERTIES

Temperature, °C	Cyclic, [i] [j] $\sigma=K(\epsilon_p/.1)^n$		Monotonic, [j] [k] $\sigma=C(\epsilon_p/.1)^m$	
	K	n	C	m
316	1005	.046	731	.078
427	944	.064	731	.078
538	869	.086	731	.078
649	777	.113	731	.078
760	665	.147	731	.078
871	528	.187	676	.078
982	361	.236	255	.146
1093	157	.297	173	.146

[i] Locus of cyclic curve tips (fig. 2)
[j] Stress (σ) in MPa, plastic strain (ϵ_p) in percent
[k] Not applicable for ϵ_p less than 0.02 percent

TABLE III. IN 100 ALLOY CREEP PROPERTIES

Temperature, °C	Creep rate, %/min., [l] $\dot{\epsilon}_{cr}=A(\sigma/6.895)^m(t)^n$		
	A	m	n
760	.00062	0.717	-0.881
871	.00012	1.709	-0.736
982	.00010	2.172	-0.654
1093	.00058	2.103	-0.634

[l] Stress (σ) in MPa, time (t) in minutes

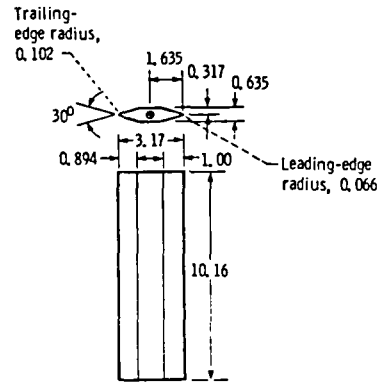

Figure 1. - Double-edge wedge. (All linear dimensions in centimeters.)

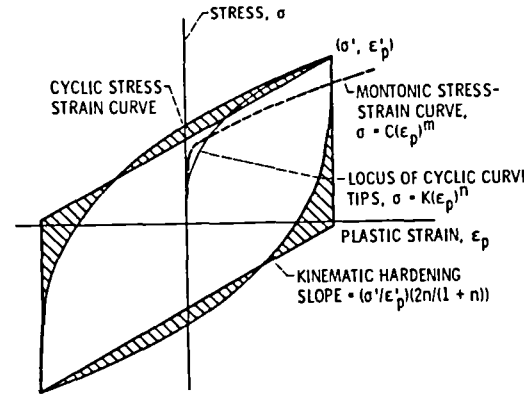

Figure 2. - Representation of stress-strain curves.

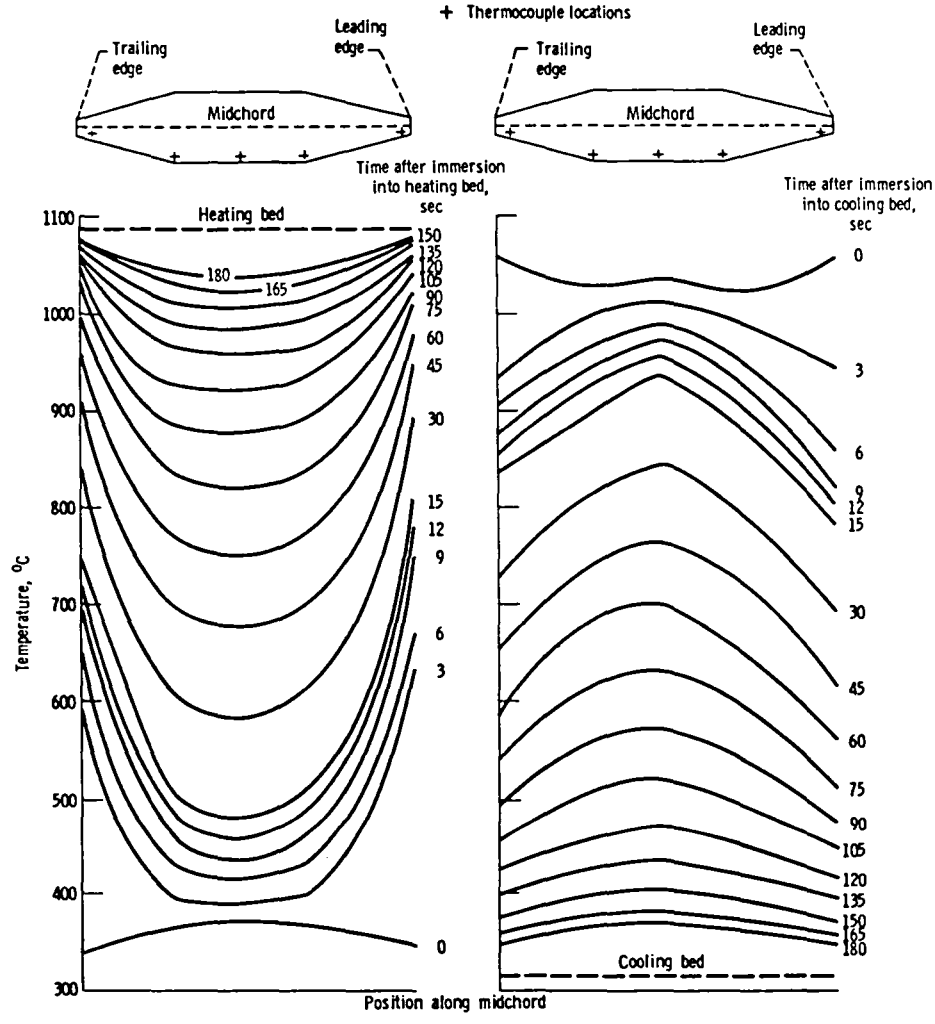

Figure 3. - Temperature of midchord at midspan at various times after immersion into fluidized beds.

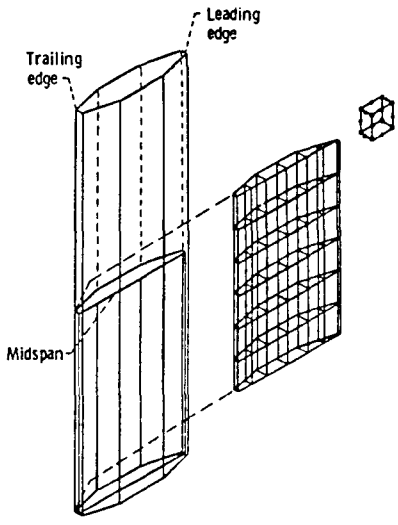

Figure 4. - Model and typical element used for MARC analysis with coordinate convention.

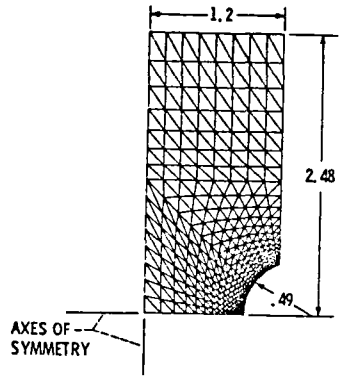

Figure 5. - Benchmark notch specimen finite element model (all dimensions in cm).

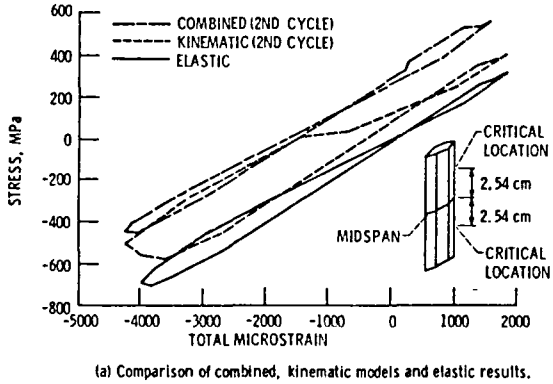

(a) Comparison of combined, kinematic models and elastic results.

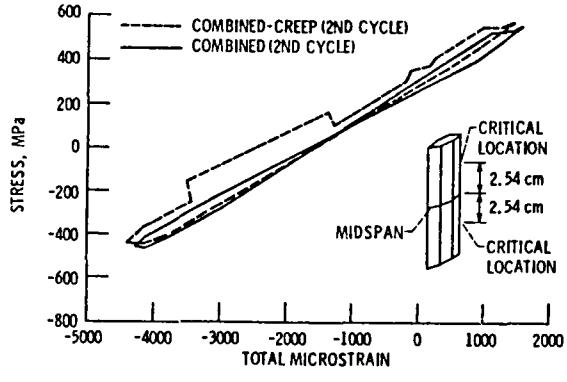

(b) Comparison of combined and combined-creep models.

Figure 6. - Effect of inelastic constitutive model on stress-strain response of wedge specimen (critical location).

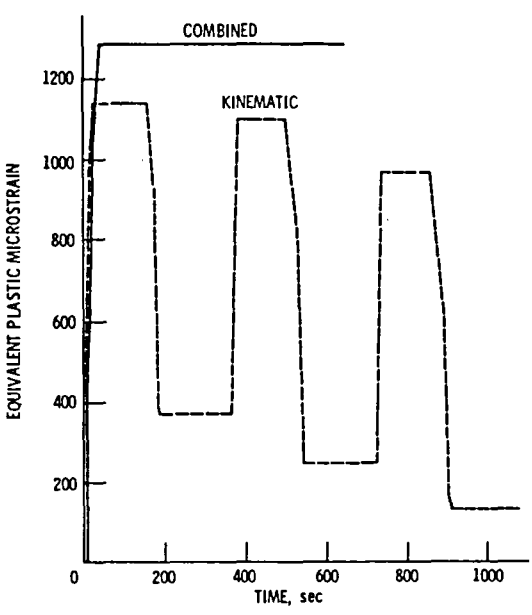

(a) Combined and kinematic models.

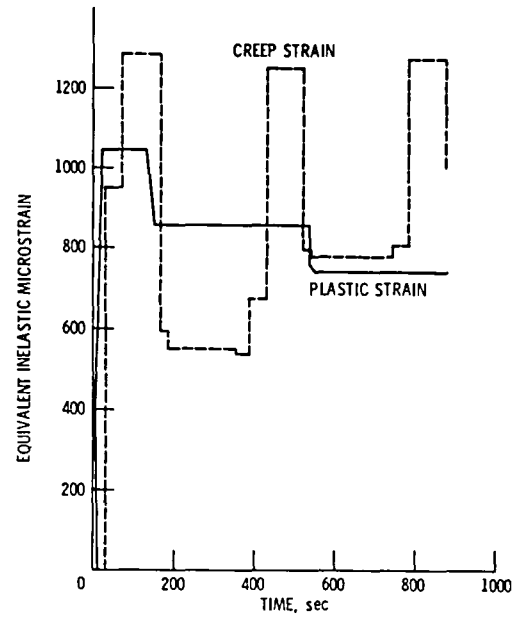

(b) Combined-creep model.

Figure 7. - Inelastic strain response at critical location of wedge specimen.

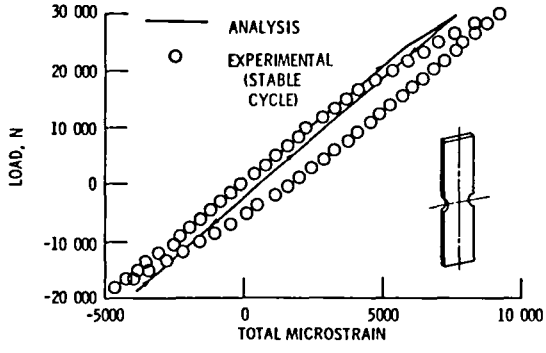

(a) Combined model.

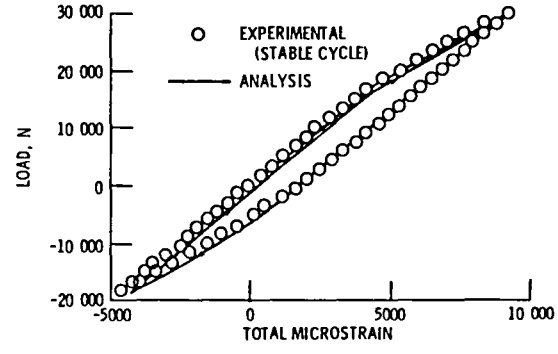

(b) Kinematic model.

Figure 8. - Comparison of benchmark notch specimen experimental and analytical results.

CONSTITUTIVE EQUATIONS FOR USE IN DESIGN ANALYSES OF LONG-LIFE ELEVATED TEMPERATURE COMPONENTS*

Claud E. Pugh and David N. Robinson
Oak Ridge National Laboratory
Oak Ridge, Tennessee 37830

EXTENDED ABSTRACT

This paper addresses design analysis needs and procedures relative to elevated temperature components in liquid metal fast breeder reactor (LMFBR) systems. Parts of LMFBR systems operate for significant portions of their 30 to 40 year design lifetimes at temperatures that are sufficiently high for time-dependent (creep) deformations to occur. Periodic shut-down events cause the components to experience thermal transients which combine with pressure loadings to produce complex inelastic behavior at temperatures within the creep regime of the structural alloys. The effects of the thermal transients on the pressure boundary components are enhanced by the excellent heat transfer properties of the liquid sodium coolant.

Design criteria for high-temperature nuclear reactor components recognize the potential occurrence of inelastic structural response. Specifically, criteria and limits, such as those in ASME Code Case N-47, have been developed that reflect a recognition of this potential and employ design-by-analysis concepts that can require that inelastic (elastic-plastic and creep) analyses be performed to satisfy the criteria and limits. However, the ASME documents have not included guidance on how inelastic analyses should be carried out, leaving it to the component owners to select the methods to be employed. Therefore, the Oak Ridge National Laboratory (ORNL) has undertaken on behalf of the Department of Energy, coordinated experimental and analytical efforts to establish appropriate constitutive equations for representing multiaxial time-dependent responses of LMFBR alloys. This presentation describes progress that has been made in recent years. Special attention is given to activities relevant to the development of equations applicable under cyclic loading conditions.

*Research sponsored by the Office of Reactor Research and Technology, U.S. Department of Energy under contract W-7405-eng-26 with the Union Carbide Corporation.

The general process through which many of the present LMFBR structural analysis guidelines have been developed is discussed in Ref. 1. This process has led to a framework that is in place for three alloys, and aspects of the inelastic analysis capabilities have been discussed earlier in Refs. 2 and 3. Most of the developments discussed here are given in terms of constitutive equations that are based on theories of continuum mechanics that separate elastic, plastic, and creep strains. However, progress is being made in developing equations that are based on "unified measures" of inelastic strains and "state variables" that do not make such a distinction. This progress is also addressed in this symposium by Robinson. A discussion of overall progress in these areas is given in Ref. 2.

The basic analytical framework is first to be discussed, but a major focus is on improved representations of interactions between time-independent (elastic-plastic) and time-dependent (creep) responses of materials. The elastic-plastic model is based on a modified linear kinematic hardening model that permits the occurrence of limited isotropic hardening. The creep model is based on an equation-of-state approach that uses strain-hardening and stress as state variables. The strain-hardening measure has been defined relative to history-dependent reference stresses in order to be applicable to cyclic loadings. Both the elastic-plastic and creep models are formulated in general multiaxial terms.

Although, it has been recognized for a long time that plastic and creep deformations influence one another at elevated temperatures, it has been difficult to understand the nature of these influences to the degree where they can be incorporated into constitutive equations intended for design use. The difficulties include identifying the potentially important interactions, understanding their magnitude and longevity, representing them with mathematical models, and understanding the consequences of interaction models for loading conditions other than the ones from which they were initially developed. The concerns about interactions have been from two perspectives. In the first, observations are made on the representation of influences of cyclic plastic straining on subsequent creep beahvior. In the second, representations of elastic-plastic behavior are examined while considering influences of prior and interspersed creep

straining or periods of stress relaxation. This presentation addresses the former more than the latter. Further observations concerning the latter can be found in Ref. 3 through 5.

Figures 1 and 2 show stress relaxation responses of a specimen of 2-1/4 Cr—1 Mo steel subjected to successive loadings to illustrate one type of interaction between creep and plastic deformations. In each sequence, the specimen is subjected to repeated stress relaxation intervals that start with approximately the same initial stress [103 MPa (15 ksi)] at 538°C (1000°F). In the first test sequence, the tensile load in the specimen is increased directly to the maximum value at the end of the constant strain (relaxation) hold period. In the second test, the specimen is loaded in the compressive direction to prescribed compressive plastic strain values and then loaded to the maximum tensile stress. (The loading histories are shown schematically in Figs. 3 and 4.) It is clearly seen that the reversed plastic loadings influence the subsequence resistance to creep deformation. The constitutive equations currently employed in LMFBR design evaluations recognize this type of interaction.

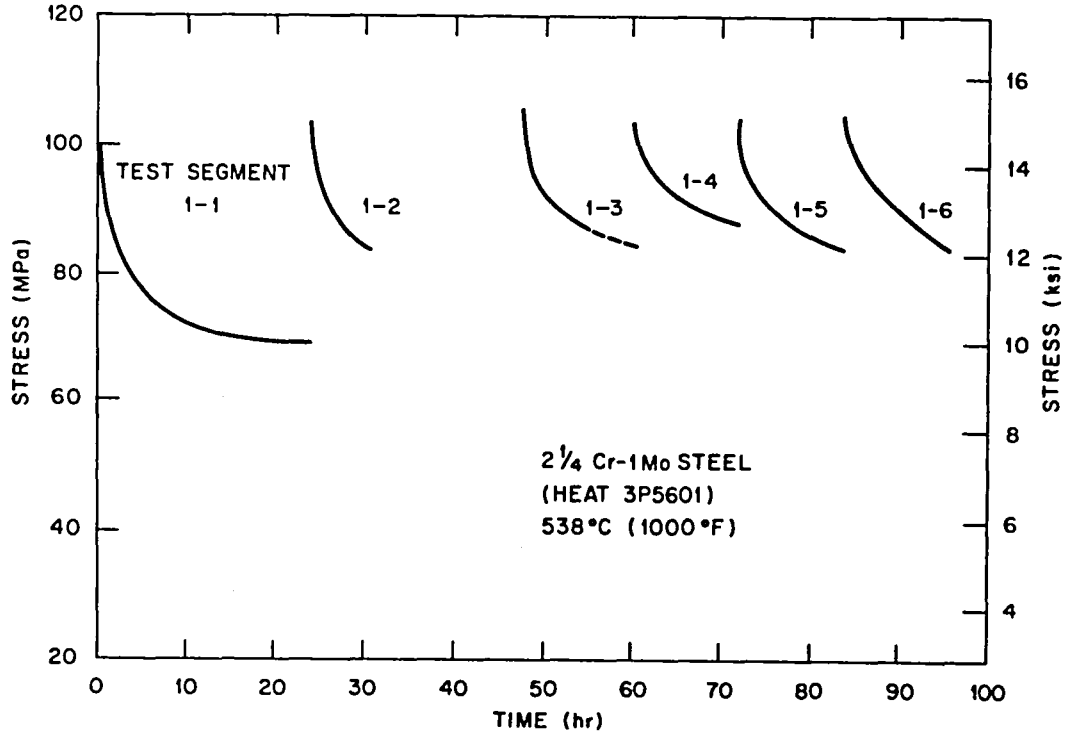

Fig. 1. Stress relaxation response of a 2-1/4 Cr—1 Mo steel specimen repeatedly loaded to an initial stress of 103 MPa (15 ksi) at 538°C (1000°F).

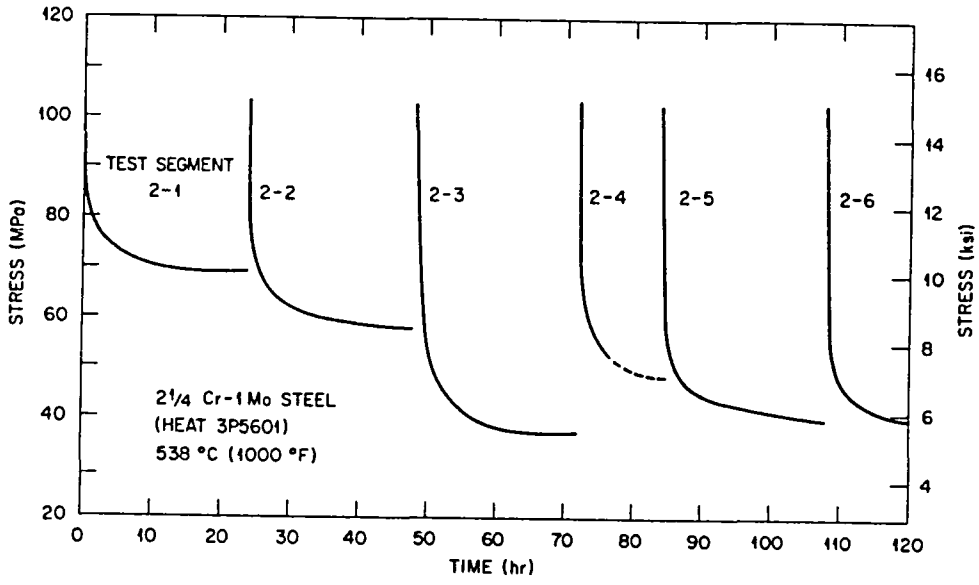

Fig. 2. Relaxation response of the 2-1/4 Cr–1 Mo steel specimen employed in Fig. 1 to successive loadings separated by reversed plastic cycles.

References

1. Pugh, C. E., "On Establishing Constitutive Equations for Use in Design of High-Temperature Fast-Reactor Structures," *Journal of Nuclear Engineering and Design*, Vol. 51, December 1978, pp. 23-27.

2. Pugh, C. E. and Robinson, D. N., "Constitutive Equations for Meeting Elevated Temperature Design Needs," in *Pressure Vessel and Piping — Design Technology — Decade of Progress*, ASME, 1982.

3. Pugh, C. E. and Robinson, D. N., "Some Trends in Constitutive Equation Model Development for High-Temperature Behavior of Fast-Reactor Structural Alloys," *Journal of Nuclear Engineering and Design*, Vol. 48, 1978, pp. 269-76.

4. Corum, J. M., "Evaluation of Inelastic Analysis Methods," *Transactions of the Fourth SMiRT Conference*, San Francisco, Vol. 4, Part L, Paper No. L 4/1, August 1977.

5. Pugh, C. E., "Progress in Developing Constitutive Equations for Inelastic Design Analysis," in *Inelastic Analysis and Life Prediction at Elevated Temperatures*, ASME Publication PVP-59, Orlando, FL, 1982.

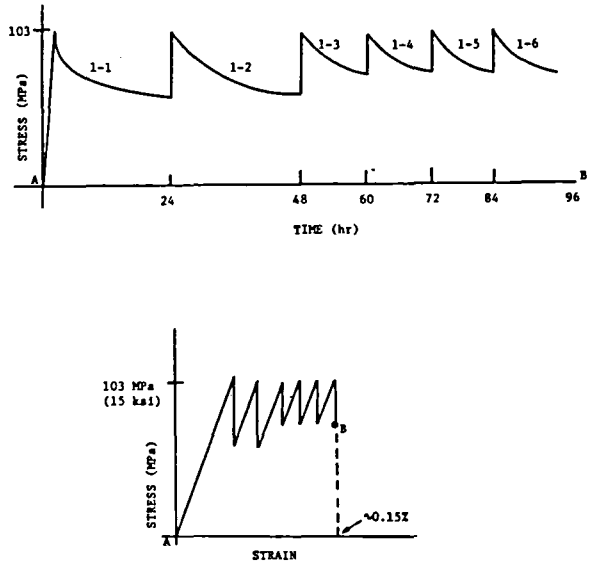

Fig. 3. Schematic of loading used in the cyclic relaxation test shown in Fig. 1 for 2-1/4 Cr–1 Mo steel specimen, 538°C (1000°F); six segments of relaxation following repeated monotonic loading to 103 MPa (15 ksi).

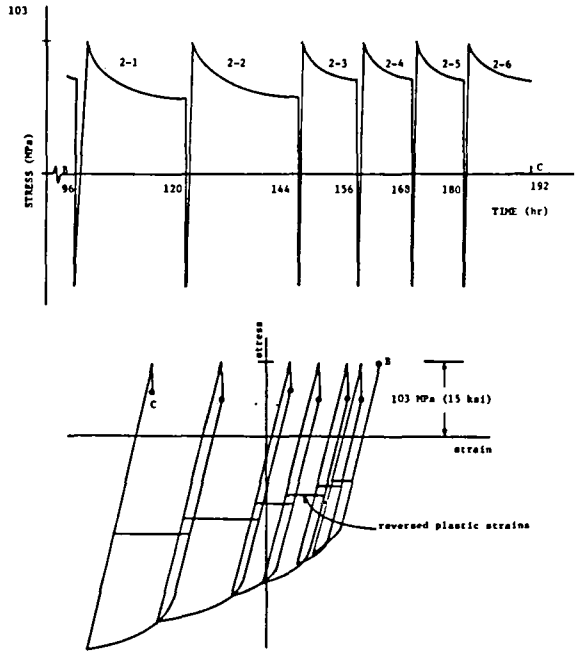

Fig. 4. Schematic of relaxation loading shown in Fig. 2 for 2-1/4 Cr–1 Mo steel specimen, 538°C (1000°F); six segments of relaxation following reversed plastic straining and reloading to 103 MPa (15 ksi).

MICROMECHANICALLY BASED CONSTITUTIVE RELATIONS FOR POLYCRYSTALLINE SOLIDS*

S. Nemat-Nasser and T. Iwakuma
Northwestern University
Evanston, Illinois 60201

ABSTRACT

A basic method is presented for the estimate of the overall mechanical response of solids which contain periodically distributed defects (inhomogeneities, regions undergoing inelastic flow, voids, cracks, etc.). This method is then applied to estimate the shape and growth pattern of voids that are periodically distributed over the grain boundaries in a viscous matrix. The interaction effects are fully accounted for, and the results are compared with calculations for a single void in an infinitely extended viscous solid, by Budiansky, Hutchinson, and Slutsky. Then, for a polycrystalline solid that undergoes relaxation by grain boundary sliding, the relaxed moduli are obtained, again fully accounting for the interaction effects. Finally, the overall inelastic nonlinear response at elevated temperatures is discussed in terms of a model which considers nonlinear power law creep within the grains, and linear viscous flow in the grain boundaries.

---

*This work was performed under NASA Grant NAG 3-134.

1. INTRODUCTION

The inelastic response of polycrystalline solids stems from a variety of microstructural changes, depending on the temperature regime, as well as the stress history. At temperatures sufficiently below 50% melting point, the rate effects are not dominant. The deformation consists of plastic slip on crystallographic planes, accompanied by the accommodating elastic lattice distortion. At higher temperature regimes the rate effects become significant, and the intracrystalline flow can be modelled adequately by a power law. At higher temperatures, creep effects are the major components in the overall response. In this case, adequate micromodelling involves a power law flow within the grains, accompanied by linearly viscous grain boundary sliding.

Various micromechanical defects that may arise in the course of deformation, contribute differently to the failure mechanisms during different temperature regimes. At low temperatures, voids are generated because of plastic flow at second phase particles, and this may lead to a reduction in ductility. At higher temperatures, on the other hand, voids are nucleated on grain boundaries, and grow in response to the applied load, as the solid creeps. Depending on the load level and the temperature regime, the mechanism of such void growth varies. For example, cavity growth is essentially crack-like, when surface diffusion is much slower than the grain boundary diffusion, whereas at a high stress level the cavity grows essentially by intragranular power law diffusion.

Under NASA-Lewis sponsorship, theoretical and experimental work has been initiated at Northwestern University on the micromechanical modelling of nonlinear constitutive relations of superalloys at various temperature regimes, addressing all the above-mentioned microscopic features. The present report summarizes some of the theoretical results on the growth of voids in viscous metals, the effects of grain boundary defects on the overall response of the polycrystal, and, finally, the over-

all creep response of the polycrystal. Elasto-plastic (rate-independent) modelling is discussed in a separate report; Iwakuma and Nemat-Nasser (1982).

The calculation of the overall response of the polycrystal is based on some fundamental results on the effect of periodically distributed defects (inhomogeneities, regions undergoing inelastic deformation, etc.) on the overall response of the solid; Nemat-Nasser et al. (1982). These results are first briefly discussed, and then applied to the estimation of the shape and growth pattern of voids that are periodically distributed over the grain boundaries in a viscous matrix. The interaction effects are fully accounted for, and the results are compared with calculations for a single void in an infinitely extended viscous solid, by Budiansky, Hutchinson, and Slutsky (1982). Then, for a polycrystalline solid that undergoes relaxation by grain boundary sliding, the relaxed moduli are obtained, again fully accounting for the interaction effects. Finally, the overall inelastic nonlinear response at elevated temperatures is discussed in terms of a model which considers nonlinear power law creep within the grains.

2. FORMULATION OF THE BASIC PROBLEM

Consider a solid containing periodically distributed sets of inhomogeneities such that it can be regarded as a collection of identical unit cells. Let D be a typical cell of volume V and exterior surface S. For simplicity assume that D is a parallelepiped of dimensions Λ_i, measured along the rectangular Cartesian coordinate axes x_i, i = 1,2,3. The results also apply to a single cell subjected on its boundary to suitable displacement or velocity fields.

Neither the matrix nor the inhomogeneities are required to be linearly elastic or rate-independent, but, for the intended applications, only small strains and rotations are considered.

To be specific, let $\underset{\sim}{\sigma}$ be the Cauchy stress and set

$$d\varepsilon_{ij} = D_{ijk\ell} d\sigma_{k\ell}, \tag{2.1}$$

where repeated indices are summed over 1, 2, 3, $d\underset{\sim}{\sigma}$ is the stress increment, and $\underset{\sim}{D} = \underset{\sim}{D}(\underset{\sim}{\sigma})$ is the instantaneous compliance which may or may not depend on stress. For rate-independent applications, $\underset{\sim}{\varepsilon}$ in (2.1) is the strain tensor. For rate-dependent cases, on the other hand, $\underset{\sim}{\varepsilon}$ is the <u>strain rate</u> tensor. For example, for non-linear creep, the strain rate is $\underset{\sim}{\varepsilon} = \underset{\sim}{F}(\underset{\sim}{\sigma})$. In this case we consider the incremental relation

$$d\underset{\sim}{\varepsilon} = \frac{\partial \underset{\sim}{F}}{\partial \sigma_{ij}} d\sigma_{ij}. \tag{2.2}$$

In particular, if power law creep is assumed, $\underset{\sim}{\varepsilon}' = \eta J^n \underset{\sim}{\sigma}'$, we obtain

$$d\varepsilon'_{ij} = \eta J^n \{\delta_{ik}\delta_{j\ell} + \frac{n\sigma'_{ij}\sigma'_{k\ell}}{2J^2}\} d\sigma'_{k\ell}, \tag{2.3}$$

where prime denotes the deviatoric part, and

$$J = (\tfrac{1}{2}\sigma'_{ij}\sigma'_{ij})^{\frac{1}{2}} \tag{2.4}$$

is the effective stress; in (2.3) n is a positive number and η is a dimensional parameter. If an inhomogeneity is linearly elastic or linearly viscous, then $\underset{\sim}{D}$ in (2.1) would be a constant tensor with suitable usual symmetries.

Let $\underset{\sim}{C}$ be the inverse of $\underset{\sim}{D}$ and rewrite (2.1) as

$$d\sigma_{ij} = C_{ijk\ell} d\varepsilon_{k\ell}. \tag{2.5}$$

Again, $\underset{\sim}{C}$ may be a function of $\underset{\sim}{\sigma}$.

Assume now that the displacement (velocity) field $\underset{\sim}{u}^0$ is prescribed on S in such a manner that the average strain (strain rate) field $\underset{\sim}{\varepsilon}^0$ is obtained. Let the corresponding average stress field be $\bar{\underset{\sim}{\sigma}}$. Consider an incremental change, $d\underset{\sim}{u}^0$, in $\underset{\sim}{u}^0$, which produces the increments $d\underset{\sim}{\varepsilon}^0$ and $d\bar{\underset{\sim}{\sigma}}$ in the average strain (strain rate) and stress fields, respectively. We seek to calculate the overall moduli $\underset{\sim}{C}^*$, defined by

$$d\bar{\sigma}_{ij} = C^*_{ijk\ell} d\varepsilon^0_{k\ell}, \tag{2.6}$$

where, in general, $\underset{\sim}{C}^*$ depends on the average stress $\bar{\underset{\sim}{\sigma}}$, as well as on the microstructure.

Within the unit cell, neither the stress increment nor the strain (strain rate) increment is uniform. Let there be M inhomogeneities, Ω_r, r = 1,2,...,M, and set

$$\begin{aligned} d\sigma^T_{ij} &= C_{ijk\ell}[d\varepsilon^0_{k\ell} + d\varepsilon_{k\ell}(\underset{\sim}{x})] \quad \text{in } D - \Omega_r \\ &= C^r_{ijk\ell}[d\varepsilon^0_{k\ell} + d\varepsilon_{k\ell}(\underset{\sim}{x})] \quad \text{in } \Omega_r, \quad r = 1,2,\ldots,M, \end{aligned} \tag{2.7}$$

where $d\underset{\sim}{\varepsilon}$ is the perturbation strain (strain rate) field due to inhomogeneities; $\underset{\sim}{C}$ is the modulus tensor of the matrix; and $\underset{\sim}{C}^r$ is that of the r^{th} inhomogeneity.

As has been shown by Eshelby (1957) for an ellipsoidal inhomogeneity in a linearly elastic, unbounded solid, the nonhomogeneous body may be replaced by a homogeneous one, provided that suitable transformation strains are prescribed in the ellipsoid. In this case, the transformation strain tensor is constant. For periodically distributed inhomogeneities, or when the inhomogeneity is not ellipsoidal, the transformation strain tensor is no longer constant. The basic concept, however, still applies, and can be quite effective, as shown by Nemat-Nasser and Taya (1981) and Nemat-Nasser et al. (1982).

Hence, in place of (2.7), one writes

$$d\sigma_{ij}^{T} = C_{ijk\ell}[d\varepsilon_{k\ell}^{0} + d\varepsilon_{k\ell} - d\varepsilon_{k\ell}^{*r}], \tag{2.8}$$

where $d\underset{\sim}{\varepsilon}^{*r}$ is zero in $D - \Omega_r$, and seeks to express this transformation strain (strain rate) increment in terms of $d\underset{\sim}{\varepsilon}^{0}$. This is done by the use of the Fourier series representation of the incremental fields, as has been discussed by Nemat-Nasser et al. (1982). The final results for the present case are as follows:

$$d\varepsilon_{k\ell}^{0} = A_{k\ell mn}^{r} d\varepsilon_{mn}^{*r}(\underset{\sim}{x}) - d\varepsilon_{k\ell}(\underset{\sim}{x}) \quad \text{in } \Omega_r, \tag{2.9}$$

$$A_{k\ell mn}^{r} = [C_{k\ell pq} - C_{k\ell pq}^{r}]^{-1} C_{pqmn}, \tag{2.10}$$

$$d\varepsilon_{jk}(\underset{\sim}{x}) = \frac{1}{V} \sum_{n_p=0}^{\pm\infty}{}' g_{jkmn}(\underset{\sim}{\xi}) \sum_{r=1}^{M} \int_{\Omega_r} d\varepsilon_{mn}^{*r}(\underset{\sim}{x}') e^{i\underset{\sim}{\xi}\cdot(\underset{\sim}{x}-\underset{\sim}{x}')} d\underset{\sim}{x}', \tag{2.11}$$

$$\xi_j = \frac{2\pi n_j}{\Lambda_j} \text{ (no sum on j)}, \quad i = \sqrt{-1}, \tag{2.12}$$

and where k,ℓ,m,n,j = 1,2,3. In (2.11), the fourth order tensor $g_{jkmn}(\underset{\sim}{\xi})$ depends on the matrix modulus tensor $\underset{\sim}{C}$. For an isotropic matrix,

$$C_{ijk\ell} = \mu(\delta_{ik}\delta_{j\ell} + \delta_{i\ell}\delta_{jk}) + \lambda\delta_{ij}\delta_{k\ell}, \tag{2.13}$$

we have

$$g_{ijk\ell}(\underset{\sim}{\xi}) = \bar{\xi}_j(\delta_{i\ell}\bar{\xi}_k + \delta_{ik}\bar{\xi}_\ell) + \bar{\xi}_i(\delta_{j\ell}\bar{\xi}_k + \delta_{jk}\bar{\xi}_\ell) - \frac{1}{1-\nu}\bar{\xi}_i\bar{\xi}_j\bar{\xi}_k\bar{\xi}_\ell + \frac{\nu}{1-\nu}\bar{\xi}_i\bar{\xi}_j\delta_{k\ell}, \tag{2.14}$$

$$\bar{\xi}_i = \xi_i/\xi, \qquad \xi = (\xi_k\xi_k)^{1/2}, \qquad \nu = \frac{\lambda}{2\lambda + 2\mu}.$$

In (2.13) and (2.14), λ, μ, and ν are material parameters for the matrix, which may depend on stress $\underset{\sim}{\sigma}$. For a linearly elastic matrix, these are the usual Lamé constants and Poisson's ratio, respectively. In the general formulation that will follow, we shall assume an anisotropic matrix. In Section 3, however, we assume an isotropic matrix, and hence use (2.14). In Section 4, on the other hand, a nonlinear creep law is considered, and this makes the tensor $\underset{\sim}{C}$ dependent on the current

stress state; then (2.14) cannot be used, and hence a more general expression is obtained.

Let f_r be the volume fraction of the r^{th} inhomogeneity,

$$f_r = V_r/V, \tag{2.15}$$

where V_r is the volume of Ω_r, and denote by $d\underset{\sim}{\bar{\varepsilon}}^{*r}$ the average value of $d\underset{\sim}{\varepsilon}^{*r}$ taken over Ω_r,

$$d\underset{\sim}{\bar{\varepsilon}}^{*r} = \frac{1}{V_r}\int_{\Omega_r} d\underset{\sim}{\varepsilon}^{*r}(\underset{\sim}{x})d\underset{\sim}{x}; \tag{2.16}$$

note that $d\underset{\sim}{\varepsilon}^{*r}$ is zero outside of Ω_r. Averaging (2.8) over D, and using (2.6) we obtain

$$(C_{ijk\ell} - C^*_{ijk\ell})d\varepsilon^0_{k\ell} = C_{ijk\ell}\sum_{r=1}^{M}\beta^r_{k\ell}, \tag{2.17}$$

where the notation

$$f_r\, d\bar{\varepsilon}^{*r}_{k\ell} \equiv \beta^r_{k\ell} \tag{2.18}$$

is used. We now substitute from (2.11) into (2.9), average the resulting equation over Ω_r to arrive at

$$f_r\, d\varepsilon^0_{jk} = A^r_{jkmn}\beta^r_{mn} - \sum_{n_p=0}^{\pm\infty}{}' g_{jkmn}(\underset{\sim}{\xi})f_r Q^r(\underset{\sim}{\xi})\sum_{s=1}^{M}\int_{\Omega_s} d\varepsilon^{*s}_{mn}(\underset{\sim}{x}')e^{-i\underset{\sim}{\xi}\cdot\underset{\sim}{x}'}\,d\underset{\sim}{x}', \tag{2.19}$$

where

$$Q^r(\underset{\sim}{\xi}) = \frac{1}{V_r}\int_{\Omega_r} e^{i\underset{\sim}{\xi}\cdot\underset{\sim}{x}}\,d\underset{\sim}{x}. \tag{2.20}$$

It has been shown by Nemat-Nasser and Taya (1981) that good accuracy is obtained if the transformation strain (strain rate) increment in the integrand in (2.19) is replaced by its average value. This then leads to

$$f_r\, d\varepsilon^0_{jk} = A^r_{jkmn}\beta^r_{mn} - \sum_{s=1}^{M} S^{rs}_{jkmn}\beta^s_{mn}, \tag{2.21}$$

where

$$S^{rs}_{jkmn} = \sum_{n_p=0}^{\pm\infty}{}' g_{jkmn}(\underset{\sim}{\xi}) f_r Q^r(\underset{\sim}{\xi}) Q^s(-\underset{\sim}{\xi}). \tag{2.22}$$

Equations (2.21) are now solved for β^r_{mn}, results substituted into (2.17), and since $d\underset{\sim}{\varepsilon}^0$ is arbitrary, the following general result is obtained:

$$C^*_{ijk\ell} = C_{ijk\ell} - C_{ijmn} \sum_{s=1}^{M} f_s \Big\{ \sum_{r=1}^{M} [A^r_{mnk\ell}\delta^{rs} - S^{rs}_{mnk\ell} f_r \Big\}^{-1}, \tag{2.23}$$

where δ^{rs} is the Kronecker delta.

In (2.23) the tensors $\underset{\sim}{C}$, $\underset{\sim}{A}^r$, and $\underset{\sim}{S}^{rs}$ may depend on the stress, $\underset{\sim}{\sigma}$, in the matrix as well as in each corresponding inhomogeneity. The estimate of the stress variation throughout the solid is indeed a formidable task. For our purposes, it seems adequate to use the overall average stress $\bar{\underset{\sim}{\sigma}}$ instead. Then the overall stress-strain (strain rate) relation can be obtained incrementally with the aid of (2.23) and (2.6). Some specific results are presented in subsequent sections. On the other hand, when necessary the local strain (strain rate) increment in, say, Ω_r can be obtained from (2.9),

$$d\varepsilon^0_{k\ell} + d\varepsilon_{k\ell}(\underset{\sim}{x}) = A^r_{k\ell mn}\, d\varepsilon^{*r}_{mn}(\underset{\sim}{x}), \tag{2.24}$$

and hence the local stress increment can be estimated from (2.7),

$$d\sigma^T_{ij}(\underset{\sim}{x}) = C^r_{ijk\ell}\, A^r_{k\ell mn}\, d\varepsilon^{*r}_{mn}(\underset{\sim}{x}) \quad \text{in } \Omega_r. \tag{2.25}$$

In a similar manner, the stress increment within the matrix can be obtained from (2.11) and (2.7).

3. GROWTH OF PERIODICALLY DISTRIBUTED VOIDS IN VISCOUS METALS

3.1 Background

At elevated temperatures, voids are nucleated at grain boundaries in polycrystalline solids. Depending on the deformation and temperature histories, the arrangement of these voids relative to the orientation of the principal applied stresses can vary considerably. For example, experiments show that voids can be concentrated on grain boundaries perpendicular to the direction of maximum tension, see, e.g., Garofalo (1965). For superalloys that are plastically deformed at room temperature, on the other hand, Dyson et al. (1976) have shown and Kikuchi and Weertman (1980) and Saegusa et al. (1980) have conclusively verified that after annealing, voids are generated at grain boundaries parallel to the direction of maximum tension. The mechanisms giving rise to the formation of these cavities are different, but their presence has similar adverse effects on the life expectancy of the structural components. An account of diffusive cavitation in polycrystalline solids is given by Chuang et al. (1979) and by Argon et al. (1981); see also Rice (1981). Here, however, a different approach is used, which considers the growth of periodically distributed cavities within a viscous metal. We make contact with the work by Budiansky et al. (1982) who examine the growth of a single cavity in an unbounded viscous medium, as well as with an earlier contribution by McClintock (1968) on the same subject.

3.2 Formulation

For a linearly viscous matrix, we have

$$\sigma_{ij} = C_{ijk\ell}\varepsilon_{k\ell}, \tag{3.1}$$

where

$$C_{ijk\ell} = 2\mu\left(I_{ijk\ell} + \frac{\nu}{1-2\nu}\,\delta_{ij}\delta_{k\ell}\right), \tag{3.2}$$

$$D_{ijk\ell} = C^{-1}_{ijk\ell} = \frac{1}{2\mu}\left(I_{ijk\ell} - \frac{\nu}{1+\nu}\,\delta_{ij}\delta_{k\ell}\right). \tag{3.3}$$

In (3.2), $I_{ijk\ell}$ is the fourth order identity tensor; in (3.1) $\underset{\sim}{\varepsilon}$ is the strain rate.

Consider a unit cell of dimensions Λ_i, and let it include an ellipsoidal void of (principal) semi-axes a_i, oriented along the coordinate axes x_i, $i = 1,2,3$. Define

$$\alpha = \frac{a_2}{a_1}, \quad \beta = \frac{a_3}{a_1}, \quad \gamma = \frac{\Lambda_2}{\Lambda_1}, \quad \zeta = \frac{\Lambda_3}{\Lambda_1}, \quad f = \frac{4\pi}{3}\frac{a_1a_2a_3}{\Lambda_1\Lambda_2\Lambda_3}. \tag{3.4}$$

Since (3.1) is linear, all the incremental relations in Section 2 can be replaced by the total ones, i.e. all the relations apply if $d\underset{\sim}{\varepsilon}^0$, $d\bar{\underset{\sim}{\sigma}}$,..., are replaced by $\underset{\sim}{\varepsilon}^0$, $\bar{\underset{\sim}{\sigma}}$,..., respectively.

From (2.8) it follows that[†]

$$\underset{\sim}{\varepsilon}^* = \underset{\sim}{\varepsilon}^0 + \underset{\sim}{\varepsilon} \tag{3.5}$$

within the void, and from (2.21) we obtain

$$\varepsilon^0_{ij} = [I_{ijk\ell} - S_{ijk\ell}]\bar{\varepsilon}^*_{k\ell}, \tag{3.6}$$

where, in view of (2.22) and (2.14),

$$\begin{aligned}
S_{1111} &= -\frac{1}{1-\nu}S_4 + \frac{2-\nu}{1-\nu}S_1, & S_{1133} &= -\frac{1}{1-\nu}S_8 + \frac{\nu}{1-\nu}S_1,\\
S_{2222} &= -\frac{1}{1-\nu}S_5 + \frac{2-\nu}{1-\nu}S_2, & S_{1122} &= -\frac{1}{1-\nu}S_9 + \frac{\nu}{1-\nu}S_1,\\
S_{3333} &= -\frac{1}{1-\nu}S_6 + \frac{2-\nu}{1-\nu}S_3, & S_{2211} &= -\frac{1}{1-\nu}S_9 + \frac{\nu}{1-\nu}S_2,\\
S_{2233} &= -\frac{1}{1-\nu}S_7 + \frac{\nu}{1-\nu}S_2, & S_{2323} &= \tfrac{1}{2}(S_2+S_3) - \frac{1}{1-\nu}S_7,\\
S_{3322} &= -\frac{1}{1-\nu}S_7 + \frac{\nu}{1-\nu}S_3, & S_{3131} &= \tfrac{1}{2}(S_3+S_1) - \frac{1}{1-\nu}S_8,\\
S_{3311} &= -\frac{1}{1-\nu}S_8 + \frac{\nu}{1-\nu}S_3, & S_{1212} &= \tfrac{1}{2}(S_1+S_2) - \frac{1}{1-\nu}S_9.
\end{aligned} \tag{3.7}$$

The infinite series $S_\ell = S_\ell(\alpha,\beta,\gamma,\zeta,f)$ in (3.7) is defined by

$$S_\ell = \sum_{n_p=0}^{\pm\infty}{}' P(\eta)h_\ell(\underset{\sim}{\xi}), \qquad \ell = 1,2,\ldots,9, \tag{3.8}$$

where

[†]Since $M = 1$, the superscript $r = 1$ is dropped.

$$h_1 = (\bar{\xi}_1)^2, \quad h_2 = (\bar{\xi}_2)^2, \quad h_3 = (\bar{\xi}_3)^2, \quad h_4 = (\bar{\xi}_1)^4, \quad h_5 = (\bar{\xi}_2)^4,$$
$$h_6 = (\bar{\xi}_3)^4, \quad h_7 = (\bar{\xi}_2\bar{\xi}_3)^2, \quad h_8 = (\bar{\xi}_3\bar{\xi}_1)^2, \quad h_9 = (\bar{\xi}_1\bar{\xi}_2)^2, \tag{3.9}$$

and, for an ellipsoidal inhomogeneity,

$$P(\eta) = f\,\frac{9(\sin\eta - \eta\cos\eta)^2}{\eta^6}, \qquad \eta \neq 0, \tag{3.10}$$

$$\eta = 2\pi R\left[n_1^2 + \left(\frac{\alpha n_2}{\gamma}\right)^2 + \left(\frac{\beta n_3}{\zeta}\right)^2\right]^{1/2}, \tag{3.11}$$

$$\xi = \frac{2\pi}{\Lambda_1}\left[n_1^2 + \left(\frac{n_2}{\gamma}\right)^2 + \left(\frac{n_3}{\zeta}\right)^2\right]^{1/2}.$$

In view of (3.5), the shape change can be defined by

$$\frac{\dot{a}_1}{a_1} = \bar{\varepsilon}^*_{11}, \quad \frac{\dot{a}_2}{a_2} = \bar{\varepsilon}^*_{22}, \quad \frac{\dot{a}_3}{a_3} = \bar{\varepsilon}^*_{33}, \quad \frac{\dot{V}_\Omega}{V_\Omega} = \bar{\varepsilon}^*_{kk}, \tag{3.12}$$

and we also note, from (3.4), that

$$\frac{\dot{\alpha}}{\alpha} = \bar{\varepsilon}^*_{22} - \bar{\varepsilon}^*_{11}, \qquad \frac{\dot{\beta}}{\beta} = \bar{\varepsilon}^*_{33} - \bar{\varepsilon}^*_{11},$$
$$\frac{\dot{\gamma}}{\gamma} = \varepsilon^0_{22} - \varepsilon^0_{11}, \qquad \frac{\dot{\zeta}}{\zeta} = \varepsilon^0_{33} - \varepsilon^0_{11}, \qquad \frac{\dot{f}}{f} = \bar{\varepsilon}^*_{kk} - \varepsilon^0_{kk}. \tag{3.13}$$

To obtain the current dimensions and other geometric variables, we integrate (3.12) and (3.13) with respect to time. This, for example, yields

$$\ell n\,\frac{a_1}{(a_1)_0} = \int_0^t \bar{\varepsilon}^*_{11}dt, \ \ldots, \quad \ell n\,\frac{\alpha}{\alpha_0} = \int_0^t (\bar{\varepsilon}^*_{22} - \bar{\varepsilon}^*_{11})dt, \ldots, \tag{3.14}$$

where the subscript 0 denotes the initial value.

Since the transformation strain rate tensor, $\bar{\underset{\sim}{\varepsilon}}^*$, characterizes the rate of change of the void geometry in accordance with (3.12) and (3.13), Eq. (3.6) relates the void change parameters to the overall strain rate tensor $\underset{\sim}{\varepsilon}^0$. To make contact with results of Budiansky et al. (1982), we relate the overall strain rates to the average stresses by

$$\bar{\sigma}_{ij} = C^*_{ijk\ell}\,\varepsilon^0_{k\ell}, \tag{3.15}$$

and note that, unlike the case of a single void in an infinitely extended solid considered by Budiansky et al. (1982), here $\underset{\sim}{C}^*$ does not equal the matrix modulus tensor $\underset{\sim}{C}$. The overall modulus in the present case is obtained by specializing (2.23) or, equivalently, by equating the overall rate of energy loss per unit volume with the average rate of loss. This results in[†]

$$C^*_{ijk\ell}\varepsilon^0_{ij}\varepsilon^0_{k\ell} = C_{ijk\ell}\varepsilon^0_{ij}\varepsilon^0_{k\ell} - f\, C_{ijk\ell}\varepsilon^0_{ij}\bar{\varepsilon}^*_{k\ell} \tag{3.16}$$

which, for $M = 1$ and because of (3.6), implies (2.23). Since $\underset{\sim}{\varepsilon}^0$ is arbitrary, (3.16) and (3.15) yield

$$\bar{\sigma}_{ij} = C_{ijk\ell}[\varepsilon^0_{k\ell} - f\,\bar{\varepsilon}^*_{k\ell}]. \tag{3.17}$$

In the present case $\underset{\sim}{C}$ is isotropic, Eq. (3.2), and if we introduce

$$S^0_{ij} = \bar{\sigma}_{ij}/2\mu \tag{3.18}$$

and eliminate $\underset{\sim}{\varepsilon}^0$ between (3.17) and (3.6), we obtain

$$\frac{1}{1+\nu}\begin{bmatrix} 1 & -\nu & -\nu \\ -\nu & 1 & -\nu \\ -\nu & -\nu & 1 \end{bmatrix}\begin{Bmatrix} S^0_{11} \\ S^0_{22} \\ S^0_{33} \end{Bmatrix} = \begin{bmatrix} 1-f-S_{1111} & -S_{1122} & -S_{1133} \\ -S_{2211} & 1-f-S_{2222} & -S_{2233} \\ -S_{3311} & -S_{3322} & 1-f-S_{3333} \end{bmatrix}\begin{Bmatrix} \bar{\varepsilon}^*_{11} \\ \bar{\varepsilon}^*_{22} \\ \bar{\varepsilon}^*_{33} \end{Bmatrix},$$

$$\begin{aligned} S^0_{12} &= (1 - f - 2S_{1212})\bar{\varepsilon}^*_{12}, \\ S^0_{23} &= (1 - f - 2S_{2323})\bar{\varepsilon}^*_{23}, \\ S^0_{31} &= (1 - f - 2S_{3131})\bar{\varepsilon}^*_{31}. \end{aligned} \tag{3.19}$$

From (3.19) it follows that

$$\begin{aligned} \frac{1-2\nu}{1+\nu}(S^0_{11} + S^0_{22} + S^0_{33}) = {} & \{1 - S_{1111} - S_{2211} - S_{3311} - f\}\bar{\varepsilon}^*_{11} \\ & + \{1 - S_{2222} - S_{1122} - S_{3322} - f\}\bar{\varepsilon}^*_{22} \\ & + \{1 - S_{3333} - S_{1133} - S_{2233} - f\}\bar{\varepsilon}^*_{33}. \end{aligned} \tag{3.20}$$

[†]The calculation is essentially the same as in Nemat-Nasser et al. (1982).

For the incompressible matrix, $\nu = 1/2$, and for (3.19) and (3.20) to yield non-trivial results, the matrix in the right-hand side of the matrix expression in (3.19) and the coefficients in the right-hand side of Eq. (3.20) should vanish.† With $\nu = 1/2$, this leads to

$$\begin{aligned} 1 - 3S_1 - S_2 - S_3 + 2(S_4 + S_8 + S_9) &= f, \\ 1 - S_1 - 3S_2 - S_3 + 2(S_5 + S_7 + S_9) &= f, \\ 1 - S_1 - S_2 - 3S_3 + 2(S_6 + S_7 + S_8) &= f, \end{aligned} \tag{3.21}$$

and, if only the infinite series S_1, S_2, and S_3 are retained, from (3.7) we deduce that

$$\begin{aligned} 1 - S_{1111} - S_{2211} - S_{3311} - f &= \frac{1-2\nu}{2(1-\nu)}\{1 - f - S_1 + S_2 + S_3\}, \\ 1 - S_{2222} - S_{1122} - S_{3322} - f &= \frac{1-2\nu}{2(1-\nu)}\{1 - f + S_1 - S_2 + S_3\}, \\ 1 - S_{3333} - S_{1133} - S_{2233} - f &= \frac{1-2\nu}{2(1-\nu)}\{1 - f + S_1 + S_2 - S_3\}. \end{aligned} \tag{3.22}$$

With these and with $\nu = 1/2$, (3.19) yields

$$\begin{Bmatrix} \bar{\varepsilon}^*_{11} \\ \bar{\varepsilon}^*_{22} \\ \bar{\varepsilon}^*_{33} \end{Bmatrix} = [T_{ij}] \begin{Bmatrix} \frac{2}{3} S^0_{11} - \frac{1}{3} S^0_{22} - \frac{1}{3} S^0_{33} \\ -\frac{1}{3} S^0_{11} + \frac{2}{3} S^0_{22} - \frac{1}{3} S^0_{33} \\ -\frac{1}{3} S^0_{11} - \frac{1}{3} S^0_{22} + \frac{2}{3} S^0_{33} \end{Bmatrix}, \tag{3.23}$$

where $[T_{ij}]$ is the inverse of the matrix

$$\begin{bmatrix} 1 - f - S_{1111} & -S_{1122} & -S_{1133} \\ -S_{2211} & 1 - f - S_{2222} & -S_{2233} \\ 1 - f - S_1 + S_2 + S_3 & 1 - f + S_1 - S_2 + S_3 & 1 - f + S_1 + S_2 - S_3 \end{bmatrix}. \tag{3.24}$$

Equations (3.23) relate the void growth parameters to the overall stress components. In terms of the stress ratios

---

†Numerical tests for spherical, cylindrical, and ellipsoidal geometries show that to within the accuracy of the estimate of the infinite series, these conditions are almost satisfied.

$$\phi = \frac{S^0_{22}}{S^0_{11}} = \frac{\bar{\sigma}_{22}}{\bar{\sigma}_{11}}, \qquad \psi = \frac{S^0_{33}}{S^0_{11}} = \frac{\bar{\sigma}_{33}}{\bar{\sigma}_{11}}, \tag{3.25}$$

one obtains

$$\begin{aligned}
\frac{3\bar{\varepsilon}^*_{11}}{S^0_{11}} &= (2T_{11} - T_{12} + 2T_{13}) + (-T_{11} + 2T_{12} + 2T_{13})\phi + (-T_{11} - T_{12} + 2T_{13})\psi, \\
\frac{3\bar{\varepsilon}^*_{22}}{S^0_{11}} &= (2T_{21} - T_{22} + 2T_{23}) + (-T_{21} + 2T_{22} + 2T_{23})\phi + (-T_{21} - T_{22} + 2T_{23})\psi, \\
\frac{3\bar{\varepsilon}^*_{33}}{S^0_{11}} &= (2T_{31} - T_{32} + 2T_{33}) + (-T_{31} + 2T_{32} + 2T_{33})\phi + (-T_{31} - T_{32} + 2T_{33})\psi.
\end{aligned} \tag{3.26}$$

Finally, the components of $\underset{\sim}{\varepsilon}^0$ are obtained from (3.6) and (3.26).

3.3 Numerical Results

Table 1 lists the initial and the loading conditions for eight different cases which are reported here for illustration. It should be noted that even in high strength metals which undergo very small overall deformations, the local deformations close to inhomogeneities or at the tip of cracks can be quite large. For this reason in Fig. 1, results for rather large strains are included. This figure shows the void volume change as a function of the overall deformation measure, L/L_0 or L_0/L, for the indicated cases associated with Table 1. For comparison, an asymptotic and additional results of Budiansky et al. (1982) are also shown. [These are read off the figures in the published paper. In the final version of the present report, these will be recalculated in order to obtain a more accurate estimate of the effect of periodicity as compared with a single void in an extended solid.] Figure 2 shows the void shape changes for the indicated cases.

4. EFFECT OF GRAIN BOUNDARY SLIDING ON NONLINEAR STEADY CREEP

At elevated temperatures, creep of polycrystals involves nonlinear flow within grains accompanied by grain boundary sliding which can be modelled by a linearly viscous relation; see Kê (1947), Zener (1948), and McLean (1957). The problem of estimating the overall creep properties of a polycrystal on the basis of different constitutive relations for the grain and the grain boundary has been examined by a number of researchers using various models; see, e.g., Zener (1948), Budiansky and O'Connell (1976), and Chen and Argon (1979). Recently, Ghahremani (1980a,b) has studied a two-dimensional model of creep using a numerical approach. Except for his work, other studies do not include the full effect of the essentially periodic structure of the grain boundary geometry, and hence the corresponding interaction effects.

In this section we shall examine the creep of polycrystals on the basis of nonlinear transgranular and linear intergranular creep laws, using a two-dimensional (plane) model.

Figure 3 shows a typical unit cell of dimensions Λ_1 and Λ_2. Within the matrix, the flow is governed by constitutive relations (2.3) which, in conjunction with a linear creep in bulk, $d\varepsilon_{kk} = \kappa\, d\sigma_{mm}$, κ = constant, yield

$$C_{ijk\ell} = \frac{1}{\eta J^n}\left[I_{ijk\ell} - \frac{n}{n+1}\frac{\sigma'_{ij}\sigma'_{k\ell}}{2J^2} - \frac{1}{2}\,\delta_{ij}\delta_{k\ell}\right] + \frac{1}{2\kappa}\,\delta_{ij}\delta_{k\ell}, \tag{4.1}$$

so that $d\sigma_{ij} = C_{ijk\ell}\, d\varepsilon_{kk}$ holds for the incremental stress, strain-rate relation within the grains. In view of (4.1), Eq. (2.14) must be replaced by

$$g_{ijmn} = \tfrac{1}{2}(N_{ik}\xi_j + N_{jk}\xi_i)C_{\ell kmn}\xi_\ell, \tag{4.2}$$

where, now, N_{jk} is

$$N_{jk} = \frac{1}{D}\left[\frac{1}{\eta J^n}\left\{\frac{1}{2}\xi^2\delta_{k} + \frac{n}{n+1}\frac{\xi_i\xi_\ell\sigma'_{im}\sigma'_{n\ell}}{2J^2}(I_{jkmn} - \delta_{jk}\delta_{mn})\right\}\right.$$

$$\left. + \frac{1}{2\kappa}(\xi^2\delta_{jk} - \xi_j\xi_k)\right], \qquad (4.3)$$

where

$$D = \frac{1}{2\eta^2 J^{2n}}\left[\frac{1}{2}\xi^4 - \frac{n}{n+1}\xi^2\frac{\xi_k\sigma'_{ki}\sigma'_{i\ell}\xi_\ell}{2J^2}\right]$$

$$+ \frac{1}{2\kappa\eta J^n}\left[\frac{1}{2}\xi^4 - \frac{n}{n+1}(\xi^2\delta_{ij} - \xi_i\xi_j)\frac{\xi_k\sigma'_{ri}\sigma'_j\ \xi_\ell}{2J^2}\right] .$$

To apply Eq. (2.23), we must calculate the quantity $Q^r(\underset{\sim}{\xi})$ for the typical r^{th} grain boundary segment. For a two-dimensional model, this is easily done and, if $\underset{\sim}{x}_0^r$ denotes the center of the segment, and θ^r its orientation relative to the x_1-axis, see Fig. 3, then we obtain

$$Q^r(\underset{\sim}{\xi}) = e^{i\underset{\sim}{\xi}\cdot\underset{\sim}{x}_0^r}\, h(\underset{\sim}{\xi},\theta^r),$$

$$h(\pm\underset{\sim}{\xi},\theta^r) = \frac{\sin z^r}{z^r}\,\frac{\sin y^r}{y^r}, \qquad (4.5)$$

$$z^r = \frac{\ell^r}{2}[\xi_1\cos\theta^r + \xi_2\sin\theta^r],$$

$$y^r = \frac{t^r}{2}[-\xi_1\sin\theta^r + \xi_2\cos\theta^r], \quad \text{no sum on r},$$

where ℓ^r is the length and t^r the thickness of the r^{th} grain boundary segment. Note that Eq. (2.21) now becomes

$$d\varepsilon^0_{ij} = A^r_{ijk\ell}\,d\bar{\varepsilon}^{*r}_{k\ell} - \sum_{s=1}^{M} f_s \sum_{n_p=0}^{\pm\infty}{}' g_{ijk\ell}(\underset{\sim}{\xi})h(\underset{\sim}{\xi},\theta^r)h(\underset{\sim}{\xi},\theta^s)\cos\{\underset{\sim}{\xi}\cdot(\underset{\sim}{x}_0^r - \underset{\sim}{x}_0^s)\}\,d\bar{\varepsilon}^{*s}_{k\ell}. \qquad (4.6)$$

Note also that when the thickness t^r is small relative to the length ℓ^r of a segment, then $\sin y^r/y^r = 1$ in $(4.5)_{2,4}$.

The unit cell shown in Fig. 3 includes a total of 9 grain boundary segments, so that M = 9 in Eq. (4.6) and in Eqs. (2.21). For each stress increment (or the strain rate increment), we first solve (2.21) to obtain $d\underset{\sim}{\bar{\varepsilon}}^{*r}$, r = 1,2,...,9. Then we calculate the stress increment and update the overall total stress. With this stress, we calculate the instantaneous moduli of the matrix from the nonlinear creep law (2.3). Equation (2.23) finally yields the overall instantaneous moduli.

Table 2 shows the geometrical data for the considered unit cell. It is easily seen that, in this case,

$$z^r = \pi R^r [n_1 \cos\theta^r + \sqrt{3}\, n_2 \sin\theta^r] ,$$
$$y^r = \pi \frac{t_0}{3} [- n_1 \sin\theta^r + \sqrt{3}\, n_2 \cos\theta^r] , \tag{4.7}$$

where $t_0 = 3t/\Lambda_1$; note that

$$f = \sum_{r=1}^{9} f_r = \frac{2t_0}{\sqrt{3}} \simeq t_0 . \tag{4.8}$$

For the numerical calculations, we have assumed

$$\frac{\underline{\kappa}}{\bar{\kappa}} = 1.001 \quad \text{so that} \quad \kappa \simeq \bar{\kappa} ,$$
$$\frac{\underline{\kappa}}{\bar{\eta}} = 0 \quad \text{so that} \quad \bar{\eta} \gg 1 , \tag{4.9}$$
$$n = 3 , \quad \text{and} \quad \rho = \frac{\bar{\sigma}_{22}}{\bar{\sigma}_{11}} = 0 \text{ (uniaxial tension).}$$

Detailed results are obtained for two cases: (1) $t_0 = 0.1$ which implies that $f \simeq 5.8\%$. We note that the model considers the linear viscous flow in a rather thick band about the grain boundary, and a nonlinear power law with n = 3 (in Eq. (2.3)) outside of this band. This model appears reasonable when we observe that instead of the local stress we have used the overall average stress in calculating the instantaneous moduli for the grains.

The results are presented in terms of the following nondimensional quantities:

$$S_{ij} = \left(\frac{\eta}{\kappa}\right)^{1/n} \sigma_{ij} , \qquad e_{ij} = \left(\frac{\eta}{\kappa^{1+n}}\right)^{1/n} \varepsilon_{ij} ,$$

$$dS_{ij} = \kappa\, C_{ijk\ell}\, de_{k\ell} , \qquad S_0 = \left(\frac{\eta}{\kappa}\right)^{1/n} \bar{\sigma}_{11} , \tag{4.10}$$

which together with

$$J = \frac{1-\rho}{2}\, S_0 \left(\frac{\kappa}{\eta}\right)^{1/n} \quad \text{and} \quad \nu \equiv (n+1)\left[\frac{(1+\rho)S_0}{2}\right]^n , \tag{4.11}$$

leads to

$$\kappa\, C_{2222} = \kappa\, C_{1111} = \frac{1}{2} + \frac{1}{2\nu} ,$$

$$\kappa\, C_{1122} = \kappa\, C_{2211} = \frac{1}{2} - \frac{1}{2\nu} , \tag{4.12}$$

$$\kappa\, C_{1212} = \kappa\, C_{2121} = \frac{n+1}{2\nu} .$$

In Fig. 4, results are plotted in terms of non-dimensional axial stress and strain measures, instead of the effective stress and strain. At stress levels near $S_0 = 1$, the lateral strain, ε_{22}, is positive (extension) and larger than ε_{11}, and κC_{1122} is negative for smaller S_0. This anomalous result stems from the assumed power law creep for the matrix. Another peculiar phenomenon at this stress level is that some of the overall moduli are negative; the shear modulus remains positive. Another anomalous behavior for power law constitutive relations has been observed by Budiansky et al. (1982), in connection with void growth. These authors report examples in which, under axial tension larger than the lateral ones, a void in a power law matrix is predicted to extend more rapidly laterally than in the axial direction.

The results in Fig. 4 are tentative, as we are now examining this problem in more detail.

REFERENCES

Argon, A. S., I.-W. Chen and C. W. Lau (1981), "Mechanics and Mechanisms of Intergranular Cavitation in Creeping Alloys." In Three-Dimensional Constitutive Relations and Ductile Fracture, edited by S. Nemat-Nasser, North-Holland Publishing Company, Amsterdam, pp. 23-49.

Budiansky, B., J. W. Hutchinson and S. Slutsky (1982), "Void Growth and Collapse in Viscous Solids." In Mechanics of Solids, The Rodney Hill 60th Anniversary Volume, edited by H. G. Hopkins and M. J. Sewell, Pergamon Press, Oxford, pp. 13-45.

Budiansky, B. and R. J. O'Connell (1976), "Elastic Moduli of a Cracked Solid," Int. J. Solids Structures, Vol. 12, pp. 81-97.

Chen, I.-W. and A. S. Argon (1979), "Grain Boundary and Interphase Boundary Sliding in Power Law Creep," Acta Met., Vol. 27, pp. 749-754.

Chuang, T.-J., K. I. Kagawa, J. R. Rice and L. B. Sills (1979), "Non-Equilibrium Models for Diffusive Cavitation of Grain Interfaces," Acta Met., Vol. 27, pp. 265-284.

Dyson, B. F., M. S. Loveday and M. J. Rodgers (1976), "Grain Boundary Cavitation under Various States of Applied Stress," Proc. Roy. Soc. London, Vol. A349, pp. 245-259.

Eshelby, J. D. (1957), "The Determination of the Elastic Field of an Ellipsoidal Inclusion, and Related Problems," Proc. Roy. Soc. London, Vol. A241, pp. 376-396.

Garofalo, F. (1965), Fundamentals of Creep and Creep-Rupture in Metals, Macmillan, New York.

Ghahremani, F. (1980a), "Effect of Grain Boundary Sliding on Anelasticity of Polycrystals," Int. J. Solids Structures, Vol. 16, pp. 825-845.

Ghahremani, F. (1980b), "Effect of Grain Boundary Sliding on Steady Creep of Polycrystals," Int. J. Solids Structures, Vol. 16, pp. 847-862.

Iwakuma, T. and S. Nemat-Nasser (1982), "Finite Elastic-Plastic Deformation of Polycrystalline Metals," in preparation.

Kê, T.-S. (1947), "Experimental Evidence of the Viscous Behavior of Grain Boundaries in Metals," Phys. Rev., Vol. 71, pp. 533-546.

Kikuchi, M. and J. R. Weertman (1980), "Mechanism for Nucleation of Grain Boundary Voids in a Nickel Base Superalloy," Scripta Met., Vol. 14, pp. 797-799.

McClintock, F. A. (1968), "A Criterion for Ductile Fracture by the Growth of Holes," J. Appl. Mech., Vol. 35, pp. 363-371.

McLean, D. (1957), Grain Boundaries in Metals, Oxford University Press, London.

Nemat-Nasser, S., T. Iwakuma and M. Hejazi (1982), "On Composites with Periodic Structure," Mechanics of Materials, Vol. 1, No. 3; to appear.

Nemat-Nasser, S. and M. Taya (1981), "On Effective Moduli of an Elastic Body Containing Periodically Distributed Voids," Q. Appl. Math., Vol. 39, pp. 43-59.

Rice, J. R. (1981), "Constraints on the Diffusive Cavitation of Isolated Grain Boundary Facets in Creeping Polycrystals," Acta Met., Vol. 29, pp. 675-681.

Saegusa, T., M. Uemura and J. R. Weertman (1980), "Grain Boundary Void Nucleation in Astroloy Produced by Room Temperature Deformation and Anneal," Met. Trans., Vol. 11A, pp. 1453-1458.

Zener, C. (1948), Fracturing of Metals, A.S.M., Metals Park, Cleveland.

Table 1: Initial and loading conditions for considered cases of void growth problems; $\alpha_0 = \beta_0 = 1.0$, and $f_0 = .005$.

Case	γ_0	ζ_0	S^0_{22}/S^0_{11}	S^0_{33}/S^0_{11}	$\dot{\varepsilon}^0_{11}$
I	10	2	0	0	.05
II	1	1	0	0	.05
III	10	2	.5	.5	.05
IV	1	1	.5	.5	.05
V	10	2	-.5	-.5	.05
VI	1	1	-.5	-.5	.05
VII	10	2	0	0	-.05
VIII	1	1	0	0	-.05

Table 2: Geometrical data for grain boundary configuration in a unit cell.

r	$\frac{x^r_{01}}{\Lambda_1}$	$\frac{x^r_{02}}{\Lambda_2}$	θ^r	R^r	f_r
1	$-\frac{7}{24}$	$\frac{3}{8}$	$\frac{\pi}{3}$	$\frac{1}{6}$	$\frac{t_0}{6\sqrt{3}}$
2	$-\frac{5}{12}$	$\frac{1}{4}$	0	$\frac{1}{6}$	$\frac{t_0}{6\sqrt{3}}$
3	$-\frac{1}{4}$	0	$-\frac{\pi}{3}$	$\frac{1}{3}$	$\frac{t_0}{3\sqrt{3}}$
4	$-\frac{5}{24}$	$-\frac{3}{8}$	$\frac{\pi}{3}$	$\frac{1}{6}$	$\frac{t_0}{6\sqrt{3}}$
5	0	$-\frac{1}{4}$	0	$\frac{1}{3}$	$\frac{t_0}{3\sqrt{3}}$
6	$\frac{5}{24}$	$-\frac{3}{8}$	$-\frac{\pi}{3}$	$\frac{1}{6}$	$\frac{t_0}{6\sqrt{3}}$
7	$\frac{1}{4}$	0	$\frac{\pi}{3}$	$\frac{1}{3}$	$\frac{t_0}{3\sqrt{3}}$
8	$\frac{5}{12}$	$\frac{1}{4}$	0	$\frac{1}{6}$	$\frac{t_0}{6\sqrt{3}}$
9	$\frac{7}{24}$	$\frac{3}{8}$	$-\frac{\pi}{3}$	$\frac{1}{6}$	$\frac{t_0}{6\sqrt{3}}$

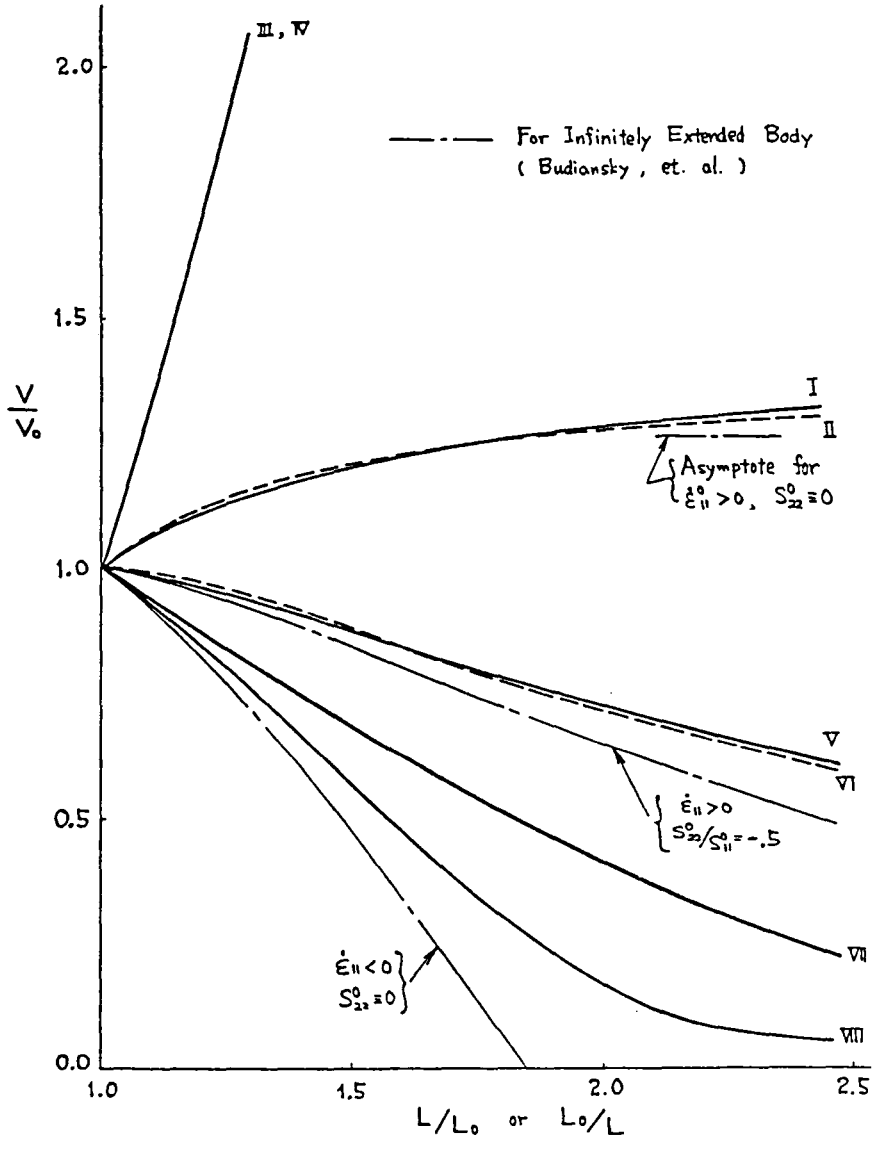
III, IV
For Infinitely Extended Body
(Budiansky , et. al.)
I
II
Asymptote for
$\dot{\varepsilon}^0_{11} > 0$, $S^0_{22} \equiv 0$
V
VI
$\dot{\varepsilon}_{11} > 0$
$S^0_{22}/S^0_{11} = -.5$
VII
VIII
$\dot{\varepsilon}_{11} < 0$
$S^0_{22} \equiv 0$
2.0
1.5
1.0
0.5
0.0
$\frac{V}{V_0}$
1.0
1.5
2.0
2.5
L/L_0 or L_0/L

FIG. 1

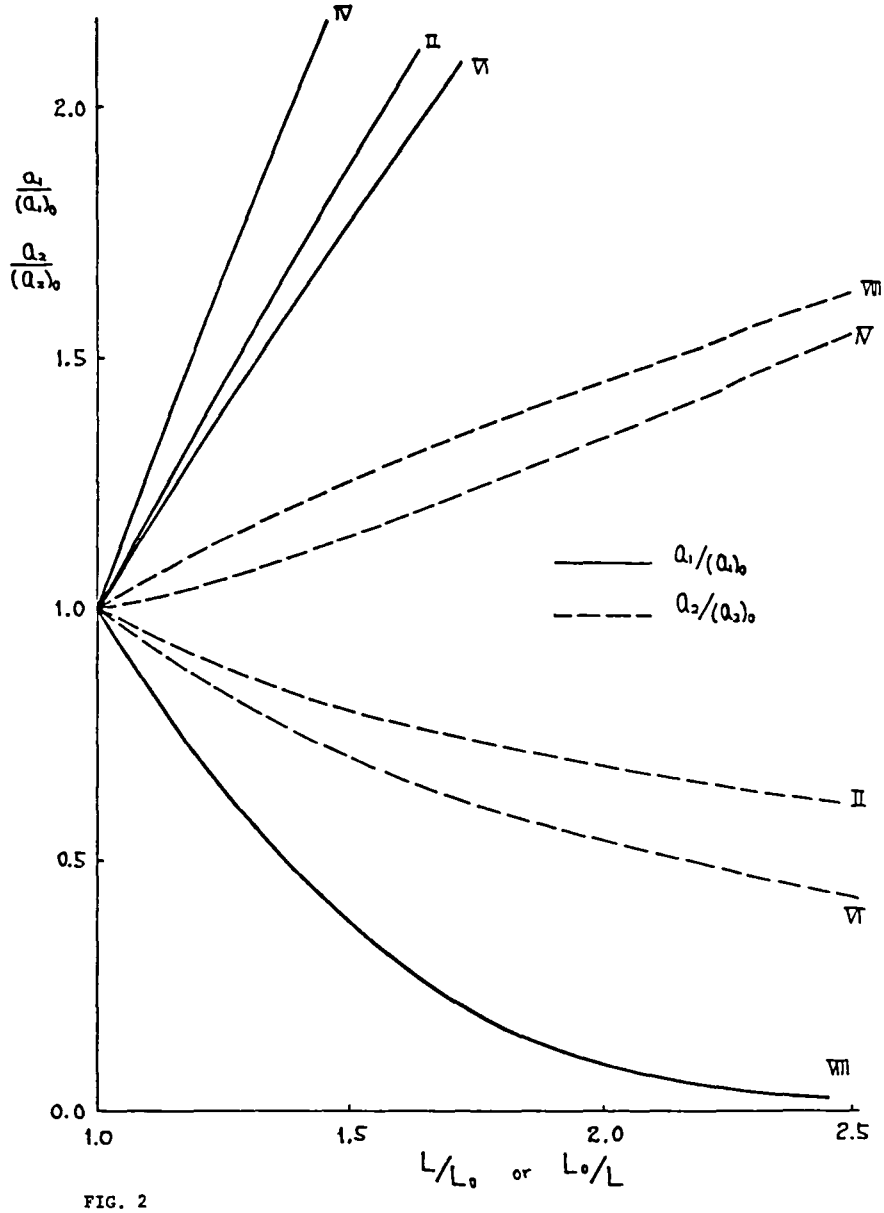
IV
II
VI
VII
V
2.0
1.5
1.0
0.5
0.0
$\frac{a_1}{(a_1)_0}$
$\frac{a_2}{(a_2)_0}$
$a_1/(a_1)_0$
$a_2/(a_2)_0$
1.0
1.5
2.0
2.5
L/L_0 or L_0/L

FIG. 2

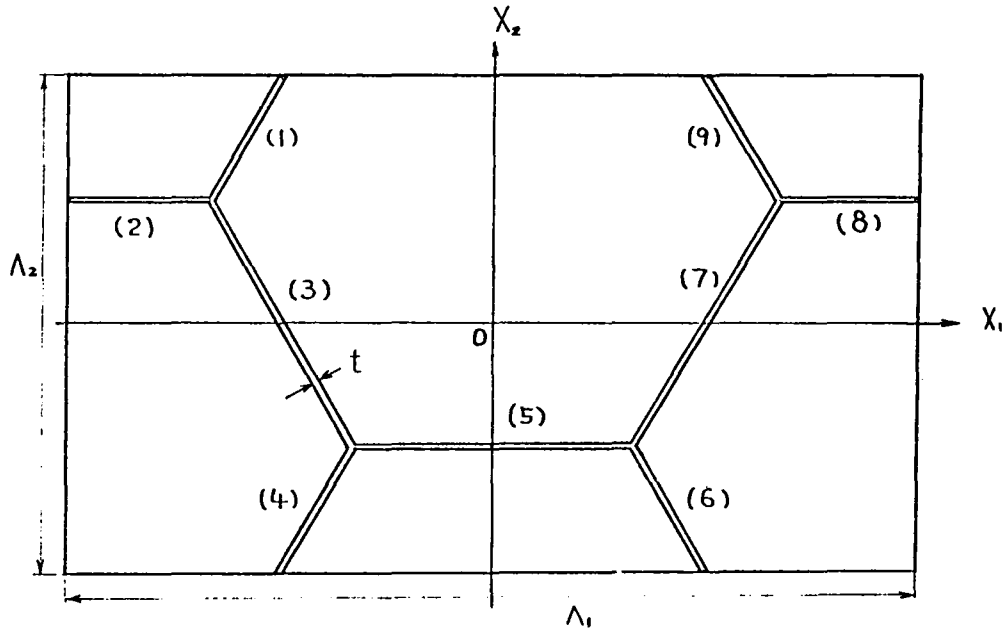

FIG. 3: A unit cell containing nine segments of grain boundary

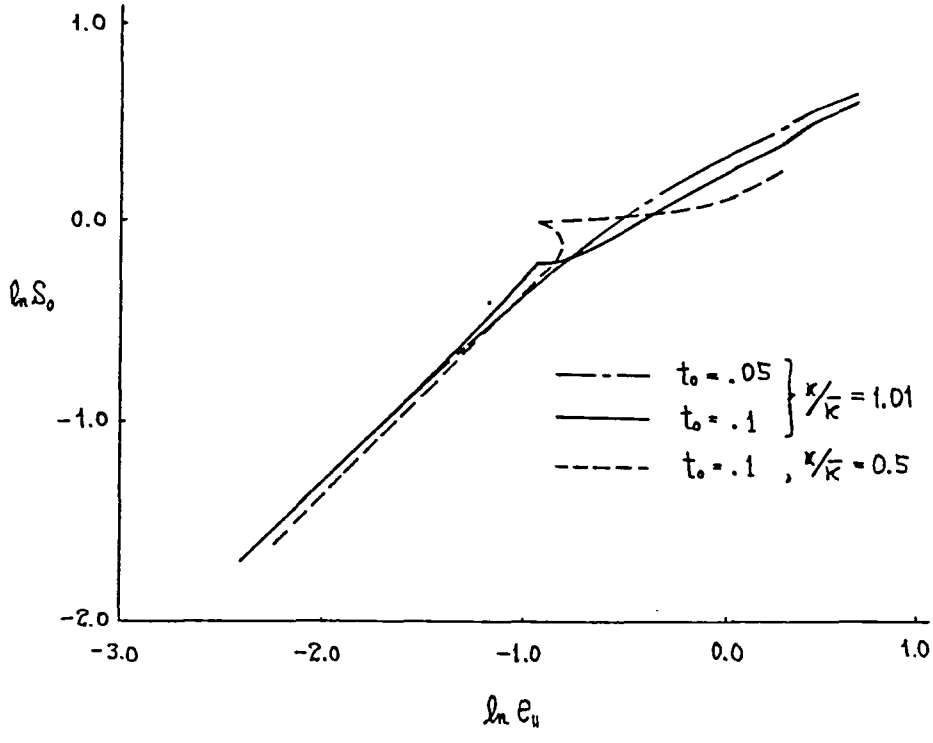

FIG. 4

A THEORY FOR THERMOVISCOPLASTICITY FOR MECHANICAL AND THERMAL LOADING

E. Krempl
Rensselaer Polytechnic Institute
Troy, New York 12181

and

E.P. Cernocky
University of Colorado
Boulder, Colorado 80302

Abstract

A coupled isotropic thermoviscoplasticity theory for small strain is proposed. The theory consists of a mechanical constitutive equation and a constitutive assumption for the heat equation. These equations are separately postulated but are coupled through their common linear dependence upon stress rate and the mechanical strain rate tensors and the time rate of temperature. The equations depend nonlinearity on the stress and strain tensors through the overstress tensor which is the difference between the stress tensor and the equilibrium stress tensor (obtained as the loading rate approaches zero) and on the absolute temperature. The concept of a yield surface is not used and the transition from linear thermoelastic behavior to nonlinear inelastic behavior is smooth. Extensions of the theory to cyclic loading are under development.

The theory is first applied to conditions of homogeneous deformation where the temperature changes in the material are induced by deformation alone. For adiabatic conditions numerical experiments (the integration of the coupled nonlinear differential equations for the conditions employed in materials testing using postulated material functions) show that the theory reproduces initial thermoelastic behavior (cooling (heating) in uniaxial tension (compression), isothermal behavior in torsion) followed by inelastic heating in any state of stress during monotonic loading. The amount of deformation induced temperature change is negligible unless the loading is very fast. During cyclic plastic loading the temperature increase can be considerable and it is shown that the predictions of the theory compare very well with experiments performed at room temperature on Type 304 Stainless Steel and on a 3.5 Ni-Mo-V steel.

When large temperature changes are imposed the deformation induced temperature changes can be neglected. The numerical experiments involve in this case the uniformly changing temperature and the mechanical loading as inputs (no heat conduction is allowed). Although other possibilities exist only the elastic modulus is assumed to be a function of temperature. The response of the model is shown for heating and thermal cycling under mechanical constraint (thermal fatigue) and for combined thermal and mechanical cycling of a uniaxial bar. It is shown that the response depends on the rate of temperature application and on the temperature at which clamping occurs.

References

1) E. P. Cernocky and E. Krempl, *Int. J. Solids and Structures, 16,* 723-741 (1980).

2) E. P. Cernocky and E. Krempl, *J. of Thermal Stresses, 4,* 69-82 (1981).

3) E. P. Cernocky and E. Krempl, *J. de Mécanique Appliquée, 5,* 293-321 (1981).

4) S. L. Adams and E. Krempl, "Thermomechanical Response of 3.5 Ni-Mo-V Steel and Type 304 Stainless Steel under Cyclic Uniaxial Inelastic Deformation," RPI Report MML-82-5, April 1982.

ON THE APPLICATION OF DEFORMATION KINETICS TO NONLINEAR CONSTITUTIVE RELATIONS AT HIGHER TEMPERATURES

K. C. Valanis and C. F. Lee
University of Cincinnati
Cincinnati, Ohio 45221

ABSTRACT

A single phenomenological constitutive equation is derived theoretically from first principles and applied to aluminum, tin and lead. The theory is based on deformation kinetics of steady creep in which the fundamental mechanism is atomic transport over potential barriers whose conformation is distorted by the application of a stress field.

The form of the functional dependence of barrier distortion and stress over the entire temperature range is found to be a sigmoidal curve which tends to straight lines of a unit slope in the small and high stress regions. With this form of barrier distortion, the constitutive equation can predict very well the steady creep behavior of aluminum, tin and lead over a wide range of temperature and stress.

1. Introduction

Experimental results on high temperature creep of pure metals and solid solution alloys during past decades, [1,2,3] fall into two main categories: those establishing a relationship between steady-state creep rate and stress under constant temperature on one hand and a relationship between constant creep rate and temperature under constant stress, on the other. The functional dependence of the constant creep rate $\dot{\varepsilon}_s$ on the stress σ under constant absolute temperature T may be divided basically into three regions whose boundaries depend on the material itself. In the low stress region, $\dot{\varepsilon}_s$ is almost linearly proportional to σ. Hence it is called a newtonian-like viscous flow region. In the intermediate stress region, $\dot{\varepsilon}_s$ appears to be proportional to σ^n, where n is a temperature dependent material parameter. The value of n lies predominatly between 4 and 7 for pure metals and between 3 and 5 for solid solution alloys. In the high stress region, $\dot{\varepsilon}_s$ is proportional to the exponential function of $\beta\sigma$, here β is a temperature dependent material parameter. The functional

dependence of $\dot{\varepsilon}_s$ on T under constant σ is assumed to be governed by a type of Arrhenius relation. As a result the activation energy of creep can be found by a temperature cycling technique or the slope of the line in the Arrhenius plot of $\log_{10} \dot{\varepsilon}_s$ vs T^{-1}. The values of activation energy thus found are very close to those of self diffusion in pure metals or the diffusion of one of the predominant elements in solid solution alloys. However, the slope of the Arrhenius plot is, in general, a function of stress and temperature. In addition the activation energy calculated from temperature cycling technique is, in general, a function of stress and strain.

Various theories of creep have been proposed in recent times. These fall basically into two broad categories: phenomenological and micromechanical, the final aim being, of course, a macroscopic constitutive equation. The first category includes theories that are strictly empirical [2-4], others that are mathematical [5], and others still which are "quasi" physical such as the internal state variable theories, a typical example being reference 6. In the second category fall theories in which the underlying micromechanisms are vacancy diffusion, dislocation climb and microcreep [7]. In the latter category belong also the absolute reaction rate theory by Eyring [8] and the very recent deformation kinetics theory of creep by the authors [9].

Micromechanical theories, where vacancies or dislocation are the building blocks, need more than one mechanism to describe the experimental phenomena over a wide range of temperature and stress. While for practical purposes this is not a disadvantage, one wonders if a single appropriate atomic mechanism cannot be found which describes steady creep phenomena over the entire range of stress and temperature.

In reference 9, we found reason to believe that this might be possible. One single constitutive equation was shown to predict very well the steady creep behavior

of AISI 316 stainless steel, pure polycrystalline aluminum and copper over a wide range of temperature and stress, above about $100^{kg/cm^2}$. The vehicle for this specific constitutive equation is deformation kinetics. The fundamental mechanism is the transport (diffusion) of atoms over potential barriers whose conformation is distorted by the application of a stress field.

In the case of one-dimensional flow, of interest here, the central element of the theory is the relation between the barrier distortion ω and the free energy gradient $-\frac{\partial \Psi}{\partial q}$ where q (an internal variable) is the statistical average of the displacement of atoms in motion facing a specific barrier. In the application of the theory [9] to uniaxial stress fields where the stress was above circa $100^{kg/cm^2}$ a linear relation between ω and $-\frac{\partial \Psi}{\partial q}$ sufficed but proved inappropriate for lower stress levels. Evidently the task at hand is to find an appropriate relation that applies to all stress levels but the form of the relation does not negate the fact that we are dealing with a single mechanism of atomic diffusion over energy barriers. This is done in Section 3.

2. Brief Review of the Theory

Particle Equations

Let N be the number of particles whose motion is impeded by a barrier of height ε_o and ω the distortion of the barrier due to the application of the stress field. See reference 9 for details. Then the number of particles N′ partaking in the net motion is given by equation (2.1)

$$N' = 2N\exp(-\varepsilon_o/kT)\sinh(\omega/kT) \tag{2.1}$$

where k is the Boltzmann constant and T the absolute temperature. Assuming a "square sinusoidal" barrier shape the average time $\bar{\tau}$ taken by the atoms to climb the barrier is given by equation (2.2)

$$\bar{\tau} = \frac{\sqrt{2}\, a}{\pi\sqrt{\varepsilon_o}}\, F\left(\frac{\pi}{2},\ \sin^{-1} k_o\right) \tag{2.2}$$

where a is the barrier width, F is the complete elliptic integral and

$$k_o = \left(\frac{\varepsilon_o - \omega}{\varepsilon_o}\right)^{\frac{1}{2}} \tag{2.3}$$

Rate (Evolution) Equation for q

The average velocity $\dot{q}$ of the atoms crossing the barrier is given by equation (2.4)

$$\dot{q} = \frac{qN'}{\bar{\tau}N} \tag{2.4}$$

Use of equations (2.1), (2.2) and (2.4) gives the desired relation between the average velocity and the barrier distortion:

$$\dot{q} = \frac{\pi\sqrt{2\varepsilon_o}}{F} \exp\ (-\varepsilon_o/kT)\ \sinh\ (\omega/kT) \tag{2.5}$$

A convenient representation for F is the following

$$F = \frac{1}{2}\ \log\ (16\varepsilon_o/\omega) \tag{2.6}$$

For $o \leqslant \omega/\varepsilon_o \leqslant 0.35$ the maximum error is less than 5% [9]. If there exists n barriers to the motion, each of height ε_o^r with distortion ω_r, then equation (2.5) applies to each such barrier.

However in steady creep only the highest barriers come into play, the lowest ones having already been climbed by the atoms in the course of the deformation. Thus one internal variable suffices (approximately) to represent the effect of these barriers, if, indeed more than one is actual active. Otherwise the representation is exact.

Free Energy Representation

In general

$$\psi = \psi(\varepsilon, q, T) \tag{2.7}$$

where in the present work T is constant. The free energy is the potential energy stored by virtue of atoms being displaced within potential wells. The mean displacement generated as a result is directly related to the elastic strain. For instance in the case of a unidirectional equispaced atoms the elastic strain is exactly equal to the atomic displacement divided by the lattice spacing. Assuming parabolic wells, the potential energy is proportional to a quadratic function of the displacement, leading to the conclusion that the free energy is a quadratic function of the elastic strain [9].

To relate the above discussion to equation (2.7) we write ψ in the quadratic form

$$\psi = \tfrac{1}{2} A_{11} \varepsilon^2 + A_{12} \varepsilon q + \tfrac{1}{2} A_{22} q^2 \tag{2.8}$$

and insist that it is a perfect square, so that the squared linear term can then be identified with the elastic strain. This is possible if $A_{12}^2 = A_{11} A_{22}$. The principle of thermodynamic stability requires that ψ be positive definite. This implies $A_{11} > 0$, $A_{22} > 0$, $A_{12}^2 - A_{22}A_{11} < 0$. However, the last inequality can be relaxed and set into equality for the purpose of steady state creep in which the metal exhibits a fluid equilibrium configuration [9]. As a result, equation (2.8) becomes

$$\psi = \tfrac{1}{2} A(\varepsilon - Bq)^2 \tag{2.9}$$

where $A = A_{11}$ and $B = -A_{12}/A$. Thus since equation (2.9) is the mathematization of the statement at the end of the last paragraph $\varepsilon - Bq$ must be identified as an elastic strain. Note that A and B may be and are, in general, functions of temperature.

To obtain the desired analytical expression for creep we appeal to a

fundamental relation of irreversible thermodynamics according to which the stress is the gradient of free energy with respect to the strain i.e., $\sigma = \partial\psi/\partial\varepsilon$. Thus $\sigma = A(\varepsilon - Bq)$. Furthermore, as a result of equation (2.9), $\partial\psi/\partial q = -B\sigma$. Since during creep the stress is constant, it follows that $\dot{\varepsilon} = B\,\dot{q}$. The strain rate can then be obtained from equations (2.5) and (2.6), i.e.,

$$\dot{\varepsilon} = 2\sqrt{2\varepsilon_o}\,\pi B e^{-\varepsilon_o/kT}\,\frac{\sinh(\omega/kT)}{\log(16\varepsilon_o/\omega)} \tag{2.10}$$

where ω is now a function of σ and T.

In the next section we will use equation (2.10) to predict the steady creep of aluminum, tin and lead, particularly under very high temperature and low stress. However before this can be done the relation between the internal force $-\partial\psi/\partial q$ and ω must be established. As noted above $-\partial\psi/\partial q = B\sigma$. The problem is therefore reduced to finding the relation between σ and ω, in this particular case.

3. Application of the Theory to Aluminum

Let the relation $\sigma(\omega)$ between σ and ω or conversely, $\omega(\sigma)$ be known. Specifically let

$$\sigma = \Sigma(\omega);\ \omega = \Omega\ (\sigma) \tag{3.1a,b}$$

Substitution of equation (3.1b) in equation (2.10) gives a constitutive relation

$$\dot{\varepsilon} = e^{-\varepsilon_o/kT}\,\mathcal{F}(\sigma,T) \tag{3.2}$$

In an inverse fashion, given the experimental relation between σ and $\dot{\varepsilon}$ at constant T, one may then use equation (2.10) to deduce the relation between σ and ω, i.e., the function $\Sigma(\omega)$.

The function of $\Sigma(\omega)$ in the case of aluminum can be found from figures 1 and 2. It may be seen that for higher values of stress the relation of σ and $\log_{10}\dot{\varepsilon}_s$ is

linear. Thus, in this range, the linear relation implies that

$$\omega = kTK_2\,\sigma\left(1 - \frac{\sigma_o'}{|\sigma|}\right) \tag{3.3}$$

where σ_o' is a threshold stress below which equation (3.3) is not applicable, and K_2 is the slope of the straight portion of the curve. Equation (3.3) was the basis of the study in reference 9, where it was shown that the linear relation persists over a wide range of temperature with the proviso that K_2 and σ_o' are temperature dependent. In this case $\mathcal{F}(\sigma,T)$ has the form

$$\mathcal{F}(\sigma,T) = \frac{K_1^o \sinh K_2(\sigma - \sigma_o')}{\log\left[\frac{16\varepsilon_o}{kT} / K_2(\sigma - \sigma_o')\right]} \tag{3.4}$$

where $K_1^o = 2\sqrt{2\varepsilon_o}\,\pi B$. The determination of the constants K_1^o, K_2 and σ_o' was discussed at length in reference 9. Note that equation (3.3) implies that the distortion is linearly related to the internal force, i.e.,

$$\omega = kTC\,(Q - Q^o) \tag{3.5}$$

where Q is defined as $-\partial\psi/\partial q$ and thus equal to $B\sigma$, $Q^o = B\sigma_o'$ and C $(=K_2/B)$ is the coefficient of proportionality.

As shown in figures 1 and 2, equations (3.2) and (3.4) predict quite well the experimental data in references 10 and 11, except the temperature at 920°k. The corresponding values of K_1^o, K_2, C and σ_o' are shown in figures 3 and 4; ε_o = 34 KCal/mole which is the value of activation energy of self diffusion. It is seen that serious deviations begin to arise below a stress level of about σ_o'. Of course this is to be expected in view of equation (3.3). Below σ_o', equation (3.3) no longer holds.

To determine $\Omega(\sigma)$ is this region we recall equation (2.10), which because of

the smallness of ω/kT we can write in the approximate form

$$\dot{\varepsilon}_s = K_1^\circ \, e^{-\varepsilon_o/kT} \, \frac{\omega/kT}{\log(16\varepsilon_o/\omega)} \tag{3.6}$$

and note that insofar as this region is concerned the experimental data at 920°k indicate a linear relation between $\log_{10} \dot{\varepsilon}_s$ and $\log_{10} (\sigma - \sigma_o'')$, when the net stress $\sigma - \sigma_o'')$, is very small [11,12]. As indicated in reference 11, σ_o'' = 3psi , below which creep was not measurable. Since log log $(16\varepsilon_o/\omega)$ is an insensitive function of ω in this small net stress region, the above observation suggests the following relation between ω and σ:

$$\log_{10} \beta\omega = \log_{10} A_o + \log_{10} (\sigma - \sigma_o'') \tag{3.7}$$

where A_o and σ_o'' are at most functions of temperature; $\beta = 1/kT$. These parameters were determined respectively from the intercept and the constraint of a unit slope of the curve. In the present case A_o is a constant $(4.6\text{x}10^{-5})$ and σ_o'' is a decreasing function of temperature (see figure 4). Indications are that as the temperature approaches the melting point (T_m), σ_o'' goes to zero at which point the metal exhibits a truly newtonian behavior.

The form of the functional dependence of ω on σ over the entire temperature range is shown in figure 5. The relationship is sigmoidal tending to a linear form in the small and high stress regions (see equations (3.7) and (3.3)). The theoretical predictions based on figure 5 are shown in figure 2.

4. Application of the Theory to Tin and Lead

The procedure of Section 3 is repeated here without change. It has been shown by a three-dimensional argument [13] that the constitutive equation (2.10) applies to pure shear without change in form. A comparison between theory and experiment is shown in figures 6 and 7. A further treatment will be the subject of a more

extensive article to appear at a later date.

5. Conclusions

In this paper we apply the theory of deformation kinetics to aluminum, tin and lead and show that equation (2.10) suffices to predict accurately steady creep behavior over a wide range of stress and temperature. We may conclude that one micromechanism, that of atomic transport over potential barriers whose conformation is distorted by the application of a stress field, is sufficient to account for the steady creep process in the entire range of temperature and stress.

References

1. Dorn, J.E., "Some Fundamental Experiments on High Temperature Creep," J. Mech. Phy. of Solids, 3, 1954, 85-116.

2. Garofalo, F., "Fundamentals of Creep and Creep-Rupture in Metals," MacMillan Co. New York, 1965.

3. Sherby, O.D. and Burke, P.M., "Mechanical Behavior of Crystalline Solids at Elevated Temperature," Progress in Material Science, ed. B. Chalmers and Hume-Rothery, Vol. 13, 1968, 325-390.

4. Nadai, A. and McVetty, P.G., "Hyperbolic Sine Chart for Estimating Working Stresses of Alloys at Elevated Temperature," Proc. ASTM, 43, 1943, 735-748.

5. Findley, W.N., Lai, J.S. and Onaran, K., "Creep and Relaxation of Nonlinear Viscoelastic Materials," North-Holland, New York, 1976.

6. Hart, E.W., "Constitutive Relations for the Nonelastic Deformation of Metals," Trans. ASME J. Engng Mat. Tech., 3, 1976, 193-202.

7. Ashby, M.F., "A First Report on Deformation-Mechanism Maps," Acta Metallurgica, 20, 1972, 887-897.

8. Krausz, A.S. and Eyring, H., "Deformation Kinetics," Wiley, New York, 1975.

9. Valanis, K.C. and Lee, C.F., "Deformation Kinetics of Steady-State Creep in Metals," Intl. J. Solids and Structures, 17, 1981, 589-604.

10. Servi, I.S. and Grant, N.J., "Creep and Stress Rupture Behavior of Aluminum as a Function of Purity," Trans. AIME. 191, 1951, 909-922.

11. Harper, J.G., Shepard, L.A. and Dorn, J.E., "Creep of Aluminum under Extremely Small Stresses," Acta Met. 6, 1958, 509-518.

12. Mohamed, F.A., Murry, K.L. and Morris, J.W. Jr., "Harper-Dorn Creep in Al, Pb, and Sn," Met. Trans. 4, 1973, 935-940.

13. Valanis, K.C., "Deformation Kinetics in Three Dimensions," submitted to the Int. J. of Solid and Structures.

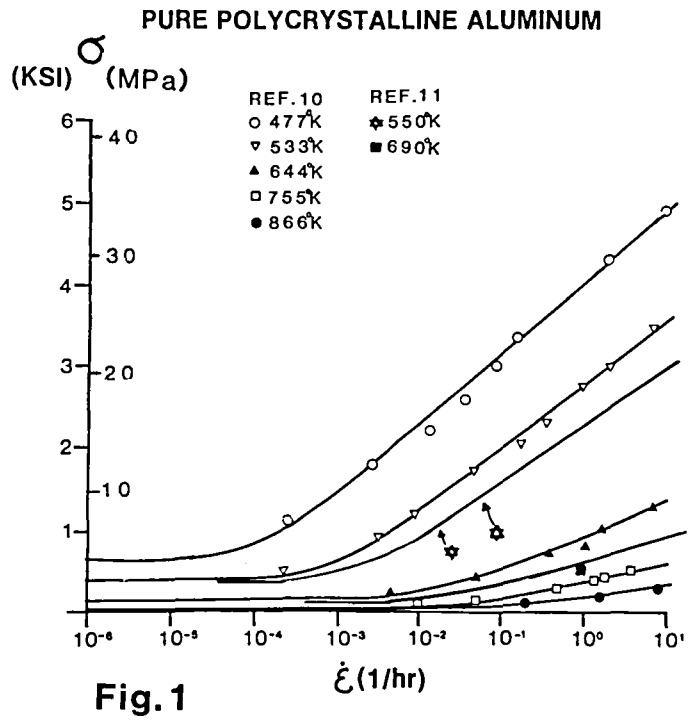
PURE POLYCRYSTALLINE ALUMINUM
σ
(KSI)
(MPa)
REF.10
REF.11
477°K
533°K
644°K
755°K
866°K
550°K
690°K
6
5
4
3
2
1
40
30
20
10
10⁻⁶
10⁻⁵
10⁻⁴
10⁻³
10⁻²
10⁻¹
10⁰
10¹
ε̇(1/hr)

Fig. 1

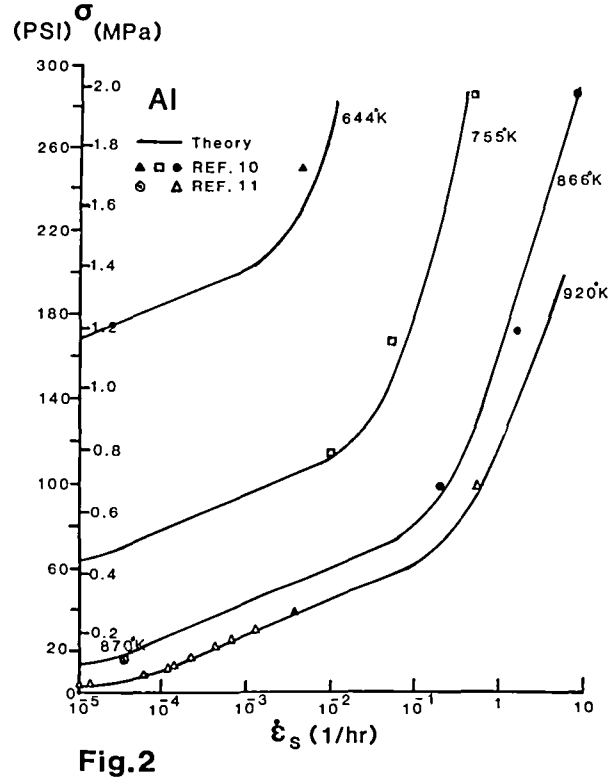
σ
(PSI)
(MPa)
Al
Theory
REF. 10
REF. 11
644°K
755°K
866°K
920°K
870°K
300
260
220
180
140
100
60
20
0
2.0
1.8
1.6
1.4
1.2
1.0
0.8
0.6
0.4
0.2
10⁻⁵
10⁻⁴
10⁻³
10⁻²
10⁻¹
1
10
ε̇s (1/hr)

Fig.2

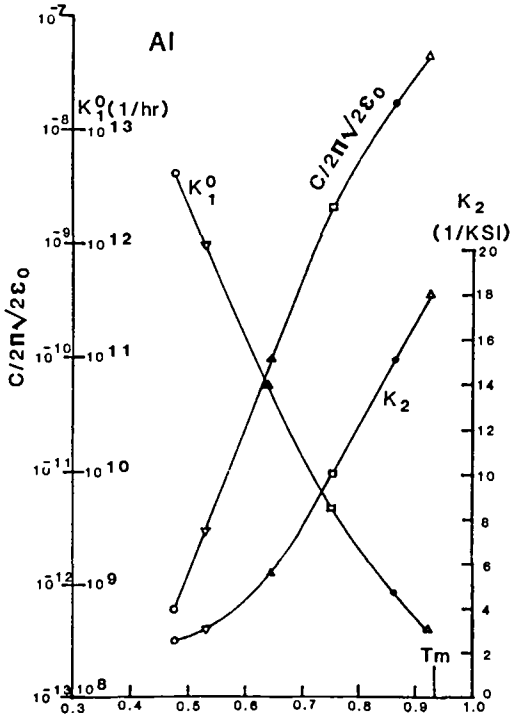

Fig.3

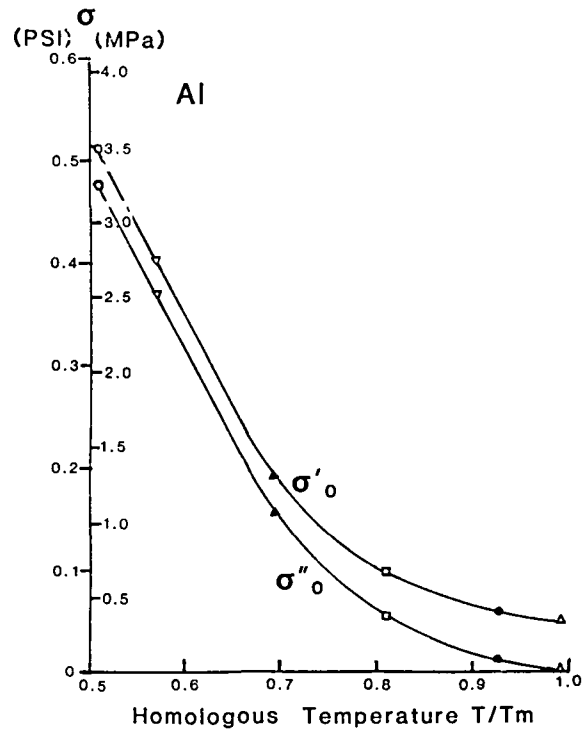

Fig.4

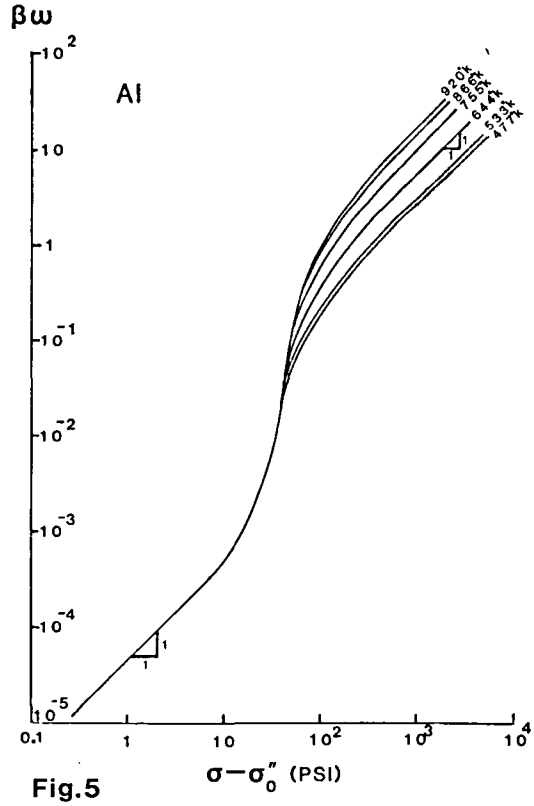

Fig.5

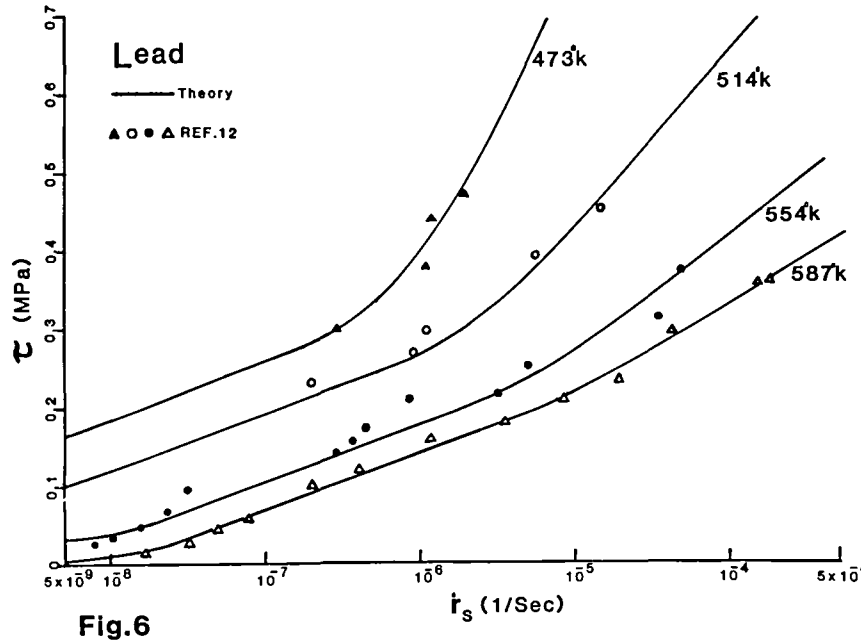
Lead
Theory
▲ ○ ● △ REF.12
473k
514k
554k
587k
τ (MPa)
0
0,1
0,2
0,3
0,4
0,5
0,6
0,7
5x10⁻⁹
10⁻⁸
10⁻⁷
10⁻⁶
10⁻⁵
10⁻⁴
5x10⁻⁴
ṙs (1/Sec)

Fig.6

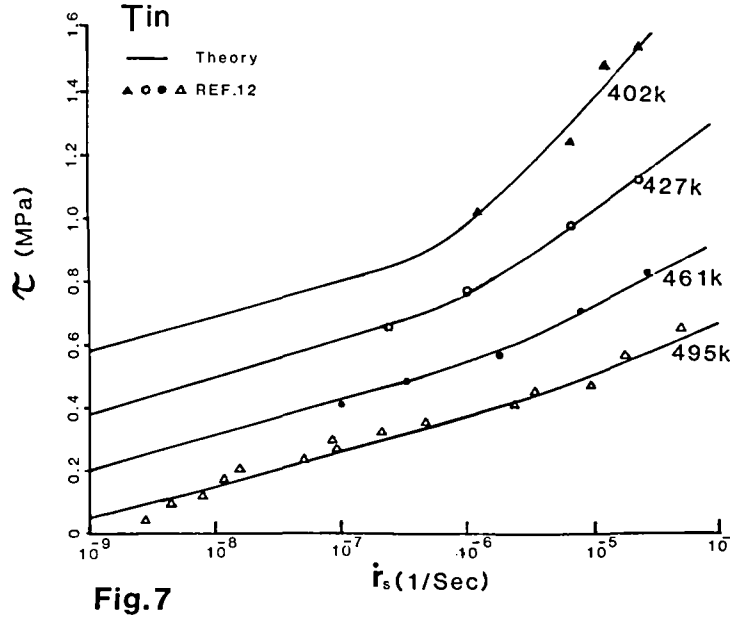
Tin
Theory
▲ ○ ● △ REF.12
402k
427k
461k
495k
τ (MPa)
0
0.2
0.4
0.6
0.8
1.0
1.2
1.4
1.6
10⁻⁹
10⁻⁸
10⁻⁷
10⁻⁶
10⁻⁵
10⁻⁴
ṙs (1/Sec)

Fig.7

A POTENTIAL FUNCTION DERIVATION OF A CONSTITUTIVE EQUATION FOR INELASTIC MATERIAL RESPONSE*

Donald C. Stouffer and Nader Abu El Foutouh
University of Cincinnati
Cincinnati, Ohio 45221

ABSTRACT

Physical and thermodynamic concepts are used to develop a potential function for application to high temperature polycrystalline material response. Inherent in the formulation is a differential relationship between the potential function and constitutive equation in terms of the state variables. Integration of the differential relationship produces a state variable evolution equation that requires specification of the initial value of the state variable and its time derivative. Analysis of these conditions showed that the initial loading rate, which is directly related to the initial hardening rate, can significantly influence subsequent material response. This effect is consistent with observed material behavior on the macroscopic and microscopic levels, and may explain the wide scatter in response often found in creep testing. The material used for the study, cast and wrought IN100 at 732°C, was tested in tension at different strain rates, creep, stress relaxation, and reversed inelastic flow.

INTRODUCTION

The research presented in this paper is directed toward developing a state variable constitutive model for metals in high temperature environment where rate effects are important. The underlying concept used in the model is to develop a consistent system of equations to predict the inelastic strain rate and evolution of the state variables that are derivable from a potential function. The essential structure of the theory is based on the maximum plastic work inequality, the rate of work hardening inequality, and dislocation dynamics.

The maximum plastic work inequality, expressed using the concept of a yield surface, can be written as (refs. 1 and 2)

$$(\sigma_{ij} - \sigma^{o}_{ij})d\varepsilon^{I}_{ij} \geq 0. \tag{1.1}$$

* This study was supported in part by the Air Force Wright Aeronautical Laboratory under contract number F33615-78-C-5199 with the University of Cincinnati.

The quantity $d\varepsilon^I_{ij}$ is the inelastic strain increment due to the stress step $\sigma_{ij} - \sigma^o_{ij}$. The stress σ_{ij} is on the current yield surface and σ^o_{ij} is any other stress either inside or on the yield surface. The inequality requires that the inelastic strain increment is normal to the yield surface and that all yield surfaces are convex. Eq. (1.1) is an axiom resulting from observed plastic behavior of metals. It is not derivable from thermodynamics and is not necessarily valid for all materials. It does, however, capture the essence of how many metals behave.

The property of work hardening, as identified with a large class of metals, can be further characterized. In these materials it has been consistently observed that the stored energy of cold work, W^h, increases with deformation at a decreasing rate during a continuous deformation history. This can be expressed by

$$dW^h_2 - dW^h_1 \leq 0 \ , \tag{1.2}$$

where dW^h_1 and dW^h_2 are the increments of stored energy associated with identical strain (or stress) increments in two different stored worked states W^h_1 and W^h_2 such that $W^h_2 > W^h_1$ (ref. 3). The exact structure of a cold worked state is not fully understood, however, it is generally accepted that the energy is stored through the development of a system of dislocations (ref. 4 and 5).

In the initial state of deformation dislocations multiply and tend to arrange themselves into groups or clusters occupying only a small fraction of the material volume. Most of the deformed material is dislocation free. As deformation increases the dislocation clusters form continuous walls separating relatively perfect cells. With further strain, secondary slip systems are activated and the density of dislocations increases with other point defects appearing. The cell size decreases at a decreasing rate as strain increases and tends to stabilize. The cell size and dislocation density at any time are influenced by the initial microstructure, temperature and loading history up to that time. In addition, it is important to recognize that a substantial portion of the character of the microstructure is established early in the load history when the observed macroscopic inelastic strain is very small.

In some cases, the stored energy is partially recovered in time at elevated temperature or fully recovered through recrystalization. This effect could be important for metals at high temperature that have been work hardened in the initial configuration. This situation is typical of cast and wrought super-alloys. In the case of recovery, $W^h_2 < W^h_1$, and the stored energy increments dW^h_1

and dW_2^h are both negative. In this case, eq. (1.2) requires the rate of change of recovery to be positive. That is, softening occurs at an increasing rate; conversely, hardening occurs at a decreasing rate, and both hardening and softening tend to stabilize.

The maximum plastic work inequality and the rate of work hardening inequality satisfy most observed response in metals at high temperature under continuous load histories. However, the essence of the theory can be easily extended by a broader class of materials and load histories by requiring the two inequalities hold together rather than individually; that is

$$(\sigma_{ij} - \sigma_{ij}^o)d\varepsilon_{ij}^I - (dW_2^h - dW_1^h) \geq 0 \ . \tag{1.3}$$

A similar relation was suggested by Ponter (refs. 5 and 6) and the consequences are extensive. First, since the stored energy is generally small compared to the total plastic work during a typical deformation history, the restriction on the hardening or softening rate (eq. (1.2)) can be softened in some cases. This allows, for example, a jump in the rate plastic working to produce a jump in the rate of work hardening that is not restricted by eq. (1.2). The effect appears possible in situations where there are jumps in strain rate early in the development of microstructure.

Another essential feature of the constitutive model is to use the result of Rice (ref. 7) showing that the components of an inelastic strain rate tensor, $\dot{\varepsilon}_{ij}^I$, are derivable, at each instant during the deformation history, from a potential function, Ω, of the stress, i.e.

$$\dot{\varepsilon}_{ij}^I = \frac{\partial \Omega[\sigma, \text{ history}]}{\partial \sigma_{ij}} \ . \tag{1.4}$$

This result is based on the physical notion of conventional crystalline deformation: At a given slipped state, the rate of permanent shearing on a particular slip system depends on the stress at that point only through the shear stress acting on the slip system. Thus, for a given prior history, eq. (1.4) was shown to give time dependent stress strain equations consistent with both plausible macroscopic and microscopic idealizations. More recently, Ponter and Leckie (ref. 8) extended the formulation to polycrystalline metals at high temperature. Following the methods in ref. 6 they established a potential function for a constitutive equation of the Baily (ref. 9) and Orowan (ref. 10) type that contains one state variable, s, to describe the hardness or stored

energy of the material. In the Ponter-Leckie development the assumption of a local (microscopic) potential was essential to establish a macroscopic potential that can be used to derive both the inelastic flow equation and state variable evolution equation. The Baily-Orowan the macroscopic flow equation contains an over stress argument of the type $\phi - s$, where ϕ is a scalar function of the stress tensor.

Another state variable constitutive equation that uses a single state variable to describe the hardness or resistance to inelastic flow was developed by Bodner and Partom (refs. 11 and 12). Inherent in the representation is the absence of a yield surface. That is, the inelastic strain rate is non-zero for all non-zero values of stress. This is a continuous flow equation without separate loading and unloading conditions. It has been used to successfully predict the response of two superalloys at high temperature (refs. 13 and 14). In part, the success may result from using the entire load history rather than excluding the load history inside the yield surface. For example, recall that the character of the dislocation substructure is established very early in the deformation history prior to classical yield.

Another key feature of the Bodner-Partom model is that the specific form of the flow equation was motivated by dislocation dynamics. Both of the well accepted representations for dislocation velocity, developed by Gilman (ref. 15) and Vreeland (ref. 16) are embodied in the Bodner-Partom formulation. One shortcoming of the Bodner-Partom representation is that the basic structure of the evolution equation for the hardness state variable is developed by phenomenological methods. The evolution equation is consistent with the observed properties of stored energy (eq. (1.2)) but does not possess a formal mathematical or physical derivation.

Specifically, in this paper it is shown that the concept of a macroscopic inelastic potential function is compatible with the essential features of high temperature material response expressed in eq. (1.3) . A potential function concept is then used to derive a state variable evolution equation directly from the inelastic flow equation. A specific example is developed using the Bodner-Partom representation. It is shown that the Bodner-Partom evolution equation has a mathematical structure very similar to the derived evolution equation. However, the derived evolution equation has a new important property. The derived representation depends on the initial hardening rate that can vary from test to test for the same initial material microstructure. The representation

is used to predict the response of IN100 at 732°C. The material constants are determined from tensile response data and the experimental response in, creep, stress relaxation and reversed inelastic flow is analyzed.

II DEVELOPMENT OF A POTENTIAL FUNCTION FORMULATION

Let us introduce a state variable Z as a macroscopic measure of the effect of the dislocation microstructure on deformation. It is designated as the hardness or resistance to inelastic flow and the units are that of stress. Similarly a macroscopic strain state variable, ε^h, is defined as a measure change in geometry associated with the development of dislocation microstructure.

The variables Z and ε^h are scalar functions of tensor valued arguments and defined so that an increment of stored energy of cold work can be calculated as

$$dW^h = Zd\varepsilon^h = d\dot{\varepsilon}^h dt \tag{2.1}$$

It is required that the stored energy increment, dW^h, and hence the valuables Z and ε^h, satisfy the conditions outlined in the Introduction. The increment of inelastic work associated with an increment of inelastic deformation is

$$dW^I = \sigma_{ij} d\varepsilon^I_{ij} = \sigma_{ij} \dot{\varepsilon}^I_{ij} dt \tag{2.2}$$

In a constant hardness state the maximum plastic work inequality (eq. (1.1)) can be written as

$$\dot{\varepsilon}^I_{ij} d\sigma_{ij} \geq 0, \quad Z = \text{const.} \tag{2.3}$$

Similarly, the rate of work hardening inequality, for constant stress eq. (1.2) can be rewritten as

$$\dot{\varepsilon}^h dZ \leq 0, \qquad \sigma_{ij} = \text{const.} \tag{2.4}$$

and the combined inequality (eq. (1.3)) is

$$\dot{\varepsilon}_{ij} \Big|_{Z = \text{const.}} d\sigma_{ij} - \dot{\varepsilon}^h \Big|_{\sigma_{ij} = \text{const.}} dZ \geq 0. \tag{2.5}$$

Using the result of Rice (eq. (1.4)) there exists a potential function $\phi(\underset{\sim}{\sigma}, Z)$ such that

$$\dot{\varepsilon}^I_{ij} = \frac{\partial \phi(\underset{\sim}{\sigma}, Z)}{\partial \sigma_{ij}} \quad . \tag{2.6}$$

Further, using the eqs. (2.5) and (2.6) , and the result of Ponter (ref. 17), let us assume that for ϕ to exist and be physically acceptable, that

$$\dot{\varepsilon}^{h} = - \frac{\partial \phi [\underset{\sim}{\sigma}, Z]}{\partial Z} \tag{2.7}$$

and

$$\frac{\partial \phi}{\partial \sigma_{ij}} d\sigma_{ij} + \frac{\partial \phi}{\partial Z} dZ = d\phi \geq 0.$$

Therefore, ϕ exists and it is convex in the space $\{\underset{\sim}{\sigma}, Z\}$ (ref. 16). The existence of the potential function $\phi(\sigma, Z)$ is consistent with the essential structure of work hardening or softening metal plasticity. As a result of the existance of ϕ and from eqs. (2.6) and (2.7) it follows that

$$\frac{\partial \dot{\varepsilon}^{h}}{\partial \sigma_{ij}} = - \frac{\partial \dot{\varepsilon}^{I}_{ij}}{\partial Z} \quad . \tag{2.8}$$

Using the idea of an instantaneous tangent modulus in one dimensional plasticity, the stress rate state variable $\dot{Z}$ can be related to the strain rate variable $\dot{\varepsilon}^{h}$ by the function h; i.e.

$$\dot{Z} = h\dot{\varepsilon}^{h} = -h \frac{\partial \phi}{\partial Z} \quad . \tag{2.9}$$

That is, h is the instantaneous slope of the $\dot{Z} \sim \dot{\varepsilon}^{h}$ response curve. For the following analysis let $h = h(Z,...)$ be independent of the current stress.

Finally, eq. (2.8) can be used to derive the state variable evolution equation directly from the flow equation. Let us assume $\dot{\varepsilon}^{I}_{ij} = \dot{\varepsilon}^{I}_{ij}(\underset{\sim}{\sigma}, Z)$ is specified, then from eq. (2.8) and (2.9)

$$d\dot{Z} = - h \frac{\partial \dot{\varepsilon}^{I}_{ij}}{\partial Z} d\sigma_{ij} + df(Z,...) \tag{2.10}$$

where f is independent of stress. Integrating on the time interval $[0,t]$, the evolution equation for the hardness can be written as

$$\dot{Z}(t) - \dot{Z}_{0} = -h \int_{\sigma_{ij}(0)}^{\sigma_{ij}(t)} \frac{\partial \varepsilon^{I}_{ij}}{\partial Z} d\sigma_{ij} + [f(Z,...) - f(Z_{0},...)] \quad . \tag{2.11}$$

The integral can be evaluated for any specific choice flow law involving only one state variable.

Embodied in eq. (2.11) is an important property that is not widely recognized. The parameters $\dot{Z}_0 = \dot{Z}(0)$ and $Z_0 = Z(0)$ are initial conditions. The parameter Z_0 describes the initial state of the microstructure that, for example, would be the same for all specimens from the same heat of material. However, Z_0 is the initial rate of hardening of the microstrucutre and would be expected to vary from test to test, depending on the initial loading conditions.

III Bodner-Partom Constitution Equations

The Bodner-Partom constitutive equation (refs. 11, 12, 18) is a fully developed three dimensional theory that has even been extended to anisotropic materials (refs. 19 and 20). Since the main purpose of the paper is to evaluate the properties of the evolution equation, it is convenient to restrict the analysis to a one dimensional form of the constitutive equation. This is consistent with the accompanying experimental program.

The isotropic constitutive theory of Bodner and Partom is based on the assumption that the total strain rate, $\dot{\varepsilon}(t)$, can be separated into elastic, $\dot{\varepsilon}^e(t)$, and inelastic, $\dot{\varepsilon}^I(t)$, components. Let E represent the elastic modulus, then the Bodner-Partom equation can be written in a one dimensional form as

$$\dot{\varepsilon}(t) = \frac{\dot{\sigma}(t)}{E} + \dot{\varepsilon}^I(t) \tag{3.1}$$

where $\sigma(t)$ is the current value of the stress. Inherent to the theory is that the inelastic strain rate is non-zero for all non-zero values of stress. The specific representation used by Bodner and his co-workers for the inelastic strain rate is given by

$$\dot{\varepsilon}^I(t) = D_0 \frac{\sigma(t)}{|\sigma(t)|} \exp\left[-\frac{(n+1)}{2n}\left(\frac{Z^2}{\sigma^2}\right)^n\right] . \tag{3.2}$$

The constant D_0 represents a limiting value of the inelastic strain rate and is generally taken at $2\text{x}10^4/\sqrt{3}$ sec^{-1} unless the strain rates are very high. The constant n controls the strain rate sensitivity and Z(t) is the hardness state variable. The general mathematical structure of eq. (3.2) is based on dislocation dynamics expressed in the context of continuum mechanics and has proven consistent with the observed response for many metals. The formulation is similar to the classical yield surface theory. The structure of the Prandtl-Reuss formulation is preserved, but a yield surface itself is not part of eqs. (3.1) and (3.2).

Necessary for the use of the above equations is a representation for the state variable Z. The specific representation proposed by Bodner et. al. (ref. 18) and used for superalloys (refs. 13, 14 and 21) is based on the concept that only the inelastic rate of working $\dot{W}^I$ and the current hardness control the rate of hardening. The representation is written as

$$\dot{Z} = m(Z_1 - Z)\dot{W}^P - AZ_1\left(\frac{Z-Z_2}{Z_1}\right)^r \tag{3.3}$$

with Z_0 designated as the inital value of Z. The two terms in eq. (3.3) are defined so that $AZ_1[(Z-Z_2)/Z_1]^r$ is negligible during rapid load histories. Thus, during a tensile test that is fast compared to creep test, eq. (3.3) reduces to the first term alone. The constant Z_1 corresponds to the maximum value for Z and m is an exponential coefficient controlling the rate of hardening. For a long time response, such as creep, a second term corresponding to hardening recovery is necessary. During the minimum creep rate both $\dot{\varepsilon}^P$ and σ are constant, thus Z is constant ($\dot{Z} = 0$) and the rate of hardening must equal the rate of recovery. The coefficient Z_2 corresponds to the minimum recoverable value of hardness, and A and r are the coefficient and exponent, respectively, controlling the rate of hardening recovery.

At this point in the paper it is now possible to carry out one specific objective: Derive an evolution equation for $\dot{Z}$ by using eq. (3.2) in eq. (2.11) and to compare the result to eq. (3.3). To begin, let us define

$$B = D_0\left(\frac{n+1}{2n}\right)^{1/2n} \quad \text{and} \quad R = \frac{n+1}{2n}\left(\frac{Z}{\sigma}\right)^{2n} \tag{3.4}$$

so that the integral in eq. (2.11) can be written as

$$I = B\int R^{-1/2n}\, e^{-R} dR\ . \tag{3.5}$$

For continuous histories eq. (3.5) can be integrated by parts N times to obtain a series representation. Letting p = 1/2n, the series can be written as

$$I(R) = B\, e^{-R} R^{-p}\left[\frac{R}{(1-p)} + \frac{R^2}{(1-p)(2-p)} + \frac{R^3}{(1-p)(2-p)(3-p)} + \ldots\right] \tag{3.6}$$

which converges for all R on $(0,\infty)$. The function I(R) is almost constant for large values of R (small values of stress) and decays with decreasing R (increasing stress). In this application of eq. (3.6) the constants D_0 and n are generally known so eq. (3.6) is totally defined.

Finally, since eq. (3.5) could be integrated to obtain eq. (3.6), then eq. (3.6) is an exact differential. This implies that the contribution of

I(R) to the current hardening rate depends only on the current value of the state, Z, and the current stress. Thus, for all histories producing the same state and stress the integral term will have the same contribution to the hardening rate.

IV PROPERTIES OF THE TWO EVOLUTION EQUATIONS

The derived evolution Equations, (eqs. (2.11) and (3.6)), can be put in a form similar to the Bodner-Partom eq. (3.3). Noting from eqs. (3.2) and (3.4) that I(R) can be written as

$$I(R) = g(\frac{\sigma}{Z})\dot{\varepsilon}^I \tag{4.1}$$

where

$$g(\frac{\sigma}{Z}) = D_0(\frac{n+1}{2n})^{1/2n} R^{-n}[\frac{R}{(1-p)} + \frac{R^2}{(1-p)(2-p)} + \frac{R^3}{(1-p)(2-p)(3-p)} + \ldots] \tag{4.2}$$

and $R(\frac{Z}{\sigma})$ is given by eq. (3.4). Thus, the derived evolution Equation, (eq. (2.11)), becomes

$$\dot{Z} = \dot{Z}_0 - h[g(\frac{Z}{\sigma}) - g_0(\frac{Z}{\sigma})]\dot{\varepsilon}^I + [f(Z,\ldots) - f(Z_0,\ldots)]. \tag{4.3}$$

The Bodner-Partom Evolution Equation (eq. (3.3)) can be rewritten for convenience as

$$\dot{Z} = m(Z_1 - Z)\sigma\dot{\varepsilon}^I - AZ_1(\frac{Z-Z_2}{Z_1})^r . \tag{4.4}$$

Direct comparison of eqs. (4.3) and (4.4) shows a very strong mathematic similarity. Both equations have two terms of similar type. One term is linear in the inelastic strain rate, $\dot{\varepsilon}^I$, and the other term is independent of the stress σ. The derived evolution equation has the initial hardening rate term $\dot{Z}_0$. The coefficient of the strain rate term in the derived equation is a product of a modulus h and a non-linear function of $(\frac{Z}{\sigma})$; whereas, the corresponding term in the Bodner-Partom is linear in both σ and Z. The function f(Z,...) in the derived equation is consistent with logarithmic function of Z in the Bodner-Partom equation. In general, eq. (4.4) can be considered almost a special case of eq. (4.3).

To evaluate the properties of the derived evolution equation further it is convenient to develop a representation for the function f(Z,...). A power series expansion of f in Z would produce a series of exponential time terms when

eq. (4.3) is solved. Since the general solution is exponential in nature, a reasonable approximation is to use a single exponential term. Thus, let us assume a linear representation, namely

$$f(Z) - f(Z_0) = -\alpha(Z - Z_0) \tag{4.5}$$

where α is a parameter that is independent of Z and σ. Further, in order for the representation for Z to approach a stable asymptotic value it is necessary for $\alpha > 0$. It is expected that this representation should contain many of the essential features.

Even though the mathematical structure of eqs. (4.3) and (4.4) is similar, the physical interpretation of the terms is different. First notice that $t = 0$, $\dot{Z} = 0$ in eq. (4.4) whereas $\dot{Z} = \dot{Z}_0$ in eq. (4.3). It is expected that the initial hardening rate should depend on the initial loading conditions, that is $\dot{Z}_0 = \dot{Z}_0(\dot{\varepsilon}_0) = \dot{Z}_0(\dot{\sigma}_0/E)$ where $\dot{\varepsilon}_0$ and $\dot{\sigma}_0$ are the initial strain and stress rates. This adds considerable flexability to the model and is consistent with the initial formation of dislocation microstructure as described earlier. Next, the strain rate term in the third term of eq. (4.3) produce basic tensile response properties and the stable value for Z. The strain rate term of eq. (4.3) and the second term of eq. (4.4) characterize the long time recovery response properties of the model.

V EXPERIMENTAL PROGRAM

Sixteen mechanical tests have been conducted on IN100 at 732°C (1350°F) at the Air Force Wright Aeronautical Laboratory, Ohio and Mar-Test Inc., Cincinnati, Ohio. The material was obtained at different times from different heats resulting in five groups of specimens designated as series C, G, T, GT and ENTEN. The experimental program, summarized in Table 1, includes eight tensile tests, seven creep tests and one combined test. The controlled experimental variable is shown in Table 1 and the observed stable values for stress or secondary creep rate is also given for the tensile and creep tests, respectively.

The results of seven tests conducted under constant strain rate control ranging from $1.4\text{x}10^{-3}$ sec^{-1} to $1.6\text{x}10^{-6}$ sec^{-1} and one test under constant head rate control at $8.3\text{x}10^{-4}$ sec^{-1} are shown in fig. 2. There is significant variation in the level of the stress response due to the imposed variation in strain and head rate. Note, however, the total accumulated strain in these tests is not important since several of the specimens were not failed. For four

different values of strain rate (Tests 2, 4, 6 and 8) the response obtained a maximum stress and maintained that value of stress for all subsequent values of strain. However for Tests 5, 7 and 9 a different response was obtained. In these experiments the value of the stress decayed from the maximum value obtained at about one percent strain. In test 5 the amount of reduction in stress to a lower stable value was small. In Test 7, at a lower strain rate, the reduction in stress to a stable value was larger; and in Test 9, the stress did not stabilize at a lower level. This wide variation in response might arise since the eight specimens are from four different heats. Since both types of response were observed at both AFWAL and Mar-Test Inc., it cannot be accepted as an experimental problem.

The results of six creep tests are shown collectively in fig. 6b for up to 100 minutes. The variation in the creep stress was almost twofold 496 to 896 MPa (72 to 130 KSI), and the corresponding minimum creep rates are given in Table 1. Although not shown, Test 10, 14 and 15 obtained tertiary creep at times ranging from 100 minutes to about 1200 minutes. The response curves do not exhibit a significant primary creep phase and most of the response is dominated by tertiary creep. This is typical of other superalloys. Test 20, creep at 896 MPa (130 KSI) shown in fig. 6b, is not ordered with respect to the other tests; however, this could result from speciments variation or loading conditions as discussed later.

If the deformation mechanism controlling the tensile tests and creep tests are the same, then the controlled and observed variables from the two types of tests shown in Table 1 correspond to the same deformation process. That is, the stable value of stress obtained in a strain rate controlled tensile tests should correspond to the creep stress with the same constant (secondary) creep rate as the tensile test. A plot of the observed and controlled variables for both the creep at tensile tests is given in fig. 1. Considering the data is over five decades of strain rate, there appears to be reasonable consistency between both types of tests. Tensile Tests 7 and 8 correspond very closely to creep Tests 19 and 18, respectively, as shown in fig. 1 and table 1. Thus, it does appear that the same basic deformation mechanisms control both creep and tensile behavior between 482 and 1100 MPa (70 and 164 KSI) at 732^{o}C (1350^{o}F).

VI APPLICATION TO IN100

The next step in predicting the response of IN100 at 732°C is to determine the remaining material parameters in the evolution equation. This exercise is divided into two steps. First, constant strain rate histories are analyzed and then the results are extended to piecewise constant strain rate histories.

Constant strain rate histories. The evolution equation that is derived from the potential function can be written as

$$\dot{Z} = \dot{Z}_0 - \alpha(Z-Z_0) + h[I(0)-I(t)] \tag{6.1}$$

for continous deformation histories using eqs. (4.5) and (4.1) in eq. (4.2). During each constant strain rate tensile test the last term approaches a step to the steady value, Δ_{ss}. An approximation of the behavior can be made by replacing the integral term in eq. (6.1) by a step function. Thus, assume eq. (6.1) can be approximated by

$$\dot{Z} \cong \dot{Z}_0 - \alpha(Z-Z_0) + \Delta_{ss}\mu[t-t_n] \tag{6.2}$$

where t_n is the time of the unit step $\mu[t-t_n]$. The solution of eq. (6.2) for the hardness variable yields

$$Z = Z_0 e^{-\alpha t} + \left(\frac{\dot{Z}_0+\alpha Z_0}{\alpha}\right)(1-e^{-\alpha t}) + \frac{\Delta_{ss}}{\alpha}\mu[t-t_n](1-e^{-\alpha(t-t_n)}) \tag{6.3}$$

which is expected to be a reasonable approximation for times up to t_n and at times much larger than t_n.

Since a significant change in response occurs early in the history, let us define t_n as the time to reach the ultimate stress under a hypothetical elastic loading conditions using the initial strain rate; ie,

$$t_n = \frac{\sigma_\mu}{E\dot{\varepsilon}_0} \tag{6.4}$$

where σ_μ and $\dot{\varepsilon}_0$ are the ultimate stress and constant strain rate during each tensile test. The elastic modulus is denoted by E. Thus, the response up to time t_n characterizes the development of the microstructure before the onset of significant macroscopic inelastic deformation. The value of hardness, Z_n, expressed from eq. (6.3) as

$$Z_n = Z_0 + \frac{\dot{Z}_0}{\alpha}(1-e^{-\alpha t_n}) \tag{6.5}$$

and the steady state value (Long time) value is

$$Z_{ss} = \frac{\dot{Z}_0 + \alpha Z_0 + \Delta_{ss}}{\alpha} \quad . \tag{6.6}$$

Equations (6.5) and (6.6) can be used to evaluate the parameters in the evolution equation at three points: the initial condition Z_0 and $\dot{Z}_0$; the onset of significant inelastic flow, Z_n; and in the fully saturated condition, Z_{ss}.

The values of Z_n and Z_{ss} can be calculated directly from the tensile data for each test. Inverting eq. (3.2) and evaluating at time t_n gives

$$Z_n = \sigma_\mu \left[\frac{-2n}{n+1} \ln\left(\frac{\dot{\varepsilon}_0}{D_0}\right)\right]^{1/2n} , \tag{6.7}$$

likewise at saturation

$$Z_{ss} = \sigma_{ss} \left[\frac{-2n}{n+1} \ln\left(\frac{\dot{\varepsilon}_0}{D_0}\right)\right]^{1/2n} . \tag{6.8}$$

Comparing eq. (6.1) to eq. (6.2) and using eq. (6.8) yields

$$\Delta_{ss} = h\left[I(0) - I\left(\frac{Z_{ss}}{\sigma_{ss}}\right)\right] \tag{6.9}$$

which can be used with eq. (6.6) to define the parameter h as

$$h = \frac{\alpha(Z_{ss}-Z_0)-\dot{Z}_0}{\left[I(0)-I\left(\frac{Z_{ss}}{\sigma_{ss}}\right)\right]} \quad . \tag{6.10}$$

The parameter h, as, expected, is a function of history noting from eq. (6.8) that (Z_{ss}/σ_{ss}) is dependent only on the imposed constant strain rate $\dot{\varepsilon}_0$. The initial hardening rate can also be determined from eq. (6.5)

$$\dot{Z}_0 = \frac{\alpha(Z_n-Z_0)}{1-e^{-\alpha t_n}} \tag{6.11}$$

noting that Z_n can be determined from eq. (6.7).

The time parameter α can by estimated from the time required to obtain the steady state response. Assuming $e^{-\alpha t}$ vanishes at $\alpha t = 5$ and using saturation strain ε_∞, then $\alpha\varepsilon_\infty/|\dot{\varepsilon}_0| = 5$. In this example

$$\alpha = C_0|\dot{\varepsilon}_0| , \tag{6.12}$$

where $C_0 = 10\ \text{sec}^{-1}$ and the time response is also dependent upon the applied strain rate. The remaining parameter Z_0 is choosen by interactive computation to obtain the best fit for the lowest strain rate response curve. The permits including the recovery effect as well as strain hardening. This, analysis produced $\alpha_0 = 3275\text{MPa}(475\ \text{KSI})$. The representations derived directly from the tensile data for use with eq. (6.7) and (6.8) are

$$\sigma_\mu = 6.8948(218.79\ x^{-0.77934} - 58.65\ x^{-2.9144})$$

and

$$\sigma_{ss} = 6.8948(162.048\ x^{-0.31697} - 0.047656\ x^{9.6381}) \tag{6.13}$$

where $x = \log \dot{\varepsilon}/\log D_0$ and stress is in MPa(KSI). The representations were established to account for two different deformation mechanisms above and below approximately 900 MPa (see fig. 6). The other constants for IN100 used in the study were taken from ref. 14. They are

$$E = 1.50\text{x}10^5\ \text{MPa}, \quad n = 0.70 \text{ and } D_0 = 2\text{x}10^4/\sqrt{3}\ \text{sec}^{-1}.$$

Piecewise Constant Histories. The representation for constant strain rate histories can be summarized by substituting eq. 6.10 into eq. 6.2 and identifying Z_{ss}/σ_{ss} from eq. (6.8) as a function of the applied strain rate, $\dot{\varepsilon}_0$, to get

$$\dot{Z} = \dot{Z}_0 - \alpha(Z-Z_0) + [\alpha(Z_{ss}-Z_0)-\dot{Z}_0]\frac{I(0)-I(\frac{Z}{\sigma})]}{[I(0)-I(\dot{\varepsilon}_0)]}. \tag{6.14}$$

Let us consider a step change in strain rate from $\dot{\varepsilon}_0$ to $\dot{\varepsilon}_1$ at time t_1. From eq. (3.1) it is seen that this produces a jump in the stress rate,

$$\Delta\dot{\sigma}_1 = E[(\dot{\varepsilon}_1-\dot{\varepsilon}_0)-(\dot{\varepsilon}^I_1-\dot{\varepsilon}^I_0)] \tag{6.15}$$

but not a jump in the stress. Further it is expected that the inelastic strain rate would remain the same; therefore, from eq. (3.2), the value of the hardness Z is the same immediately before and after the jump in the strain rate. This implies that the microstructure does not change instantaneously. Note that eq. (6.15) also shows that separate unloading conditions are not required. If $\dot{\varepsilon}_1 = -\dot{\varepsilon}_0$, then $\Delta\dot{\sigma}_1 = -2E\dot{\varepsilon}_0$, which is very large compared to a stress rate near zero before the jump if the material is in the plastic range. Also, note that since the one test with reverse plastic flow does not indicate a significant amount of Bauschinger Effect, it is reasonable to assume an "isotropic hardening

rule" and use the same hardening rate equation for loading in both tension and compression.

It is expected, however, that a jump in strain rate would produce a jump in the hardening rate, $\dot{Z}$. From eq. (6.14), a jump in the value of $\dot{\varepsilon}_0$ to $\dot{\varepsilon}_1$ should produce a jump in $I(\dot{\varepsilon}_0)$, Z_{ss} and α. It is necessary to update $I(\dot{\varepsilon}_0)$ to $I(\dot{\varepsilon}_1)$ to maintain the asympotic value for Z. In this case, as time becomes large, $\dot{Z}$ approaches zero for any choice of Z_{ss} and α. Thus, Z_{ss} and α define the new microstructure corresponding new strain rate and time required to arrive at the new structure. For IN100,it was found that updating Z_{ss}, especially after several strain rate steps, produces erroneous results and estimating Z_{ss} from the initial strain rate produced much better results. Thus, due to the lack of more specific information, Z_{ss} was determined from the initial value of strain rate. This implies that the microstructure generated during the initial load secquence establishes some of the major features of the microstructure for all subsequent deformations. This appears to be reasonable for the simple deformation histories used in current study; but, may not be valid for all materials and all deformations. Finally, from the lack of better data during creep and stress relaxation testing, as fully explained later, it was decided to use the same value for α the entire history as a first approximation. Thus, for step changes in strain rate, the hardening rate described in eq. (6.14) is used with the values of α and Z_{ss} determined by the initial strain rate.

Extension to continuously varying strain rate histories could perhaps be modelled by using the current value for strain rate as described above. However, in the current paper only piecewise constant strain rate histories were used in the experimental program so it is difficult to test this hypothesis. Extension to other histories and materials requires additional development along with a better experimental description of microstructural changes.

VII CALCULATED AND PREDICTED RESULTS

The observed and calculated tensile response curves are shown in fig. 2. The calculated curves match the observed response with remarkable detail. The constants were determined with only two parameters, Z_0 and C_0, being determined by computational techniques. This was done using Curve 9 only. Further only

tensile data was used to determine the constants in eq. (6.13). All other predictions were made using only these constants.

It is interesting to note that the shape of both the observed and calculated response curves are not uniform. Curves 5, 6, 7 and 9 show elements of softening and hardening effects. Notice that there is the same ordering of the softening in curves 7 and 9, with almost no softening in curve 8. The value of $G = [I(0)-I(Z/\sigma)]/[I(0)-I(\dot{\varepsilon}_0)]$ in eq. (6.14) for the tensile curves is shown in fig. 3. The effect of this term becomes important at about the yield strain. Thus, it is responsible for describing the majority of the macroscopic plastic flow. Further, shape of the curve is consistent with the step function approximation used in eq. (6.2) for determining the material parameters. The initial hardening rate term, $\dot{Z}_0$ in eq. (6.11) is responsible for characterizing the initial microstructure and influences the subsequent inelastic response. The transistion, from one term to the other, depends on strain rate and produces the various responses in calculated curves. This effect arose as a direct result of the potential function formulation.

If the initial hardness, Z_0, is lowered to near zero, the response becomes unstable between cycles of strain hardening and recovery as shown in fig. 4a. This effect has been observed in chemical lead at 29°C by Morrow and Halford (ref. 22) as shown in fig. 4b). They documented the effect as cyclic hardening and recovery. The calculated response in fig. 4a underscores the importance of the Z_0 and $\dot{Z}_0$ terms.

The predicted and observed response to a hysteresis loop with a 25 second hold in compression is shown in fig. 5. The overall dimensions on the observed and predicted response are close including the compressive stress relaxation response. The shape of the predicted curve near yield on loading in compression and reloading in tension reflects the assumption of isotropic hardening. Obviously, there is a small element of kinematic hardening being observed in the response.

Next, let us investigate the effect of initial load history on the subsequent creep response. This was done for the four initial strain rate histories and one creep stress as shown in fig. 6a. The predicted response curves have a very pronounced variation. Increasing the initial strain rate from $1.33\text{x}10^{-1}$ Sec^{-1} to $8.33\text{x}10^{-4}$ in four steps produces increases in creep strain rate.

The observed creep response for IN100 for six levels of creep stress is shown in fig. 6b. It was expected that increasing stress would produce creep curves ordered with increasing creep rates. However, creep curve 20 is not ordered with respect to the other curves. If the increase creep stress of 21 MPa between curves 19 and 20 is accompanied by a decrease in the initial strain rate, the observed response could be predicted.

Further evidence of the effect of initial strain rate on the subsequent response is shown in fig. 7 for Rene' 95 at 649°C. All four tests were run using the creep stress of 1034.3 MPa. Two tests were run on a creep frame with the weights placed, one at a time, on a load pan. This produced a "slow" initial strain rate. The other two tests were run in a hydraulic closed loop testing system with the initial load applied rather rapidly producing a "fast" initial strain rate. There is significant variation in the observed creep response that might be attributed to the variation in initial strain rate. However, the two sets of tests were run in different laboratories on different heats of the material.

The effect of initial strain rate on stress relaxation was also investigated. Shown in Fig. 8 are four stress relaxation curves that were calculated using four different initial strain rates to a strain of 0.01. The initial strain rate has a dramatic influence on the initial stress as might be expected from the tensile curves. The initial rate of stress relaxation and the final stress level both appear to depend on the initial strain rate. The observed stress relaxation from 0.01 strain is also shown. This curve is part of a creep and recovery history with a subsequent deformation to 0.01 strain.

VIII SUMMARY

The potential function formulation for the state variable evolution equation was based on a combined inequality that allowed for both strain hardening and recovery. The resulting evolution law demonstrated both of these properties. In particular the derived evolution equation required initial values for both the state variable, Z, and its rate, $\dot{Z}$. In a given heat of material, with a fixed initial microstructure, the corresponding initial value for the state variable, Z, is assumed constant for all tests. However, the initial hardening rate, $\dot{Z}$, depends on how the specimen is initially loaded. This permits the equation to account for the formation of different initial microstructures with different properties that can effect the subsequent macroscopic inelastic flow.

This effect was investigated and the results can produce response curves that are not similar or even ordered under various loading conditions. These effects were observed in IN100, Rene' 95 and chemical lead at high temperature. Thus, it is possible that the variations in the initial loading condition could account for atleast some of the variations observed high temperature tests. This could be particularly useful for explaining the large amount of scatter observed in creep tests.

REFERENCES

1. Hill R., Mathematical Theory of Plasticity, Oxford University Press, 1950, Chapter III.

2. Drucker D.C., "Plasticity," Structural Mechanics (Proceedings First Symposium on Naval Structural Mechanics), Goodier J.H. and Hoff N.J., ed. Pergamon Press, 1960, p. 407.

3. Reed-Hill R.E., Physical Metallurgy Principles,, Van Nostrand, 1973.

4. Narayana A.D., "A Representation for the Deformation of a Metal Including the Effects of Strain Hardening and Recrystallization." Ph.D. Dissertation, University of Cincinnati, 1979.

5. Moteff J., "Deformation Induced Microstructural Changes in Metals," Proceedings Workshop on a Continuum Mechanics Approach to Damage and Life Prediction, Stouffer D.C., Krempl E. and Fitzgerald E.J., ed., Carrollton Kentucky, 1980, p. 11.

6. Ponter A.R.S., "Dynamic Behavior of Structures Composed of Strain and Work Hardening Visco-Plastic Materials," Journal of Solids and Structures, V 16, 1980, p. 793.

7. Rice J.R., "On the Structure of Stress Strain Relations for Time-Dependent Plastic Deformation of Metals," Journal Applied Mechanics, V37, pp 728-737, 1970.

8. Ponter A.R.S. and F.A. Leckie, "Constitutive Relationships for the Time Dependent Deformation of Metals," Journal of Engineering Materials and Technology," V98, pp 47-51, 1976.

9. Bailey R.W., "Note on the Softening of Strain Hardening Metals and its Relation to Creep," Journal of the Institute of Metals, V 35, pp 27-40, 1926.

10. Orowan E., "The Creep of Metals," J. West Scot Iron and Steel Institute, V 54, pp 45-53, 1946.

11. Bodner S.R. and Partom Y., "A Large Deformation Elastic-Viscoplastic Analysis of Thick-Walled Spherical Shell," Journal Applied Mechanics, V 39, pp 751-757, 1972.

12. Bodner S.R. and Partom Y., "Constitutive Equations for Elastic Viscoplastic Strain Hardening Materials," Journal Applied Mechanics, V 42, pp 385-389, 1975.

13. Stouffer D.C. and Bodner S.R., "A Relationship Between Theory and Experiment for a State Variable Constitutive Equation" ASTM-STP 765, Mechanical Testing and Deformation Model Development, 1982.

14. Stouffer D.C., "A Constitutive Representation for IN100," AFWAL-TR-81-4039, Wright Patterson AFB Ohio.

15. Gilman J.J., Micromechanics of Flow, McGraw-Hill New York, 1969.

16. Vreeland T.J., "Dislocation Velocity Measurements," Techniques of Metals Research, 2.1, Bunshak R.F. ed., Interscience Publ. p. 341, 1968.

17. Ponter A.R.S., Convexity and Associated Continuum Properties of a Class of Constitutive Relationship, Journal De Mécanique, 5.4, pp 527-541, 1976.

18. Merzer A. and Bodner S.R., ASME Journal of Engineering Materials and Technology, Vol. 101, 1979, pp 254-257.

19. Stouffer D.C. and Bodner S.R., "A Constitutive Equation for Deformation Induced Anisotropic Behavior of Metals," Intern. Journ. Engrg. Science, 17, 1979, p. 737.

20. Bodner S.R. and Stouffer D.C., "Comments on Anisotropic Plastic Flow and Incompressibility" to appear. Intern. Journ. Engrg. Science, 1982.

21. Stouffer D.C., Papernik L., and Bernstein H.L., "An Experimental Evaluation of the Mechanical Response Characteristics of René 95." Technical Report AFWAL-TR-80-4136, Air Force Wright Aeronautical Laboratory, Dayton, Ohio, 1980.

22. Morrow J. and Halford G.R., "Creep under Repeated Stress Reversals," Joint International Conference on Creep, New York, 1969, pp 343-47.

TABLE 1. SUMMARY OF THE EXPERIMENTAL PROGRAM

Test No.	Type of Test	Spec. No.	Control Variable	Observed Variable	Comments
2	Tensile	G1	$\dot{\varepsilon} = 1.42\times10^{-3}s^{-1}$	σ = 1116 MPa	
3	Tensile	T1	$\dot{X} = 8.33\times10^{-4}s^{-1}$		Const. Hd. Rate
4	Tensile	T3	$\dot{\varepsilon} = 8.33\times10^{-4}s^{-1}$	σ = 1068 MPa	
5	Tensile	G2	$\dot{\varepsilon} = 6.33\times10^{-5}s^{-1}$	σ = 951 MPa	
6	Tensile	ENTEN 1	$\dot{\varepsilon} = 5.5\times10^{-5}s^{-1}$	σ = 978 MPa	
7	Tensile	GT7	$\dot{\varepsilon} = 1.33\times10^{-5}s^{-1}$	σ = 889 MPa	
8	Tensile	ENTEN 4	$\dot{\varepsilon} = 6.67\times10^{-6}s^{-1}$	σ = 841 MPa	
9	Tensile	G3	$\dot{\varepsilon} = 1.67\times10^{-6}s^{-1}$		
10	Creep	C1	σ = 496 MPa	$\dot{\varepsilon} = 1.8\times10^{-8}s^{-1}$	
14	Creep	GT6	σ = 627 MPa	$\dot{\varepsilon} = 5.0\times10^{-8}s^{-1}$	
15	Creep	GT5	σ = 620 MPa	$\dot{\varepsilon} = 1.2\times10^{-7}s^{-1}$	
16	Creep	C4	σ = 696 MPa		Relax. Obs
18	Creep	GT4	σ = 827 MPa	$\dot{\varepsilon} = 4.5\times10^{-6}s^{-1}$	
19	Creep	C5	σ = 875 MPa	$\dot{\varepsilon} = 7.74\times10^{-6}s^{-1}$	
20	Creep	ENTEN 2	σ = 896 MPa	$\dot{\varepsilon} = 4.17\times10^{-6}s^{-1}$	
21	Combined History	C3	$\dot{\varepsilon} = 4.0\times10^{-3}s^{-1}$		Hyst. Loop

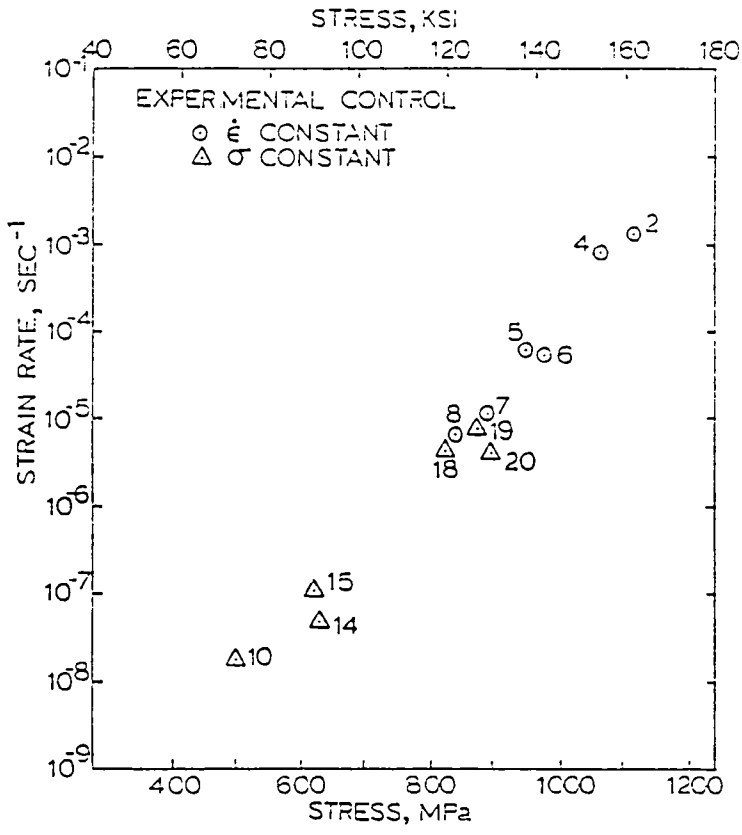

Figure 1. Stable values of stress and strain rate from both tensile and creep experiments. Test number refer to table 1.

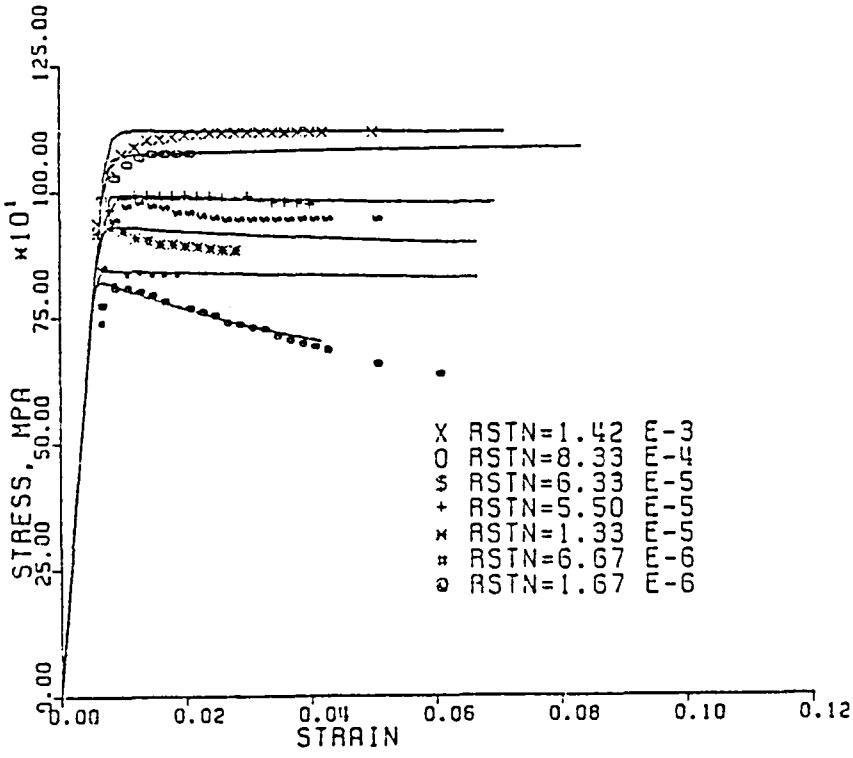

Figure 2. Calculated and observed tensile response curves for IN100 at 732°C for several constant strain rate load histories.

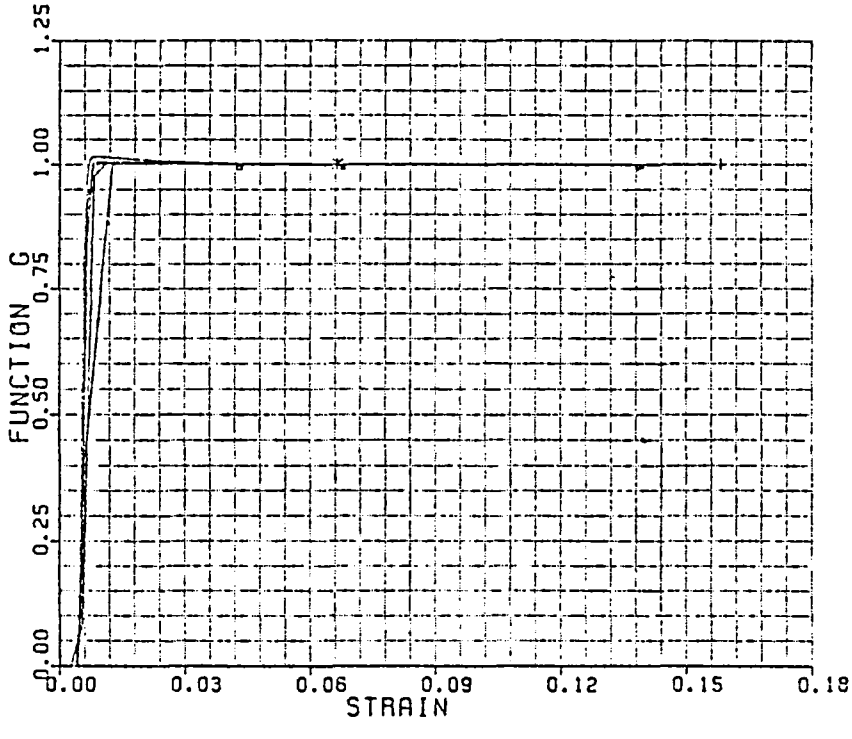

Figure 3. Response function $G = [(I(0) - I(R)]/[I(0) - I(\dot{\epsilon}_0)]$ for the tensile response histories shown in figure 1.

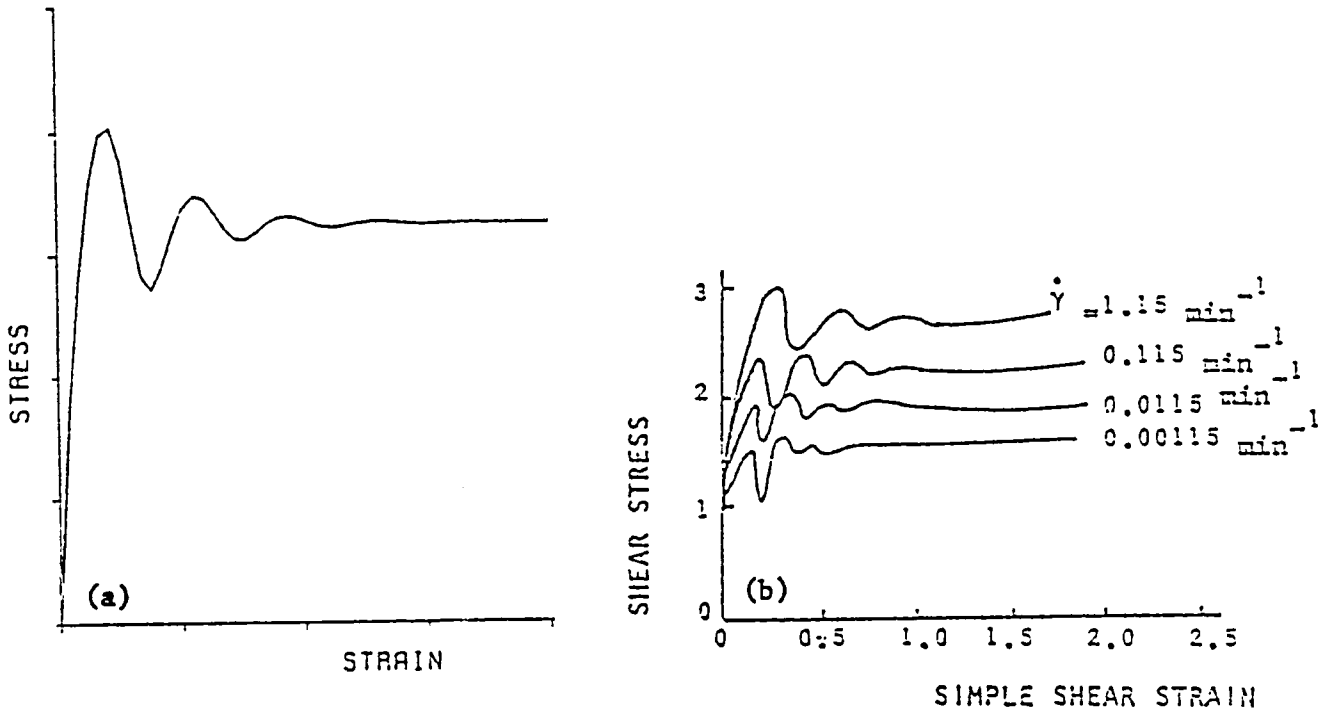

Figure 4. (a) Tensile responses characteristics of the model for an initial hardness near zero.

(b) Observed tensile response for chemical lead at 29°C in simple shear. (After Morrow and Halford [22]).

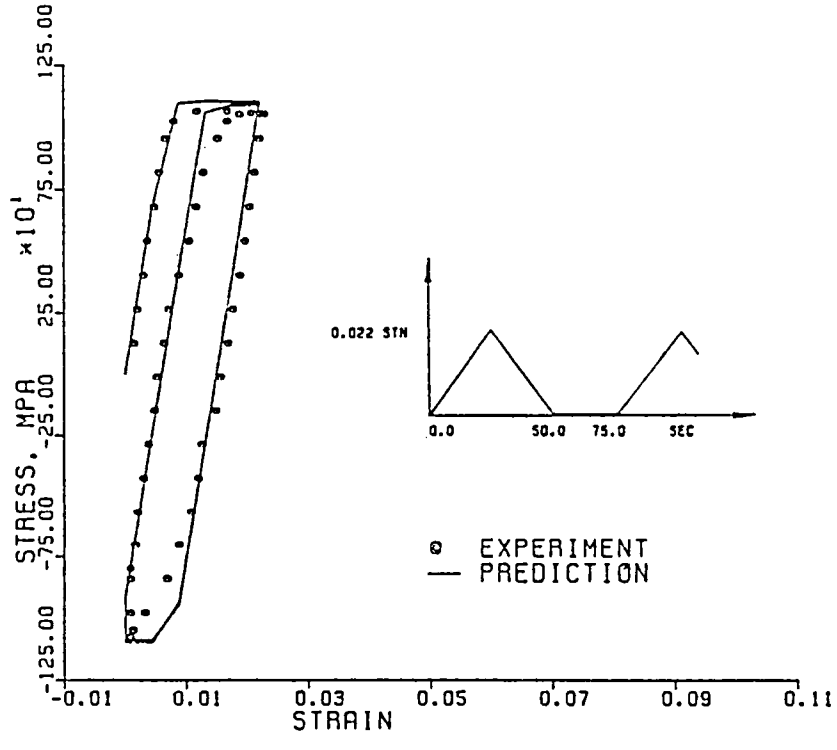

Figure 5. Predicted and observed hysteresis loop response of IN100 at 732°C.

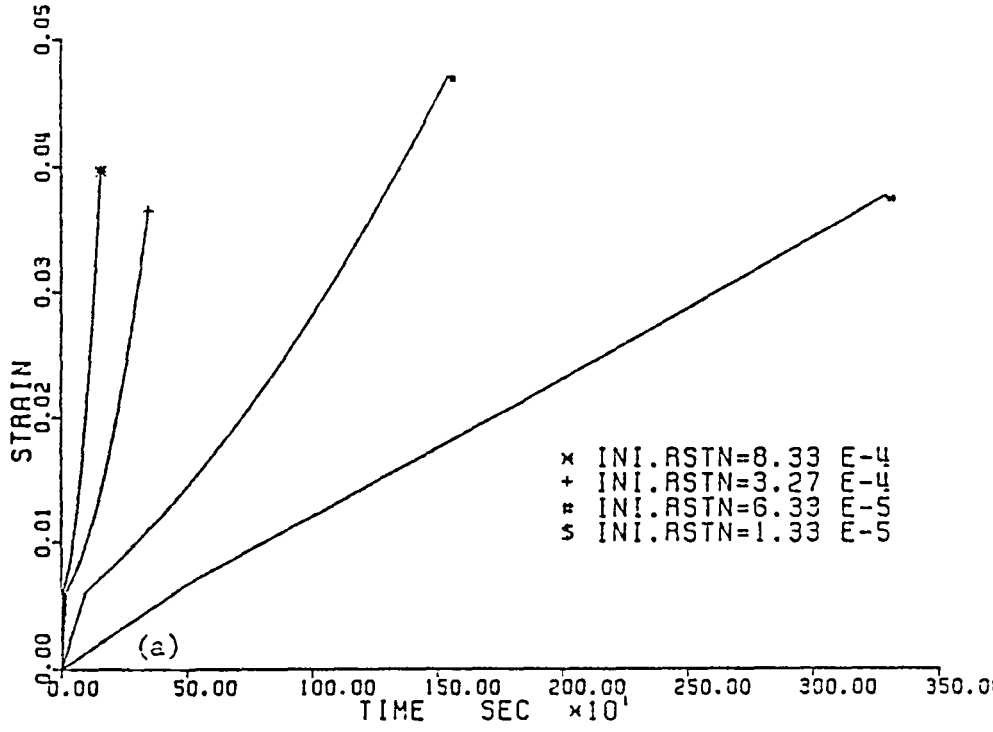

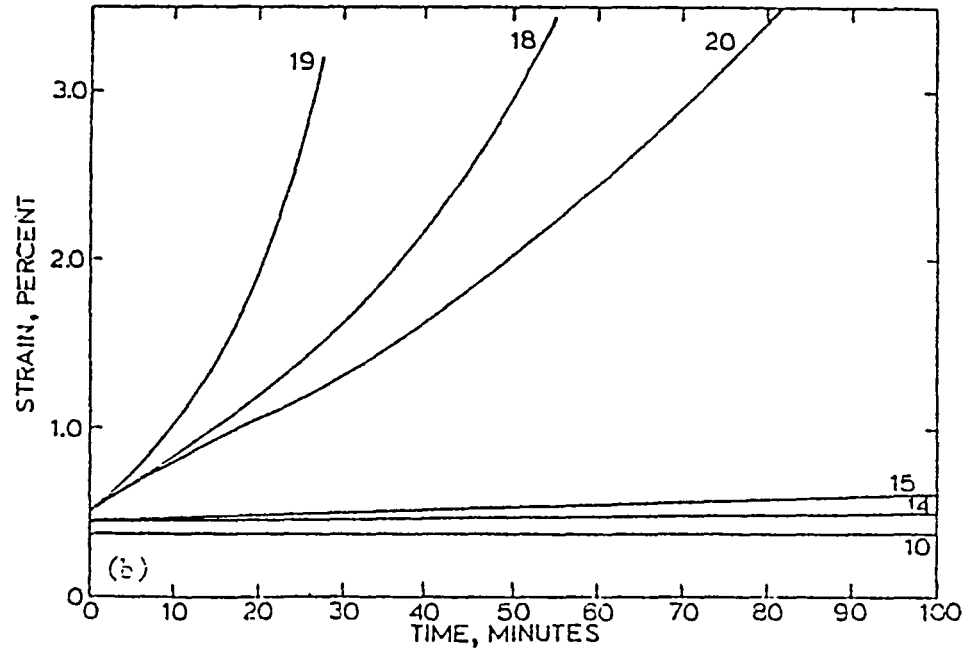

Figure 6. (a) Predicted tensile creep response of IN100 at 732°C for a Creep stress of 896 MPa and several different initial load rates.

(b) Observed tensile creep response of IN100 at 732°C for several different stress histories with random initial load rates.

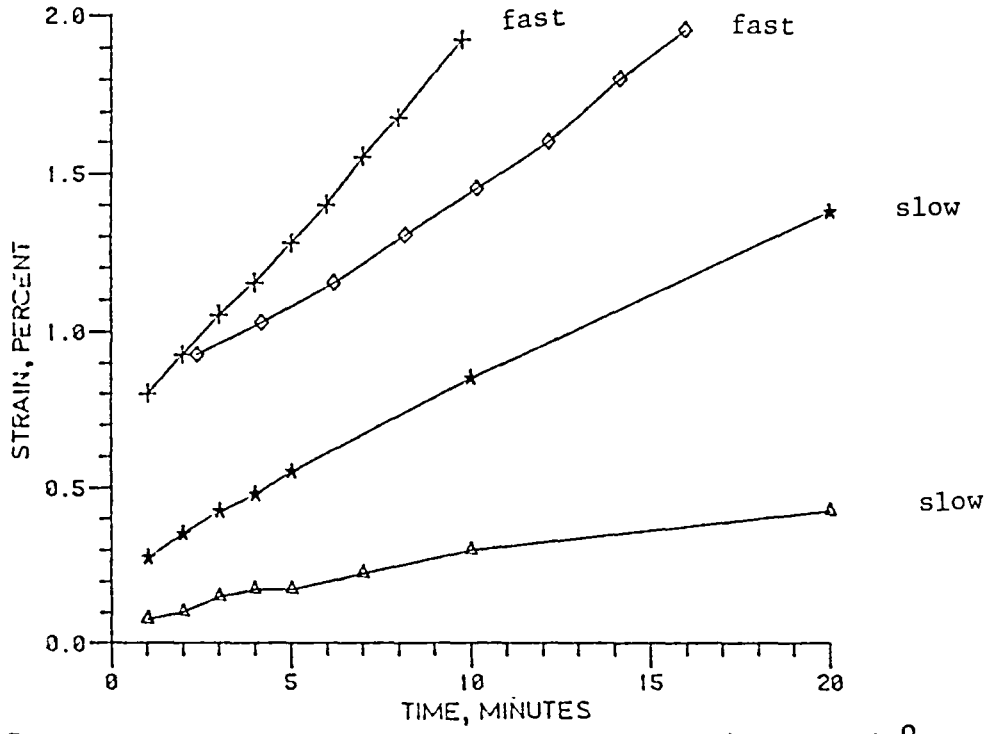

Figure 7. Observed tensile creep response of Rene' 95 at 649°C at 1034.3 MPa with "fast" and "slow" initial load rates.

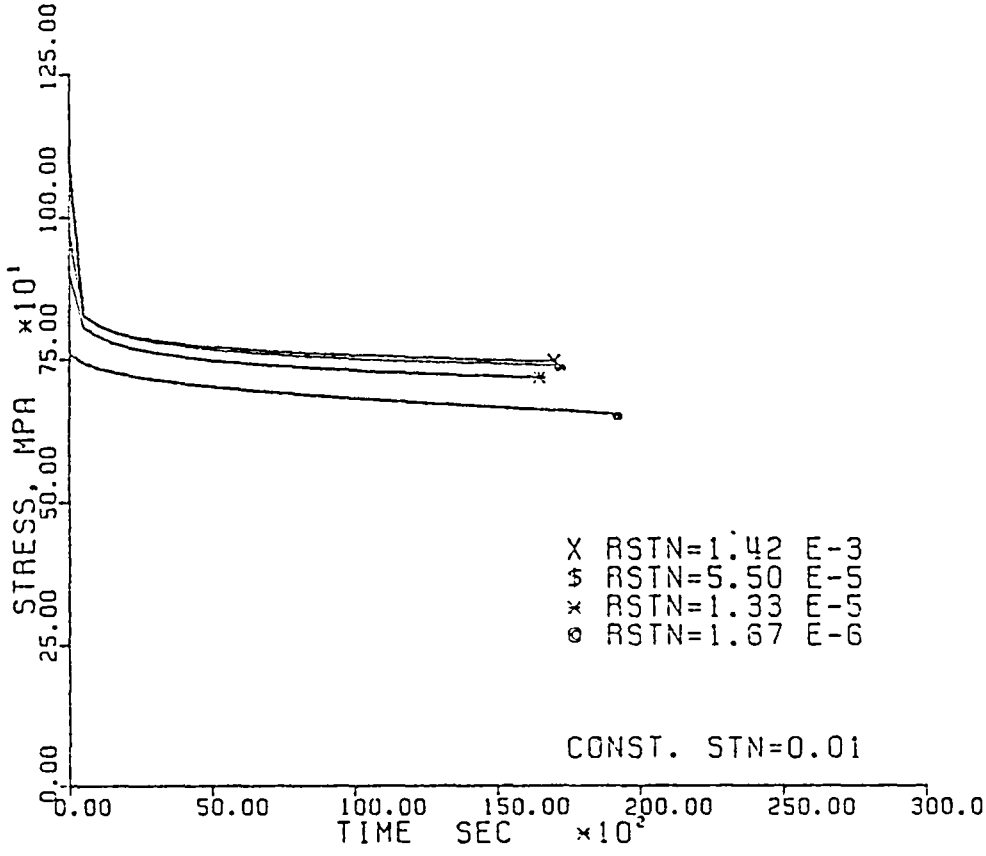

Figure 8. Predicted and observed stress relaxation responses of IN100 at 732°C at 0.01 strain with several initial load rates. Observed response at the same strain but with an unknown initial load history.

A UNIFIED CONSTITUTIVE RELATIONSHIP FOR THE TIME-DEPENDENT BEHAVIOR OF FAST BREEDER ALLOYS*

D. N. Robinson
Oak Ridge National Laboratory
Oak Ridge, Tennessee 37830

EXTENDED ABSTRACT

Constitutive equations based on classical concepts of creep and plasticity generally rest on the assumption that the inelastic strain can be decomposed into two distinct and additive contributions, one time-dependent (creep) and the other time-independent (plastic). Experimental data collected on structural alloys at high temperature (500 to 600°C), however, suggest that an improved approach is to adopt a unified representation in which creep and plasticity are characterized as occurring simultaneously and interactively and time is an essential ingredient throughout.

Examples of the inherent time dependency exhibited by some fast breeder alloys (particularly 2-1/4 Cr—1 Mo steel) at elevated temperature are rate-dependency under monotonic and cyclic straining, thermal recovery (Fig. 1), and strong creep-plasticity interaction. One manifestation of the latter is illustrated in Fig. 2 which shows the strong influence of the recent history of plastic straining on stress relaxation. Account of such behavior is important in structural problems related to the design of fast breeder components.

A creep-plasticity-recovery constitutive model has been under development at Oak Ridge National Laboratory (ORNL) in recent years[1,2,3] that allows for some of the more important nonclassical features observed in the behavior of fast breeder alloys. The ORNL model is based on the Bailey-Orowan theory of competing hardening and recovery mechanisms and incorporates some aspects of the work of several authors, e.g., Rice,[4] Ponter and Leckie,[5] and Lagneborg.[6] A notable distinction between this constitutive model and the related state-variable theories of Krieg[7] and Miller[8] lies in an accompanying set of inequalities that, in effect, delineate analytically different regions of the "state space." This approach in so structuring the state space follows the work of Onat[9]

*Research sponsored by the Office of Reactor Research and Technology, U.S. Department of Energy under contract W-7405-eng-26 with the Union Carbide Corporation.

and Larrson and Stöakers[10] and admits a representation of analytically discontinuous response such as that observed before and after reductions or reversals of stress and exemplified in Figs. 1 and 2.

Figures 3 through 6 provide a qualitative demonstration of the ability of the ORNL unified model to represent key features of high temperature uniaxial response. Figure 3 illustrates creep behavior (in arbitrary nondimensional units) under constant stress conditions, indicating saturation of the state variable α at steady state creep. Figure 4 shows the predicted response in an interrupted creep test and is characterized by the occurrence of state recovery with zero creep strain recovery (cf. Fig. 1). The state variable α is seen, in this case, to decrease during the period at zero stress. Figure 5 illustrates the capability of the model, coupled with linear elasticity, to represent rate-dependent plasticity. Shown are several monotonic stress strain curves corresponding to different strain rates. Finally, Fig. 6 demonstrates the ability of the unified equations to model the complex behavior depicted in Fig. 2. A saturated hysteresis loop predicted on the basis of the ORNL unified equations is shown in Fig. 6a, the numbers indicating points from which the stress is relaxed. The corresponding predictions of stress relaxation are given in Fig. 6b. Figure 6c depicts the limit cycle in state space corresponding to the saturated hysteresis loop of Fig. 6a and shows the trajectories followed by the state points during stress relaxation. The relaxation behavior is seen to be strongly dependent on the initial inelastic state even for points of equal starting stress.

References

1. D. N. Robinson et al., in "Specialists' Meeting on High-Temperature Structural Design Technology of LMFBRs, 1976," International Atomic Energy Agency, IWGFR/11, p. 44 (1976).

2. C. E. Pugh and D. N. Robinson, "Some Trends in Constitutive Equation Model Development for High-Temperature Behavior of Fast-Reactor Structural Alloys," *Journal of Nuclear Engineering and Design*, Vol. 48, pp. 269-76 (1978).

3. C. E. Pugh and D. N. Robinson, "Constitutive Equations for Meeting Elevated Temperature Design Needs," in *Pressure Vessel and Piping — Design Technology — Decade of Progress*, ASME, 1982.

4. J. R. Rice, "On the Structure of Stress-Strain Relations for Time-Dependent Plastic Deformations in Metals," *J. Appl. Mech., Trans. ASME*, 37, Series E, No. 3, pp. 728-37 (September 1970).

5. A. R. S. Ponter and F. A. Leckie, "Constitutive Relationships for the Time-Dependent Deformation of Metals," *J. Eng. Mater. Technol., Trans. ASME*, 98, pp. 47-51 (1976).

6. R. Lagneborg, "A Modified Recovery-Creep Model and Its Evaluation," *Met. Sci. J.*, 6, pp. 127-33 (1972).

7. R. D. Kreig, "Numerical Integration of Some New Unified Plasticity-Creep Formulations," *Transactions of the Fourth SMiRT Conference*, San Francisco, Vol. 4, Part M, Paper M 6/4 (August 1977).

8. A. K. Miller, "An Inelastic Constitutive Model for Monotonic, Cyclic and Creep Deformation," *Journal of Engineering Materials and Technology, Transactions of the ASME*, Vol. 98, pp. 97-113 (1976).

9. E. T. Onat, *Representation of Inelastic Behavior*, Yale University Report to Oak Ridge National Laboratory, ORNL/Sub-3863/2 (November 1976).

10. B. Larsson and B. Störakers, "A State Variable Interpretation of Some Rate-Dependent Inelastic Properties of Steel," *Journal of Engineering Materials and Technology, Transactions of the ASME*, Vol. 100, pp. 395-401 (October 1978).

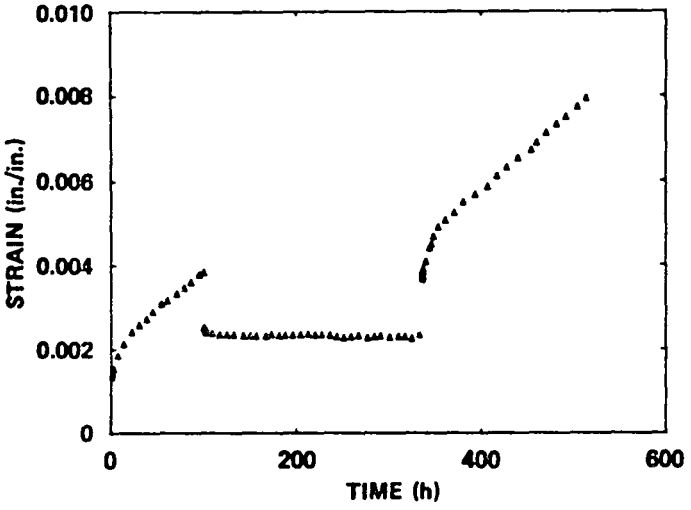

Fig. 1. Response of 2-1/4 Cr-1 Mo steel at 538°C in interrupted creep test. Stress alternates as 124 MPa, 0 MPa, 124 MPa.

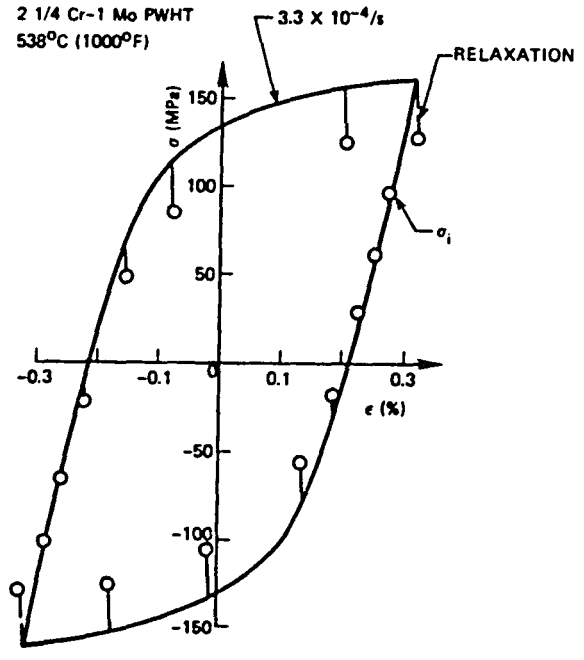

Fig. 2. Stress relaxation in one hour from various points around a saturated hysteresis loop.

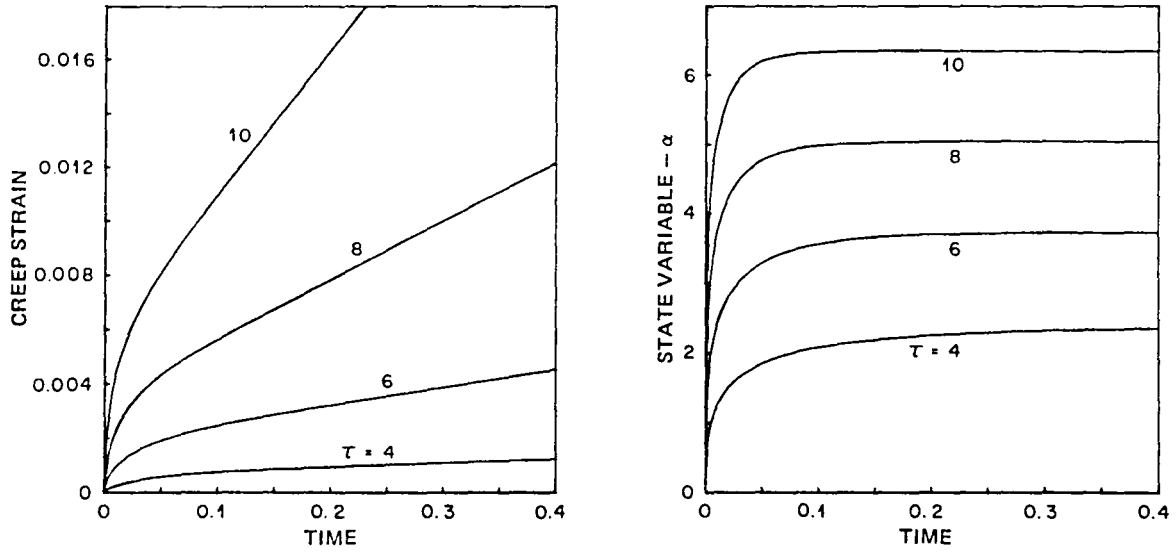

Fig. 3. Prediction of creep strain vs time and state variable α vs time under constant stress (τ = const.) conditions. Units are arbitrary and nondimensional.

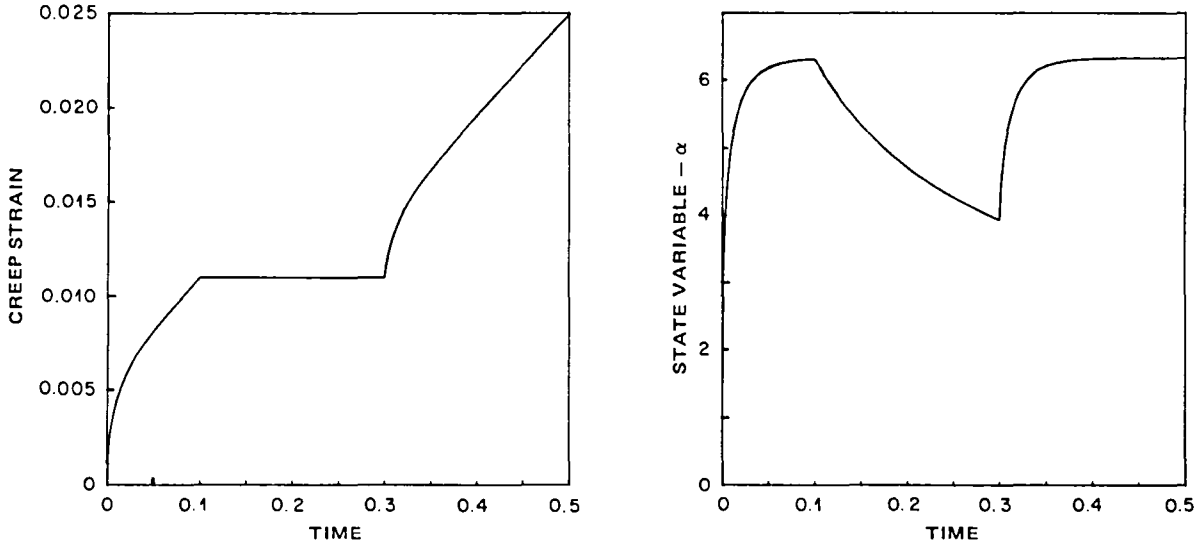

Fig. 4. Prediction of response in interrupted creep test. Creep strain vs time and state variable α vs time (cf. Fig. 1). Arbitrary, nondimensional units.

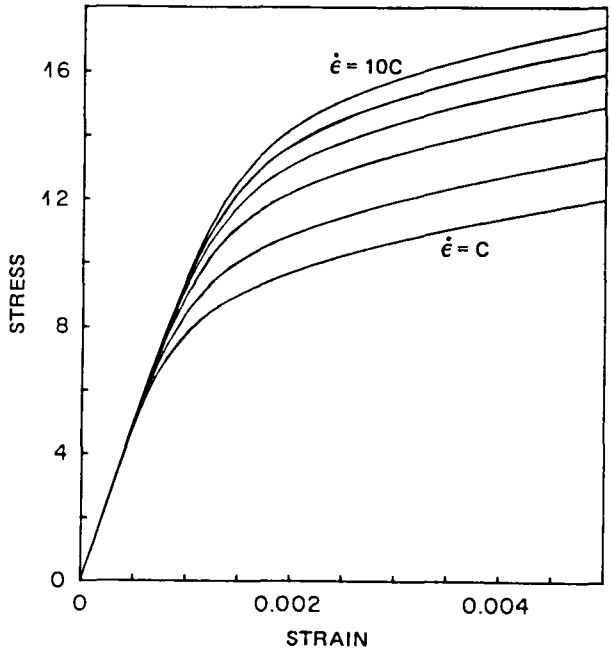

Fig. 5. Prediction illustrating rate sensitive plasticity. Stress vs strain under constant strain rate. Variation in strain rate is one decade. Arbitrary, nondimensional units.

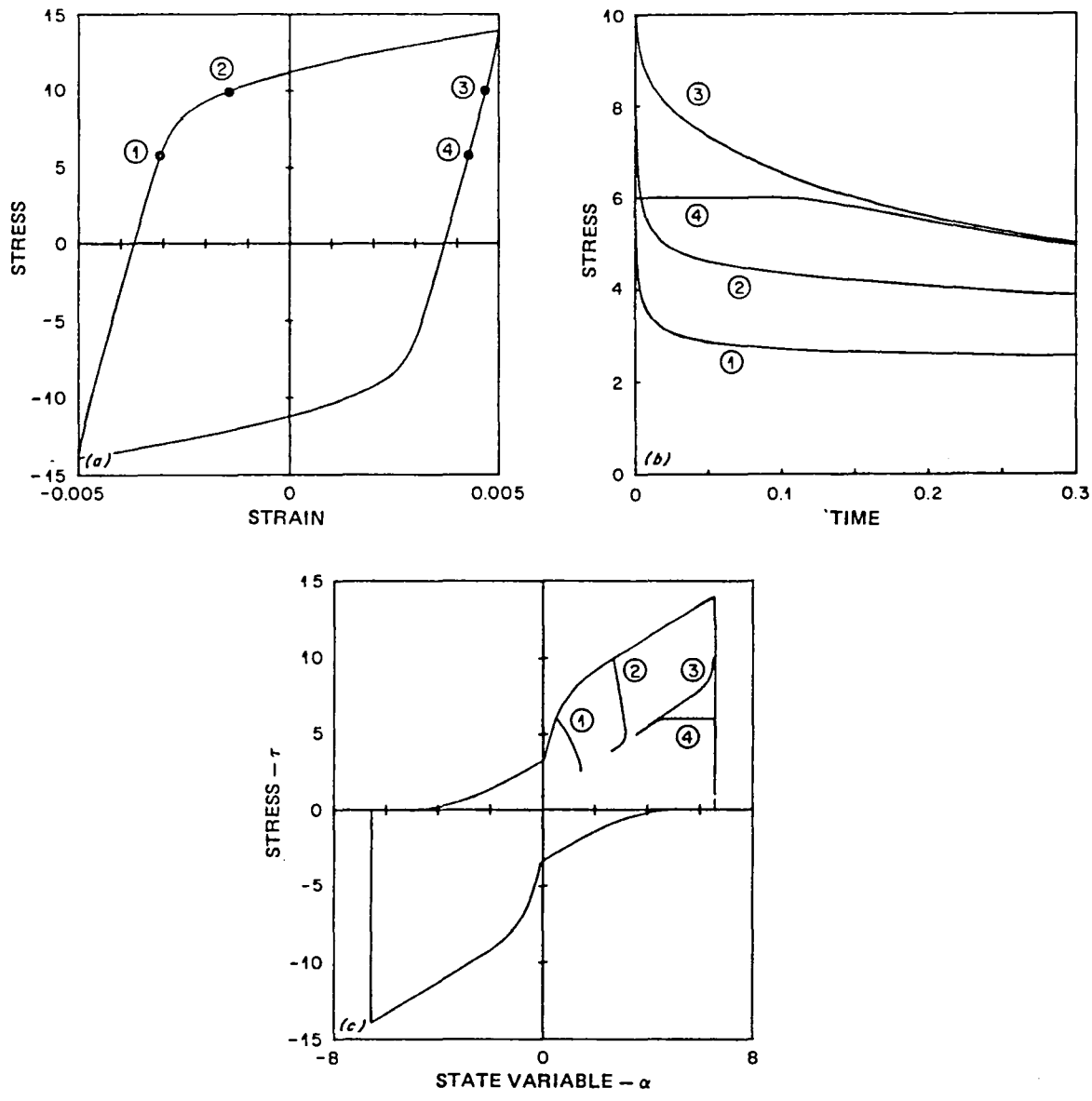

Fig. 6. (a) A saturated hysteresis loop at constant strain rate. Numbers indicate points from which stress is relaxed. (b) Stress relaxation curves corresponding to points in (a). (c) Saturated limit cycle in state space τ vs α showing trajectories followed during stress relaxation. Units are arbitrary and nondimensional.

APPLICATION OF AN UNCOUPLED ELASTIC-PLASTIC-CREEP CONSTITUTIVE MODEL TO METALS AT HIGH TEMPERATURE

Walter E. Haisler
Texas A&M University
College Station, Texas 77843

Abstract

A uniaxial, uncoupled constitutive model for predicting the response of thermal and rate dependent elastic-plastic material behavior is presented. The model is based on an incremental classical plasticity theory extended to account for thermal, creep, and transient temperature conditions. Revisions to the combined hardening rule of the theory allow for better representation of cyclic phenomenon including the high rate of strain hardening upon cyclic reyield and cyclic saturation. Also, an alternative approach is taken to model the rate dependent inelastic deformation which utilizes hysteresis loops and stress relaxation test data at various temperatures. Evaluation of the model is performed by comparison with experiments involving various thermal and mechanical load histories on 5086 aluminum alloy, 304 stainless steel and Hastelloy-X.

The uncoupled model assumes that there is a temperature below which the total strain consists essentially of elastic and rate independent inelastic strains only. Above this temperature, the rate dependent inelastic strain (creep) dominates. Experimentally, Bradley has shown for Hastelloy-X that such an uncoupling appears feasible.

The rate independent inelastic strain component is modelled in an incremental form with a yield function, flow rule and hardening law. However, the model is able to predict kinematic-isotropic hardening behavior, cyclic saturation, asymmetric stress-strain response upon stress reversal, and variable Bauschinger effect. The rate dependent inelastic strain component is modelled using a rate equation in terms of back stress, drag stress and exponent n as functions of temperature and strain. A sequence of hysteresis loops and relaxation tests are utilized to define the rate dependent inelastic strain rate (see Bradley).

Numerical testing of the constitutive model against experiment has thus far centered primarily at the low temperature range where the rate dependent component is negligible. Figure 1 presents results for 5086 Aluminum subjected to a cyclic thermomechanical loading. Numerical results are in excellent agreement with experiment. Figure 2 shows the cyclic response of 304 stainless to strain-controlled cycling at 1000°F. The model uses a variable hardening ratio and accounts for the asymmetry in tension-compression response exhibited by the experimental data. Figures 3 and 4 show the room temperature experimental and model results, respectively, for Hastelloy-X during strain-controlled cycling at several strain rates. Cyclic saturation is modelled reasonably well as shown in Figure 4. Numerical comparison of model predictions and experiment at elevated temperature where rate dependent inelastic strain is significant are currently being obtained.

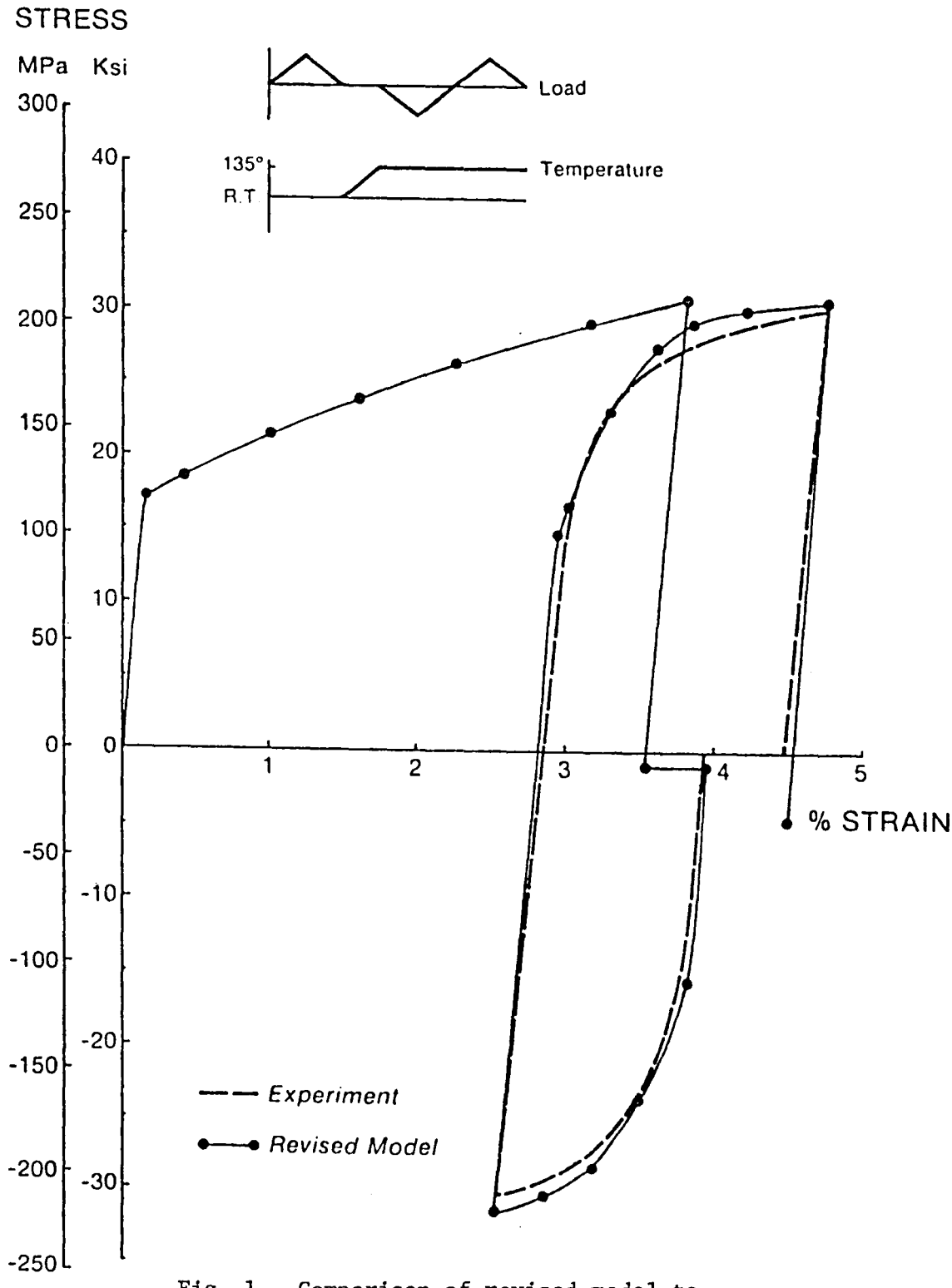

Fig. 1 Comparison of revised model to experiment for aluminum cyclic load test

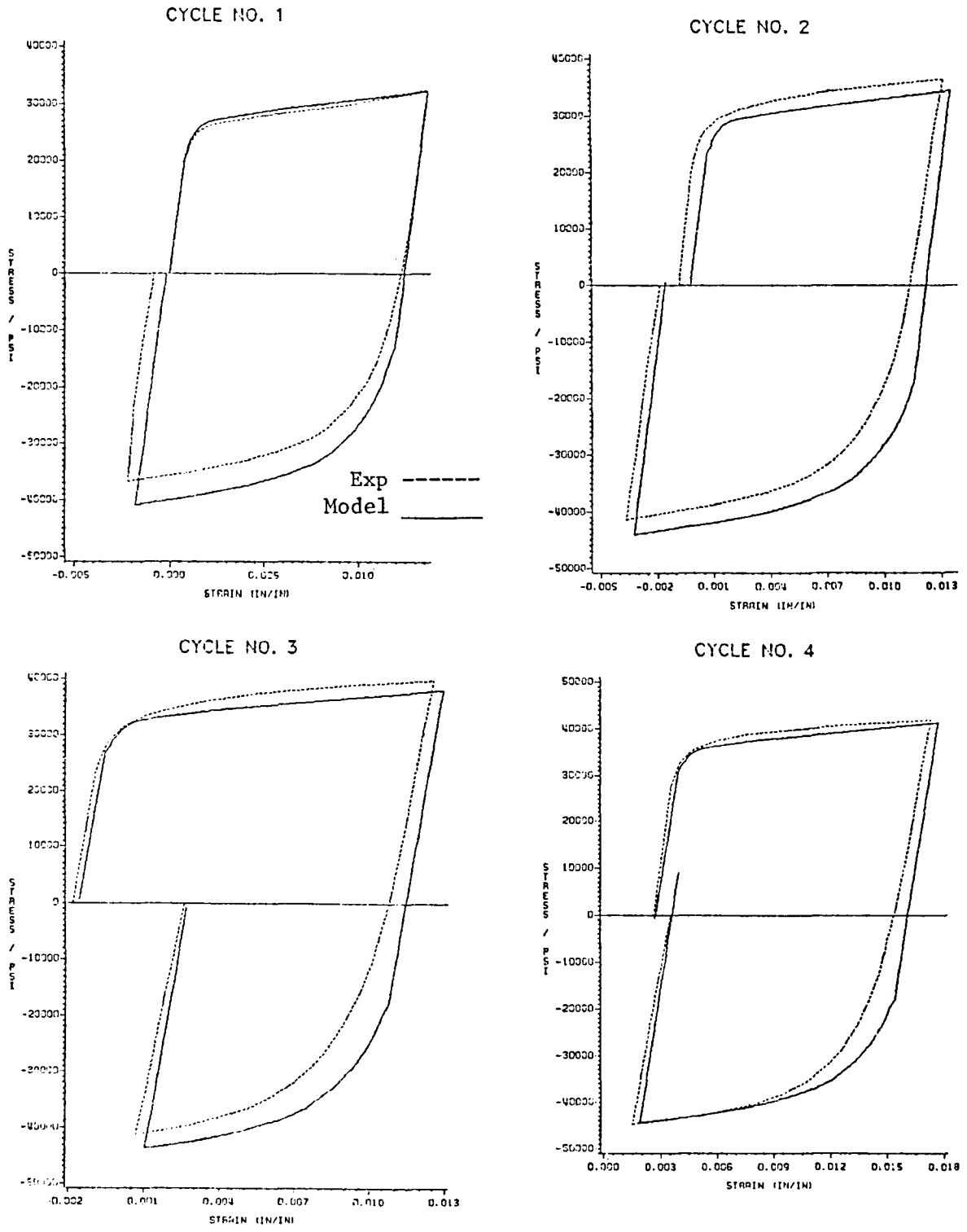

Fig. 2 Comparison of model and experiment for 304 stainless steel at 1000°F using first cycle data as input. A hardening ratio of 0.2 in tension and 0.35 in compression was used

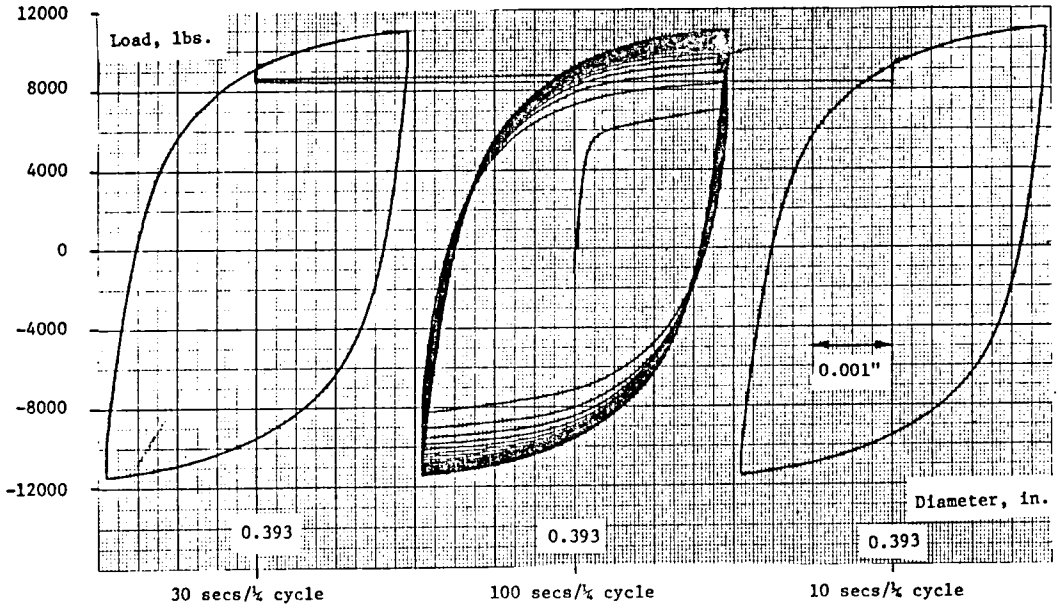

Fig. 3 Experimental hysteresis loops for hastelloy-X at room temperature

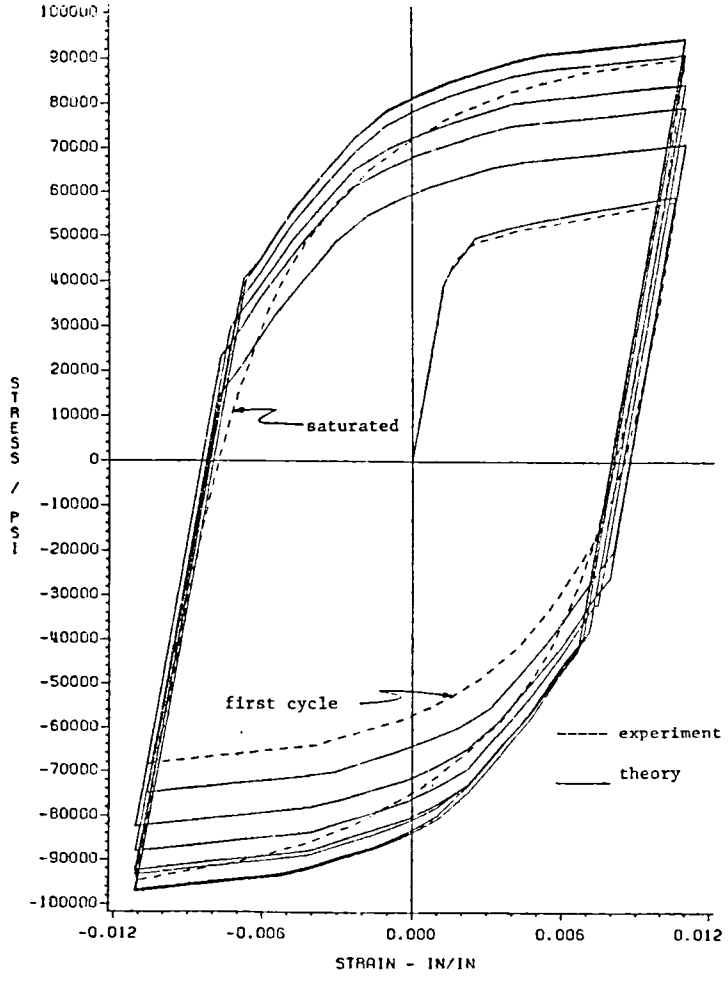

Fig. 4 Cyclic saturation of hastelloy-X at room temperature

SOME RECENT DEVELOPMENTS IN THE ENDOCHRONIC THEORY WITH APPLICATION TO CYCLIC HISTORIES

K. C. Valanis and C. F. Lee

University of Cincinnati
Cincinnati, Ohio 45221

ABSTRACT

Constitutive equations with only two easily determined material constants can predict with computational ease the stress (strain) response of normalized mild steel to a variety of general strain (stress) histories, without a need for special unloading-reloading rules that are otherwise so evident in the literature.

These equations are derived from the endochronic theory of plasticity of isotropic materials with an intrinsic time scale defined in the plastic strain space. Agreement between theoretical predictions and experiments are excellent quantitatively in cases of various uniaxial constant strain amplitude histories, variable uniaxial strain amplitude histories and cyclic relaxation. The cyclic ratcheting phenomenon is also predicted by the present theory, in routine fashion.

INTRODUCTION

In recent years, cyclic plasticity, which deals with the rate-independent inelastic response of materials to cyclic stress or strain histories, has become an important subject of research in applied mechanics and engineering design. Past experimental work, theoretical studies and engineering analysis are well documented in the literature. For details see, typically, References /1-16/.

On the basis of existing experimental results, one concludes that generally, when subjected to symmetric stress or strain cycles, annealed or soft materials will harden and will tend to a stable response, while cold-worked or hard materials will soften. When a stable response is reached, hysteresis loops in the stress-strain space become stable, closed and symmetric. Also stable loops at various strain (or stress) amplitudes are similar in shape. This has led to the definition of a cyclic stress-strain curve which is the locus of the tips of stable hysteresis loops. It is found that some metals, e.g. 7075-T6 aluminum, follow the Masing rule. However, some metals, e.g. normalized mild steel, do not follow this rule at all /8/.

In the presence of a history of unsymmetric stress cycles, the material response involves a progressive increase of plastic (or total) strain in the

direction of mean stress. This is called cyclic "creep" or "ratcheting". On the other hand, a history of unsymmetric strain cycles, will result in "cyclic stress relaxation" toward zero mean stress. Both phenomena occur whether the material response is stable or not.

Under variable amplitude cycling, metals have a strong memory of their most recent point of reversal.

If the number of cycles is large enough, then effects of prior plastic history tend to disappear. More precisely a material has a "fading" memory, in terms of the intrinsic time scale ζ, of the history of plastic deformation that preceded the cyclic history $\underline{\bar{7}}$, as the latter progresses.

Attempts to describe the above phenomena analytically in terms of constitutive laws have been tried. However, so far, an elegant, simple but realistic constitutive law is still not at hand.

In this paper, we use a recent model of endochronic theory in the study of cyclic plasticity of stable materials. This model, proposed by Valanis [13], has been applied to metals by authors [14]. In the case of normalized mild steel, it is shown that the constitutive equations derived from the theory can predict quantitatively stable hysteresis loops pertaining to various strain amplitudes. The broader capability of the theory is critically tested by demonstrated agreement with the observed cyclic response of normalized mild steel to variable uniaxial strain amplitude histories. In the final section we show that cyclic ratcheting and cyclic relaxation are phenomena which are readily predicted by the present theory.

1. A BRIEF REVIEW OF THE ENDOCHRONIC THEORY

In the late 1960's, the formulation of constitutive theories of visco-elastic materials from concepts of irreversible thermodynamics and internal state variables reached an advanced level of development. It was natural to inquire if a similar approach could be used to establish a theory of plasticity, and the attempt by Valanis to explore this question led to the development of the endochronic theory in 1971 [15].

In its early stages of development, the theory rested on the notion that the stress response of dissipative materials is a function of the deformation (strain) path. When the material behavior considered is rate-independent, the path in question must also be rate independent. The early version of the endochronic theory was constructed in terms of a path in the strain space ε_{ij}. In this space, every point represents a deformation (strain) state. A sequence of strain states traces a path in this space (Figure 1). The distance along the path between the two strain states P and P' is denoted by $d\zeta$. If P, a fourth order positive definite tensor, is the metric of the space, then

$$d\zeta^2 = P_{ijkl}\, d\varepsilon_{ij}\, d\varepsilon_{kl} \tag{1.1}$$

The tensor $\underset{\approx}{P}$ is a material property in the sense that in general it will vary from material to material. Since successive strain states on a strain path are distinct and $d\zeta$ is always positive, the latter can serve as a time measure which is a property of the material at hand, since $\underset{\approx}{P}$ is such. The length of the path ζ is then an intrinsic time scale where "time" is used here in a very general sense. The stress at point P is not determined simply by the strain

at P, but by the history of the strain along the path OP. Materials for which the stress is a function of the history of strain with respect to an intrinsic time scale, have been called "endochronic" by the first author and the theory of the mechanical response of such materials is called "endochronic theory".

In the applications, it was found that it is appropriate to define an intrinsic time scale z which is related to the intrinsic time measure ζ, by the relation:

$$dz = \frac{d\zeta}{f} \tag{1.2}$$

where f is a function of the history of strain. The function f, generally considered to be a function of ζ, is of thermodynamic origin and is related proportionally to the degree of internal friction in a material. If a material hardens, $f(\zeta)$ increases with ζ; if it softens, f decreases with ζ and is constant otherwise.

The power of the thermodynamic development that follows lies in the fact that it does not depend on an explicit definition of z. Thus one can envision a thermodynamic framework, applicable to a large class of materials, from which an explicit constitutive equation, pertaining to a sub-class, can be obtained by simply choosing the appropriate form of z.

The intrinsic time defined by equation (1.2) leads to a so-called simple endochronic theory. In the case of linear isotropic theory the constitutive equations so derived can be decomposed into deviatoric and hydrostatic parts. The deviatoric stress $\underset{\sim}{s}$ is related to the history of the deviatoric strain $\underset{\sim}{e}$ by the linear functional relation:

$$\underset{\sim}{s} = 2 \int_0^z \mu(z - z') \frac{\partial \underset{\sim}{e}}{\partial z'} \, dz' \tag{1.3}$$

where in the reference configuration, $\underset{\sim}{s}$ is zero, $z = 0$, and the shear modulus, $\mu(z)$, is given by a Dirichlet series, i.e.,

$$\mu(z) = \lambda_\infty + \sum_{r=1}^{n} \lambda_r e^{-\beta_r z} \tag{1.4}$$

where λ_∞, λ_r and β_r are positive constants. The hydrostatic stress, σ_H, is related to the history of volumetric strain, θ, in a similar fashion by the linear functional relation:

$$\sigma_H = \int_0^z K(z - z') \frac{\partial \theta}{\partial z'} \, dz' \tag{1.5}$$

where $\sigma_H = \sigma_{kk}/3$ and $\theta = \varepsilon_{kk}$, in the usual notation where the summation convention is employed. The bulk modulus, $K(z)$, is given by a Dirichlet series of the form of equation (1.4). Note again that $\sigma_H = 0$ in the reference configuration.

For further details of the derivation of equations above see [15], where it is shown that both $\mu(z)$ and $K(z)$ are composed of finite sums of positive exponentially decaying terms. In particular, $\mu(0)$ and $K(0)$ are the shear and bulk elastic moduli, respectively.

The simple endochronic theory has been applied with success to a number of problems of practical interest [7,15,16].

Despite this fact, it failed to predict closed hysteresis loops for "small" unloading-reloading processes in one-dimensional conditions. For

such deformation histories, the theory predicted a slope at the reloading point that was smaller than the unloading slope at the same point. This feature of the theory is at odds with the observed behavior of most metals.

It was shown that the openness of the hysteresis loops is thermodynamic in nature and has to do with the fact that the intrinsic time rate of dissipation at the onset of unloading is equal to the intrinsic time rate of dissipation upon continuation of loading. However, from experience, most rate-insensitive materials initially unload in an elastic manner and, therefore, with essentially zero rate of dissipation. In view of this, the discrepancy between prediction and observation was bound to arise /17/.

It was subsequently demonstrated, however, that if the measure of intrinsic time is redefined in terms of the increment of plastic strain, the rate of dissipation at the onset of unloading and reloading is, in fact, zero. Therefore, it was appropriate to adopt the plastic strain increment as the measure of intrinsic time. Moreover, the constitutive equations (1.3) and (1.5) are recast in a form whereby the stress is related to the history of plastic strain. This was done by the first author recently /17/. This model was used to prove mathematically the existence of yield surface and that the kinematic hardening rule is a consequence of the theory. Of greater theoretical and practical consequence, however, is the fact that new measure of intrinsic time makes feasible the complete elimination of the yield surface by shrinking its size to zero and thereby reducing the surface to a point. This is done by introducing weakly singular kernel functions in the linear functional representation of stresses in terms of history of plastic strain by allowing the kernel functions to possess an integrable singularity at the origin (i.e. $z = 0$). On the basis of the above considerations, endochronic constitutive equations of

isotropic materials, which exhibit yielding immediately upon application of loading, are as follows

$$\underset{\sim}{s} = 2\int_0^{z_D} \rho\,(z_D - z_D')\,\frac{\partial \underset{\sim}{e}^p}{\partial z_D'}\,dz_D', \quad \rho\,(0) = \infty \tag{1.6}$$

$$\sigma_{kk} = 3\int_0^{z_H} \kappa\,(z_H - z_H')\,\frac{\partial \epsilon_{kk}^p}{\partial z_H'}\,dz_H', \quad \kappa\,(0) = \infty \tag{1.7}$$

and

$$\int_0^{z_H} \kappa\,(z_H')dz'_H < \infty\ ; \quad \int_0^{z_D} \rho\,(z_D')dz'_D < \infty\ , \text{ for all finite } z_H \text{ and } z_D,$$

where D and H denote the deviatoric and hydrostatic state, respectively. Also

$$d\underset{\sim}{e}^p = d\underset{\sim}{e} - \frac{d\underset{\sim}{s}}{2\mu_1} \tag{1.8}$$

$$d\epsilon_{kk}^p = d\epsilon_{kk} - \frac{d\sigma_{kk}}{3K_1} \tag{1.9}$$

where μ_1 and K_1 are the appropriate elastic moduli. The intrinsic time scale increments dz_H and dz_D are related to the intrinsic time measures by the equations:

$$dz_D = d\zeta_D / f_D(\zeta_D) \tag{1.10}$$

$$dz_H = d\zeta_H / f_H(\zeta_H) \tag{1.11}$$

where

$$d\zeta_D = |de^p_{ij}\ de^p_{ij}|^{\frac{1}{2}} \tag{1.12}$$

$$d\zeta_H = |d\varepsilon^p_{kk}| \tag{1.13}$$

Here $|\cdot|$ denotes the absolute value. Other more general definitions are possible, see reference /13/. The kernels ρ and κ are given by the series

$$\rho(z_D) = \sum_{r=1}^{\infty} \rho_r\, e^{-\alpha_r z_D} \tag{1.14}$$

$$\kappa(z_H) = \sum_{r=1}^{\infty} \kappa_r\, e^{-\omega_r z_H} \tag{1.15}$$

which must be convergent for all values of $z > 0$, but should diverge at $z = 0$. The above equations summarize the new model of the isotropic endochronic theory.

In conclusion, two significant results are accomplished: (1) The slope of the deviatoric (or hydrostatic) stress-strain curve at points of unloading and reloading or strain rate reversal is always elastic, i.e., equal to the slope at the origin of the appropriate stress-strain curve. (2) The hysteresis loops in the first quadrant of the stress-strain space are always closed. For details see reference /13/.

Constitutive Relations in Tension-Torsion

The constitutive equations that apply in this specific case are found from equations (1.6) and (1.7) and are given below.

$$\tau = 2\int_0^{z_D} \rho(z_D - z_D')\,\frac{\partial \eta^p}{\partial z_D'}\,dz'_D \tag{1.16}$$

$$\sigma_1 = 2\int_0^{z_D} \kappa(z_D - z_D')\,\frac{\partial}{\partial z_D'}\,(\varepsilon_1^p - \varepsilon_2^p)\,dz'_D \tag{1.17}$$

$$\sigma_1 = 3\int_0^{z_D} \kappa(z_H - z_H')\,\frac{\partial}{\partial z_H'}\,(\varepsilon_1^p + 2\varepsilon_2^p)\,dz'_H \tag{1.18}$$

where ε_i^p and σ_i are the axial plastic strains and stresses, respectively, along the axes x_i and $\varepsilon_2^p = \varepsilon_3^p$ to satisfy the condition of isotropy. Also τ and η^p stand for s_{12} and e_{12}^p, respectively, in the notation of equation (1.6).

Because in the experiments to be investigated the hydrostatic strain was not measured we shall proceed to make the usual (approximate) assumption of elastic hydrostatic response, in which case equation (1.7) does not apply, but instead the plastic incompressibility condition

$$\varepsilon_1^p + 2\varepsilon_2^p = 0 \tag{1.19}$$

is used. In the following, we will omit the subscripts D and H.

In light of the above hypotheses and in view of equations (1.16) and (1.19) the appropriate constitutive equations in tension-torsion are the following:

$$\tau = 2\int_0^{z} \rho(z - z')\,\frac{\partial \eta^p}{\partial z'}\,dz' \tag{1.20a}$$

$$\sigma_1 = \int_0^z E(z - z') \frac{\partial \varepsilon_1^p}{\partial z'} dz' \tag{1.20b}$$

$$\varepsilon_1 + 2\varepsilon_2 = \frac{\sigma_1}{3K_1} \tag{1.20c}$$

where

$$E(z) = 3\,\rho(z) \tag{1.21}$$

$$dz = dz_D = \frac{d\zeta}{f(\zeta)} \tag{1.22}$$

$$d\zeta = d\zeta_D = \left|\left[\frac{2}{3} (d\varepsilon_1^p - d\varepsilon_2^p)^2 + 2(d\eta^p)^2 \right]^{\frac{1}{2}}\right| \tag{1.23a}$$

Alternatively, $d\zeta$ can be expressed in terms of the engineering shear strain $\gamma^p = 2\eta^p$, in which case, upon using equation (1.19),

$$d\zeta = \left|\left[\frac{3}{2} (d\varepsilon^p)^2 + \frac{1}{2} (d\gamma^p)^2 \right]^{\frac{1}{2}}\right| \tag{1.23b}$$

Here $\varepsilon^p = \varepsilon_1^p$.

In the applications that follow we will use the above equations in the study of cyclic response to a variety of test conditions.

2. APPLICATIONS TO STEADY CYCLIC RESPONSE

In subsequent applications, it is expedient to rescale $d\zeta$ by a constant $\sqrt{2}$ so that

$$d\zeta = \left|\left[3(d\varepsilon^p)^2 + (d\gamma^p)^2\right]^{\frac{1}{2}}\right| \tag{2.1}$$

The values of $\rho(z)$ and $E(z)$ are rescaled by the same constant.

Cyclic Shear Response

It follows from equation (2.1) that in pure shear

$$d\zeta = |d\gamma^p| \tag{2.2a}$$

In addition, if the cyclic response is steady, then $f(\zeta)$ is a constant, which we set equal to 1. Thus equation (1.22) becomes

$$dz = |d\gamma^p| \tag{2.2b}$$

In reference /13/, we let $\rho(z)$ be a function of the form

$$\rho(z) = \rho_o\, z^{-\alpha} \tag{2.3}$$

where ρ_o and α are material constants and $0 < \alpha < 1$. This type of kernel satisfies the constraint imposed by equation (1.6) and leads to the Ramberg-Osgood equation for the tensile response. In view of these remarks, we use equation (2.3) for the present study.

Upon substitution of equation (2.3) in equation (1.20a), the shear stress is expressed as a function of the history of plastic strain as follows:

$$\tau = \int_0^z \frac{\rho_o}{(z - z')^{\alpha}} \frac{d\gamma^p}{dz'} dz' \tag{2.4}$$

At the completion of n reversals and by virtue of equations (2.2a, b) and (2.4), the following relation applies,

$$\tau = \sum_{i=1}^{n} \int_{z_{i-1}}^{z_i} (-1)^{i-1} \frac{\rho_o}{(z - z')^{\alpha}} dz' + (-1)^n \int_{z_n}^{z} \frac{\rho_o}{(z - z')^{\alpha}} dz' \tag{2.5a}$$

where z_i denotes the value of z at the point where the ith reversal has been completed and $z_o \stackrel{def}{=} 0$. By simple analysis, the above equation leads to the result

$$\tau = \frac{\rho_o}{1-\alpha} \left[z^{1-\alpha} + 2 \sum_{i=1}^{n} (-1)^i (z - z_i)^{1-\alpha} \right] \tag{2.5b}$$

Equation (2.5b) is suitable for the prediction of the stress response, once the functional relationship between z and the (plastic) shear strain history is known.

Cyclic Uniaxial Response --

In this case, we use equations (2.1) and (2.2a, b) to obtain the essential relation.

$$dz = d\zeta = \sqrt{3} \left| d\varepsilon^p \right| \tag{2.6}$$

In the fashion outlined above, the steady cyclic uniaxial response is found from equations (1.20b), (1.21), (2.3) and (2.6) and is given by the relations,

$$\sigma = \frac{\sqrt{3}\,\rho_o}{1-\alpha}\left[z^{1-\alpha} + 2\sum_{i=1}^{n}(-1)^i\,(z - z_i)^{1-\alpha}\right] \tag{2.7}$$

If, instead of using equation (2.6), we use

$$dz = \left|d\varepsilon^p\right| \tag{2.8}$$

then equation (2.7) becomes

$$\sigma = \frac{3\rho_o}{1-\alpha}\,\frac{1}{3^{\alpha/2}}\left[z^{1-\alpha} + 2\sum_{i=1}^{n}(-1)^i\,(z - z_i)^{1-\alpha}\right] \tag{2.9}$$

The scaling of the intrinsic time by a constant is a matter of convenience and may be done at will, without interference with the theory. We observe that equations (2.5b) and (2.9) obey the linear homogeneous transformation between indicated stresses and strains given below:

$$\tau = \sigma/\sqrt{3}\ ,\ \gamma^p = \sqrt{3}\,\varepsilon^p \tag{2.10a,b}$$

To test the validity of the theory, we appeal to the experimental results on normalized mild steel obtained by Jhansal and Topper [6].

Constant Uniaxial Strain Amplitude --

We consider the class of metals whose asymptotic stress response to sustained cyclic strain excitation at constant strain amplitude is a periodic

stress history with constant amplitude. Specifically in a uniaxial test of this type, the axial stress amplitude $\Delta\sigma$ is constant and therefore the axial plastic strain amplitude $\Delta\varepsilon^p$ is also constant, following equation (1.8). Thus

$$\Delta\varepsilon^p = \Delta\varepsilon - \frac{\Delta\sigma}{E_1} \tag{2.11}$$

where $\Delta\varepsilon$ is the axial strain amplitude and E_1 is Young's modulus. As a result, the value of z during cyclic tension and compression can be found by integrating equation (2.8). After an odd number n of reversals has been completed, the value of $z - z_n$ can be calculated by integrating the relation $dz = -d\varepsilon^p$ with $\Delta\varepsilon^p$ as the lower limit of integration. If n is even, then the relation $dz = d\varepsilon^p$ applies with $-\Delta\varepsilon^p$ as the lower limit of integration. The results are as follows:

$$z = 2n\Delta\varepsilon^p \mp \varepsilon^p \tag{2.12a}$$

and

$$z_n = (2n - 1)\ \Delta\varepsilon^p \tag{2.12b}$$

where in equation (2.12a) "-" is used for n = odd and "+" for n = even. Equation (2.12b) applies to both cases.

Upon substitution of equations (2.12a, b) in equation (2.9), one obtains the result

$$\sigma(\varepsilon^p) = \frac{3\rho_o}{1-\alpha} \frac{1}{3^{\alpha/2}} (\Delta\varepsilon^p)^{1-\alpha} F_n(\alpha,x) \tag{2.13}$$

$$x = \varepsilon^p / \Delta\varepsilon^p \tag{2.14a}$$

$$F_n(\alpha,x) = (2n \pm x)^{1-\alpha} + 2 \sum_{i=1}^{n} (-1)^i (2n - 2i + 1 \pm x)^{1-\alpha} \tag{2.14b}$$

where the "+" and "-" signs correspond to n even and n odd, respectively. The algebraic value of the peak stress (i.e., stress amplitude) is found from equation (2.14b) by choosing n odd and setting x = 1 in equation (2.14b), i.e.,

$$F_n(\alpha) = (2n - 1)^{1-\alpha} + 2 \sum_{i=1}^{n} (-1)^i (2n - 2i)^{1-\alpha} \tag{2.14c}$$

where n = 1, 3, 5, · · ·. The peak stress at n = even is given by the same equation, i.e., equation (2.14c). Thus equation (2.14c) is applicable for all n. It can be shown that, in the limit of $n \to \infty$, F_n converges to a constant $F_\infty(\alpha)$, where F_∞ varies with α but is essentially close to unity. For instance, for α = 0.864, F_∞ is equal to 1.03 /14/. Thus the asymptotic value of Δσ as n tends to infinity is given by the equation

$$\Delta\sigma = \frac{3\rho_o}{1-\alpha} \frac{1}{3^{\alpha/2}} (\Delta\varepsilon^p)^{1-\alpha} F_\infty(\alpha) \tag{2.15}$$

This is the equation of the cyclic stress-(plastic) strain curve.

Cyclic steady response in shear can be found in a similar fashion or by using equations (2.10a, b).

To test the validity of the theory, we use experimental data on normalized mild steel [6]. In reference [6], a set of stable uniaxial hysteresis loops corresponding to various constant strain amplitudes was presented in the stress-strain space. A propos of the ensuing theoretical predictions we note that the geometric shape of the loops is given by equation (2.13), whereas the peak stresses are given by equation (2.15). We also note that there are only two undetermined parameters in these equations, α and ρ_o. The form of equation (2.15) was corroborated in reference [14] where a semi-logarithmic plot of the experimental values of $\Delta\sigma$ vs $\Delta\varepsilon^p$ gave rise to a linear relation. The plot also determines α and ρ_o which were found to be 0.864 (a pure number) and 48.4 MPa (7.02 ksi), respectively. These values are then used in equation (2.13), and the shape of the hysteresis loops is thereby calculated. Agreement between theory and experiment is excellent as shown in Figure 2.

We wish to devote a few lines to these powerful results. The reader will note that two constants are sufficient to define the cyclic stress- (plastic) strain response as well as the hysteretic behavior of normalized mild steel. It is also pertinent to mention that the analytical expressions involved (equations (2.13) and (2.15)) are not empirical formulae but closed forms derived from a general constitutive equation pertaining to three-dimensional histories. Also of importance is that the prediction of unloading and reloading behavior did not necessitate special rules or special treatment but was dealt with routinely, as part of the total experimental history of interest. Specifically, the celebrated Bauschinger effect is predicted quantitatively and correctly from one and the same constitutive equation.

We make in passing, an observation of historical interest. Equation (2.15) agrees with the empirical relationship proposed by Landgraff et al. [2]

for steels, i.e.,

$$\Delta\sigma \sim (\Delta\varepsilon^p)^{1-\alpha}$$

where $1-\alpha$ ranges from 0.12 to 0.17. In our case, $1-\alpha = .136$.

Variable Uniaxial Strain Amplitudes --

To extend the experimentally verified domain of validity of the theory and to broaden our view of its capabilities, we test it under conditions of variable uniaxial strain amplitude histories. The stress response to such histories is found by using equations (2.13) and (2.14b). The analytical results are compared with the experimental data on normalized mild steel [6]. The experiment consists of a constant uniaxial strain amplitude cyclic test (until stable hysteresis loops are reached) followed by a variable uniaxial strain amplitude test. The experimental data are shown in Figure 3. Despite the complexity of the history, agreement between theory and experiment is obtained and shown in Figure 3. Again the theory predicts the stress history routinely without the use of special rules present in other theories [3,5,6,10, 14]. At this point, we may reasonably conclude that the theory as expressed by equation (2.5b) (or equation (2.9)) is suitable for the prediction of the stress response to cyclic straining, in the case of normalized mild steel.

Cyclic Relaxation --

Here we address the case where the plastic shear strain is increased monotonically to a value γ_+^p, and is followed by a cyclic shear strain history with amplitude $\Delta\gamma^p$ about a mean value γ_o^p.

To calculate the stress response we use equation (2.5b). The cyclic shear strain history is shown in Figure 4. With reference to Figure 4, to make the following definitions

$$\gamma_+^p = \gamma_o^p + \Delta\gamma^p \tag{2.16a}$$

$$\gamma_-^p = \gamma_o^p - \Delta\gamma^p \tag{2.16b}$$

The value z_i of z at ith reversal, is found from equation (2.2b). Thus

$$z_i = \gamma_o^p + (2i - 1)\Delta\gamma^p \ , \quad i = 1, 2, \ldots n. \tag{2.17}$$

After n reversals have been completed, the value of z at the current shear strain γ^p is

$$z = 2n\ \Delta\gamma^p + \gamma_o^p \mp \bar{\gamma}^p \tag{2.18}$$

where

$$\bar{\gamma}^p = \gamma^p - \gamma_o^p \tag{2.19}$$

and the minus and plus signs correspond to n odd and even respectively. The shear response, after n reversals is found upon using equations (2.5b), (2.17) and (2.18). Specifically,

$$\tau = \frac{\rho_o}{1-\alpha} (\Delta\gamma^p)^{1-\alpha} F_n(\alpha, x_o, x) \tag{2.20}$$

where

$$F_n(\alpha, x_o, x) = (2n + x_o \mp x)^{1-\alpha} + 2 \sum_{i=1}^{n} (-1)^i (2n - 2i + 1 \mp x)^{1-\alpha} \qquad (2.21)$$

and

$$x_o = \gamma_o^p / \Delta\gamma^p \qquad (2.22a)$$

$$x = \bar{\gamma}^p / \Delta\gamma^p \qquad (2.22b)$$

If n = odd, then x varies from 1 to -1; while if n = even, then x varies from -1 to 1.

Equations (2.21) and (2.14b) differ only in the first term on their right-hand side. It is x_o which allows cyclic relaxation to take place. The results are shown in Figure 4 where the material constants, found previously, were used.

We notice that as n is very large, the effect of x_o in equation (2.21) disappears as a result of the relation $\lim_{n\to\infty} F_n(\alpha, x_o, x) = F_\infty(\alpha, x)$. The hysteresis loops then become stable and symmetric with respect to γ_o^p and have exactly the same shape as those with zero mean shear strain.

Other Complex Histories

A strain history of practical importance is shown in Figure 5, where a cyclic strain history at a fixed strain amplitude is followed by another at a lower strain amplitude. The experimental results are shown in Figure 5. In

order to predict the stress response, we use the numerical scheme developed in the section on variable uniaxial strain amplitudes. The theoretical results obtained are also shown in Figure 5. Again agreement between theory and experiment is demonstrated.

It is important to observe that the decreasing effect of the previous history on the stress response to a periodic strain history (cyclic test at constant strain amplitude) is the natural consequence of the monotonically decaying kernel function used in the present theory, i.e., in equation (2.3). This type of kernel does indeed impart to the material a fading memory with respect to the endochronic time scale.

3. CYCLIC RATCHETING

In this case the cyclic stress history is given. The numerical scheme developed in the previous sections is still useful. In addition, an iterative method is used to ensure the correct value of the stress at the point of reversal. Such schemes are easy to implement in the computer program. For purposes of theoretical study, the constitutive equations for shear under symmetric and unsymmetric stress cycles were used. Specifically, equation (2.5b) with material constants of normalized mild steel found previously, predicted the cyclic ratcheting phenomena shown in Figures 6(A) - 6(D). It is clear that, under unsymmetric stress cycles, the increment of plastic shear strain per cycle $\delta\gamma_N^p$ is positive and decreasing but not equal to zero, as shown in Figure 6(D). This indicates that, whether the material response is stable or not, the direction of progressive (plastic) shear strain is in the "direction" of mean shear stress. However, in the case of symmetric stress

cycles, the first stress cycle gives rise to a hysteresis loop which lies toward the right-hand side in the stress-strain space. The subsequent cycles will then cause the hysteresis loops to move toward the left-hand side until a stable symmetric hysteresis loop is reached. Due to the effects of the first stress cycle, the center of stably symmetric hysteresis loops does not lie at the origin of the stress-strain space. We find that the sign of the "off-center" value of the strain is the same as the sign of the strain at the point of first reversal. This phenomenon is essentially the counterpart of the cyclic relaxation after initial loading as indicated in Figure 4.

Comparisons between theoretical predictions and experiments must await further experimental information.

4. CONCLUSIONS

On the basis of the results presented in this paper, we conclude that the constitutive equations derived from the endochronic theory are very suitable for the analytical prediction cyclic response of stable materials under a variety of conditions. Moreover, the theory has its origins in irreversible thermodynamics of internal variables shown to be a powerful tool in the derivation of constitutive theories for several classes of materials (e.g. viscoelastic, plastic and viscoplastic materials).

Also noteworthy is the fact that a constitutive equation with <u>two</u> material constants, which are easily determined, can predict with computational ease the stress (strain) response of a material to a variety of general strain (stress) histories, without a need for special rules that are otherwise so evident in the literature.

REFERENCES

1. Morrow, J., "Cyclic Plastic Strain Energy and Fatigue of Metals," ASTM STP 378, Internal Friction, Damping and Cyclic Plasticity, 1965, pp. 45-87.

2. Landgraf, R.W., Morrow, J., and Endo, T., "Determination of the Cyclic Stress-Strain Curve," J. of Materials, Vol. 4, 1969, pp. 176-188.

3. Mroz, Z., "An Attempt to Describe the Behavior of Metals Under Cyclic Loads Using a More General Work-Hardening Model," Acta Mech., Vol. 7, 1969, pp. 199-212.

4. Landgraf, R.W., "The Resistance of Metals to Cyclic Deformation," ASTM STP 467, Achievement of High Fatigue Resistance in Metals and Alloys, 1970, pp. 3-36.

5. Krempl, E., "Cyclic Plasticity: Properties of the Hysteresis Curve of Structure Metals at Room Temperature," J. of Basic Engr., Trans. ASME, June 1971, pp. 317-323.

6. Jhansale, H.R. and Topper, T.H., "Engineering Analysis of the Inelastic Stress Response of a Structure Metal Under Variable Cyclic Strains," in ASME STP 519, Cyclic Stress-Strain Behavior-Analysis, Experimentation, and Failure Prediction, 1973, pp. 246-270.

7. Valanis, K.C., "Effect of Prior Deformation on Cyclic Response of Metals," J. of Appl. Mech., Trans. ASME, 1974, pp. 441-447.

8. Jhansale, H.R., "A New Parameter for the Hysteretic Stress-Strain Behavior or Metals," J. of Eng. Mat. Techn., Trans. ASME, 1975, pp. 33-38.

9. Liu, M.C.M., Krempl, E., and Nairn, D.C., "An Exponential Stress-Strain Law for Cyclic Plasticity," J. of Eng. Mat. Techn., Trans. ASME, 1976, pp. 322-329.

10. Dafalias, Y.F. and Popov, E.P., "Plastic Internal Variables Formalism of Cyclic Plasticity," J. of Appl. Mech., Trans. ASME, 1976, pp. 645-651.

11. Lamba, H.S. and Sidebottom, O.M., "Cyclic Plasticity for Nonproportional Paths: Part 1 - Cyclic Hardening, Erasure of Memory, and Subsequent Strain Hardening Experiments; Part 2 - Comparison with Predictions of Three Incremental Plasticity Models," J. of Eng. Mat. Techn., Trans. ASME, 1978, pp. 96-110.

12. Drucker, D.C. and Palgen, L., "On Stress-Strain Relations Suitable for Cyclic and Other Loading," J. of Appl. Mech., Trans. ASME, 1981, pp. 479-485.

13. Valanis, K.C., "Endochronic Theory with Proper Hysteresis Loop Closure Properties," Topical Report, SSS-R-80-4182, System, Science and Software, San Diego, California, USA, Aug. 1979.

14. Valanis, K.C. and Lee, C.F., "A Comprehensive Study of the Behavior of Mild Steel Using the Endochronic Theory," to be published in the Nuclear Engr. and Design.

15. Valanis, K.C., "Irreversible Thermodynamics of Continuous Media-- Internal Variable Theory," Springer-Verlag, New York, 1972.

16. Valanis, K.C. and H.C. Wu, "Endochronic Representation of Cyclic Creep and Relaxation of Metals," J. Appl. Mech., Trans. ASME, 1975, pp. 67-73.

17. Valanis, K.C., "Fundamental Consequences of a New Intrinsic Time Measure: Plasticity as a Limit of the Endochronic Theory," Arch. of Mech., 1980, pp. 171-191.

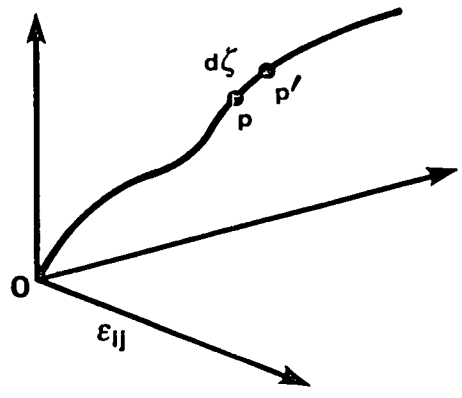

Fig. 1 Path in strain space.

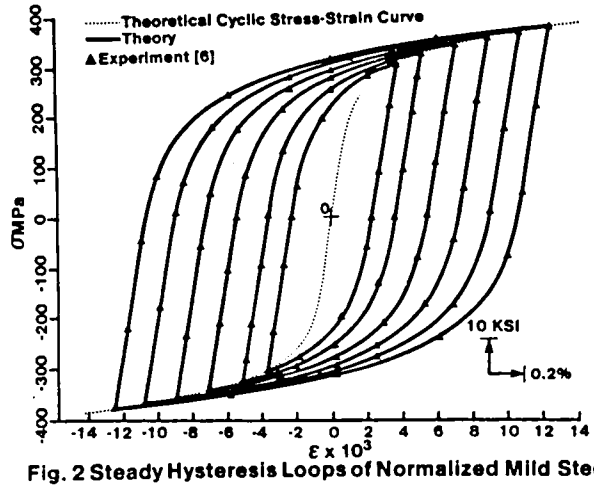

Fig. 2 Steady Hysteresis Loops of Normalized Mild Steel

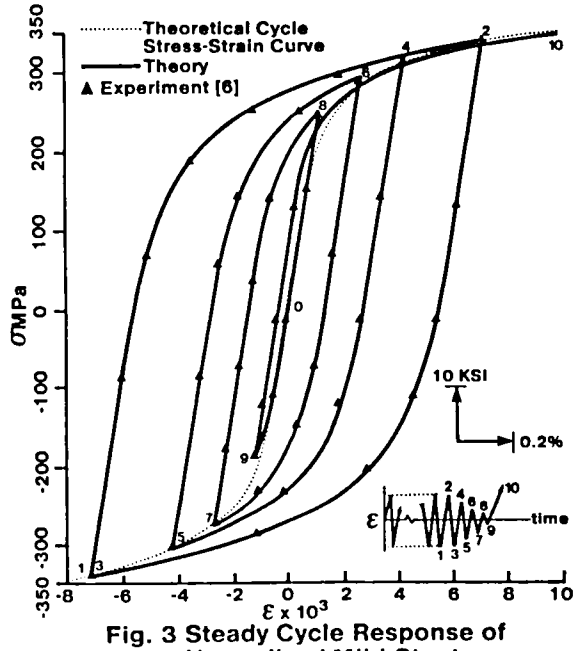

Fig. 3 Steady Cycle Response of Normalized Mild Steel

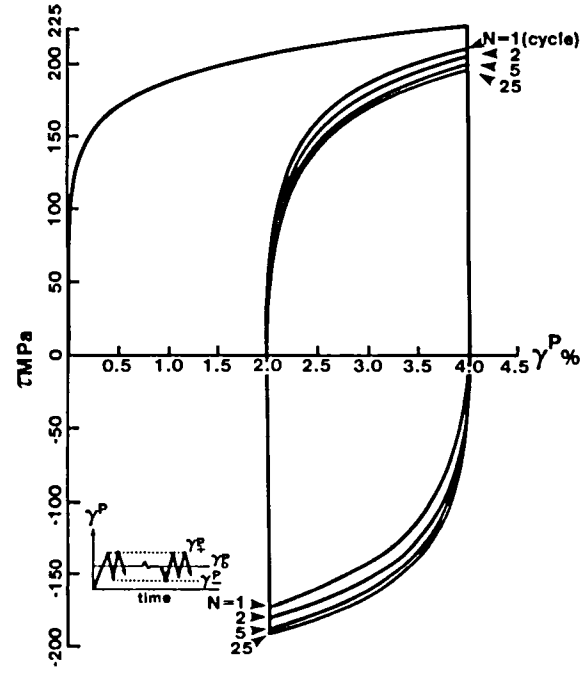

Fig. 4 Shear Cyclic Relaxation of Normalized Mild Steel

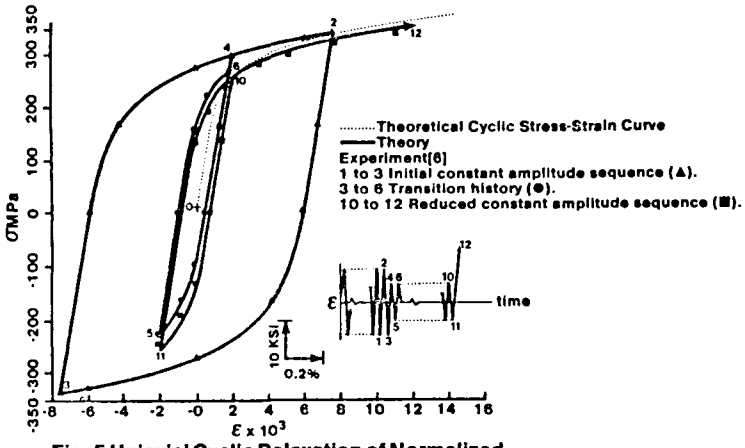

Fig. 5 Uniaxial Cyclic Relaxation of Normalized Mild Steel

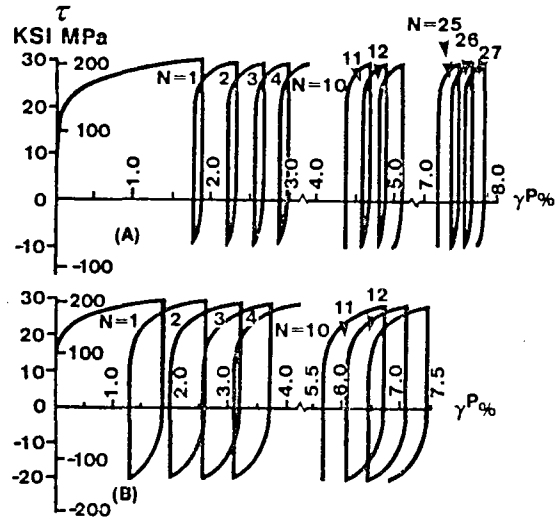

Figs. 6(A)&(B) Shear Ratcheting of Normalized Mild Steel Under Unsymmetric Stess Cycles

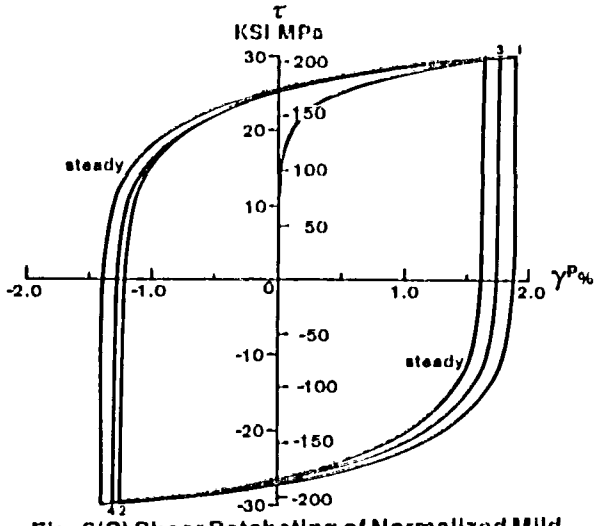

Fig. 6(C) Shear Ratcheting of Normalized Mild Steel Under Symmetric Stress Cycles

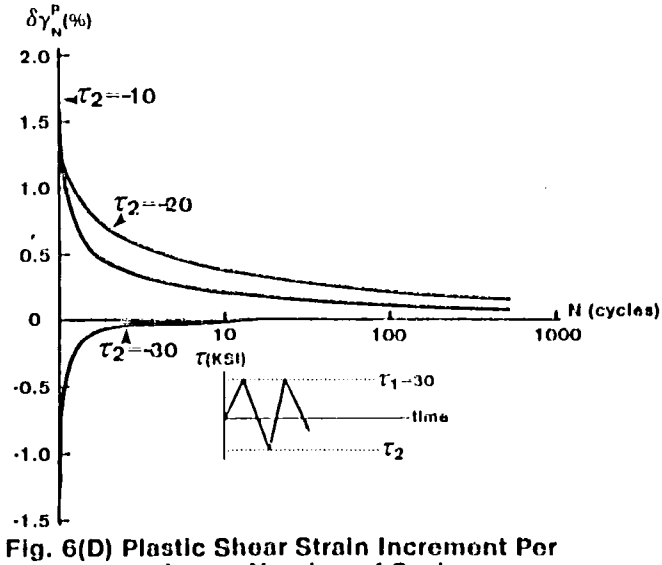

Fig. 6(D) Plastic Shear Strain Increment Per cycle v.s. Number of Cycles

A NEW UNCOUPLED VISCOPLASTIC CONSTITUTIVE MODEL*

Walter L. Bradley and Shik Yuen
Texas A&M University
College Station, Texas 77843

INTRODUCTION

A new uncoupled viscoplastic model has been developed which assumes a portion of the inelastic strain is rate independent (or at least rate insensitive). Unlike earlier uncoupled models, this model recognizes that some of the inelastic strain which occurs during a load change is rate sensitive (or thermally activated). To separate the rate dependent and rate independent contributions, hysteresis loops are run in strain control at temperatures that are sufficiently low that essentially identical loops are obtained for a 40s, 120s, and 1200s period. This $\sigma - \varepsilon$ loop is assumed to define the stress/rate-insensitive, inelastic strain behavior for all temperatures. Subsequent tests at higher temperatures will include rate-sensitive and rate-insensitive components of inelastic strain. However, since the magnitude of the rate-insensitive inelastic strain at each stress and temperature is already known from the low temperature hystersis loop measurements, the rate sensitive inelastic strain component can be determined by subtraction. The stress/rate-sensitive, inelastic strain is then modelled using standard viscoplastic models.

At higher temperatures, and therefore, lower stresses, the rate independent inelastic strain contribution is found to be negligible and the predictions of the model are exactly those of standard viscoplastic models. However, at lower temperatures and the resultant higher stresses, the rate independent, inelastic strain is significant and accounts for the rounded corners that are currently a problem for viscoplastic models which assume all inelastic strain to be rate sensitive.

In this paper we will present the physical basis for the uncoupled viscoplastic model, describe the various experiments used to evaluate the material constants, and compare predictions of stress relaxation behavior by the model to experimental results where the material constants have been determined using hysteresis loop data.

PHYSICAL BASIS FOR MODEL

Deformation of metals and alloys occurs by dislocation glide, cross-slip and climb. Additional flow may result from grain boundary sliding, though some dislocation deformation in the grains

* This work was sponsored by NASA under direction of Dr. Robert Thompson

is required even here for compatibility. In the low temperature regime ($0-0.20T_m$), the yield strength and flow stress are found to vary significantly with temperature. This is particularly true for materials with a body centered cubic lattice structure. The fairly small activation energy for thermally assisted dislocation motion at these low temperatures is usually associated with dislocations overcoming lattice friction (Peirels stress) or possibly dislocation intersections.

Between $0.20-0.40T_m$, the thermal assistance to overcoming such barriers is more than adequate, allowing dislocation glide to occur equally easily at various temperatures and/or strain rates in this temperature range. Here, the flow stress depends more on the inelastic strain and the resultant strain hardening it produces than on the strain-rate. While short range barriers to glide such as Peirels stress are easily overcome with thermal assistance at these temperatures, the thermal energy is relatively small and generally ineffective in giving much thermally assisted recovery via dislocation cross-slip, climb, etc. The activation barriers for such processes are relatively large compared to the phonon energies (thermal energy), making these processes quite sluggish; thus, their contribution to the overall deformation is quite small. In summary, between 0.20 and $0.4T_m$, thermally activated processes are either so rapid (e.g., overcoming Peirels stress) or so slow(e.g., dislocation climb) that very little rate sensitivity observed over this temperature range. We may say the deformation behavior in this temperature range is rate insensitive and over a range of strain-rates of 50-100X will be essentially rate independent. It will be shown later that Hastelloy-X specimens tested under fully reversible strain conditions over a temperature range of 298K to 533K (0.2 to $0.35T_m$) and over a 30X strain-rate range (9.70×10^{-4} to 3.23×10^{-5} s^{-1}) at each temperature have essentially identical hysteresis loops and material constants for Ω and K. At 755K ($0.49T_m$), the hysteresis loop is changing slightly, though rate dependence over the strain-rate range (30X) we have studied is still not significant.

As the specimen deformation temperature is raised above $0.5T_m$, rate sensitive, inelastic deformation becomes apparent. Hysteresis loop size (and shape to a degree) changes with changing strain-rate. At these higher temperatures, thermally activated cross-slip and climb now becomes possible, particularly at the slower strain-rates, which lowers the peak stress achievable in the hysteresis loop. We will associate our rate sensitive, inelastic strain with the additional increments of deformation made possible by the thermally assisted overcoming of these larger barriers to deformation, i.e., dynamic recovery, or softening. The rate sensitivity is seen principally in the circumventing of various barriers by cross-slip or climb rather than in the subsequent glide to the next barrier. Nevertheless, all of the inelastic strain that results from the combined cross-slip (or climb) and subsequent glide will be included in the rate sensitive, inelastic strain.

We have implicitly divided our inelastic strain into a component which results in strain hardening and a component which

does not. Even during the portion of the hysteresis loop where strain hardening is occuring, the inelastic strain may contain rate dependent (no strain hardening) as well as rate independent (strain hardening) components. It should be emphasized that net strain hardening continues until the back stress reaches a level where recovery and strain hardening are balanced. Ideally, the stress is dependent on the rate insensitive, inelastic strain and the rate sensitive, inelastic strain-rate. A transient dependence of stress on the rate sensitive, inelastic strain (as well as strain-rate) is sometimes observed and is equivalent to primary creep. Since we are initially interested in modelling hysteresis loop behavior for saturated loops, such transients are not expected to be significant. They do probably play a role in the initial "shakedown" where dislocations are gradually being rearranged into more stable cell structure configurations.

In summary, we believe that the inelastic strain may be uncoupled into two components, one associated principally with dislocation glide resulting in strain hardening and a second associated with dynamic recovery processes including dislocation cross-slip and climb. To a first approximation, the flow stress should depend on the rate insensitive, inelastic strain and the rate dependent, inelastic strain-rate. The stress/rate- sensitive inelastic strain-rate relationship can be modelled using viscoplastic models. The stress/rate-insensitive, inelastic strain relationship is determined from hysteresis loops taken at a suitably low temperature ($0.2\text{-}0.3T_m$). At higher temperatures, the flow stress is relatively low and the inelastic strain is essentially all rate-sensitive, resulting from dynamic recovery processes. At lower temperatures and the resultant higher flow stresses, a significant portion of the total inelastic strain will be rate insensitive deformation. The more gently rounded corners of the hysteresis loop observed at these temperatures are a consequence of this rate-insensitive, inelastic strain.

In this next section, the constitutive model will be defined in mathematical equations and the experiments required to characterize the various constants will be described.

CONSTITUTIVE MODEL

The total strain-rate is assumed to be divisible into three components; an elastic component $\dot{\varepsilon}_e$, a rate-insensitive inelastic component $\dot{\varepsilon}_{ii}$, and a rate-sensitive inelastic component $\dot{\varepsilon}_{ir}$; i.e.

$$\dot{\varepsilon}_t = \dot{\varepsilon}_e + \dot{\varepsilon}_{ii} + \dot{\varepsilon}_{ir} \tag{1}$$

The rate-sensitive strain rate $\dot{\varepsilon}_{ir}$ is modelled using the relationship typically used in unified theories for inelastic strain rate (note unified theory assumes all inelastic strain is rate sensitive); namely,

$$\dot{\varepsilon}_{ir} = \left(\frac{\sigma - \Omega}{K}\right)^n \tag{2}$$

where σ is the applied stress, Ω is the back stress and K is the

drag stress. The elastic strain-rate is modelled in the usual way as

$$\dot{\varepsilon}_e = \dot{\sigma}/E \tag{3}$$

Finally, the rate-insensitive, inelastic strain is modelled with an empircally determined strain hardening function $f(\sigma,\sigma_{max})$ as follows:

$$\dot{\varepsilon}_{ii} = f(\sigma, \sigma_{max})\, \dot{\sigma} \tag{4}$$

where $f(\sigma,\sigma_{max}) = \frac{d\varepsilon_{ii}}{d\sigma}$ as measured from hysteresis loops for different strain ranges, and therefore, σ_{max} values, as shown in Figure 1. It should be noted that the hystersis loops even at these lower temperatures are slightly asymmetric so the sign of the σ_{max} before the stress reversal as well as its magnitude must be specified to define the particular f value for a given value of σ in a stress reversal. The results for $f(\sigma,\sigma_{max})$ determined from the data in Figure 1 is summarized in Table 1. The stress-rate may be calculated from Equations (1)-(4) for a given axial strain-rate of $\dot{\varepsilon}_t$ as follows:

$$\dot{\sigma} = \frac{\dot{\varepsilon}_t - \left(\frac{\sigma-\Omega}{K}\right)^n}{\frac{1}{E} + f(\sigma, \sigma_{max})} \tag{5}$$

or

$$\Delta\sigma = \frac{\Delta\varepsilon_t - \left(\frac{\sigma-\Omega}{K}\right)^n \Delta t}{\frac{1}{E} + f(\sigma, \sigma_{max})} \tag{6}$$

The evaluation of $\Delta\varepsilon_t$ is given by $\dot{\varepsilon}_t \Delta t$ where the total axial strain-rate for a constant diametral strain rate dD/dt is

$$\dot{\varepsilon}_t = \frac{\frac{-2}{D_0}\frac{dD}{dt}}{1 - \frac{1}{E}\frac{d\sigma}{d\varepsilon}(1-2\nu)} \tag{7}$$

It should be noted that the appropriate time step Δt is selected by monotonically decreasing the value of Δt until the simulated σ-ε hysteris loops for two successive choices of Δt are essentially identical.

The material constants which must be determined empirically in Equation 5 are $\Omega(\sigma,T,N)$, $K(\dot{\sigma},T,N)$, $E(T)$, $f(\sigma,\sigma max)$ and $n(T)$ where N and T refer to the cycle number and temperature respectively. For the initial phase of this program, we chose to evaluate only saturated hystersis loop behavior, eliminating for the moment "N" as a variable. It was further assumed that for a saturated hystersis loop, "K" would retain a constant value around the loop whereas Ω was assumed to vary with σ around the loop. The rational for this assumption is that the drag stress is physically associated with the dislocation cell structure, or dislocations in stable configurations while Ω is associated with the metastable dislocation

arrangements such as pileups, multiple loops around particles, etc. Once a stable dislocation cell structure is formed (i.e., at saturation), it is reasonable to assume it does not change appreciably as we traverse a strain cycle. It may also be reasonably expected that the cycle to cycle changes leading to saturation will be associated with an N dependence of K, with Ω independent of N, at least to a first approximation.

Stress relaxation tests were made in an attempt to determine "n" and "Ω" over the entire range of temperatures studied (755K-1144K). Using an analysis first suggested by J.C.M. Li (1), it was determined that the back stress decreased significantly during the stress relaxation tests for temperatures of 978K (1300°F) and above, giving erroneous results for both "n" and "Ω". This was subsequently confirmed by drop stress/strain transient tests used to measure the back stress. Thus, stress relaxation tests were only used over the temperature range of 755K-922K to determine "n" and "Ω". At higher temperatures (978K-1144K), stress drop/strain transient tests were used to determine the back stress Ω. Then abrupt strain-rate change tests were used to determine the value of "n". The strain-rate was decreased by a factor of 3x and by a factor of 30x with the resultant flow stress measured. It was assumed that "K" remained constant during these strain-rate changes but that "Ω" changed to a new value during 0.5s transient that occured before a new "steady-state" flow stress was attained. The plotting of $(\sigma-\Omega)$ vs. $\dot{\varepsilon}_{ir}$ allowed the stress exponent "n" to be evaluated.

At all temperatures, "K" was subsequently evaluated using Equation 2 at the same stress where "n" and "Ω" had previously been evaluated (usually on the plateau of the hysteresis loop or near σ_{max} at lower temperatures where no plateau was reached). With n, Ω, and K determined for one σ-ε position on the hysteresis loop and assuming n and K are constant for a saturated loop at a given temperature and strain-rate, one may then calculate Ω for other points around the hysteresis loop using Equation 2. Typical results for Ω vs. ε(orσ) are shown in Figure 2.

EXPERIMENTAL PROCEDURES AND DATA REDUCTION

Round tensile bars with a gage section 4 cm long by 1 cm in diameter were prepared from Hastelloy-X. They were then inserted into a 100 Kip MTS materials testing system with special water cooled grips and a diametral extensometer which utilizes quartz rods. Induction heating was used with an Ircon optical controller to heat the specimens. The temperature variaton at 1144K was ±1.1K. An absolute accuracy of ±3K was attained by calibrating the optical controller using Hastelloy-X in a conventional furnace. High purity thermocouple wires and a precision digital thermometer were used to establish the actual temperature. Several thermocouples were used to verify the absence of significant temperature gradients in the small Hastelloy-X specimen used in calibration as well as in the tensile specimens' gage length during temperature maintenance

by induction heating. The calibration of the optical controller is checked every three months and recalibrated as needed.

Special alignment procedures were used to reduce an initial variation in axial strain measurements at three equally spaced positions around the circumference from 30% to 5% maximum. This was verified on several successive specimens and then was not checked thereafter. Only one specimen was buckled in testing, and this specimen had a fatigue crack which had grown across about 20% of the cross-section.

Specimens were tested at ten temperatures ranging from 298K ($0.20T_m$) to 1144K ($0.75T_m$). At each temperature, specimens were tested at three diametral strain-rates with gage axial strain-rates of approximately 10, 3.3 and $0.33 \times 10^{-4} s^{-1}$, the instantaneous strain-rate varying slightly around these values depending on the relative amounts of elastic and inelastic strain. The strain range used was ±1% axial strain and the specimens were cycled until the loop saturated, which required as few as two cycles at higher temperatures but as many as 40-50 cycles at lower temperatures.

Diameter measurements were converted into total axial strain using the easily derived relationship

$$\varepsilon_t = \frac{\sigma}{E}(1 - 2\nu) - 2\frac{\Delta D}{D_o} \tag{8}$$

where E and ν are the elastic modulus and Poisson's ratio, D_o is the initial diameter and ΔD is the change in diameter. The axial inelastic strain is easily calculated as the difference in the total strain and the elastic strain,

or

$$\varepsilon_i = \frac{-2\nu\sigma}{E} - \frac{2\Delta D}{D_o} \tag{9}$$

Equations for the total strain rate $\dot{\varepsilon}_t$ and the inelastic strain rate $\dot{\varepsilon}_i$ are also easily derived in terms of the measured load/diameter relationships and give

$$\dot{\varepsilon}_t = \frac{\frac{-2}{D_o}\frac{dD}{dt}}{1 - \frac{1}{E}\frac{d\sigma}{d\varepsilon_t}(1-2\nu)} \tag{10}$$

$$\dot{\varepsilon}_i = \frac{-2}{D_o}\frac{dD}{dt}\left[\frac{1 - \frac{1}{E}\frac{d\sigma}{d\varepsilon_t}}{1 - \frac{(1-2\nu)}{E}\frac{d\sigma}{d\varepsilon_t}}\right] \tag{11}$$

where

$$\frac{d\sigma}{d\epsilon_t} = \frac{1}{\left(\frac{1-2\nu}{E} - \frac{2}{D_o}\frac{dD}{d\sigma}\right)} \qquad (12)$$

Since $\frac{dD}{dt}$ is specified in programming the MTS function generator and $dD/d\sigma$ is easily measured, the total and inelastic strain-rates $\dot{\epsilon}_t$ and $\dot{\epsilon}_i$ are also easily determined from load/diameter measurements.

With the strain hardening function $f(\sigma, \sigma_{max})$ defined from hysteresis loops at lower temperatures where all inelastic strain is rate insensitive, Equation 4 can be used to quantify the rate insensitive inelastic strain-rate for any temperature and stress rate, $\dot{\sigma}$. Since the total inelastic strain-rate may be calculated from Equation (11) and the rate insensitive strain-rate calculated through using Equation (4), the rate sensitive strain-rate is easily calculated as the differnce in these two quantities. Thus, the elastic, inelastic rate-insensitive and inelastic rate-sensitive contributions to the total strain-rate may all be evaluated from the experimentally measured load-displacement curves. Once the rate-sensitive component of strain-rate is evaluated, the Ω can be calculated for various measured values of σ and calculated values of "n" and "K".

The stress relaxation tests were run under constant diameter conditions imposed by interrupting the diametral strain cycling at various points on the hysteresis loop. The stress-time response during the interruption of strain cycling is measured using a second recorder so as to not interfere with the load-diameter measurements. The axial, rate-sensitive strain-rate is determined from the load time record using the relationship

$$\dot{\epsilon}_{ir} = \frac{-2\nu}{E}\dot{\sigma} \qquad (13)$$

derived assuming stress relaxation under constant diameter conditions. Load versus dP/dt is taken and used to evaluate $\dot{\epsilon}_{ir}$. The value for "n" in Equation 2 may be determined by plotting $\ln \dot{\epsilon}_{ir}$ vs. $\ln (\sigma - \Omega)$. assuming Ω does not change during the test.

Experimental Results and Discussion

Typical stress/total strain and stress/ rate-sensitive inelastic strain results are seen in Figures 3 and 4 respectively. Results at room temperature ($0.20T_m$) and $533K(0.35T_m)$ at three strain-rates gave essentially identical hysteresis loops, indicating the inelastic strain over this temperature range is all rate insensitive. Additional hystersis loops were run at room temperature for strain amplitudes of ± 0.05%, 0.1%, 0.2%, 0.3%, 0.4%, 0.6%, 0.8%, with the ± 1% having been run previously. These results are presented in Figure 1 with the $f(\sigma, \sigma_{max})$ values tabulated in Table 1.

The various material constants required for characterization of the rate sensitive, inelastic strain are summarized in Table II. The elastic constants as a function of temperature are summarized in Table III. It should be noted in Table II that "n" varies from 3.63 to 5.57. This is in sharp contrast to unified models where the "n" value at lower temperatures may be as high as 60-100. We too found "n" values of 50-100 if we ran strain-rate cycling tests at lower temperatures and analyzed the results assuming all of the inelastic strain was rate sensitive (or rate dependent) as the unified theory does.

The back stress is seen to increase with increasing stress as one might expect. At higher temperatures, the slower strain-rate gives the lower back stress. At temperatures below 978K, the back stress does not seem to be a sensitive function of strain-rate. At 978K and above "K" is seen to systematically decrease with increasing temperature. This indicates an increasing mobile dislocation density, possibly resulting from an increased cell size which is both the source of mobile dislocations and a place where they may be entrapped. At lower temperatures "K" increases with decreasing strain-rate, again indicating the expected lower mobile dislocation density at lower strain-rates. These differences in calculated "K" are a result of stress relaxation data for different prior strain-rates being displaced vertically in a $\ell n \dot{\varepsilon}_{ir}$ vs. $\ell n\,(\sigma-\Omega)$ plot. The constant "K" values at various strain-rates at higher temperatures are assumed in the analysis, this assumption being justified by a careful analysis of the strain-rate cycling tests.

Table IV summarizes the results of analysis of the inelastic strain-rate just before and just after the strain cycling is interrupted for a stress relaxation test. The inelastic strain is given from equations (1), (2) and (4) as

$$\dot{\varepsilon}_{ii} + \dot{\varepsilon}_{ir} = f\,(\sigma, \sigma_{max})\,\dot{\sigma} + \left(\frac{\sigma-\Omega}{K}\right)^{n} \qquad (14)$$

Since $\dot{\sigma}$ goes from positive to negative as one interrupts the strain cycling for stress relaxation and since $f\,(\sigma, \sigma_{max})$ is essentially zero just after a load reversal, the rate insensitive strain-rate experiences a discontinuous change from a positive value to zero. Since the stress is continuous at this time, one would expect the rate-sensitive inelastic strain-rate to be continuous. Thus, a large decrease in inelastic strain-rate as one interrupts the strain cycling indicates that the inelastic strain-rate during strain cycling is principally rate-insensitive. If the inelastic strain-rate before and after the interruption is essentially the same, this indicates that the inelastic strain during cyclic straining must have been essentially all rate sensitive. Thus, inelastic strain-rate continuity is a good measure of to what degree the inelastic strain is rate sensitive. A large discontinuity indicates significant rate-insensitive strain. Table IV summarizes such results over a wide range of strain rates and temperatures. The trends as expected show a greater degree of rate-dependent inelastic-strain (smaller discontinuity) for higher temperatures and slower

strain-rates. These results show a gradual transition from about 100% rate insensitive flow at high strain-rates and lower temperatures (as in classical plasticity) to 100% rate sensitive flow as in the unified theories. It should be noted that our constitutive model will cover this entire range as it explicitly accounts for both types of inelastic strain.

PREDICTIONS

The constitutive model as described in Equations 1-4 and reformulated into Equations 5-7 may be used to predict strain cycling, stress relaxation or other phenomena if used with the approximate material constants. Such constants for Hastelloy-X are summarized in Tables I, II and III. To first see if the model is self consistent in being able to predict the original strain cycling curves from which Tables I, II and III were determined, all of the input strain cycling curves were simulated using Equations 6 and 7 and the material constants in Tables I, II and III. The original curves and the simulated curves were found to be in excellent agreement over the whole range of temperatures and strain-rates, as seen in the selected examples presented in Figure 5. Gently rounded corners are well simulated at the lower temperatures using this uncoupled approach. The unified theory with its high "n" values always gives square corners at lower temperatures.

Stress relaxation simulations are presented in Figure 6. At the lower temperature, the results are reasonable; however, at the higher temperature the actual asymptotic stress value is much lower than the predicted one. This is because we have not yet accounted for thermal recovery of our state variables Ω and K. The back stress does decrease during stress relaxation at higher temperatures as has been previously noted. We are still assuming a constant value for Ω and K during stress relaxation.

SUMMARY

A new uncoupled viscoplastic model has been proposed along with experiments and analysis to define the various material constants. Distinguishing between rate sensitive and rate insensitive strain allows the rate sensitive strain to be modelled over a wide range of temperatures with very little variation in the stress component "n". Furthermore, it allows the rounded corners on stress-strain hysteresis loops to be achieved very naturally.

Table I. Values for Rate Independent, Inelastic Strain Function $f(\sigma, \sigma_{max})$

σ(MPa)	$f(\sigma, \sigma_{max})MPa^{-1}$
for σ_{max} = 149 MPa	
Loading	
-149	0
-106	0
106	0
149	0
Unloading	
149	0
106	0
-106	0
-149	0
for σ_{max} = 286	
Loading	
-286	0
0	0
106	0.187E-6
212	0.406E-6
286	0.161E-5
Unloading	
286	0
0	0
-106	0.275E-6
-212	0.580E-6
-286	0.148E-5
for σ_{max} = 392 MPa	
Loading	
-403	0
0	0.319E-6
106	0.165E-5
212	0.259E-5
318	0.435E-5
392	0.124E-4
Unloading	
392	0
0	0.232E-6
-106	0.186E-5
-212	0.270E-5
-318	0.417E-5
-403	0.107E-4
for σ_{max} = 435 MPa	
Loading	
-446	0
0	0.652E-6
106	0.258E-5
212	0.432E-5
318	0.620E-5
392	0.126E-4
424	0.246E-4
435	0.680E-4
Unloading	
435	0
0	0.551E-6
-106	0.214E-5
-212	0.441E-5
-318	0.694E-5
-392	0.108E-4
-424	0.184E-4
-446	0.522E-4

σ(MPa)	$f(\sigma, \sigma_{max})MPa^{-1}$
for σ_{max} = 467 MPa	
Loading	
-477	0
-106	0.145E-6
0	0.113E-5
106	0.255E-5
212	0.559E-5
318	0.880E-5
424	0.187E-4
461	0.455E-4
467	0.134E-3
Unloading	
467	0
106	0.145E-7
0	0.104E-5
-106	0.294E-5
-212	0.546E-5
-318	0.890E-5
-424	0.165E-4
-459	0.329E-4
-477	0.913E-4
for σ_{max} = 520 MPa	
Loading	
-530	0
-106	0.681E-6
0	0.164E-5
106	0.330E-5
212	0.732E-5
318	0.114E-4
424	0.197E-4
477	0.333E-4
509	0.754E-4
520	0.196E-3
Unloading	
520	0
106	0.127E-6
0	0.135E-5
-106	0.383E-5
-212	0.723E-5
-318	0.110E-4
-424	0.177E-4
-477	0.310E-4
-509	0.541E-4
-530	0.157E-3
for σ_{max} = 562 MPa	
Loading	
-567	0
-106	0.986E-6
0	0.225E-5
106	0.394E-5
212	0.658E-5
265	0.862E-5
318	0.126E-4
371	0.164E-4
424	0.220E-4
477	0.328E-4
509	0.461E-4
530	0.600E-4
552	0.111E-3
562	0.291E-3

σ(MPa)	$f(\sigma, \sigma_{max})MPa^{-1}$
for σ_{max} = 562 MPa	
Unloading	
562	0
106	0.783E-6
0	0.174E-5
-106	0.388E-5
-212	0.677E-5
-318	0.120E-4
-371	0.164E-4
-424	0.217E-4
-477	0.314E-4
-509	0.403E-4
-530	0.565E-4
-546	0.796E-4
-557	0.132E-3
-567	0.388E-3
for σ_{max} = 610 MPa	
Loading	
-615	0
-106	0.141E-5
0	0.288E-5
106	0.429E-5
212	0.723E-5
318	0.126E-4
371	0.175E-4
424	0.232E-4
477	0.307E-4
530	0.448E-4
562	0.629E-4
583	0.868E-4
605	0.162E-3
610	0.229E-3
Unloading	
610	0
106	0.681E-6
0	0.188E-5
-106	0.367E-5
-212	0.630E-5
-318	0.103E-4
-371	0.159E-4
-424	0.194E-4
-477	0.274E-4
-530	0.416E-4
-562	0.572E-4
-583	0.894E-4
-605	0.186E-3
-615	0.372E-3

Table II. Values for Back Stress(for $\sigma=\sigma_{max}$),n,Drag Stress(K) and K^n

Temp. (K)	Temp. (°F)	Ω (MPa) strain rate ($10^{-4}s^{-1}$) 10	3.3	0.33	n	K_1 ($MPaS^n$) strain rate ($10^{-4}s^{-1}$) 10	3.3	0.33	K^n (MPa^nS) strain rate ($10^{-4}s^{-1}$) 10	3.3	0.33
755	900	468	468	474	5.50	390	513	1045	1.78×10^{14}	8.05×10^{14}	4.03×10^{15}
810	1000	252	265	318	4.96	1186	1260	1704	1.77×10^{15}	2.39×10^{15}	1.07×10^{16}
866	1100	255	226	237	5.57	905	978	1274	2.94×10^{16}	4.53×10^{16}	1.98×10^{17}
922	1200	161	164	163	4.31	1690	1829	2597	8.17×10^{13}	1.15×10^{14}	5.20×10^{14}
978	1300	141	136	115	5.57	800	800	800	1.48×10^{16}	1.48×10^{16}	1.48×10^{16}
1033	1400	118	111	82	4.75	672	672	672	2.69×10^{13}	2.69×10^{13}	2.69×10^{13}
1089	1500	76	66	43	4.70	488	488	488	4.32×10^{12}	4.32×10^{12}	4.32×10^{12}
1144	1600	41	38	28	3.63	532	532	532	7.85×10^{9}	7.85×10^{9}	7.85×10^{9}

900°F - 1200°F: Ω, n & K obtained from stress relaxation tests.

1300°F - 1600°F: n obtained from strain rate change test
Ω obtained from stress drop tests.
K assumed to be constant for all strain rates

Table III. Values for Young's Modulus and Poisson's Ratio

Temp. (K)	Temp. (°F)	Temp. (C°)	T/T_m*	(10^6psi)	E(GPa)
294	70	21	0.19	28.6	197
533	500	260	0.35	26.3	182
755	900	482	0.49	24.0	166
810	1000	538	0.53	23.4	162
866	1100	593	0.57	22.8	158
922	1200	649	0.60	22.3	154
978	1300	704	0.64	21.7	150
1033	1400	760	0.67	21.1	146
1089	1500	816	0.71	20.5	142
1144	1600	871	0.75	19.9	137

$\nu = 0.32$ (assumed constant for all temp.)

*melting range is 1260-1255°C

Table IV. Inelastic Strain Rate Continuity at Various Temperatures

$\dot{\varepsilon}_t = 1 \times 10^{-3} s^{-1}$ (10S/½ cycle)

$\dot{\varepsilon}_t = 3.3 \times 10^{-4} s^{-1}$ (30S/½ cycle)

$\dot{\varepsilon}_t = 3.3 \times 10^{-5} s^{-1}$ (300S/½ cycle)

A) $\dot{\varepsilon}_t = 1 \times 10^{-3} s^{-1}$

Temp. (K)	Temp. (°F)	σ (MPa)	$\dot{\varepsilon}p^-$ ($10^{-4} s^{-1}$)	$\dot{\varepsilon}p^+$ ($10^{-4} s^{-1}$)	$\dot{\varepsilon}p^+/\dot{\varepsilon}p^-$ (%)
755	900	434 558	8.76 9.57	.21 .10	2 1
810	1000	492	9.51	1.22	13
866	1100	386 455	9.18 9.57	2.12 1.01	23 11
922	1200	405 458	9.34 9.59	2.34 1.95	25 20
978	1300	330	9.40	9.01	96
1033	1400	277	9.80	9.80	100
1089	1500	185	9.61	9.61	100
1144	1600	119	9.83	9.83	100

$\dot{\varepsilon}p^-$ = plastic strain rate before the beginning of stress relaxation test

$\dot{\varepsilon}p^+$ = plastic strain rate after the beginning of stress relaxation test

B) $\dot{\varepsilon}_t = 3.3 \times 10^{-4} s^{-1}$

Temp. (K)	Temp. (°F)	σ (MPa)	$\dot{\varepsilon}_p^-$ ($10^{-4} s^{-1}$)	$\dot{\varepsilon}_p^+$ ($10^{-4} s^{-1}$)	$\dot{\varepsilon}_p^+/\dot{\varepsilon}_p^-$ (%)
755	900	450 568	2.95 3.19	.41 .24	14 8
810	1000	394 471	2.98 3.16	.40 .69	13 22
866	1100	376 439	3.10 3.20	.68 .54	22 17
922	1200	381 431	3.14 3.22	1.21 1.38	39 43
978	1300	327	3.19	3.09	97
1033	1400	236	3.27	3.27	100
1089	1500	154	3.21	3.21	100
1144	1600	96	3.29	3.29	100

C) $\dot{\varepsilon}_t = 3.3 \times 10^{-5} s^{-1}$

Temp. (K)	Temp. (°F)	σ (MPa)	$\dot{\varepsilon}_p^-$ ($10^{-5} s^{-1}$)	$\dot{\varepsilon}_p^+$ ($10^{-5} s^{-1}$)	$\dot{\varepsilon}_p^+ / \dot{\varepsilon}_p^-$ (%)
755	900	592	3.19	.82	26
810	1000	373	2.97	.80	27
866	1100	354	3.05	1.84	60
922	1200	352	3.15	2.38	76
978	1300	246	3.20	3.19	100
1033	1400	163	3.27	3.27	100
1089	1500	100	3.22	3.22	100
1144	1600	59	3.29	3.29	100

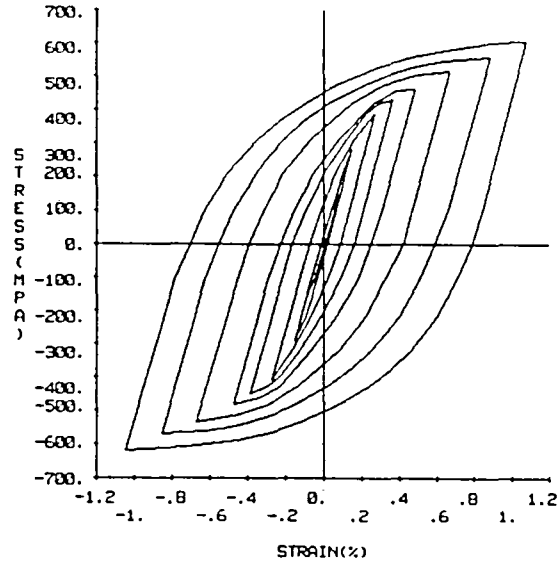

Figure 1. Saturated stress-strain results for Hastelloy-X at room temperature for total strain amplitudes of 0.05%,0.1%,0.2%, 0.3%,0.4%,0.5%,0.6%,0.8%,1.0%.

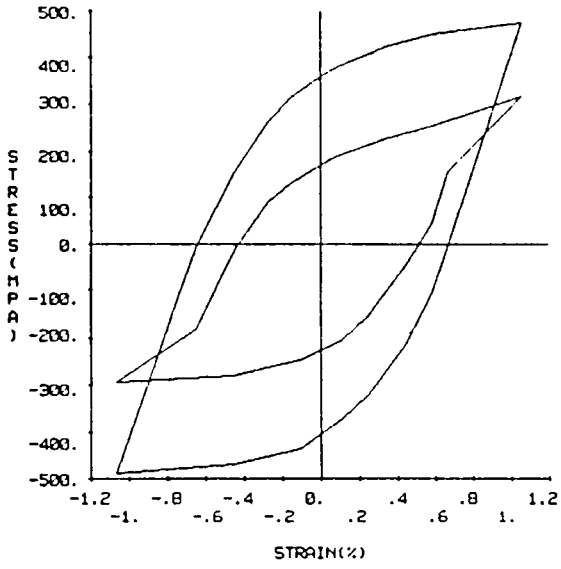

(a)

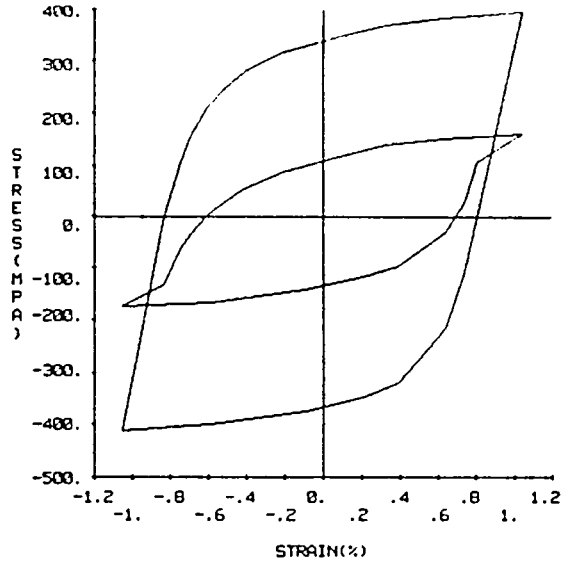

(b)

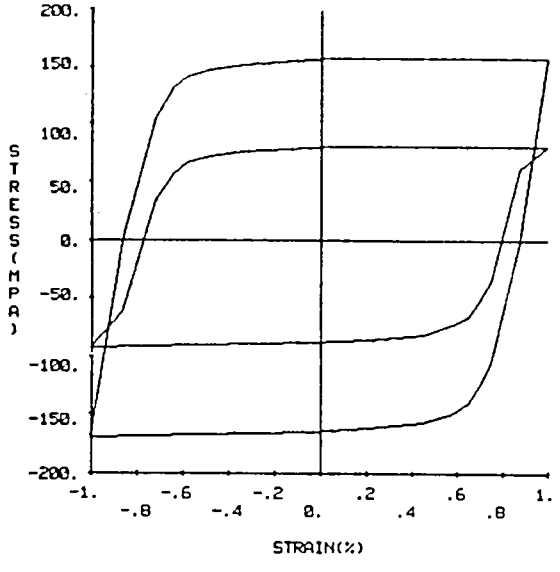

(c)

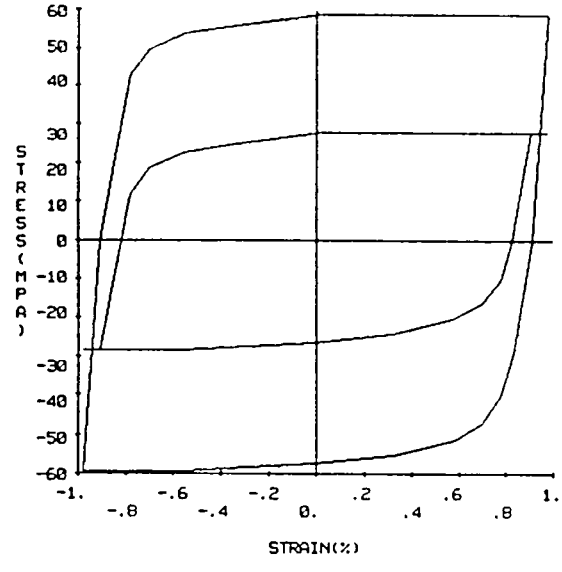

(d)

Figure 2. Stress and back stress as a function of strain as calculated from model for a)810K and $\dot{\epsilon}$=3.3X10^{-5}s^{-1};b)922K and $\dot{\epsilon}$=3.3X10^{-5}s^{-1};c) 1033K and $\dot{\epsilon}$=3.3X10^{-5}s^{-1};d)1144K and $\dot{\epsilon}$=3.3X10^{-5}s^{-1}.

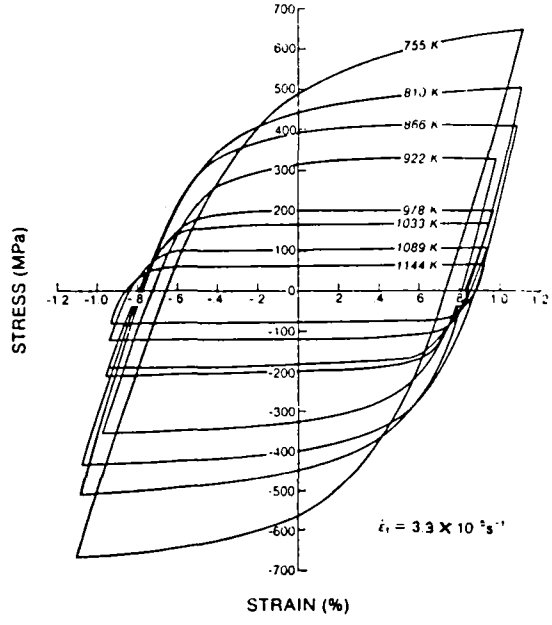

Figure 3. Saturated hysteresis loops of stress vs. total strain for Hastelloy-X at various temperatures.

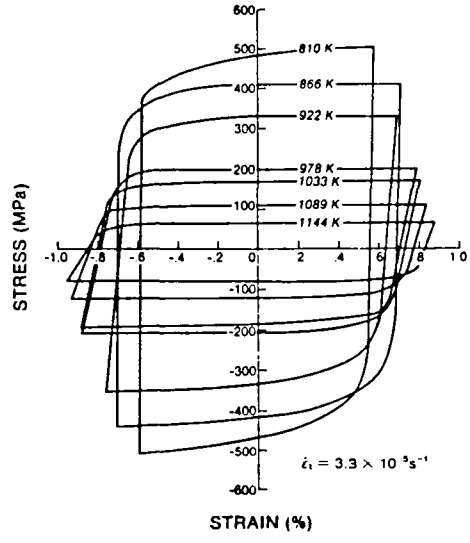

Figure 4. Saturated hysteresis loops of stress vs. rate dependent inelastic strain for Hastelloy-X at various temperatures.

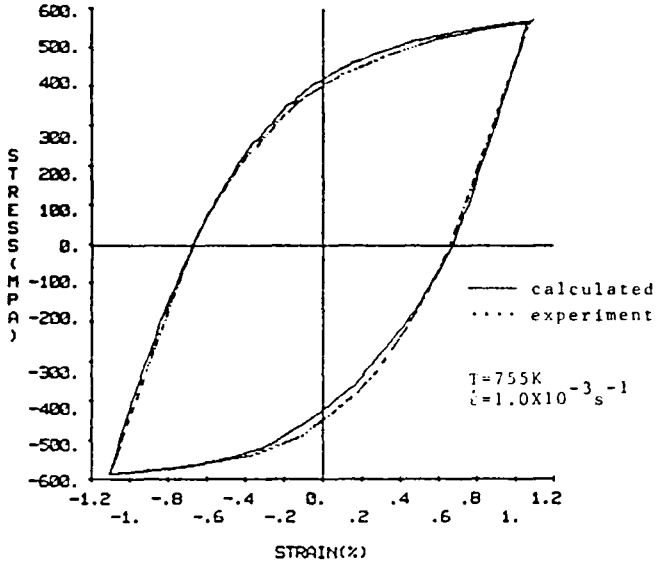

(a)

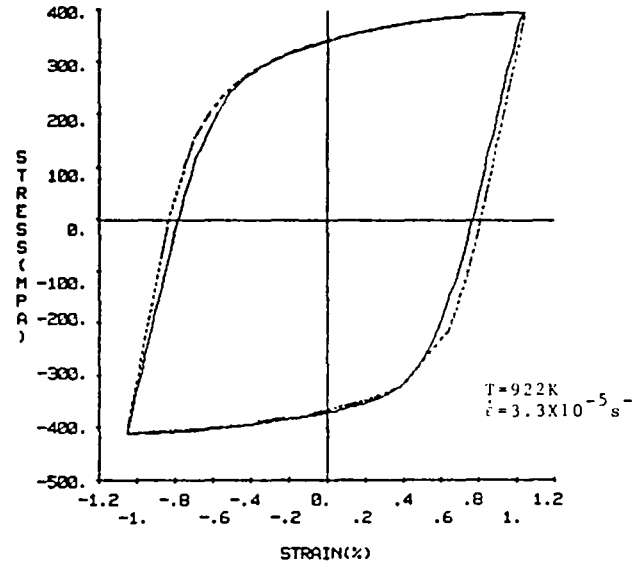

(b)

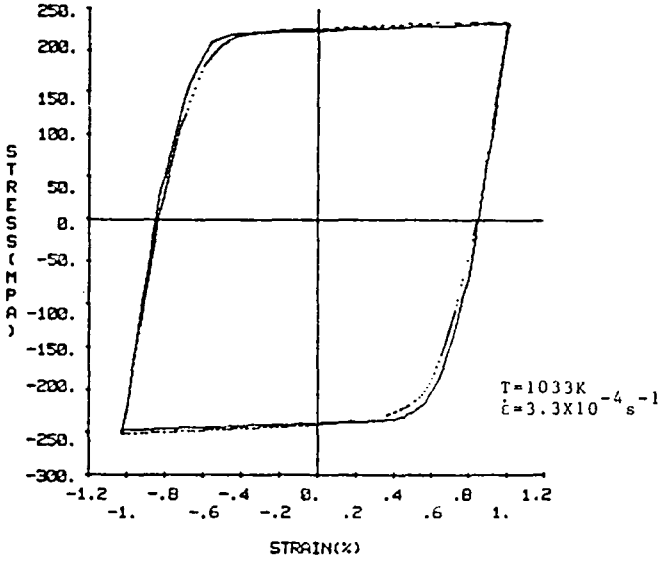

(c)

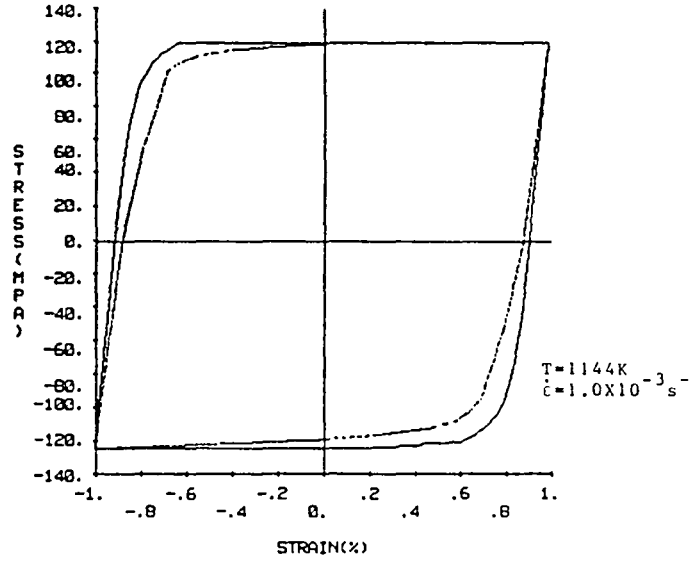

(d)

Figure 5. Stress/total strain hysteresis loops as measured and as calculated for Hastelloy-X at several different temperatures and strain rates.

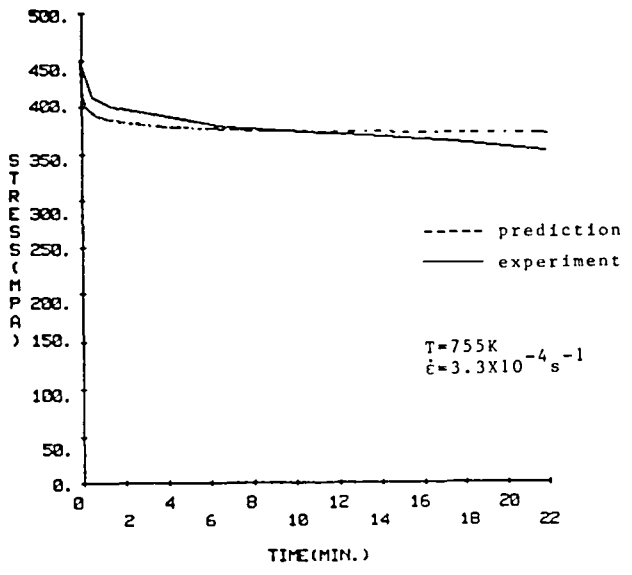

(a)

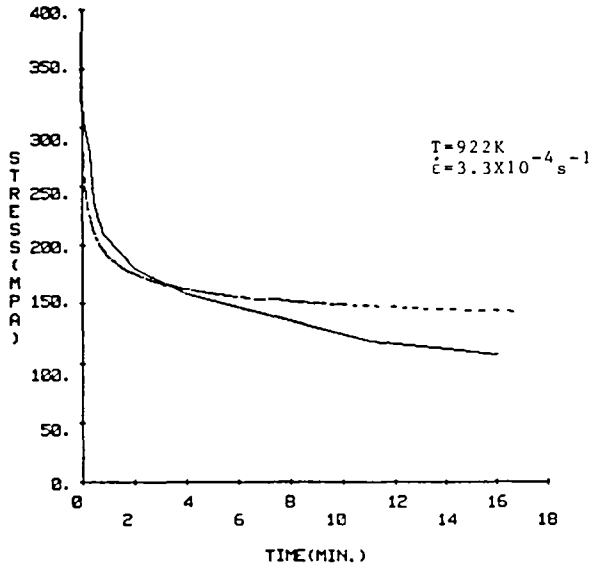

(b)

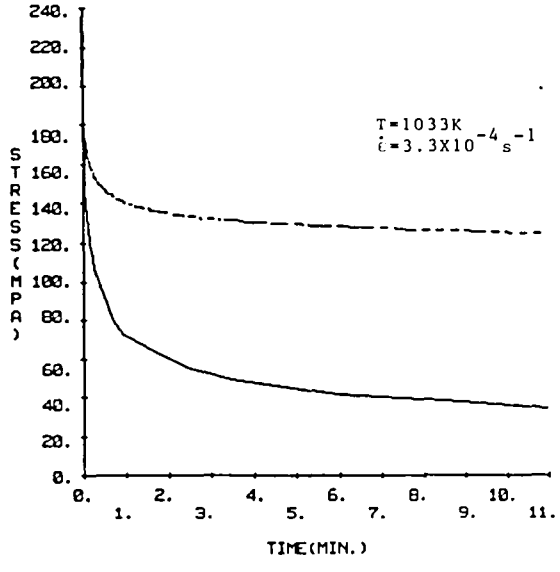

(c)

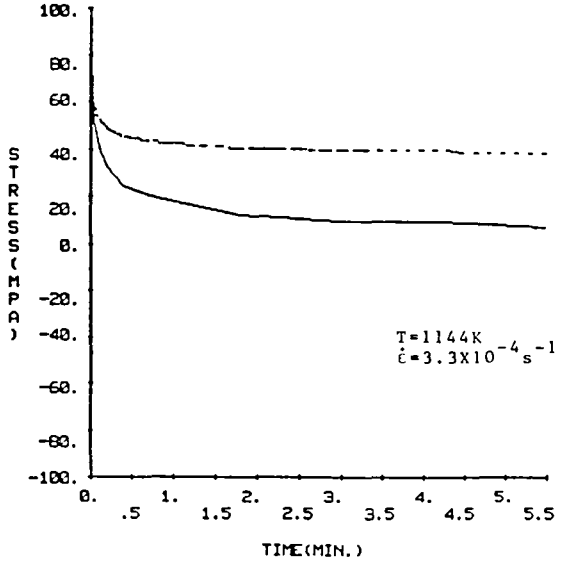

(d)

Figure 6. Stress relaxation behavior of Hastelloy-X as predicted by model and as measured experimentally.

CORRELATIONS BETWEEN METALLURGICAL CHARACTERIZATION STUDIES, EXPLORATORY MECHANICAL TESTS, AND CONTINUUM MECHANICS APPROACHES TO CONSTITUTIVE EQUATIONS*

J. Moteff
University of Cincinnati
Cincinnati, Ohio 45221

and

C. E. Pugh and R. W. Swindeman
Oak Ridge National Laboratory
Oak Ridge, Tennessee 37830

Austenitic stainless steels, such as types 316 and 304, are widely used as pressure vessel materials in the temperature range of 425 to 650°C. Depending on the loading rate, the deformation behavior may fall into categories classified in continuum mechanics as either time-dependent plasticity or time-dependent creep. Ad hoc rules are sometimes needed to accommodate interaction effects. Some of the rules for interaction effects can be better understood by taking into account the dynamic nature of the dislocation-dislocation and dislocation-precipitate substructure and how it responds to transient stress, strain, and temperature conditions. The variation in this structure includes changes in mobile dislocation density, dislocation link lengths, cell sizes and misorientation angles, and precipitate sizes and distributions.

Although somewhat limited in its use for understanding kinematic hardening behavior, microscopy is a valuable tool in the study of isotropic hardening, especially as it is affected by the Orowan-Bailey concept of strain hardening versus thermal recovery and acceleration of aging phenomena due to cyclic strain. Indeed, a better understanding of metallurgical phenomena needs to be developed in order to establish the useful range of accumulated strain as a state variable.

In considering type 304 stainless steel that exhibits a creep behavior characterized by a relatively high stress exponent of creep rate and the development of subgrains during creep deformation of recrystallized material,

---

*Research sponsored, in part, by the Office of Reactor Research and Technology, U.S. Department of Energy under Contract W-7405-eng-26 with the Union Carbide Corporation.

and for tests conducted under constant stress (σ), temperature (T), and environments (E), the creep rate, $\dot{\varepsilon}$, may be given as:

$$\dot{\varepsilon}(\sigma,T,E,S)_{\sigma,T,E} = \dot{\varepsilon}(S) \ .$$

Here S is a parameter that describes microstructure, which for dislocation creep is characterized by the following parameters:

$$S = S[\lambda,\rho,\theta,F(\theta),f(p)] \ ,$$

where λ is the subgrain size, ρ the dislocation density, θ is the average misorientation angle between subgrains, $F(\theta)$ is the distribution function of the misorientation angle, and $F(p)$ is some function of dislocation-second phase interactions.

Figures 1 through 3 show creep curves (strain-time) of some exploratory mechanical tests performed at temperatures 704, 650, and 593°C. Specimens were tested to rupture at two different stress levels σ_1 and σ_2 ($\sigma_1 > \sigma_2$) to establish the normal strain-time behavior. A subsequent test was performed in which the specimen was crept at the higher stress (σ_1) to the beginning of the secondary stage of creep, presumed to be the strain/time conditions at which a steady state microstructure is developed, and then the stress was reduced to the lower level (σ_2). In most of the conditions studied, it was observed that some incubation time period (Δt) would prevail at which the strain, other than elastic strain recovery, would show no measurable change. In some cases, such as a stress change to 48 or 33 percent of the initial stress for tests conducted at 650°C and an initial stress, σ_1, of 207 MPa, a negative strain would prevail for a period of time. As the test temperature is decreased, the incubation period is significantly increased such as the 160 hours observed at the 593°C with a stress drop of about 25%.

The associated microstructure, S, and significance of this microstructure on the creep strain-hardening model for variable uniaxial loads were assessed and found to be consistent with the use of creep-recovery models at high stresses and temperatures and strain-hardening models at low stresses and temperatures.

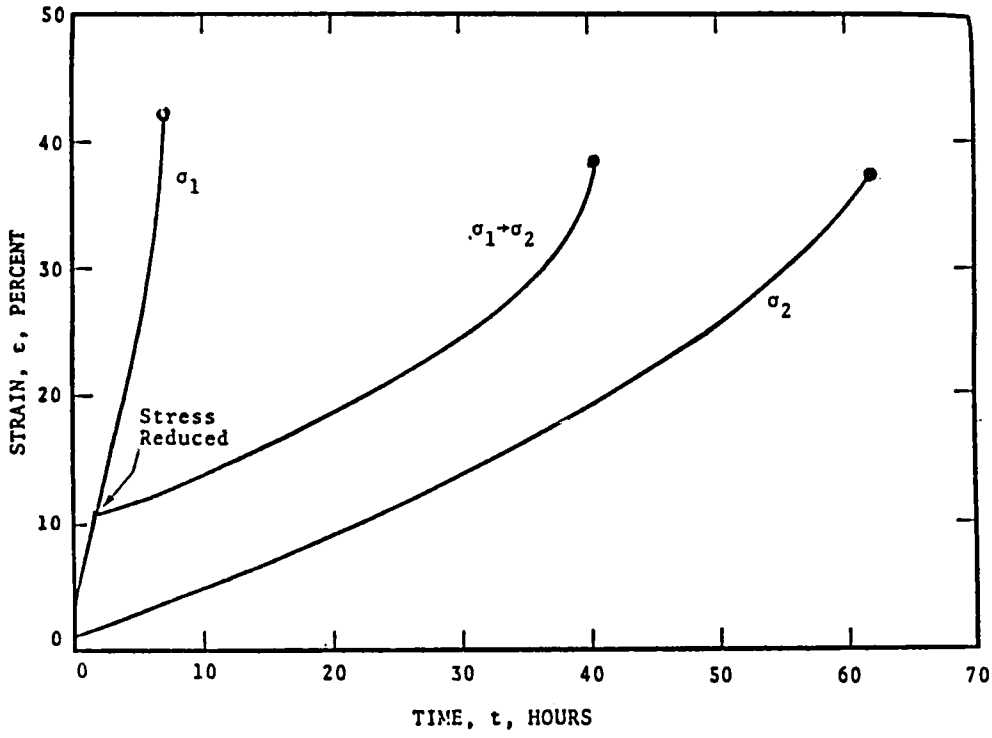

Fig. 1. Strain-time curves for 304 stainless steel tested at 704°C (σ_1 = 207 MPa, σ_2 = 151 MPa).

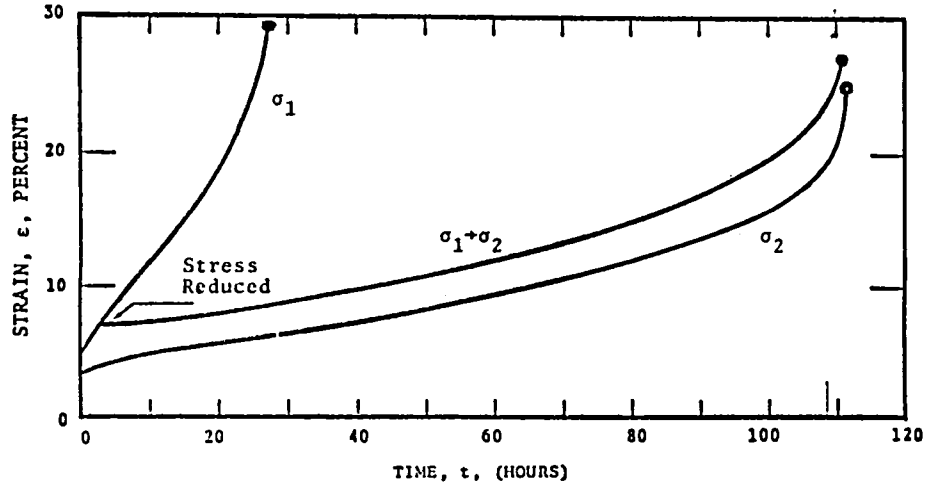

Fig. 2. Strain-time curves for 304 stainless steel tested at 650°C. (σ_1 = 172 MPa, σ_2 = 138 MPa)

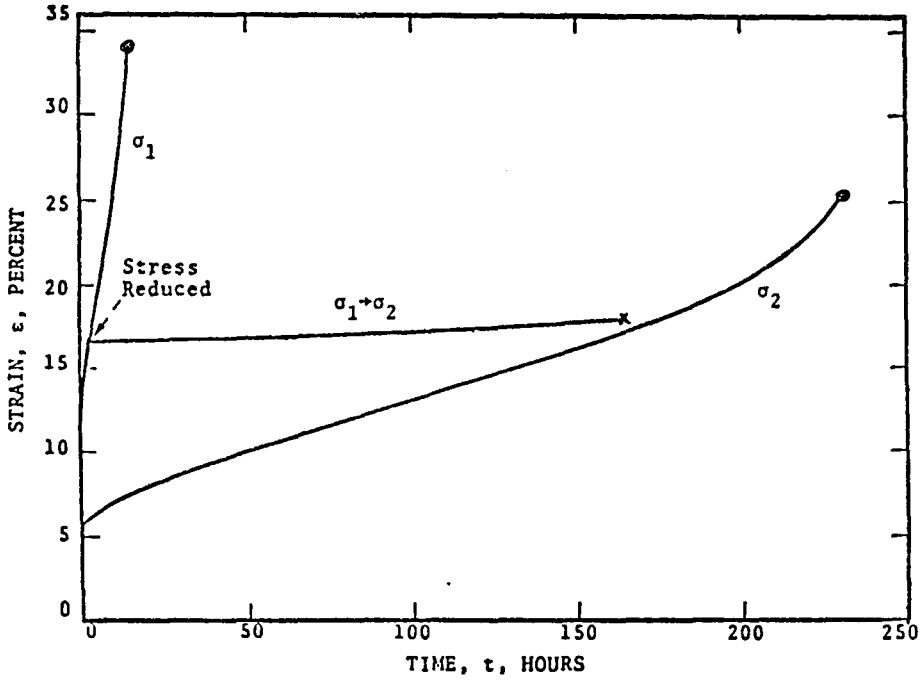

Fig. 3. Strain-time curves for 304 stainless steel tested at 593°C. (σ_1 = 276 MPa, σ_2 = 207 MPa)

A NONVOLUME PRESERVING PLASTICITY THEORY WITH APPLICATIONS TO POWDER METALLURGY*

Brice N. Cassenti
United Technologies Research Center
East Hartford, Connecticut 06108

ABSTRACT

A plasticity theory has been developed to predict the mechanical response of powder metals during hot isostatic pressing. The theory parameters were obtained through an experimental program consisting of hydrostatic pressure tests, uniaxial compression and uniaxial tension tests. A nonlinear finite element code was modified to include the theory and the results of the modified code compared favorably to the results from a verification experiment.

INTRODUCTION

In the Hot Isostatic Pressing (HIP) process a sheet metal container is fabricated in the approximate shape of a component to be manufactured. The container is evacuated, filled with a powder metal and sealed. The container is then placed in a HIP facility where it is subjected to high temperatures and pressures. For powder metals consisting of nickel base superalloys typical HIP temperatures are 1150C at pressures of 1000 atm. During the HIP all the void space is squeezed out from between the particles. After HIP the container is removed and the solid component remains.

* Work performed as a part of AFOSR Contract F49620-78-C-0090

The HIP process is ideally suited to the manufacture of turbine and compressor disks in jet engines and is cost competitive with forging. Unfortunately the final shape of the hot isostatic pressed component is not a photographic replica of the original container shape. Non-photographic distortions are introduced by several sources. Some of these include: intrinsic differences in the stiffness of the container at different locations, and distortions due to gravitational loading. The cost for constructing components by HIP could be substantially reduced if the final shape of the component resulting from a given container shape could be predicted.

The permanent volume reductions inherent to the HIP process, of about 35 percent, cannot be predicted by classical plasticity theory, which assumes no permanent volume changes. Therefore classical plasticity theory must be modified to include permanent volume changes. Additionally, volume reductions of 35 percent imply linear strains of 10 to 15 percent and therefore large strain measures must be employed.

There have been previous attempts, Refs. 1-9, to describe the deformation mechanics of powder metals, but none of these has been successfully applied to the prediction of the final shape of hot isostatic pressed components.

A nonvolume preserving plasticity theory has been developed for this purpose. The parameters for the theory were found through the execution of an experimental program. The theory was added to the MARC* computer code. The computer code was used to model a simple verification experiment and the

* MARC Analysis Research Corporation

results predicted by the code compared favorably to the results of the experiment. Each of the above topics will be discussed in the following sections.

ACKNOWLEDGEMENTS

The author would like to acknowledge Dr. David Parks for his help in developing the plasticity theory and especially for the development of Eqs. (14) through (19). The author would also like to thank Dr. Kenneth Cheverton for his aid in defining the early stages of the program.

PLASTICITY THEORY

A finite strain plasticity theory requires: (1) specification of a yield surface to delineate regions of elastic and plastic response, (2) a hardening rule for the expansion of this yield surface, and (3) a flow rule for relating stress and strain increments. This flow rule must be formulated using large strain, stress and stress rate measures. Each of these topics will be considered separately below.

Yield Surface Formulation

A yield surface can be developed based on heuristic arguments. Since the powder particle orientation is random, the powder aggregate should initially respond isotropically. Thus the yield function must be an isotropic function and depend on only the stress through its three invariants. Also, yielding must occur under hydrostatic pressure and the yield function must approach that of a metal as densification progresses. Since invariant

I_1 is a linear multiple of the hydrostatic component of stress, and yield surfaces for metals are usually defined in terms of invariant J_2, which is the second invariant of the deviatoric stress tensor, both of these invariants must appear in the yield function

$$f = f(I_1, J_2, J_3, h_\alpha) = 0 \tag{1}$$

where the third invariant, J_3, of the deviatoric stress tensor has been included for completeness, and

$I_1 = \sigma_{KK}$

$J_2 = 1/2 S_{ij} S_{ij}$

$J_3 = 1/6 \epsilon_{ijk} \epsilon_{lmn} S_{il} S_{jm} S_{kn}$ is the determinant of the deviatoric stress tensor

$S_{ij} = \sigma_{ij} - 1/3 \delta_{ij} \sigma_{kk}$ is the deviatoric stress tensor, and

σ_{ij} is the stress tensor

δ_{ij} is the Kronecker delta

ϵ_{ijk} is the permutation tensor

The parameters h_α were determined experimentally and depend on deformation measures, η_α.

Assume that a HIP powder metal has unequal responses in tension and compression, and that the yield surface has no sharp corners. A simple yield function satisfying the above assumptions is

$$\beta^2 \left(\frac{I_{1+\alpha}}{3} \right)^2 + J_2 = \sigma_o^2/3 \tag{2}$$

A yield function of the form of Eq. (2) has previously been proposed by Green in Ref. 4, Shima and Oyane in Ref. 7, and Kuhn and Downey in Ref. 8. Equation

(2) is an ellipse in I_1, $\sqrt{J_2}$ space (Fig. 1), with deformation dependent parameters, α, β and σ_o. The yield surface is plotted in principal stress space with σ_3 zero in Fig. 2, for the case $\alpha = 0$.

A large strain theory of plasticity based on Eq. (2) can be developed by decomposing the symmetric part of the velocity gradient tensor, D_{ij} into elastic and plastic parts, or

$$D_{ij} = \frac{1}{2}\left(\frac{\partial v_i}{\partial x_j} + \frac{\partial v_j}{\partial x_i}\right) = D^e_{ij} + D^p_{ij} \tag{3}$$

The plastic deformation rate D^p_{ij} is assumed to be given by an associated flow rule

$$D^p_{ij} = \dot{\lambda}\frac{\partial f}{\partial \sigma_{ij}} \tag{4}$$

Where $\dot{\lambda}$ is a scalar function greater than zero. The choice of the deformation parameters, η_α, and the specification of the flow rule will be discussed in the following two sections.

Choice of Hardening Deformation Parameters

In this section, strain hardening of a compacting metal powder is discussed and parameters to characterize hardening are identified. This is necessary to complete the specification of the plastic deformation. Initially, the yield surface of the powder aggregate will be small. During the compaction and sintering process yield strength will grow and the yield surface will expand. Compaction alone will cause growth of the yield surface along only the I_1 axis (Fig. 1) with a theoretical limit corresponding to full densification. Yield stress in shear will be less affected by compaction. Additionally, yield strength will grow

in all directions of stress space with increased sintering time. Thus, there exists a time dependent hardening phenomenon unique to powder metallurgy. Since plastic deformations are assumed to occur instantaneously, time enters the plasticity theory as a parameter defining yield surface size at the time of plastic deformation.

The process of strain-hardening in triaxial pressure will primarily be a geometric effect on the microscopic scale. There could also be a contribution to the apparent macroscopic hardening due to real strain hardening of the particles as they experience large plastic shearing deformations. Such an effect could raise the effective yield strength of the metal particles. The separate contributions of matrix hardening and void reduction can be determined from systematic experiments using different initial volume fractions.

Initially, powder particles contact each other at isolated points. As pressure is applied, the contact areas and the powder stiffness increase. The macroscopic result is strain hardening of the powder due to macroscopic shrinkage. In the limit the powder is completely compacted and the response to further pressure increments is elastic dilation; the plastic bulk molulus has become infinite.

An obvious choice for a deformation measure, η_1, is the void volume fraction. The void volume fraction is a measure of the macroscopic shrinkage and should reflect an increase in stiffness due to an increase in contact area between the individual particles, or

$$\eta_1 = v \tag{5}$$

The void volume fraction does not represent any permanent changes that occur during plastic deformation. If as in classicial plasticity theory the effective

plastic strain is used this would not represent all of the permanent deformations since permanent volume changes would not be represented. A third deformation measure, the plastic volume change would then be required.

Rather than use the permanent volume change and the effective plastic strain as two independent deformation measures, a single measure, the plastic work, would be sufficient to represent both effects. Therefore, let

$$\eta_2 = W^P = \int_o^t \sigma_{ij} D^P_{ij} dt \tag{6}$$

In classicial volume preserving plasticity theory using either the plastic work or the effective plastic strain produces exactly the same result. The plastic work, or equivalently the inelastic energy dissipation has been used previously to describe nonlinear material response, for example, in Refs. 9 and 10.

Development of Flow Rule

It is now possible to describe the symmetric part of the velocity gradient tensor, D_{ij} in terms of the stress rate, for small strains, using Hooke's Law for the elastic response and Eq. (4) for the plastic response in the form

$$\dot{\sigma}_{ij} = L^{e.p}_{ijkl} D_{k\ell} = L^{e.p}_{ijkl} \dot{\varepsilon}_{k\ell} \tag{7}$$

where for small strains

$$D_{k\ell} = \dot{\varepsilon}_{k\ell} \tag{8}$$

In general the yield function is of the form

$$f(\sigma_{ij}, h_\alpha) = 0 \tag{9}$$

where elastic deformations occur when $f < 0$ and plastic deformations occur when $f = 0$ and where h_α are parameters in the yield surface dependent on deformation history measures η_β, or

$$h_\alpha = h_\alpha\ (\eta_\beta)$$

Assume that the plastic deformations are given by an associated flow rule

$$\dot{\varepsilon}^p_{ij} = \lambda \frac{\partial f}{\partial \sigma_{ij}} \tag{10}$$

Using Hooke's law for the elastic deformations

$$\dot{\varepsilon}^e_{ij} = \frac{1}{E}\ (1+\nu)\dot{\sigma}_{ij} - \nu\sigma_{kk}\delta_{ij} \tag{11}$$

the total strain rate can be written as

$$\dot{\varepsilon}_{ij} = \dot{\varepsilon}^e_{ij} + \dot{\varepsilon}^p_{ij} \tag{12}$$

Equation (9) can be equivalently written as

$$\dot{f} = \frac{\partial f}{\partial \sigma_{ij}}\ \dot{\sigma}_{ij} + \frac{\partial f}{\partial h_\alpha}\ \frac{\partial h_\alpha}{\partial \eta_\beta}\ \dot{\eta}_\beta = 0 \tag{13}$$

In Ref. 11, Parks has shown that

$$\dot{\eta}_\beta = \dot{\lambda} k_\beta \tag{14}$$

where

$$(\dot{}) = \partial(\ )/\partial t \tag{15}$$

The quantity k_1 can be determined from

$$\dot{\eta}_1 = \dot{v} = (1-v)D_{kk} = \dot{\lambda}k_1 \tag{16}$$

and k_2 can be found from

$$\dot{\eta}_2 = \dot{W}^p = \sigma_{ij}D^p_{ij} = \dot{\lambda}k_2 \tag{17}$$

For the yield surface of Eq. (2), from Ref. 11

$$k_1 \approx \frac{2}{3}\ (1-v)\ \beta^2(I_1+\alpha) \tag{18}$$

$$k_2 = \frac{2}{3}\left[\sigma_o^{\,2} - \alpha\beta^2\left(\frac{I_1+\alpha}{3}\right)\right] \tag{19}$$

Equations (7) through (13) can be solved to give

$$L^{e\cdot p}_{ijkl} = \frac{E}{1+\nu}\left\{ \delta_{ik}\delta_{jl} - \frac{\frac{\partial f}{\partial \sigma_{ij}}\frac{\partial f}{\partial \sigma_{kl}}}{\frac{\partial f}{\partial \sigma_{mn}}\frac{\partial f}{\partial \sigma_{mn}} - \left(\frac{1+\nu}{E}\right)H} \right.$$

$$\left. + \left(\frac{\nu}{E}\right)\frac{\left[\delta_{ij} - \frac{\frac{\partial f}{\partial \sigma_{mm}}\frac{\partial f}{\partial \sigma_{ij}}}{\frac{\partial f}{\partial \sigma_{mn}}\frac{\partial f}{\partial \sigma_{mn}} - \left(\frac{1+\nu}{E}\right)H}\right]\left[\delta_{kl} - \frac{\frac{\partial f}{\partial \sigma_{nn}}\frac{\delta f}{\delta \sigma_{kl}}}{\frac{\partial f}{\partial \sigma_{mn}}\frac{\partial f}{\partial \sigma_{mn}} - \left(\frac{1+\nu}{E}\right)H}\right]}{\frac{1-2\nu}{E} + \left(\frac{\nu}{E}\right)\left[\frac{\frac{\delta f}{\delta \sigma_{mm}}\frac{\delta f}{\delta \sigma_{nn}}}{\frac{\partial f}{\partial \sigma_{mn}}\frac{\partial f}{\partial \sigma_{mn}} - \left(\frac{1+\nu}{E}\right)H}\right]} \right\} \quad (20)$$

where

$$H = \frac{\partial f}{\partial h_\alpha}\frac{\partial h_\alpha}{\partial \eta_\beta}k_\beta \quad (21)$$

The quantities $\frac{\partial h_\alpha}{\partial \eta_\beta}$ are hardening parameters which are determined from the mechanical test results and described in the section on Material Property Determination. A more detailed discussion of the plastic flow rule can be found in Ref. 12.

Large Strain Flow Rule Considerations

Following McMeeking and Rice, Ref. 13, when using the current deformed state as the reference configuration, all stress measures coincide. However, the rates associated with these stress measures do not coincide. A stress rate which is useful for expressing large deformation consitutive laws is the Jaumann, or corotational rate (Ref. 14). The Jaumann rate of Cauchy stress is

$$\overset{\nabla}{\sigma}_{ij} = \dot{\sigma}_{ij} - \sigma_{ip}\Omega_{pj} + \Omega_{ip}\sigma_{pj} \quad (22)$$

where σ_{ij} is the material time rate of Cauchy stress σ_{ij} and

$$\Omega_{ij} = \frac{1}{2} (\partial v_i/\partial x_j - \partial v_j/\partial x_i)$$

The constitutive law of interest is of the form

$$\overset{\nabla}{\sigma}_{ij} = L_{ijkl} D_{kl} \tag{23}$$

where L denotes the rate moduli, D_{ij} is the symmetric part of the velocity gradient tensor.

L_{ijkl} is developed in Ref. 15 for large strains as

$$L_{ijkl} = L^{e\cdot p}_{ijkl} - \frac{1}{2} \left[\delta_{ik}\sigma_{jl} + \delta_{jk}\sigma_{il} + \delta_{il}\sigma_{jk} + \delta_{jl}\sigma_{ik} \right] + \sigma_{ij}\delta_{kl} \tag{24}$$

and $L^{e\cdot p}_{ijkl}$ is the small strain elastic-plastic stiffness in Eq. (21). The tensor L_{ijkl} is not symmetric due to the presence of the last term, or

$$L_{ijkl} \neq L_{klij}$$

For a hydrostatic pressure

$$\sigma_{ij} = P\delta_{ij}$$

the tensor is symmetric and since this should be the primary part of the loading during the HIP process, the last term should produce a nearly symmetric stiffness. It, therefore, was decided to separate the last term into symmetric and unsymmetric parts, and add the symmetric part to the stiffness matrix and transfer the unsymmetric part to the loading side of the governing equations.

MATERIAL PROPERTY DETERMINATION

To predict the mechanical response of metal powder subjected to the HIP process it is necessary to know the mechanical properties of the metal during the HIP cycle. These mechanical properties can be obtained by removing test specimens from the HIP facility at various stages in a HIP cycle. The partial HIP samples would represent the powder at various stages for a pressure-temperature history. A complete description of the mechanical properties can then be obtained by postulating yield surfaces, flow rules, hardening laws and creep properties and comparing these predictions to the results of mechanical tests on the partial HIP samples.

Partial HIP Tests

The UTRC HIP facility has been utilized to process powder metals through temperature-pressure-time profiles closely paralleling the procedure used to fabricate full size turbine disks to near net shape.

The HIP facilities allow several partial HIP samples to be preheated simultaneously. Since the powder is initially weak a container is required to retain the powder shape for temperatures exceeding 2000 F (1100 C). Therefore, all specimens were preheated at 2000 F (1100 C) and 1 atm for 12 hr. During the preheat cycle the powder is encapsulated in quartz and attains sufficient strength from sintering to be handled. During the preheat the density changed from 60 to 65 percent of full density initially to 65 to 70 percent of full density upon completion of the cycle.

After the completion of the preheat cycle the samples have the quartz container removed and a glass container substituted. At HIP temperatures the inside surface of the glass container fuses with the outer powder metal particles and forms a gas tight seal about the powder metal, and the glass has no strength or stiffness. Consequently, a uniform hydrostatic stress is transmitted to the powder metal. The glass container with the preheated or sintered powder metal is next placed in the HIP facility and subjected to a specified temperature, pressure time cycle.

A set of tests was performed at 1800 F (982 C) and various pressure, with the maximum temperature and pressure acting for 10 minutes only. These tests successfully produced partially dense samples. The test regime was expanded to include 1600 F (871 C), 1900 F (1638 C) and 2000 F (1093 C) at appropriate pressures and again the time at maximum temperature and pressure was held to 10 min.

Some understanding of the compaction process can be obtained by applying the hydrostatic pressure plastic compaction model (Ref. 16), where the yield pressure was represented by

$$\frac{P_y}{\sigma_y} = \frac{2}{3}\left[-\ln\left(\frac{v}{v_i}\right) - \left(1-\frac{v}{v_i}\right)^2 \ln v_i + a\left(\frac{v}{v_i}\right)\left(1-\frac{v}{v_i}\right)\right] \qquad (25)$$

$$a = \frac{C\, v_i}{(1-v_i)\, \tan^2\theta} - 1 \qquad (26)$$

and

$$\cos\theta = \frac{\rho_i}{4} + \sqrt{\left(\frac{\rho_i}{2}\right)\left(\frac{1+\rho_i}{8}\right)} \quad , \text{ and} \qquad (27)$$

where v_i = the initial void volume fraction

$\rho_i = 1-v_i$ is the initial relative density, and

$C \approx 2.75$

In order to apply the model the yield stress of the powder particle material must be known. This data does not exist and therefore the short time partial HIP data has to be reduced to determine the yield stress. For each of the temperatures, 1600 F (871 C), 1800 F (982 C) and 2000 F (1093 C), the yield stress was estimated and Eq. (25) was applied to determine the relative density for various applied pressures. Figure 3 presents the results of the calculations and demonstrates good agreement for the yield stresses given by

$$\sigma_y = \left(1.1 \times 10^9 \text{ ksi}\right) e^{-\frac{T}{120.7\ R}} = \left(7.58 \times 10^{12} \text{ nt/m}^2\right) e^{\frac{-T}{67\ K}} \qquad (28)$$

Equation 28 results in yield stresses that are somewhat low for superalloys. Three facts could account for this: (1) the yield stress for the pre-HIP powder metal is generally lower than for the fully consolidated power, (2) the strain rate during a partial HIP cycle is relatively slow and therefore produces a somewhat lower effective yield stress, and (3) the creep rates at high temperatures are relatively high, producing an apparently lower yield stress.

Mechanical Tests

To determine the shape of the yield surface several types of mechanical tests are required. Each type of test produces one point on the yield surface. There is one point on the surface that is known: the hydrostatic

pressure of the HIP process. A compression test performed at temperature will provide a second point on the yield surface and will also provide some information on the elastic, hardening and plastic flow of the material. Tension tests performed at temperature, when compared to a compression test performed at temperature, will determine the symmetry of the yield surface. The compression tests are the most important tests to be performed since they produce a hydrostatic pressure which is the predominant loading feature during a HIP cycle. Two deformation measures will be used to characterize the yield surface; the void volume fraction and the plastic (nonrecoverable) work. Therefore, the measurement of the axial length change is not sufficient to determine the mechanical response and a measurement of the volume will also be required. The final volume of a compression specimen was measured after a completed test but this does not provide a complete description of the path to the final state.

More than thirty compression tests were performed. Three of these tests were used to size the compression specimens and determine the test conditions. The remaining tests were all completed in a similar manner. The specimens consisted of a right circular cylinder 0.5 in (.127 cm) long by 0.2 in. (0.51 cm) in diameter. Each specimen was placed in a furnace in an inert gas and brought up to the temperature at which the specimen was hot isostatically pressed. At temperature the specimen was subjected to compression crosshead displacement rate of 0.0025 in./min (0.00635 cm/min) and the load was recorded. After the load leveled out, the crosshead rate was doubled to 0.005 in./min (0.00127 cm/min).

The average values for the height, diameter, and volume change measurements are presented in Table 1 along with the standard deviations. From the last column in Table 1 it can be seen that over all the samples there was a significant decrease in the height and a significant increase in the diameter, while there was essentially no change in the volume.

A total of 14 tensile tests were completed and resulted in significantly lower yield stress values than the compression tests, especially at 2000 F (1093 C). The low tensile yield stresses could be a result of the presence of voids which would be adjacent to the particle interfaces. Tensile stresses, which are amplified at the void, would tend to separate the particles producing a smaller apparent yield than compression stresses which would tend to close the voids. Microscopic examination and room temperature tensile tests (Ref. 14), indicated the powder was not contaminated.

The uncertainty associated with the tensile test results necessitated the use of the experimental observation that the volume was conserved during compression.

Interpretation of Mechanical Test Results

The mechanical tests indicated that there is little or no volume change in compression. Coupling this fact with the hydrostatic pressure yield stress, P_y, and the compressive yield stress σ_c will determine all of the yield parameters in Eq. (9) as

$$\alpha = \sigma_c \tag{29}$$

$$\beta^2 = \frac{3}{q^2} \tag{30}$$

$$\sigma_o = \sigma_c \tag{31}$$

where

$$q = \frac{3\ P_y}{\sigma_c} - 1 \tag{32}$$

The experimental results for the tensile yield stress, σ_T, were not reliable but can be determined from Eq. (2) as

$$\sigma_T = \left(\frac{q^2-1}{q^2+1}\right) \sigma_c \tag{33}$$

Normalizing the compressive yield stress data, σ_c, with respect to the initial powder particle yield stress, σ_y, shows that this ratio is approximately a linear function of relative density as shown in Fig. 4, or

$$\frac{\sigma_c}{\sigma_y} = b\left(\frac{v_i - v}{1-v_i}\right) \tag{34}$$

where P_y is evaluated from Eq. (61) by setting P equal to P_y

v is void volume fraction

v_i is initial void volume fraction, and

b can be determined by requiring the tensile yield stress to vanish at the initial void volume fraction, or

$\sigma_T = 0$ at $v = v_i$

From Eqs. (32) and (33), the above condition on b is

$$\lim_{v \to v_i} \frac{P_y}{\sigma_c} = \frac{2}{3} \tag{35}$$

Then from Eqs. (25) and (34)

$$b = \frac{C}{\tan^2 \theta} \tag{36}$$

where θ is given by Eq. (27) and $C \approx 2.75$.

The temperature, T, and strain rate, $\dot{\varepsilon}$, dependence have been included in the initial particle yield stress, σ_y. A good fit occurs when

$$\sigma_y = \sigma_{y_o} e^{-\frac{T}{T_o}} \left[1+\alpha \ln\left(\frac{\dot{\varepsilon}}{\dot{\varepsilon}_o}\right)\right] \tag{37}$$

for uniaxial stress conditions.

A good fit to the specimens partially densified in the HIP facility occurs if

$$\dot{\varepsilon} \approx 0.00315/\text{min.}$$

The parameters in Eq. (37) are

σ_{y_o} = 1.074×10^{10} kis (7.41×10^{13} nt/m^2)

T_o = 120.7 R (67.06 K)

α = 0.03403, and

$\dot{\varepsilon}_o$ = 8.148×10^{8}/min.

Equations (29) through (37) are the plastic formulation added to the MARC code, and are compared to the experimental measurements in Figs. 3, 4, and 5. The agreement is good if the volumetric creep under hydrostatic pressure is included (Fig. 3). Volumetric creep will move points subject to HIP for more than 10

min (the solid symbols in Fig. 3) to the right of the line representing instantaneous plastic deformation.

Although little work hardening was observed during the compression tests, it may have an influence on the final deformations, and therefore an approximate hardening law of the form of Eq. (38) below was assumed.

$$\sigma_c = b\left(\frac{v-v_i}{1-v_i}\right)\sigma_y\left[1 - a_1\, e^{-a_2 W^P}\right] \tag{38}$$

where W^P is the plastic work, a_1, a_2 are constant work hardening parameters.

From the uniaxial compression tests it was noted that the compressive yield stress seems to level off at about 1.4 times the initial compressive yield stress and therefore the constant a_1 is given by

$$a_1 = 0.286 \tag{39}$$

The constant a_2 was found to vary with temperature approximately by the relation

$$\frac{1}{a_2} = \begin{cases} C_2\left(\frac{T_c-T}{\Delta T_o}\right) & T \le T_c \\ 0 & T \ge T_c \end{cases} \tag{40}$$

where C_2 = 9090 psi ($6.26 \times 10^6 \frac{nt}{m^2}$)

T_c = 2020 F (1104 C)

ΔT_o = 420 F (216 C)

A more complete discussion of the work hardening evaluation is given in Ref. 14.

The elastic constants are required to complete the formulation but only Young's modulus can be derived from the compression test data. The Young's

Modulus, E, was assumed to be linear function of void volume fraction, v, and an exponential function of temperature, T, given below

$$E = E_1 \, e^{-\frac{T-T_o}{T_1}} \left(\frac{v_i - v}{v_i}\right) \tag{41}$$

where v_i is the initial void volume fraction, and E_1, T_o and T_1 were chosen to provide a good fit to the data, as

$$E_1 = 1.5 \times 10^6 \text{ psi}$$

$$T_o = 1900 \text{ F } (1038 \text{ C})$$

$$T_1 = 163 \text{ F } (72.8 \text{ C})$$

Figure 6 compares the analytical expression with the resulting mechanical test data. The comparison is within the experimental error. Since it was not possible to measure radial deflections during the testing, Poisson's ratio could not be determined.

It should be noted that if the tensile strengths were accurately measured, a yield surface utilizing: the hydrostatic yield pressure, the compression yield stress, the tension yield stress and the fact that volume was preserved during compression, could have been taken as

$$\beta^2 \left(\frac{I_1+\alpha}{3}\right)^2 + J_2 \left\{1+\gamma \left(1+ \frac{9\, J_3}{2\sqrt{3}\, J_2^{3/2}}\right)\right\} - \frac{\sigma_o^2}{3} = 0 \tag{42}$$

where β, α, and σ_o are given by Eqs. (29-31), and

$$\gamma = \frac{1}{2}\left\{\left(\frac{\sigma_c}{\sigma_T}\right)^2 - 1 - \frac{\left(\frac{\sigma_c}{\sigma_T} + 1\right)^2}{\left(\frac{3\ P_y}{\sigma_c} - 1\right)^2}\right\} \tag{43}$$

and J_3 is the third invariant of the deviatonic stress tensor

Note that if σ_T is given by Eq. (33) the parameter γ vanishes.

With the experimental specification of the parameters the yield surface is completely determined.

MODEL VERIFICATION

Verification Criteria

The validation tests were designed to avoid duplication of the uniform hydrostatic stress state of the partial HIP tests. The experiments must therefore result in a nonvanishing shear stress within the sintered material. A nonhydrostatic stress state can be achieved with the application of the uniform external pressure if the material has nonhomogenous properties. This may be achieved by imbedding in the metal powder a different material, for example, steel spheres or fully compacted powder spheres or cylinders. Such an experimental configuration will produce a nonhydrostatic stress state and will make use of existing hardware and techniques. Metal foil could be placed tangent to a steel sphere and the resulting displacements measured and compared to the predicted displacements.

Plastic Analysis for Spherical Inclusions

Before proceeding with the verification experiments, a finite element

model of the experiment was analyzed using a version of the MARC code modified to include the powder metal constitutive properties of 7 axisymmetric elements illustrated in Fig. 7. Constraints were set to insure only spherically symmetric radial displacement would result, The steel sphere was modeled as rigid, and therefore the radial displacements were fixed in the powder at the surface of the steel sphere. The analysis considered only the plastic deformations that would result in raising the external pressure to 1000 atm. In Fig. 8, the model resulted in predictions that the void volume fraction decreased near the sphere or the density is highest near the sphere. At an applied external pressure of 1000 atm all points in the specimen are more than 90 percent of full density. The deflections of the foil can be easily calculated using the radial displacements and are presented as a function of the distance from the center of the foil, as shown in Fig. 8. At about 8 ksi (533 atm) the edge of the foil should be nearly flat. These conditions had been run during the partial HIP tests and produced a relative density of about 0.85, which agrees with the predicted results presented in Fig. 8,

Verification Results

The specimen design consists of a steel sphere imbedded in a sintered rod. A layer of nickel foil is placed tangent to the sphere. One, two, or three sphere and nickel foil configurations are placed within the sintered bar. Figure 9 illustrates a typical configuration. The first verification experiment consisted of a test to insure the configuration would HIP properly and was successfully completed,

Two sintered bars were hot isostatic pressed, based on the above success and the finite element results for a maximum of 10 min at 1800 F, (982 C) and 8 psi (533 atm). These bars contained a total of five 0.25 (0.63 cm) diameter spheres.

Foil displacement measurements were successfully obtained from three of the five spheres and the results of these measurements are presented in Fig. 10, along with the prediction from the finite element model.

The lack of agreement near the center may be due to either the relative elasticity of the sphere and powder including thermal effects, which were not modeled, or due to the weight of the sphere. The rapid decrease in error with position indicates the error may be due to the elastic effects. Another source for the difference can be attributed to the fact that the foil and the upper and lower bar segments may not have been in contact and gradually brought into contact as the HIP progressed. The numerical predictions and the experimental measurements agree to within the accuracy of the experiment, and verify that an accurate mechanical description of the powder response has been developed.

CONCLUSIONS

In the analysis developed, classical plasticity theory has been extended to include the large permanent changes in volume of about 30 percent that are incurred during HIP. The theory developed assumes an isotropic yield surface and uses an associated flow rule. The assumed yield surface includes all three invariants of the stress tensor although presently the yield surface

only uses the first invariant of the stress tensor, and the second invariant of the deviatoric stress tensor.

The parameters in the theory were obtained through an experimental program consisting of hydrostatic pressure tests, uniaxial compression and uniaxial tension tests. From the hydrostatic pressure tests a simple analytical expression was developed that predicted the change in density as a function of pressure and temperature. Results of the compression tests indicated that there is no measurable change in volume in compression and that the compression yield stress is a linear function of void volume fraction. The uniaxial tension tests were inconclusive and the results were used for comparison with prediction from the theoretical model only.

Isotropic hardening of the yield surface was assumed to depend on void volume fraction and plastic work accumulated. Experimental results showed that the primary dependence was on void volume fraction.

A nonlinear finite element code was modified to include the plasticity theory and an experiment was run to verify the theory and the code modifications. The verification experiment consisted of steel spheres imbedded in partially dense bars of powder metal. Each of the spheres had a layer of foil placed tangent to the sphere. The bar, with spheres and foil, was placed in a furnace and subjected to a pressure loading of 8 ksi (533 atm) at 1800° F. The resulting distortion of the foil was measured and compared to the results of a finite element analysis using the modified code. The numerical prediction and the experimental measurements agreed to within the accuracy of the experiment.

As a result a modified finite element code exists capable of predicting the mechanical reponse of powder metals and is now being applied to predict the final shape of components manufactured by the HIP process.

REFERENCES

1. Wilkinson, D. S. and Ashby, M. F., "The Development of Pressure Sintering Maps," Sintering and Catalysis Materials Science Research, Vol. 10, G. C. Kuczynski, Ed., Plenum Press, 1975, pp. 473-492.

2. Ramquist, L., "Theories of Hot Pressing, Power Metallurgy," Vol. 9, No. 17, 1966, pp. 1-25.

3. Torre, C., "Berg-Hutterman, Montash, Montan," Hochschule Loeben, Vol. 93, 1948, p. 62.

4. Green, R. J., "A Plasticity Theory for Porous Solids," International Journal for Mechanical Sciences," Vol. 14, 1972, pp. 215-224.

5. Suh, N. P., "A Yield Criterion for Plastic, Frictional, Work-Hardening Granular Materials," International Journal of Powder Metallurgy, Vol. 5, 1969, pp. 69-87.

6. Needleman, A., "Void Growth in an Elastic Plastic Medium," Journal of Applied Mechanisms," Vol. 38, 1972, pp. 964-970.

7. Shima, S. and Oyane, M., "Plasticity Theory for Porous Metals," International Journal of Mechanical Science, Vol. 18, 1976, pp. 285-291.

8. Kuhn, H. A. and Downey, C. L., "Deformation Characteristics and Plasticity Theory of Sintered Powder Materials," Internal Journal of Powder Metallurgy, Vol. 7, 1971, pp. 15-25.

9. Corapcioglu, Y. and Uz, T., "Constitutive Equations for Plastic Deformation of Porous Materials," Powder Technology, Vol. 21, 1978, pp. 269-274.

10. Bodner, S. R. and Partom, Y., "Constitutive Equations for Elastic-Visco Plastic Strain Hardening Materials," Journal of Applied Mechanics, Transation of the ASME, pp. 385-389, June 1975.

11. Parks, D. M., "Finite Deformation Plasticity Formutation for Compacting Metal Powders," Communication to B. N, Cassenti, dated March 25, 1979.

12. Cassenti, B. N., "Analytical Modeling of the Hot Isostatic Pressing Process," AFOSR-TR-81, Air Force Office of Scientific Research, Bolling Air Force Base, Washington, D. C., July 1980.

13. McMeeking, R. M. and Rice, J. R., "Finite-Element Formulations for Problems of Large Elastic-Plastic Deformation," International Journal of Solids and Structures, Vol. 10, 1974, pp. 321-339.

14. Prager, W., "Introduction to Mechanics of Continua," Ginn and Co., Boston, 1961.

15. Nagtegaal, J. C. and deJong, J. E., "Some Computational Aspects of Elastic-Plastic Large Strain Analysis," MARC Analysis Research Corporation, Palo Alto, California.

16. Cassenti, B. N., "The Manufacture of Disks by the Hot Isostatic Pressing Process," AIAA Paper No. 80-1111, AIAA/SAE/ASME 16th Joint Propulsion Conference, June 30 - July 2, 1980, Hartford, CT.

TABLE 1

STATISTICAL GEOMETRY CHANGES FOR
COMPRESSION TESTS

Ratio, Final/Initial	Mean m	Std. Dev. s	m-1 / s
Height	0.9345	0.029	-2.25
Diameter	1.0330	0.010	3.31
Volume	0.9975	0.015	-0.17

TABLE 2

RESULTS OF ROOM AND HIGH TEMPERATURE TENSILE TESTS

Specimen No.	Relative Density	Room Temperature Yield Stress (ksi) 0.2 Percent	Room Temperature Ultimate Stress (ksi)	Yield Stress (ksi) at 1800 deg. F
1004	0.990	144	168	0.022
1098*	0.900	-	82.4	0.126
1114	0.977	102	156	2.30
1115	0.984	138	164	-

* Failed in grip

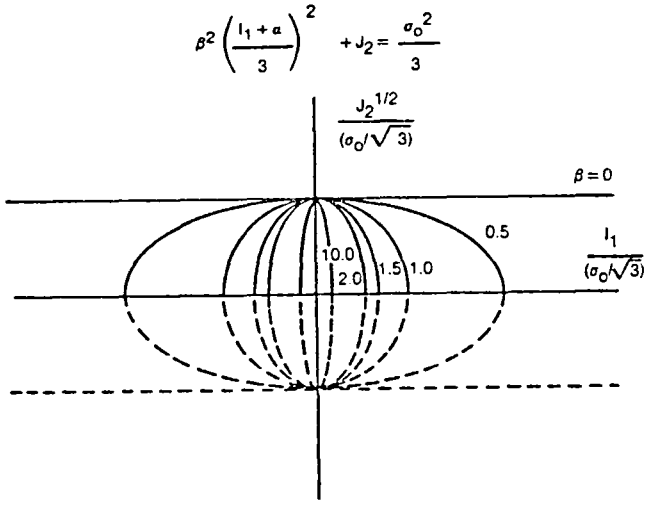

Fig. 1. Assumed yield surface in $I_1, J_2^{1/2}$ stress space for $\alpha = 0$

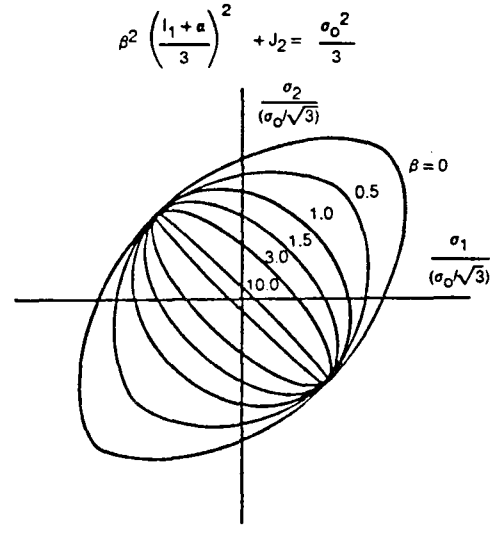

Fig. 2. Assumed yield surface in principal stress space for $\sigma_3 = 0, \alpha = 0$

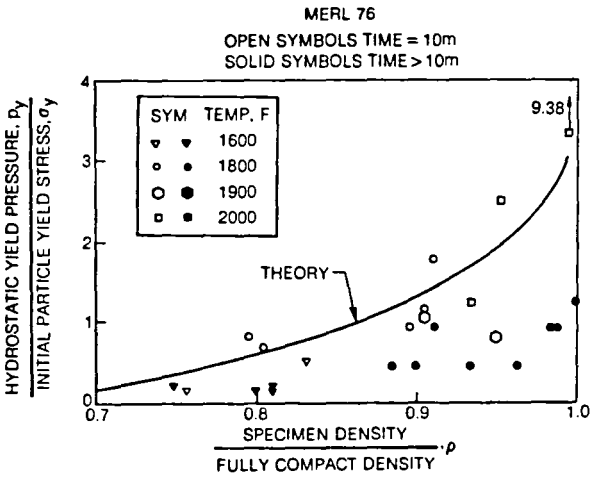

Fig. 3. Hydrostatic yield pressure test results

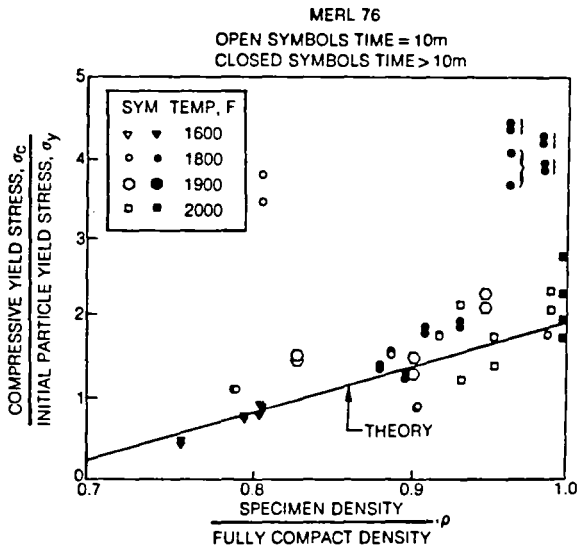

Fig. 4. Compressive yield stress results

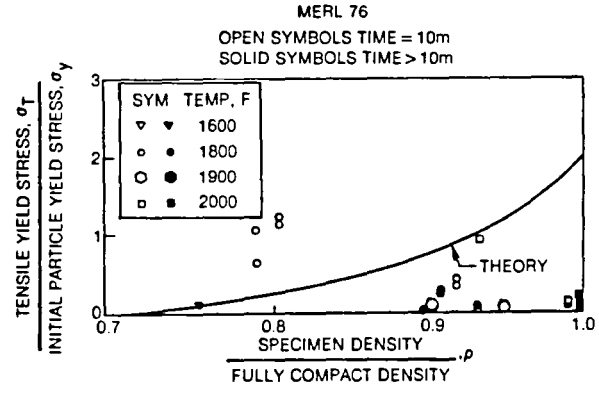

Fig. 5. Tensile yield stress results

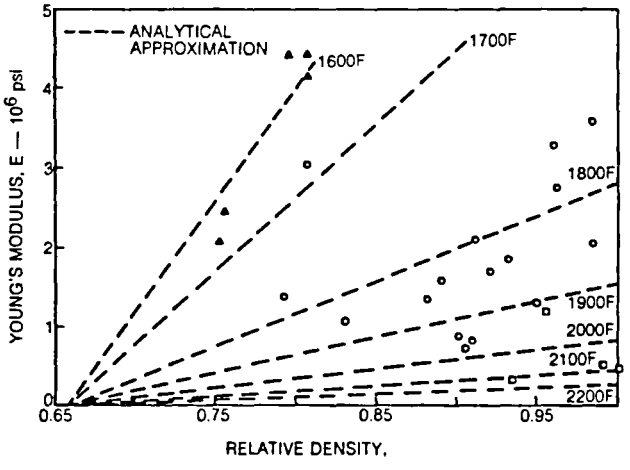

Fig. 6. Young's modulus for partially dense MERL 76

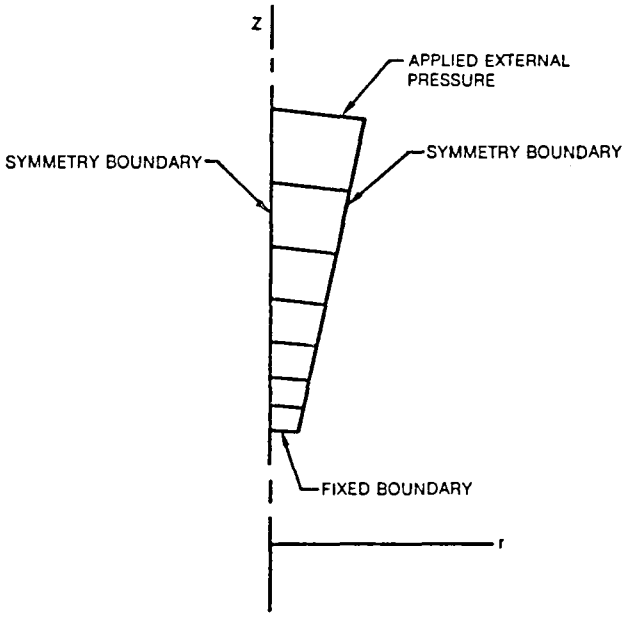

Fig. 7. Verification experiment finite element model

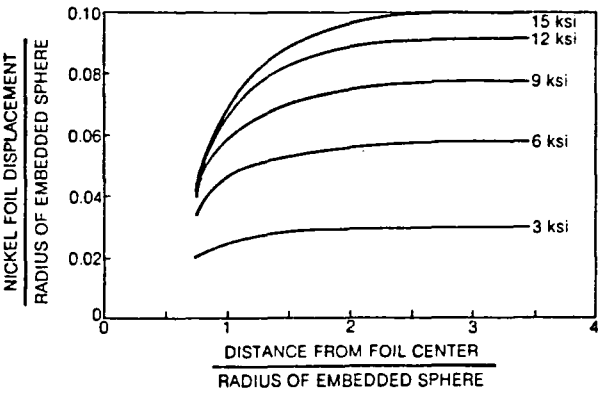

Fig. 8. Predicted nickel foil displacement for verification experiment

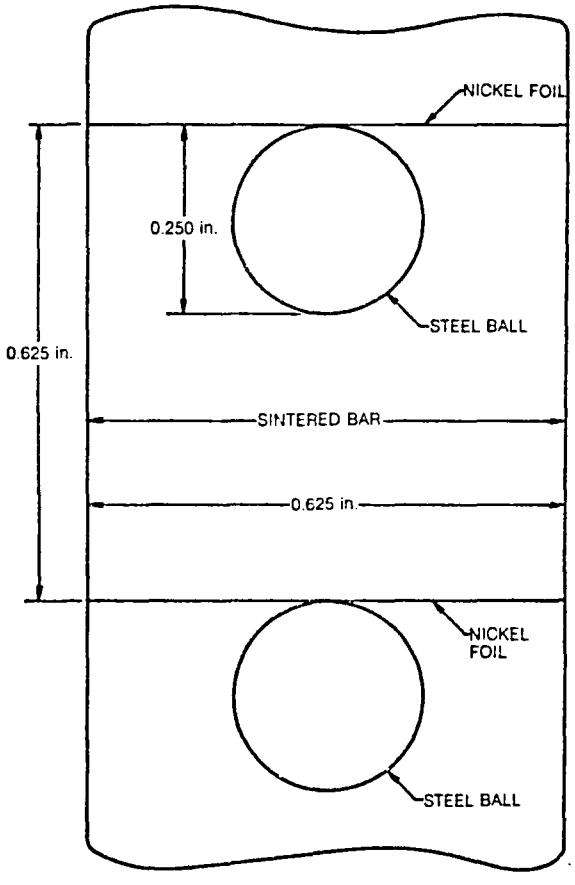

Fig. 9. Typical configuration of verification experiment

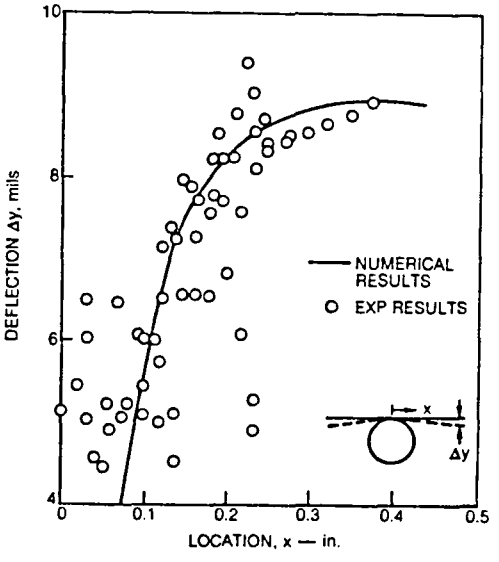

Fig. 10. Verification experiment

CONSTITUTIVE MODELS BASED ON COMPRESSIBLE PLASTIC FLOWS

A. M. Rajendran
University of Dayton Research Institute
Dayton, Ohio 45409

1. INTRODUCTION

The need for describing materials under time or cycle dependent loading conditions has been emphasized in recent years by several investigators (Ref. 1 through 4). In response to the need, various constitutive models describing the nonlinear behavior of materials under creep, fatigue, or other complex loading conditions were developed. The developed models for describing the fully dense (non-porous) materials were mostly based on uncoupled plasticity theory. The improved characterization of materials provides a better understanding of the structural response under complex loading conditions. However, the constitutive models describing the fully dense materials will be inadequate for characterizing the regions of the material where voids (porosity) develop due to various complex micromechanisms. For instance, voids may nucleate under high temperature loading conditions due to intergranular cavity formation around the second phase particles (Ref. 5). The necked portion of a tensile specimen and the ductile material at the crack tip are the few examples where the initially non-porous material becomes a porous aggregate due to debonding of the hard particles from the matrix. In these regions, the stress-strain relationship of the porous aggregate starts deviating from the matrix material behavior.

Several authors considered this aspect of the problem. Among them, Gurson (Ref. 6) presented a continuum theory of ductile rupture by void nucleation and growth and he came up with a constitutive equation for void containing materials, which explicitly considered the void volume fraction and the matrix stresses.

The constitutive models for compressible porous materials based on Gurson's yield criterion, was employed by Yamamota (Ref. 7) and also by Needleman and Triantafyllidis (Ref. 8) in a study of shearband localization in metal sheets and the influence of void growth on forming limit diagrams, respectively. These authors, while describing the porous aggregate, used an idealized simple rate-independent power-law type constitutive model to describe the incompressible matrix material. Their main purpose was to

predict the onset of localized necking or shearband localization through an approximate description of the porous aggregate and the matrix material. However, it is important to describe the matrix material behavior more accurately in order to properly characterize the porous region of the solid material under complex loading conditions.

The present paper provides a simple methodology to introduce void nucleation and its growth into the nonlinear incompressible constitutive equation through Gurson's yield criterion which is based on compressible plastic flow. This yield criterion is combined with the state variable flow theory of Bodner and Partom (Ref. 4), for the incompressible solid. Stouffer and Bodner (Ref. 9), have demonstrated the predictive ability of the state variable theory by applying it to high temperature nickel base super-alloys, such as IN100 and Rene' 95. Since the matrix material behavior is well characterized, this will result in an improved description of the porous material under complex loading conditions.

The usefulness of the present approach is its capability for establishing meaningful stress-strain behavior of a localized damage zone in which void initiation and growth is occurring and also of the surrounding zone of void free material.

2. CONSTITUTIVE MODEL FOR COMPRESSIBLE SOLID

To describe the void containing aggregate, the slightly modified version of Gurson's yield criterion as proposed by Tvergaard is considered (Ref. 10). The corresponding yield criterion used in the present paper is

$$\Phi = \frac{3J_2}{Y_m^2} + 2q_1 f \cosh\left(\frac{q_2 I_1}{2Y_m}\right) - q_3 f^2 - 1 = 0 \qquad (1)$$

where J_2 is the second invariant of the stress deviator, I_1 is the first stress invariant, Y_m is the equivalent stress of the matrix material, f is the current void volume fraction, and q_1, q_2, and q_3 are the void shape factors. The yield function, based on the spherically symmetric deformation of a rigid perfectly plastic body around a spherical void, as derived by Gurson (Ref. 6) can be retrieved by setting $q_1 = q_2 = q_3 = 1$ in equation 1.

Since the plastic work done by the aggregate is equal to the plastic work done by the matrix material, the plastic strain-rates in the aggregate ($\dot{\varepsilon}^p_{ij}$) and the matrix ($\dot{D}^p_m$) are related by the following expression

$$\sigma_{ij}\ \dot{\varepsilon}^{p}_{ij} = (1 - f)\ Y_m\ \dot{D}^{p}_{m} \ . \tag{2}$$

where σ_{ij} is the aggregate stress and the dot represents the time derivative.

The plastic strain-rates of the aggregate can be expressed in terms of the flow rule of the yield function as,

$$\dot{\varepsilon}^{p}_{ij} = \Lambda \frac{\partial \Phi}{\partial \sigma_{ij}} \tag{3}$$

where $\partial\Phi/\partial\sigma_{ij}$ is the partial derivative of the yield function with respect to the aggregate stresses. The proportionality factor, Λ, can be obtained by combining the equations (2) and (3) and the plastic strain-rates of the porous aggregate can be shown as

$$\dot{\varepsilon}^{p}_{ij} = \frac{(1 - f)\ Y_m\ \dot{D}^{p}_{m}}{\frac{\partial \Phi}{\partial \sigma_{kl}}\ \sigma_{kl}} \frac{\partial \Phi}{\partial \sigma_{ij}} \tag{4}$$

where repeated indices k and l mean summation.

The nonlinear constitutive relationship for the porous aggregate can expressed in terms of total strain-rate as sum of the elastic and plastic components. The corresponding relationship is given by,

$$\dot{\varepsilon}_{ij} = \frac{(1+\nu)}{E}\ \dot{\sigma}_{ij} - \frac{\nu}{E}\ \delta_{ij}\ \dot{\sigma}_{kk} + \frac{(1-f)\ Y_m\ \dot{D}^{p}_{m}}{\frac{\partial \Phi}{\partial \sigma_{kl}}\ \sigma_{kl}} \frac{\partial \Phi}{\partial \sigma_{ij}} \tag{5}$$

where ν and E are poisson's ratio and elastic modulus, respectively. The above equation describes the porous aggregate for a given stress-strain behavior of the matrix material.

The void volume fraction rate ($\dot{f}$) of the aggregate consists of two parts. The nucleation rate of voids ($\dot{f}_n$) at various stages of the deforming solid contribute to the current void volume fraction rate as the first part. The second part is due to the growth ($\dot{f}_g$) of the already nucleated voids. The growth law is easily obtained by equating the volume change of the voids to the dilation as

$$\dot{f}_g = (1 - f)\ (\dot{\varepsilon}^{p}_{11} + \dot{\varepsilon}^{p}_{22} + \dot{\varepsilon}^{p}_{33}) \tag{6}$$

There are few models at present, available in the literature to approximately model the nucleation rate of the voids at room temperatures. However, for high temperature applications, it is important to consider a nucleation model based on an appropriate micromechanism, such as the intergranular cavitation around an inclusion (Ref. 5). For completion, in the present work, the plastic strain controlled void nucleation model as proposed by Goods and Brown, (Ref. 11) is arbitrarily considered. The particular form used by Chu and Needleman (Ref. 12) is given by

$$\dot{f}_n = \frac{\Psi}{s\sqrt{2\pi}} e^{-\frac{1}{2}\left(\frac{D_m^p - e_n}{s}\right)^2} \cdot \dot{D}_m^p \tag{7}$$

where s is the standard deviation of the distribution and Ψ is determined so that the total void of volume nucleated is consistent with the volume fraction of second phase particles. e_n is a mean equivalent plastic strain for nucleation.

The total void volume fraction rate is then expressed as

$$\dot{f} = (1-f)(\dot{\varepsilon}_{11}^p + \dot{\varepsilon}_{22}^p + \dot{\varepsilon}_{33}^p) + \frac{\Psi}{s\sqrt{2\pi}} \dot{D}_m^p e^{-\frac{1}{2}\left(\frac{D_m^p - e_n}{s}\right)^2} \tag{8}$$

To complete the description of the voided aggregate, it is now necessary to describe the matrix material with an appropriate constitutive model. For this purpose, the model developed by Bodner and Partom (Ref. 4) based on state variable theory is considered. The main advantage of this theory is its ability to describe the material response under various loading conditions. The following equation describes the constitute relationships in terms of second invariant of the strain-rate (D_2^p) to the second invariant of the stress deviator (J_2), as

$$D_2^p = D_o^2 \exp\left[-\left(\frac{Z^2}{3J_2}\right)^n \left(\frac{n+1}{n}\right)\right] \tag{9}$$

where $D_2^p = 1/2\ \dot{e}_{ij}^p\ \dot{e}_{ij}^p$. Here, $\dot{e}_{ij}^p$ are the plastic strain-rate tensors of the matrix material, n is the strain-rate sensitivity parameter, Z is the inelastic state variable, and D_o is the limiting value of the plastic strain-rate in shear.

The evolution equation for Z is given by Bodner as

$$\frac{\dot{Z}}{Z} = 2m\left(1 - \frac{Z}{Z_1}\right)\left(D_2^p J_2\right)^{\frac{1}{2}} - A\left(\frac{Z - Z_2}{Z_1}\right)^2 \tag{10}$$

where m, Z_1, Z_2, r, and A are material constants. M is a parameter that controls the rate of work hardening, Z_1 and Z_2 are saturation values of Z, and the value of Z corresponds to the complete non-work hardened condition, respectively. The constants A and r are needed to describe the recovery process of the material.

The main equation (9) can be written in terms of equivalent stress and strain of the matrix material and it is given by

$$\dot{D}_m^p = \frac{4}{3} D_o^2 \exp\left[-\left(\frac{Z}{Y_m}\right)^{2n}\left(\frac{n+1}{n}\right)\right] \tag{11}$$

The equations (10) and (11) together complete the description of the matrix material.

The nonlinear constitutive relationships for the compressible (porous) material are described by equations (5) through (11), along with the consistency condition for plastic loading ($\dot{\Phi} = 0$). However, to demonstrate the stress-strain behavior of the aggregate, uniaxial stress-strain relations can be obtained from the already derived governing equations. The following section describes the aggregate and the matrix stress-strain relations explicitly under uniaxial stress state.

3. UNIAXIAL CASE

The necessary equations to describe the voided aggregate under uniaxial stress state condition can be deduced from the governing equations (equations (1) through (11)). Uniaxial matrix plastic strain-rate ($\dot{e}_m^p$) can be obtained from equation (11) as

$$\dot{e}_m^p = \frac{2D_o}{\sqrt{3}} \exp\left[-\tfrac{1}{2}\left(Z/Y_m\right)^{2n}\left(\frac{n}{n+1}\right)\right] \tag{12}$$

The corresponding matrix stress-rate can be obtained from the definition of total strain-rate as sum of the elastic and plastic components and it is given by

$$\dot{Y}_m = E(\dot{e}_m - \dot{e}_m^p) \tag{13}$$

The aggregate plastic strain-rates in the principal directions can be written using equation (5) as

$$\dot{\varepsilon}_1^p = \frac{(1-f)\ Y_m\ \dot{e}_m^p}{\sigma} \tag{14}$$

$$\dot{\varepsilon}_2^p = \frac{(1-f)\ Y_m\ \dot{e}_m^p\ (H-\sigma)}{\sigma(2\sigma+H)} \tag{15}$$

$$\dot{\varepsilon}_3^p = \dot{\varepsilon}_2^p \tag{16}$$

where $$H = q_1\ q_2\ f\ Y_m\ \text{Sinh}\ \xi \text{ and } \xi = q_2\sigma/2Y_m. \tag{17}$$

Here, σ represents the uniaxial aggregate stress.

An expression for the void volume fraction rate can be obtained by combining equations (14) through (17) with equation (8) as

$$\dot{f} = \frac{3(1-f)^2 H\ Y_m\ \dot{e}_m^p}{\sigma(2\sigma+H)} + \frac{\Psi}{s\sqrt{2\pi}}\ e^{-\frac{1}{2}\left(\frac{e_m^p - e_n}{s}\right)^2}\ \dot{e}_m^p \tag{18}$$

The aggregate stress-rate ($\dot{\sigma}$) can be obtained from the consistency condition ($\dot{\Phi} = 0$) for loading and it is expressed as

$$\dot{\sigma} = \frac{-2Y_m^3(q_1 \cosh\ \xi - f q_3)\dot{f} + \sigma(2\sigma+H)\ \dot{Y}_m}{(2\sigma+H)Y_m} \tag{19}$$

The uniaxial stress-strain relationships for the aggregate can be expressed through the total strain-rate as the sum of elastic and plastic components and they are given by

$$\dot{\varepsilon}_1 = \frac{\dot{\sigma}}{E} + \frac{(1-f)\ Y_m\ \dot{e}_m^p}{\sigma} \tag{20}$$

$$\dot{\varepsilon}_2 = -\frac{\nu\dot{\sigma}}{E} + \frac{(1-f)\ Y_m\ \dot{e}_m^p\ (H-\sigma)}{\sigma(2\sigma+H)} \tag{21}$$

$$\dot{\varepsilon}_3 = \dot{\varepsilon}_2 \tag{22}$$

The equations (12) through (22) can be simultaneously solved through numerical integration and the aggregate stress-strain response can be computed for various matrix stress or strain-rate conditions.

4. RESULTS

The stress-strain behavior of the aggregate with voids is computed by simultaneously solving the uniaxial equations through an appropriate numerical integration. The computations are made for an imposed matrix under constant stress or strain-rate conditions to facilitate comparing the reduced strength (or stiffness) of the aggregate to that of the fully dense matrix material.

Since the material constants for describing the materials Rene' 95 and IN100 at 650°C and 730°C, respectively, under complex loading conditions are readily available, the stress-strain response of the porous aggregate is calculated assuming that these materials represent the matrix materials in this study. Apart from the arbitrarily chosen nucleation model as explained in Section 2, for illustrative purposes, a simple nucleation criterion based on voids being nucleated at the onset of plastic deformation, is assumed in these calculations. The assumed value for the void volume fraction represents the initial void constant of the aggregate.

The void shape factors q_1, q_2, and q_3 that appear in the yield function described by equation 1, can be determined based on (a) the values already available in the literature and (b) the results obtained from the experiments on sintered materials. The effect of various values of these constants on the yield function is shown in Figure 1, for f = 0.15. As can be seen in the figure, the yield function is shown as the variation of $\sqrt{3J_2}/Y_m$ with respect to (I_1/Y_m) for a given value of f and the other constants. For f = 0, the yield criterion becomes obviously independent of the hydrostatic pressure (I_1) and represents the von-mises yield criterion for an incompressible solid. Whereas for $f \neq 0$, the yield functions represented by the curves A or B show the dependency on the level of void contents. The curve A represents the Gurson's yield function ($q_1 = q_2 = q_3 = 1$) while the curve B is the yield function used by Tvergaard (Ref. 10) with $q_1 = 1.5$, $q_2 = 1.0$, and $q_3 = 2$. The experimentally obtained single point* as shown in the

*Experiments Conducted in Air Force Materials Laboratory, Wright-Patterson Air Force Base, Dayton, Ohio.

figure, represents the results of an uniaxial compression test on a sintered material of void volume fraction, f, equals 0.15. It can be seen from these results that the yield criterion based on the values of q_1, q_2, and q_3 which are available in the literature, is significantly off from the experimental result. However, when improved values for q_1, q_2, and q_3, obtained by trial and error, were used, the theoretical predictions for f = 0.15 and f = 0.25 were quite compatable with the experimental values at least for the case of uniaxial stress state as shown in Figure 2.

To demonstrate the effect of the various q_1, q_2, and q_3 on flow stress, the uniaxial stress-strain curves of the porous aggregate for a constant matrix strain-rate of 1.4×10^{-3} sec^{-1} are shown in Figure 3. These curves clearly show the differences in the predictive stress levels by the three sets of values chosen for these constants. However, in the present calculations, the improved values of q_1, q_2, and q_3 are used to describe the porous material behavior under uniaxial stress-state.

The various levels of flow stress of a porous aggregate with IN100 as the matrix material for different void contents are shown in Figure 4 using the simple nucleation criterion. The dotted line corresponds to the flow stress level of fully dense matrix material. The reduced strength of the material due to the presence of ten percent void content can be seen from this figure. The initially nucleated voids grow during the plastic deformation according to the growth law represented by equation (6). The increasing void volume fraction (f) normalized by the initial value f_o is shown in Figure 5 for the three values of f_o, corresponding to the earlier Figure 4. It can be seen from the figure that the growth levels are almost the same in these cases. Since the plastic strain levels under uniaxial stress conditions are of the same order, the plastic strain-rate based growth law predict the same order of growth.

To demonstrate the effect of void nucleation model on the flow stress, solutions were obtained for the nucleation model discussed in Section 2. The results for various nucleation strains are shown in Figure 6. For $\Psi = 0.05$ and s = 0.01 (narrow range of nucleation strain), the curve corresponds to $e_n = 0.01$ shows the entire nucleation to occur between A and B. The rapidly reducing strength of the material due to the entire void nucleation occurring in the narrow range, stabilizes beyond point B. The

steady drop in the flow stress level later on depends mainly on the void growth in the material.

For $e_n = 0.05$, the nucleation process starts at point C and the stress-strain behavior of the aggregate is the same as that of the matrix due to the absence of any void up to point C. The stress-strain curve for the aggregate and the matrix material are identical for the case $e_n = 0.1$ due to the absence of void nucleation up to the strain corresponding to point D. The variations of void volume fraction with respect to the aggregate strain for $e_n = 0.01$ and $e_n = 0.05$ are shown in Figure 7. The rapid increase in f as shown by the curves between AB and CD are due to the nucleation of new voids and the growth of existing voids. When the nucleation process is completed over the narrow range of strain, the increase in void volume fraction, later is due to the growth of the nucleated voids alone. The rate of increase stabilizes beyond the points B and D as shown in the figure.

As an additional exercise, the effect of the standard deviation, s, of the nucleation strain distribution on the flow stress for $e_n = 0.01$ and $\Psi = 0.05$ is shown in Figure 8. It can be seen from the figure as the distribution takes place over a broad range of strain (s = 0.05 and 0.1) the decay in strength due to void nucleation and growth is less pronounced with a steady decline. The corresponding increase in the void volume fractions are shown in Figure 9.

The effect of strain-rate on the stress-strain response using the simple nucleation model is shown in Figure 10. The response of the fully dense matrix material (IN100) and also of the porous aggregate are obtained through the numerical solutions for various matrix strain-rates ($\dot{D}_m$). The reduced strength of the material due to the presence of a low void content (two percent) can be seen from this figure.

As an additional description of the modeling procedure the creep response of the voided aggregate with a Rene' 95 matrix is demonstrated in Figure 11, when the matrix material creeps at different stress levels (Y_m = 1206 and 903 MPA). The aggregate stresses are calculated for two different creep stress levels applied to the matrix material. For the higher matrix stress level, the stress in the aggregate is reduced due to five percent voids in the material. However, for the lower stress (Y_m = 903 MPA), since the plastic flow has not yet initiated within the time shown in

Figure 11 (1200 seconds), voids are not nucleated. Thus, both the matrix and the aggregate with no voids creep at the same stress. Also, the corresponding strain responses are obviously the same as shown in Figure 12. Whereas the responses corresponding to higher stress, show the distinct difference for two different values of void volume fraction (f = 0.05 and 0.10).

Thus, it can be seen from these results that the response of a porous aggregate to rate or time dependent loading conditions can depend on various material parameters that appear in the yield function and as well as in the nucleation model.

5. SUMMARY

The accuracy of modeling the porous aggregate behavior depends mostly on the (a) yield function which characterizes the compressible yield behavior, (b) description of the matrix material, and (c) nucleation model. It is demonstrated in the present studies that an approximate yield function to describe the porous aggregate can predict significantly different stress levels which may be inaccurate. It is important to test the yield function and its validity through carefully designed experiments under various stress conditions. As an example, it is shown that the values of the shape factors which appear in the yield function can be improved based on the experimentally obtained stress state at yielding. However, the values selected in this report based on two experiments may not be unique. Nevertheless, under uniaxial stress state conditions, these values may better characterize the yield function.

The improved characterization of the matrix material behavior under complex loading conditions through various nonlinear constitutive theories has been successfully achieved by several investigators. If the well defined and accurately described matrix material models are appropriately built into the constitutive models for the porous aggregate, that would substantiously improve the characterization of the porous solid as demonstrated in the present studies.

The description of the porous material through an improved yield function and the matrix material model, may be accurate for a homogeneous, isotropic material with randomly distributed voids, such as the sintered

materials. However, for materials which were initially non-porous but developed porosity at some stage of the deformation due to various micro-mechanisms operating at the void nucleation site, the improved characterization of the porous aggregate will then also depend on the models for describing the nucleation process. The dependency of the flow stress on the parameters that describe the nucleation process is demonstrated for a model which was arbitrarily selected for illustrative purposes. For high temperature applications, it is important to select a model on a sound fundamental basis. Unfortunately, a continuum mechanics approach in this area is still lacking and needs more rigorous research efforts to model the complex nucleation process. The growth process of the nucleated voids seemed to be more or less temperature independent and also it is reasonably well established as a process which depends on the plastic strains (Ref. 13).

In summary, the present studies demonstrate that the rate or time dependency of the response of a porous aggregate can be incorporated into the nonlinear constitutive behavior of a porous solid by appropriately modeling the incompressible matrix behavior. It is also shown that the yield function which was determined by a continuum mechanics approach must be verified by appropriate experiments on void containing sintered materials in order to obtain meaningful numbers for the constants that appear in the yield function.

REFERENCES

1. Allen, D. H., Haisler, W. E., "The Application of Thermal and Creep Effects to Combined Isotropic-Kinematic Hardening Model," Tech. Report No. 3275-79-3, Texas A&M Univ., 31 May 1979.

2. Valanis, K. C. and Wu, H. C., "Endochronic Representation of Cyclic Creep and Relaxation of Metals," J. of Appl. Mech., 1975.

3. Laflen, J. H. and Stouffer, D. C., "An Analysis of High Temperature Metal Creep," Vol. 100, October 1978.

4. Bodner, S. R. and Partom, Y., "Constitutive Equations for Elastic-Viscoplastic Strain-Hardening Materials," J. of Applied Mech., June 1975.

5. Rishi Raj and Ashby, M. F., "Intergranular Fracture at Elevated Temperature," Acta. Met., Vol. 23, June 1975.

6. Gurson, A. L., "Porous Rigid-Platic Materials Containing Rigid Inclusions-Yield Function, Plastic Potential, and Void Nucleation," Advances in Research on Strength and Fracture of Materials, Vol. 2a, Tablin, D. M. R., ed., Pergamon Press, New York, 1977.

7. Yamamoto, H., "Conditions for Shear Localization in the Ductile Fracture of Void-Containing Materials," International Journal of Fracture, Vol. 14, No. 4, 1978.

8. Needlemen, A. and Triantafyllidis, N., "Void Growth and Local Necking in Biaxially Stretched Sheets," ASME Journal of Engr. and Mat. Tech., Vol. 100, April 1978.

9. Stouffer, D. C. and Bodner, S. R., "A Relationship Between Theory and Experiment For a State Variable Constitutive Equation," AFWAL-TR-80-4194, Tech. Report, January 1981.

10. Tvergaard, V., "Influence of Voids on Shear Band Instabilities Under Plane Strain Conditions," Report No. 159, Danish Center for Applied Math and Mech., June 1979.

11. Goods, S. H. and Brown, L. M., "The Nucleation of Cavities by Plastic Deformation," Acta Metallurgica, Vol. 27, 1979.

12. Chu, C. C. and Needlemen, A., "Void Nucleation Effects in Biaxially Stretched Sheets," J. of Engr. Mat. and Tech. Vol. 102, July 1980.

13. Lagneborg, R., "Creep of Engineering Materials and Structures," Edited by Bernasconi and Piatti, 1980.

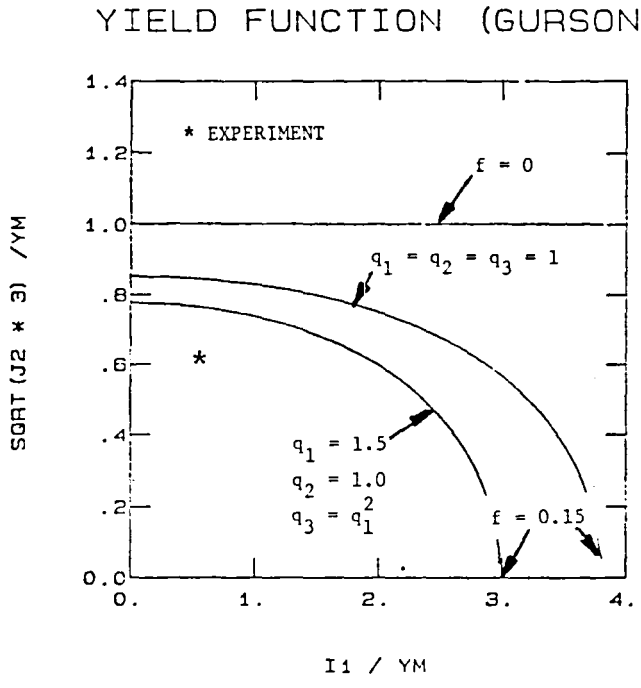

Fig. 1. Effect of the Shape Factors on the Yield Function for a Porous Solid.

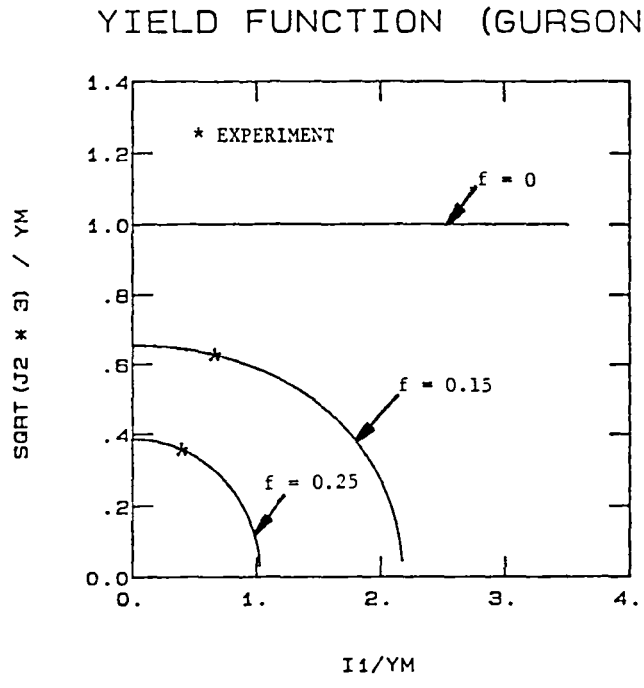

Fig. 2. Gurson's Yield Function With $q_1 = 2.2$, $q_2 = 1.0$, $q_3 = 4$ For f = 0.15 and f = 0.25.

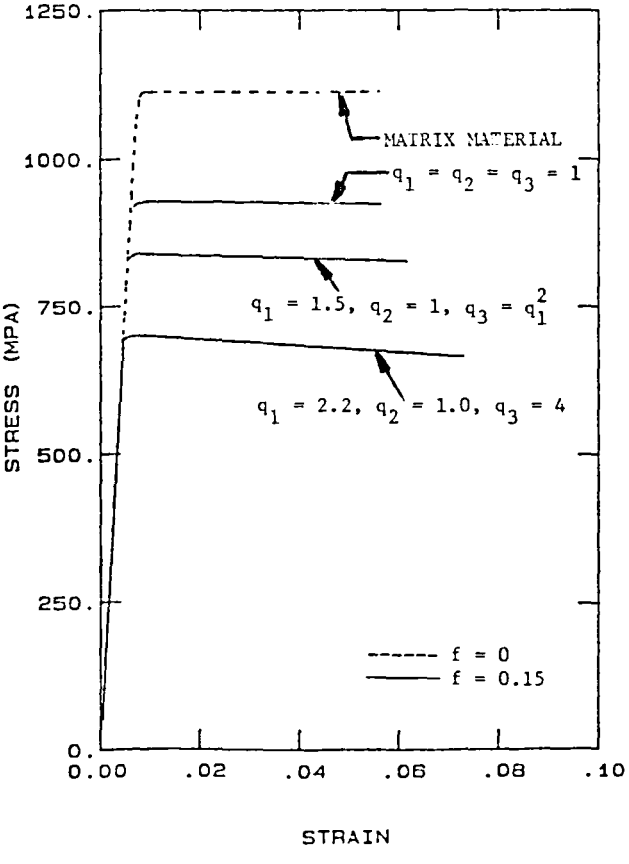

Fig. 3. Effect of the Shape Factors on the Uniaxial Stress-Strain Curves for a Porous Aggregate With IN100 as Matrix Material.

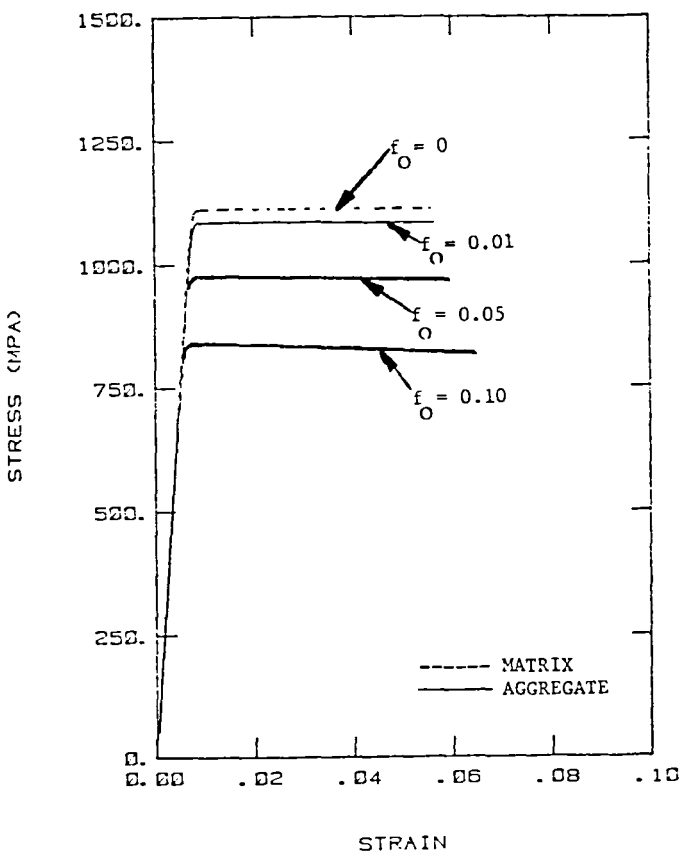

Fig. 4. Effect of Void Volume Fraction on the Flow Stress. f_o is the Initial Value of f. $\dot{D}_m$ is the Strain-Rate in the IN100 Matrix.

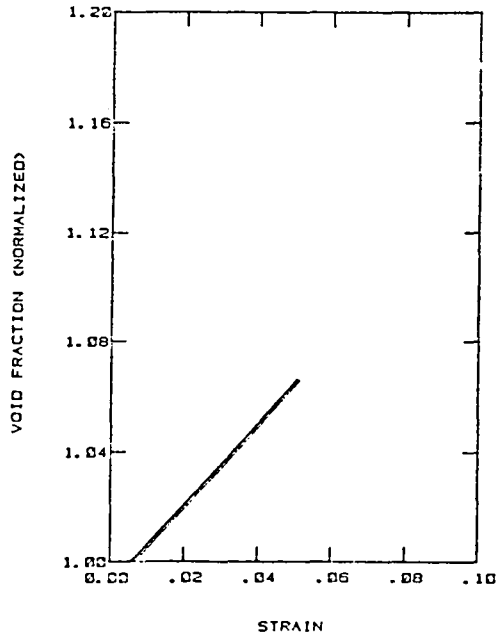

Fig. 5. Variation of Void Growths With Respect to the Strain in the Porous Aggregate for Different Initial Void Volume Fraction Levels.

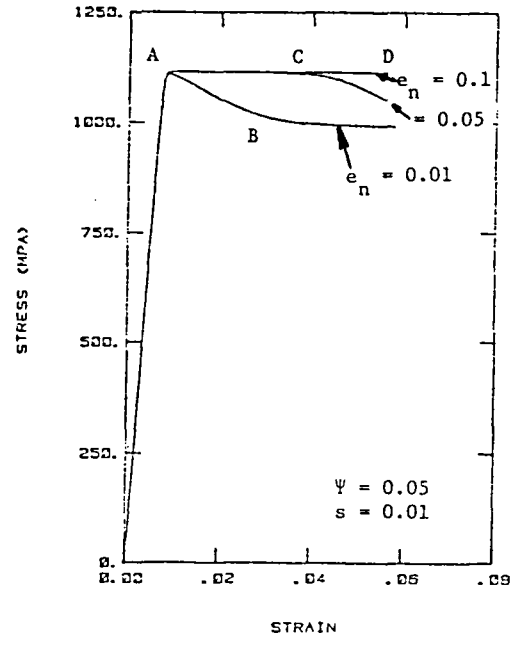

Fig. 6. Effect of Void Nucleation Model on the Flow Behavior of the Voided Aggregate for $\dot{D}_m = 1.4 \times 10^{-3}$ sec^{-1}.

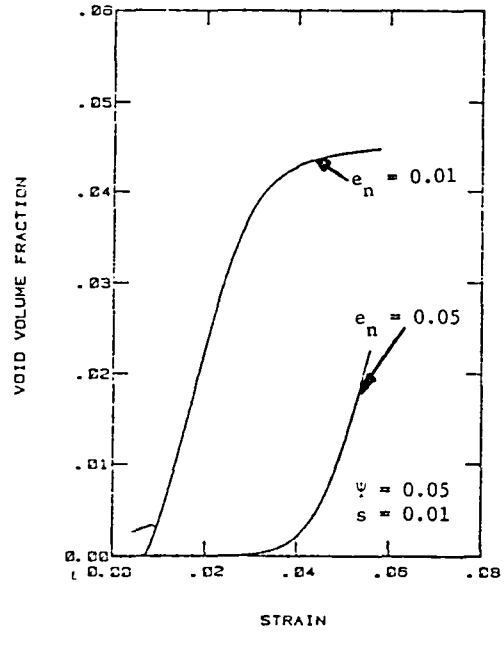

Fig. 7. Effect of Nucleation Strain (e_n) on the Growth of Void Volume Fraction with Respect to Strain.

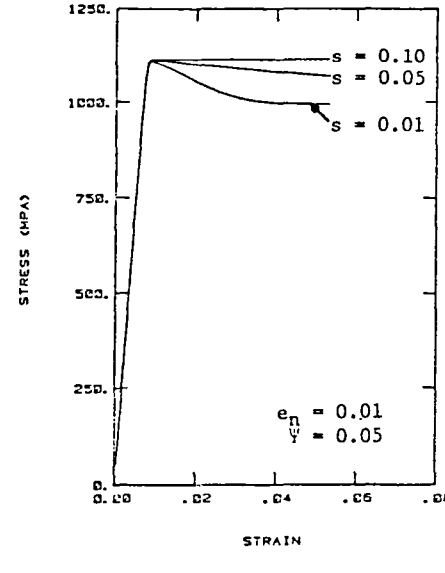

Fig. 8. Effect of Standard Deviation (s) of the Nucleation Strain Distribution on the Voided Aggregate Flow Stress for a Constant Matrix Strain-Rate ($\dot{D}_m = 1.4 \times 10^{-3}$/sec).

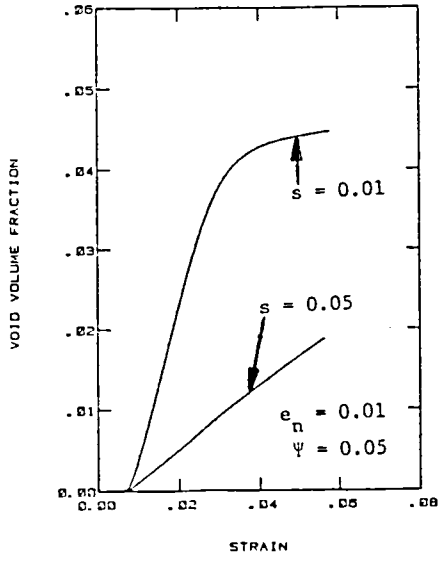

Fig. 9. Effect of 's' on the Void Volume Fraction with Respect to the Strain in the Aggregate.

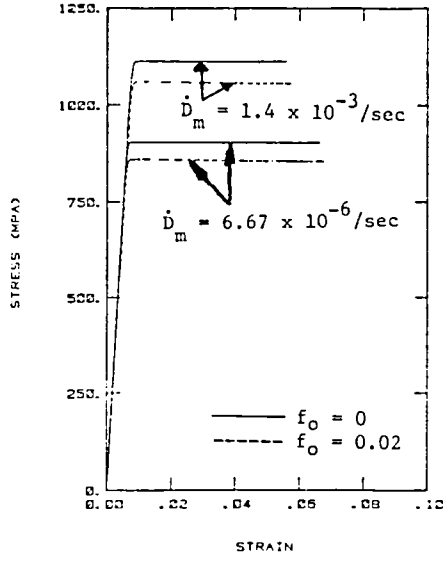

Fig. 10. Effect of Strain-Rate on the Matrix (IN100) and the Voided Aggregate. $\dot{D}_m$ is the Matrix Strain-Rate. f_o is the Initial Void Volume Fraction.

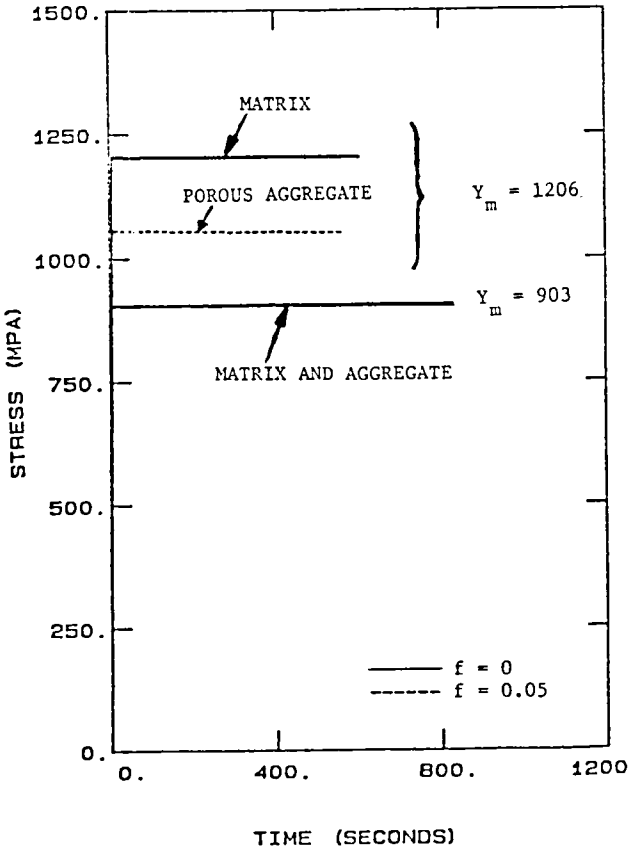

Fig. 11. Effect of Creep in the Aggregate for Various Matrix Creep Stress Levels at 650°C. Y_m is the Matrix (Rene' 95) Stress.

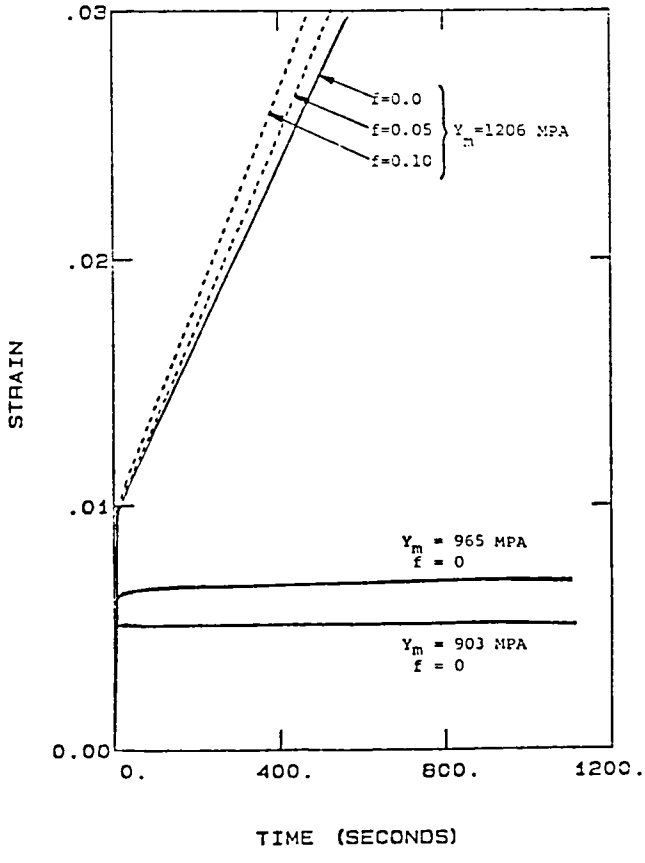

Fig. 12. Creep Response of the Aggregate and the Matrix at 650°C. Y_m is the Matrix Stress, f is the Void Volume Fraction.

TIME-INDEPENDENT ANISOTROPIC PLASTIC BEHAVIOR BY MECHANICAL SUBELEMENT MODELS*

Theodore H. H. Pian
Massachusetts Institute of Technology
Cambridge, Massachusetts 02139

ABSTRACT

The paper describes a procedure for modelling the anisotropic elastic-plastic behavior of metals in plane stress state by the mechanical sub-layer model. In this model the stress-strain curves along the longitudinal and transverse directions are represented by short smooth segments which are considered as piecewise linear for simplicity. The model is incorporated in a finite element analysis program which is based on the assumed stress hybrid element and the viscoplasticity-theory.

1. INTRODUCTION

For time-independent elastic-plastic behaviors a very convenient model to represent kinematic hardening is to use an assembledge of elastic-perfectly-plastic elements to represent the stress-strain relation which is approximated by a curve with several piecewise linear segments. This model, which has been widely used for numerical analysis of multiaxial elastic-plastic behavior is named mechanical sublayer or overlay models [refs. 3,4,5]. For more general case including three-dimensional solid, the method should perhaps be called mechanical sub element method.

For plane stress problems the corresponding mechanical model is a laminated plate with layers of elastic-perfectly-plastic materials of different yield stresses. Differential equations for the solutions of plane stress elastic-plastic and isotropic stress-strain relations has been obtained for model with two layers, one of which is elastic and the other is elastic-perfectly-plastic [ref. 6]. The

*Work performed under NASA Grant NAG 3-33.

equations are non-linear and for the case of uniaxial loading the resulting strain hardening behavior will not be a straight line. Thus, for a material with uniaxial stress-strain relation approximated by straight line segments, it is, strickly speaking, not possible to obtain exact representation by a mechanical sublayer described above. In Ref. 6, a relationship has been obtained between the ratio of the initial tangant modulus and the elastic modulus and the thickness ratio of the two layers. It is however, reasonable to assume that by using sufficiently small segments a piecewise linear model can be adopted.

Hunsakier et al. [ref. 5] have also obtained a corresponding relationship for three-dimensional isotropic solids. In that case, for a material represented by one elastic subelement and one elastic-plastic subelement, the resulting uniaxial stress-strain relation will have linear strain hardening behavior. The proportion of the volume of the elastic-plastic element to the total volume V_1/V is expressed simply as

$$\frac{V_1}{V} = \frac{E_1 - E_2}{E_1 - \frac{1-2\nu}{3} E_2}$$

where E_1 is the elastic modulus and E_2, the tangent modulus. In this case, when the uniaxial stress-strain relation is represented by linear segments a corresponding subelement model can be constructed exactly.

The present paper is to extend the mechanical sublayer model to materials with anisotropic plastic behavior. Again the plane stress problem is considered. Finite element method for elastic-plastic analysis based on the viscoplasticity theory and the stress hybrid model is used in conjunction with the present mechanical subelement model. An example solution of a time-independent elastic-plastic problem is presented.

Acknowledgement - The author acknowledges the assistance of Ms. Susan E. French and Mr. Hely Savio for obtaining the numerical results.

2. Mechanical Sublayer Model for Anisotropic Plasticity Problems

Figure 1 is a plate with two layers under plane stress loading. Layer 1 is elastic-perfectly-plastic and is considered tranversely isotropic with yield stresses Y_x and Y_y respectively along the longitudinal and transverse directions. Layer 2 is elastic. The elastic constants E and Poisson's ratio ν for both layers are identical. The yield condition for layer 1 is governed by the Hill's generalized yield criterion

$$f = [F(\sigma_{x_1}-\sigma_{y_1})^2 + G(\sigma_{y_1}-\sigma_{z_1})^2 + H(\sigma_{z_1}-\sigma_{x_1})^2 + K\,\sigma_{xy_1}^2]^{1/2} - \bar{\sigma} = 0 \qquad (1)$$

where $\bar{\sigma} = Y_x$ under uniaxial loading along x direction. With yield stresses under uniaxial loading along y and z direction equal to Y_y, we can express the constants F, H etc. in terms of the yield stresses and obtain the following yield conditions for the plane stress problem

$$f = [\sigma_{x_1}^2 - \sigma_{x_1}\sigma_{y_1} + \alpha\,\sigma_{y_1}^2 + \alpha_s\,\sigma_{xy_1}^2]^{1/2} - Y_x = 0 \qquad (2)$$

where

$$\alpha = (Y_x/Y_y)^2$$
$$\alpha_s = (Y_x/Y_{xy})^2 \qquad (3)$$

The flow rule is

$$\dot{\varepsilon}^p_{x_1} = (\sigma_{x_1} - \tfrac{1}{2}\,\sigma_{y_1})\,\dot{\lambda}$$
$$\dot{\varepsilon}^p_{y_1} = (\alpha\,\sigma_{y_1} - \tfrac{1}{2}\,\sigma_{x_1})\,\dot{\lambda} \qquad (4)$$
$$\dot{\varepsilon}^p_{xy_1} = \alpha_s\,\sigma_{xy_1}$$

Now, consider the behavior of the laminated plate under inplane loading conditions. From testing tension coupons cut along the x and y directions, the elastic modulus for both direction is given as E_1 while the initial tangent moduli are represented, respectively, by E_{x_2} and E_{y_2} as shown in Figure 2. Let σ_x and σ_y represent the average in-plane stresses, then the stress rate σ_y is

$$\dot{\sigma}_y = \dot{\sigma}_{y_1} \frac{t_1}{t} + \dot{\sigma}_{y_2} \frac{t_2}{t} = 0 \tag{5}$$

where t is the total thickness and t_1 and t_2 are the individual thickness. The thickness ratio then is,

$$\frac{t_1}{t_2} = - \frac{\dot{\sigma}_{y_2}}{\dot{\sigma}_{y_1}} \tag{6}$$

Here, layer 2 is elastic hence,

$$\dot{\sigma}_{y_2} = \frac{E_1}{1-\nu^2} (\dot{\varepsilon}_y + \nu \dot{\varepsilon}_x) \tag{7}$$

From $\dot{f} = 0$, we obtain,

$$\dot{\sigma}_{x_1} (2 \sigma_{x_1} - \sigma_{y_1}) + \dot{\sigma}_{y_1} (2\alpha\sigma_{y_1} = \sigma_{x_1}) = 0 \tag{8}$$

Thus, at initial yield when $\sigma_y = \sigma_{y_1} = \sigma_{y_2} = 0$

$$\frac{\dot{\sigma}_{y_1}}{\dot{\sigma}_{x_1}} = 2 \tag{9}$$

and from Eq. (4),

$$\dot{\varepsilon}_{x_1}^{p} = -2\dot{\varepsilon}_{y_1}^{p} \tag{10}$$

We also have

$$\dot{\varepsilon}_{x_1}^{p} = \dot{\varepsilon}_x - \frac{1}{E_1} (\dot{\sigma}_{x_1} - \nu \dot{\sigma}_{y_1}) \tag{11}$$

and $$\dot{\varepsilon}_{y_1}^{p} = \dot{\varepsilon}_y - \frac{1}{E_1}(\dot{\sigma}_{y_1} - \nu\dot{\sigma}_{x_1}) \tag{12}$$

From Eqs. (9) to (12), we obtain,

$$\dot{\sigma}_{x_1} = \frac{E_1}{5 - 4\nu}(\dot{\varepsilon}_x + 2\ \dot{\varepsilon}_y) \tag{13}$$

$$\dot{\sigma}_{y_1} = \frac{E_1}{5 - 4\nu}(2\dot{\varepsilon}_x + 4\ \dot{\varepsilon}_y) \tag{14}$$

Now from the given uniaxial loading conditions the strain rate along y is given by

$$\dot{\varepsilon}_y = \dot{\varepsilon}_y^{e} + \dot{\varepsilon}_y^{p}$$

$$= -\nu\ \dot{\varepsilon}_x^{e} - \frac{1}{2}\dot{\varepsilon}_x^{p} \tag{15}$$

Substituting $$\dot{\varepsilon}_x^{p} = \dot{\varepsilon}_x - \dot{\varepsilon}_x^{e} \tag{16}$$

and $$\dot{\varepsilon}_x^{e} = \frac{\dot{\sigma}_x}{E_1} = \frac{\dot{\varepsilon}_x E_{x_2}}{E_1} \tag{17}$$

into Eq. (15) we obtain

$$\dot{\varepsilon}_y = \dot{\varepsilon}_x\left[-\frac{1}{2} + \left(\frac{1}{2} - \nu\right)\frac{E_{x_2}}{E_1}\right] \tag{18}$$

Substituting into Eqs. (7) and (14) and then into Eq. (16), the following thickness ratio is obtained,

$$\frac{t_1}{t_2} = \frac{5 - 4\nu}{4\ (1 - \nu^2)}\left(\frac{E_1}{E_{x_2}} - 1\right) \tag{19}$$

From which

$$\frac{t_1}{t} = \frac{t_1}{t_1 + t_2} = \frac{E_1 - E_{x_2}}{E_1 - \beta\ E_{x_2}} \tag{20}$$

where

$$\beta = \frac{(1 - 2\nu)^2}{5 - 4\nu} \tag{21}$$

It is noted that this factor β is the same for isotropic materials for which Eqs. (9) and (10) hold. For one dimensional problem the ratio of the area of plastic element to the total area is

$$\frac{A_1}{A} = \frac{E_1 - E_2}{E_1} \tag{22}$$

Thus β is the modification factor for plane stress problems. For $\nu = 0.3$, of Eq. (22) $\beta = (1-2\nu)^2/(5 - 4\nu) = 0.0421$. Thus, the modification is very small when the uniaxial behavior along the longitudinal direction is used to determine the thickness ratio.

Now if a coupon is cut along the y-axis, then when $\sigma_x = \sigma_{x_1} = \sigma_{x_2} = 0$,

$$\frac{\dot{\sigma}_{x_1}}{\dot{\delta}_{y_1}} = 2\alpha \tag{23}$$

and

$$\dot{\varepsilon}_{y_1}^{p} = - 2\alpha \, \dot{\varepsilon}_{x_1}^{p} \tag{24}$$

Following the same derivation given above, if the tangent modulus is E_{y_2}, the thickness ratio becomes

$$\frac{t_1}{t} = \frac{E_1 - E_{y_2}}{E_1 - \beta^1 E_{y_2}} \tag{25}$$

where

$$\beta' = \frac{(1 - 2\alpha \nu)^2}{1 - 4\nu\alpha + 4\alpha^2} \tag{26}$$

For $\nu = 0.3$ and for α between 0.5 and 2, the values of β' is in the range of 0 to 0.35.

Equating Eqs. (19) and (26) and solving for E_1' we obtain a relation between E_{x_2} and E_{y_2},

$$E_{y_2} = \frac{(1 - \beta) E_1 E_{x_2}}{(1 - \beta') E_1 - (\beta - \beta') E_{x_2}} \tag{27}$$

Thus for anisotropic material represented by the mechanical sublayer model the initial tangent moduli for the two directions are not the same. When the stress-strain curves for two perpendicular directions are given, a mechanical sublayer can be obtained according to the following procedure.

(1) For the stress-strain curves, for both x-and y-direction determine the initial yield stresses Y'_{x_1} and Y'_{y_1}. These are also the yield stresses Y_{x_1} and Y_{y_1} of the sublayer and are euqal to $E_1 \varepsilon_{x_1}$ and $E_1 \varepsilon_{y_1}$, respectively.

(2) Based on one of the curves say for the x direction try an initial tangent modulus E_{x_2}. Knowing Y_{x_1}, Y_{y_1}, and E_{x_2}, α and β for layer 1 can be determined, hence, t_1/t can be calculated from Eq. (2) and the initial tangent modulus E_{y_2} for the y-direction, from Eq. (27).

(3) The 2-sublayer model is then used to analyze two uniaxial loading problems and to obtain the stress-strain curves for both directions. The intersections of these lines to the actual stress-strain curves now determines the second set of transition points at which the second layer yields. The stresses and strains are respectively Y'_{x_2} and Y'_{y_2} and ε_{x_2} and ε_{y_2} as shown in Figure 3. In general, the yield stresses Y_{x_2} and Y_{y_2} of the new sublayer are not equal to $E_1 \varepsilon_{x_2}$ and $E_1 \varepsilon_{y_2}$, although in the case of subelement model for uniaxial problems, the yield stress for the second subelement is equal to $E_1\varepsilon_2$.

For 3-D problems with isotropic plastic behavior, Hunsaker has obtained closed form solutions for the case of a 2-subelement model. For a typical case with $E_2 = 0.5\ E_1$ and $\varepsilon_2 = 3\ \varepsilon_1$ the difference between Y'_2 and $E_1\ \varepsilon_2$ is only 5%.

The choice of the initial tangent modulus E_{x_2} must be such that the second set of transition points do fall on the actual stress-strain curve. In general, an iterative procedure is required.

(4) The plate is now considered as a new two-layer model with the yield stresses for the two directions equal to Y_{x_2} and Y_{y_2}. Then by choosing a tangent modulus E_{x_3} for the next segment, values of $(t_1 + t_2)/t$, E_{y_3}, and Y_{x_3}, Y'_{y_3}, Y_{x_3}, and Y_{y_3} can be determined following the same steps (2) and (3) above using

$$\frac{t_1 + t_2}{t} = \frac{E_1 - E_{x_3}}{E_1 - \beta E_{x_3}} \tag{28}$$

and

$$E_{y_3} = \frac{(1 - \beta) E_1 E_{x_3}}{(1 - \beta') E_1 - (\beta - \beta') E_{x_3}} \tag{29}$$

for the value of β' Eq. (26) is used with $\alpha = (Y_{x_2}/Y_{y_2})^2$.

(5) The mechanical sublayer model may be constructed using the stress-strain curve for the transverse direction as reference. In that case, Eq. (25) as used to determine the thickness ratio's and Eq. (27) is used to solve for E_{x_i} in terms of E_{y_i}.

In the solution of a plane stress problem given in this paper a simplified procedure was adopted. The stress-strain curves for either the longitudinal or the transverse directions is replaced by a curve with linear segments. With one of the tangent moduli given, the other tangent modulus can be obtained and is again considered constant. Thus, the intercept of this linear segment to the actual stress-strain curve can be determined. The yield stresses for sublayers are obtained by the simple formulas,

$$Y_{x_i} = E_1 \varepsilon_{x_i} \tag{30}$$

and

$$Y_{y_i} = E_1 \varepsilon_{y_i}$$

3. Finite Element Method Based on Viscoplasticity Theory

Time independent elastic-plastic analysis can be made by using viscoplasticity models [ref. 7]. In the case of elastic-perfectly-plastic material, it is only necessary to consider the rate of viscoplastic strain components ε^{vp} as

$$\dot{\varepsilon}^{vp} = \gamma < \phi > \frac{\partial F}{\partial \underset{\sim}{\sigma}} \tag{31}$$

where $F(\underset{\sim}{\sigma}) = 0$ represents the yield surface and

$$< \phi > = \begin{cases} \bar{\sigma} - \sigma_y & \text{for } \sigma > \sigma_y \\ 0 & \text{for } \sigma \leq \sigma_y \end{cases} \tag{32}$$

$\bar{\sigma}$ = equivalent stress

σ_y = yield stress under uniaxial loading

γ = a fluidity parameter which is arbitrary for the corresponding elastic-plastic analysis.

A corresponding viscoplastic model for the mechanical sublayer model is an arrangement of viscoplastic elements in parallel as shown in Figure 4.

In the finite element analysis of a plane stress problem, the entire panel is discretized into N finite elements, the thickness of each of which is divided into M sublayers according to the modelling described in the previous section. A finite element method for the creep problem has been formulated by the initial strain approach using the assumed stress hybrid model [8,9]. The method is extended to the present multilayer model. For the incremental solution of the elastic-plastic problem, the procedure is as follows,

(1) An elastic solution of nodal displacements due to a given load increment is made using the assumed stress hybrid elements,

(2) The stress increments at selected Gaussian stations in each element are evaluated,

(3) The stresses in each sublayer at each Gaussian station are updated and the corresponding equivalent stress $\bar{\sigma}$ evaluated,

(4) A time increment Δt is chosen and the increments of viscoplastic strains are $\Delta \underset{\sim}{\varepsilon}^{vp} = \dot{\underset{\sim}{\varepsilon}}^{vp} \Delta t$ for all sublayers at all Gaussian stations. Here the viscoplastic strain rates are determined by Eqs. (31) and (32).

(5) The equivalent nodal forces due to the viscoplastic strain increments can be evaluated. They are used for the determination of nodal displacements for the time increment.

(6) Steps (2) and (5) are repeated until the changes in stresses within the time increment become less than a small prescribed limit.

At this stage, the equivalent stress $\bar{\sigma}$ in each sublayer is either equal or smaller than the yield stress of that sublayer and stabilized stress state for this loading increment is obtained. The use of successive time increments is equivalent to an iterative procedure for this elastic-plastic problem.

A guideline for the choice of the time increment Δt to assure numerical stability is, according to Cormeau [ref. 10],

$$\Delta t \leq \frac{4\ (1+\nu)}{3\ E\ \gamma} \tag{33}$$

where E is the Young's modulus

4. Anisotropic Analysis of Shear Lag Structure

To illustrate the finite element solution using the present anisotropic model, a shear lag structure which was tested in 1963 at Massachusetts Institute of Technology is used [ref. 11]. The structure shown in Figure 5 was integrally

machined from thick 2024-T4 aluminum alloy plate. It is a rectangular panel 27.94 cm x 25.4 cm x .203 cm, stiffened by tapered stiffners along the loading (y) axis. The stiffness became flush with the panel at the center, where the stresses and strains are the highest under the applied tension load through the stiffners.

Fitted stress-strain curves for both the longitudinal or x-direction and the transverse or y-direction were obtained from tension tests as shown in Figure 6. An average of these two curves is also shown.

A mechanical sublayer model for this material was constructed by the simplified procedure indicated in section 2. The corresponding curves with piecewise linear senments are shown in Figure 7. The yield stress under shear was not obtained in the original experiment. For the mechanical sublayer model, the values of Y_{xy} for each layer is set equal to $Y/\sqrt{3}$ where Y is the larger of Y_x and Y_y. Of the five sublayers used in the models the last one is considered elastic. The strain disbribution of the panel, thus, is determined directly by the elastic strains of this layer. Table 1 lists the thickness ratios and yield stresses of the various sublayers.

For the finite element analysis one quarter of the panel is used. It is subdivided into 7 x 7 rectangular plane stress elements as shown in Figure 8. The tapered stiffness is also modelled as plane stress elements with constant thickness in each element. For the finite element solution all numerical integrations were obtained by using 2 x 2 Gaussian quadrature.

The resulting strains ε_x and ε_y at the center of the panel were determined by extrapolating from the two Gaussian stations along the diagonal line of the element at closest to the center. Their variations with respect to the applied load are shown in Figure 9. Also plotted for comparison are:

(1) A finite element solution obtained by the present method but by modelling as an isotropic material based on the average stress-strain curve shown in Figure 6.

(2) A finite element solution obtained by Jensen et al. [ref. 12], using 144 constant strains triangular elements and by modelling as an isotropic material.

(3) Experimental results obtained in Ref. 11.

It is seen that the solutions by the three finite analyses are comparable although they do not agree with the experimental result, especially, for the ε_y component. In this particular case the approximate solution obtained by considering the material property to isotropic appears to be very close to that by the present modelling of anisotropic material.

5. Conclusions

A method has been developed for the modelling of anisotropic plastic behaviors for metals by the mechanical subelement model. It has been incorporated in a finite element analysis program based on the assumed stress hybrid model and, on the viscoplasticity theory.

REFERENCES

1. P. Duwez, "On the Plasticity of Crystals," Physical Review, 47, 494-501, 1935.

2. J. F. Besseling, "A Theory of Plastic-flow for Anisotropic Hardening in Plastic Deformation of an Initially Isotropic Material," Nat. Aero Research Inst. Rept. S410, Amsterdam, 1953.

3. J. W. Leech, E. A. Witmer and T. H. H. Pian, "Numerical Calculation Technique for Large Elastic-Plastic Transient Deformations of Thin Shells," AIAA Journal 6, 2352-2359, 1968.

4. O. Z. Zienkiewicz, G. C. Nayak and D. R. J. Owen, "Composite and Overlay Models in Numerical Analysis of Elastic-Plastic Continua," Foundations of Plasticity, A. Sawszuk ed. Noordhoff, Leyden, 107-123, 1973.

5. B. Hunsaker, W. E. Haisler and J. A. Stricklin, "On the Use of Two Hardening Rules of Plasticity in Incremental and Pseudo Force Analyses," Constitutive Equation's in Viscoplasticity: Computational and Engineering Aspect, ASME, AMD-Vol. 20, 139-170, 1973.

6. T. H. H. Pian, Unpublished lecture notes on Plasticity, 1966.

7. P. Perzyna, "Fundamental Problems in Viscoplasticity," Advances in Applied Mechanics," Academic Press, New York, Vol. 9, 243-377, 1966.

8. T. H. H. Pian, "Nonlinear Creep Analysis by Assumed Stress Finite Element Methods," AIAA Journal, Vol. 12, 1756-1758, 1975.

9. T. H. H. Pian, and S. W. Lee, "Creep and Viscoplastic Analysis by Assumed Stress Hybrid Finite Elements," Finite Elements in Nonlinear Solid and Structural Mechanics, Ed. by P. G. Bergan et al. Tapir Publisher Trondheim, Norway,807-822, 1978.

10. I. C. Cormeau, "Numerical Stability in Quasi-State Elasto/Viscoplasticity," Int. J. Num. Meth. Engng., 9, 109-127, 1975.

11. J. H. Percy, W. A. Loden and D. R. Navaratua, "A Study of Matrix Analysis Methods for Inelastic Structures," Air Force Dynamics Laboratory Report, RTD-TDA-63-4032, Oct. 1963.

12. W. R. Jeusen, W. E. Falby and N. Prince, "Matrix Analysis Methods for Anisotropic Inelastic Structures," Air Force Flight Dynamics Lab. Report AFFDL-TR-65-220, April 1966.

Table 1. Constants for Mechanical Sublayer Model (Anisotropic Plasticity)

Layer Number i	1	2	3	4	5
t_i/t	0.360	0.351	0.130	0.130	0.029
E_{x_i} GPa	69.6	45.2	20.8	11.5	2.08
E_{y_i} GPa	69.6	44.7	20.3	11.2	2.01
ε_{x_i} 10^{-3}	5.01	5.33	5.52	6.01	10.0
ε_{y_i} 10^{-3}	3.24	4.52	6.22	8.44	14.0
Y_{x_i} $(=E_i\varepsilon_{x_i})$ MPa	349	371	385	419	ELASTIC
Y_{y_i} $(=E_i\varepsilon_{y_i})$ MPa	226	315	433	587	
$\alpha_i = (Y_{x_i}/Y_{y_i})^2$	2.39	1.39	0.789	0.508	
$\alpha_{s_i} = (Y_{x_i}/Y_{s_i})^2$	7.17	4.17	3	3	

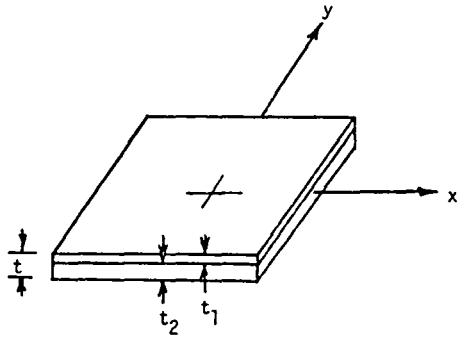

Figure 1. Two-Layer Model Representing Strain Hardening Behavior

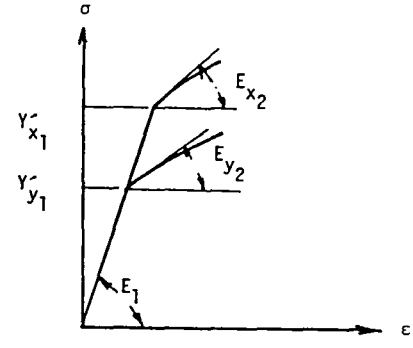

Figure 2. Uniaxial Stress-Strain Relations for Two-Layer Model

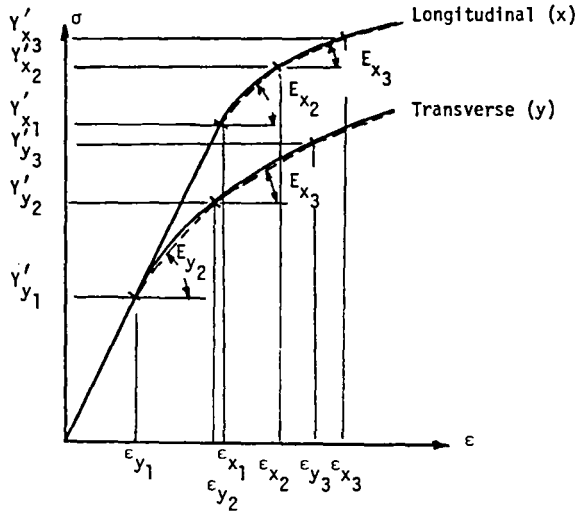

Figure 3. Stress-Strain Relations by Mechanical Sublayer Model

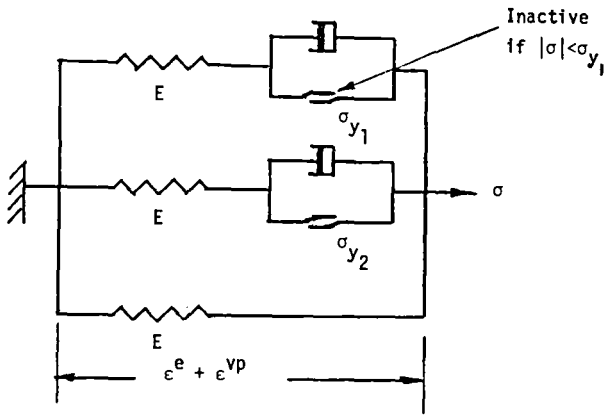

Figure 4. Viscoplastic Model for Mechanical Sublayers

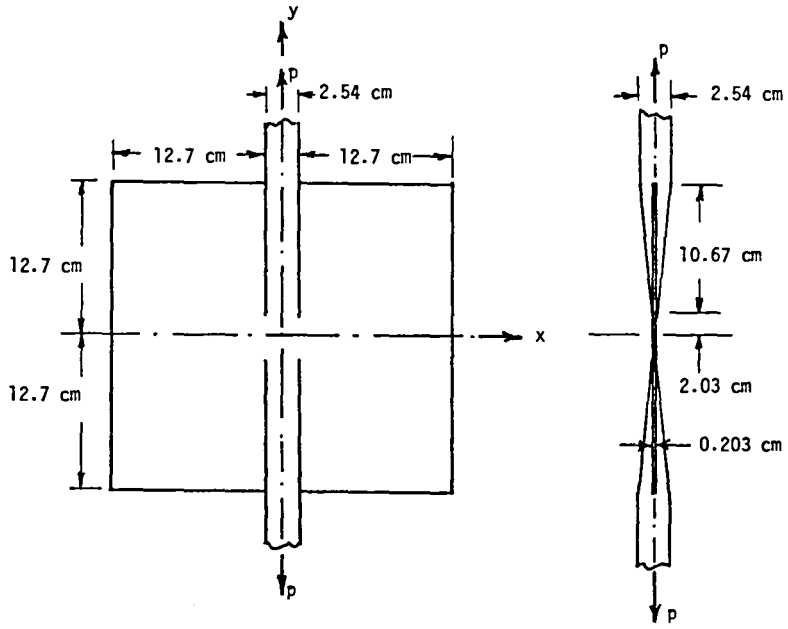

Figure 5. Dimensions of Shear Lag Structure

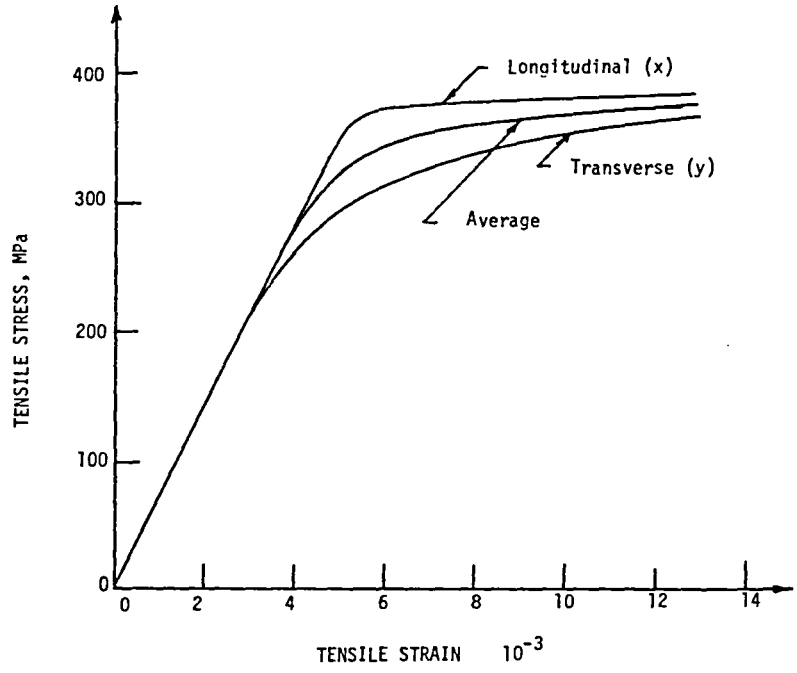

Figure 6. Fitted Stress-Strain Curves of 2024-T4 Aluminum Alloy Plate

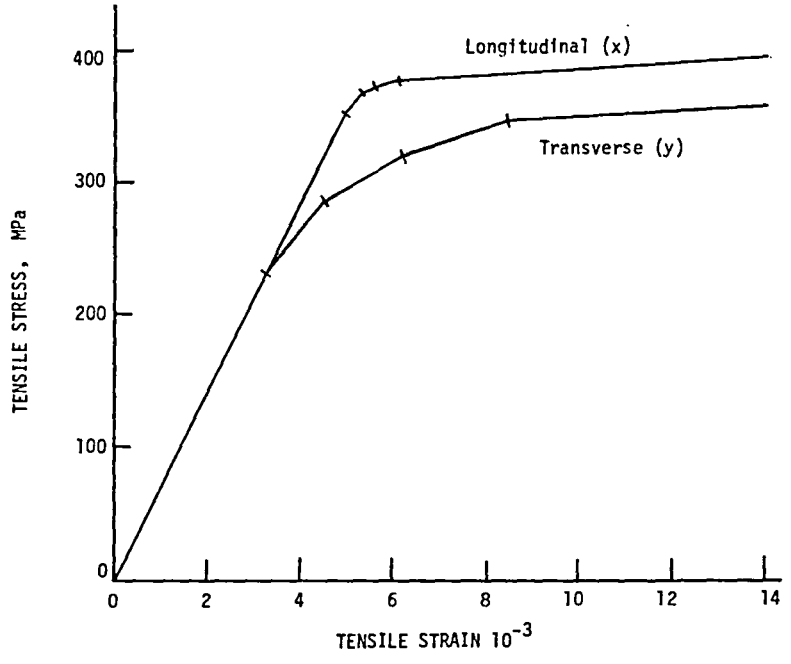

Figure 7. Approximate Stress-Strain Curves by Mechanical Sublayer Model (2024-T4)

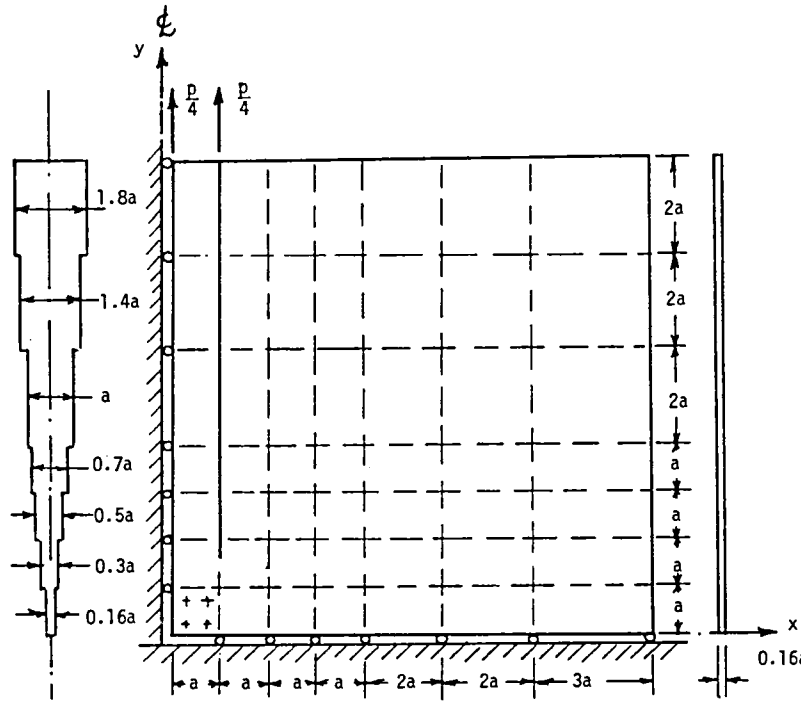

a = 1.27 cm

Figure 8. Finite Element Mesh for Shear Lag Structure

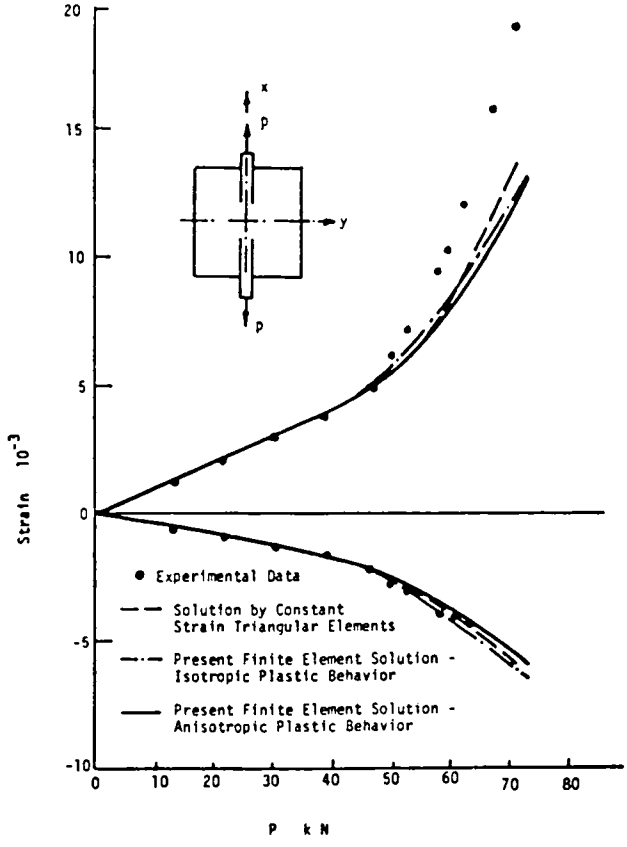

Figure 9. Strain Components at Center of Shear Lag Structure - Comparison of Different Finite Element Solutions

CONSTRAINED SELF-ADAPTIVE SOLUTIONS PROCEDURES FOR STRUCTURE SUBJECT TO HIGH TEMPERATURE ELASTIC-PLASTIC CREEP EFFECTS*

Joseph Padovan and Surapong Tovichakchaikul
University of Akron
Akron, Ohio 44325

Currently, the design of engineering structures which operate in a creep range involves the use of either approximate methods [1-3] or iterative/incremental schemes [4]. As has noted by Corum [5], Hayhurst and Krzeczkowski [6], among others [7,8], the current status of time-iterative or incremental schemes in creep analysis is such that a poor choice of time step size can lead to instabilities in the solution or to erroneous results. Because of this, even the highly skilled user is faced with extremely expensive parametric studies in order to determine requisite time stepping.

In the context of the foregoing, the paper will develop a new solution strategy which can handle elastic-plastic-creep problems in an inherently stable manner. This is achieved by introducing a new constrained time stepping algorithm which will enable the solution of creep initiated pre/postbuckling behavior where indefinite tangent stiffnesses are encountered. Due to the generality of the scheme, both monotone and cyclic loading histories can be handled.

The solution to the foregoing problem is made possible through the use of closed piecewise continuous least upper bounding constraint surfaces which control the size of successive dependent variable excursions arising out of the time stepping process. Because of the manner of constraint, the overall algorithm in addition to being architectur-

*This work has been supported by NASA Lewis under Grant NAG 3-54.

ally flexible has self adaptive attributes which enable the stable and efficient solution of problems involving elastic-plastic-creep properties exhibiting severe nonlinearities. Specifically, the scheme can be easily modified to handle a wide variety of constitutive formulations. Additionally, regardless of the constitutive relation employed, the approach can handle situations exhibiting indefinite tangent properties potentially leading to large deformation and strain pre-post-buckling behavior.

The presentation will give a thorough overview of current solution schemes and their short comings, the development of constrained time stepping algorithms, as well as illustrate the results of several numerical experiments which benchmark the new procedure. These give special attention to tracing the degradation of structural integrity and stability as cyclical loading proceeds.

As a preview of the paper, Fig. 1 illustrates the finite element simulation of an arch subject to a cyclical load history at elevated temperatures. Figure 2 depicts the force-deflection response of the arch as the external loading is cycled. As can be seen, while the loading is initially well below the buckling limit of the arch, due to significant structural distortion caused by creep, the load carrying capacity is severely degraded with increasing time. Since the problem involves very large kinematic distortions, the capability of the new constrained time stepping algorithm is clearly illustrated. The presentation will highlight several such examples as well as benchmark the approach with other schemes.

References

1. Leckie, F. A., "A Review of Bounding Techniques in Shakedown and Ratchetting at Elevated Temperatures", Report No. 195, Pub. Welding Res. Council, New York 1974.

2. Leckie, F. A., and Hayhurst, D. R., "Creep Rupture of Structures", Proc. Roy. Soc. London Vol. 340, pp 323-347, 1974.

3. Leckie, F. A., Hayhurst, D. R., and Morrison, "The Creep Behavior of Sphere-Cylinder Shell Intersections Subjected to Internal Pressure", Proc. Roy. Soc. London V349, pp 9-34, 1976.

4. Penny, R. K., Marriot, D. L., Design for Creep, McGraw-Hill, New york 1971.

5. Corum, J. M., "Pressure Vessels and Piping: Verification and Qualification of Inelastic Analysis Computer Programs", forward to the Proceedings of the 2nd National Congress on Pressure Vessels and Piping, ASME, San Francisco CA, 1975.

6. Hayhurst, D. R. and Krzeczkowski, "Numerical Solution of Creep Problems", Comput. Meth. in Appl. Mech. and Eng., Vol. 20, pp 151, 1979.

7. Padovan, J. and Tovichakchaikul, S., "Self-Adaptive Predictor-Corrector Algorithms for Static Nonlinear Structural Analysis", Computers and Structures (in press), also NASA CR 165410, September 1981.

8. Padovan, J. and Tovichakchaikul, S., "On the Solution of Creep Induced Buckling in General Structure", Computers and Structures (in press).

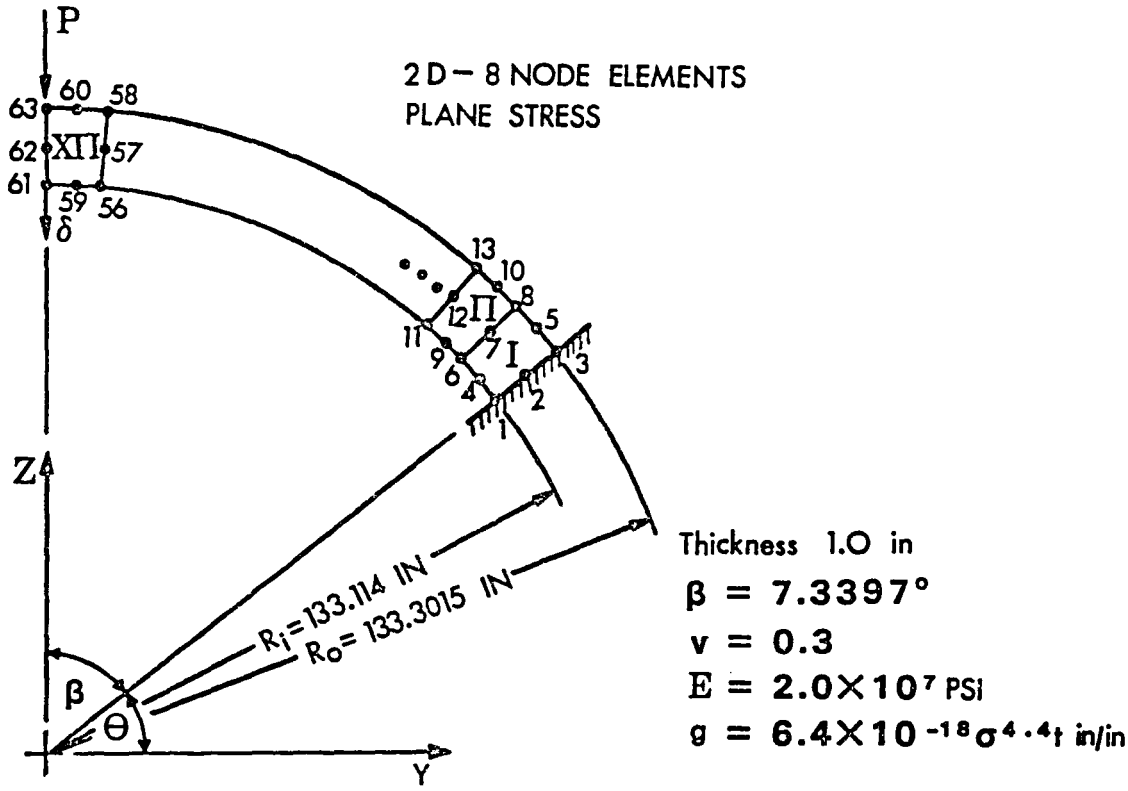

FIG. 1 GEOMETRY,MATERIAL PROPERTIES AND FE MESH OF CENTRALLY LOAD ARCH.

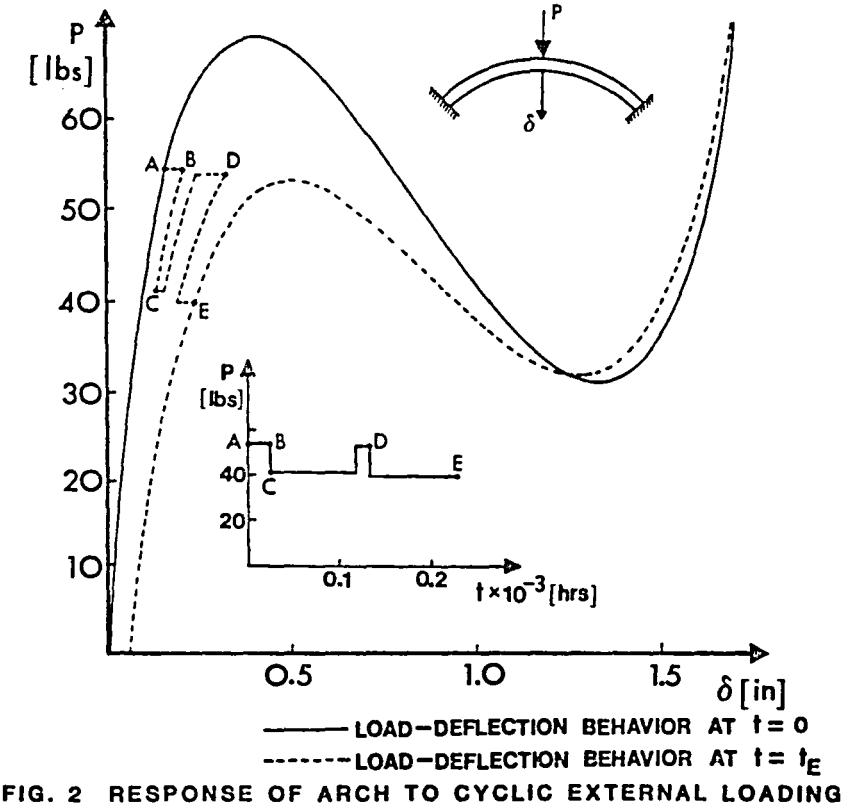

FIG. 2 RESPONSE OF ARCH TO CYCLIC EXTERNAL LOADING AT ELEVATED TEMPERATURE.

STRESS AND FRACTURE ANALYSES UNDER ELASTIC-PLASTIC AND CREEP CONDITIONS: SOME BASIC DEVELOPMENTS AND COMPUTATIONAL APPROACHES*

K. W. Reed, R. B. Stonesifer,** and S. N. Atluri
Georgia Institute of Technology
Atlanta, Georgia 30032

Abstract:

In Part I of this paper a new hybrid-stress finite element algorithm, suitable for analyses of large quasi-static deformations of inelastic solids, is presented. Principal variables in the formulation are the nominal stress-rate and spin. As such, a consistent reformulation of the constitutive equation is necessary, and is discussed. The finite element equations give rise to an initial value problem. Time integration has been accomplished by Euler and Runge-Kutta schemes and the superior accuracy of the higher order schemes is noted. In the course of integration of stress in time, it has been demonstrated that classical schemes such as Euler's and Runge-Kutta may lead to strong frame-dependence. As a remedy, modified integration schemes are proposed and the potential of the new schemes for suppressing frame dependence of numerically integrated stress is demonstrated. The applicability of explicit and implicit forward gradient schemes to improve the stability of time-integration in large deformation problems is investigated. The feasibility and performance of the present methods are demonstrated in a number of problems, and it is found that the stresses obtained by the present method are of exceptional accuracy, much more than could be expected of an assumed-velocity based finite element algorithm.

In Part II of this paper, the topic of the development of valid creep fracture criteria is addressed. Until now, the so-called C* integral, intro-

*A report of research supported under NASA Grant NAG 3-38.

**Formerly a Doctoral Candidate (now graduated and in private eng. practice).

duced by Goldman and Hutchinson, was attempted to be used in the literature to correlate creep crack growth rate. In the present work, a new path-independent integral parameter ($\underline{\dot{T}}$) which has a considerably more degree of generality and validity than the C* integral, is introduced. The mathematical aspects of this parameter are first reviewed by deriving generalized vector forms of the parameters ($\underline{\dot{T}}$) and $\underline{C}^*$; using conservation laws which are valid for arbitrary, three-dimensional cracked bodies with (macro)-crack surface tractions, body forces, inertial effects and large deformations. Two principal conclusions are that ($\underline{\dot{T}}$) is a valid crack-tip parameter during nonsteady as well as steady-state creep and that ($\underline{\dot{T}}$) has an energy rate interpretation whereas $\underline{C}^*$ does not. Using this new integral, and a finite element analysis procedure, several fundamental aspects of creep crack-growth are studied numerically. Specifically numerical results are presented for a double-edge-crack specimen for which experimental results are available. Finally, a simplified methodology for predicting creep growth behaviour is presented, based on the conclusions drawn from the present numerical simulations of experimental data.

Part I: Stress Analysis of Inelastic Solids Using Assumed Stress Finite Elements

Nomenclature:

$C(\tau)$ configuration (image of the body in space at time τ)

$\underline{X}$ position vector in space at time τ

$\underline{x}$ position vector in space at (present) time t

$\nabla = \underline{e}^i \, \partial/\partial x^i$; $\nabla_X = \underline{e}^I \, \partial/\partial X^I$; $\dot{a} = \partial a/\partial t + \underline{V}.\nabla a$ material derivative of 'a'

$\underline{\chi}_\tau$ deformation function; maps $C(\tau)$ to $C(t)$ as

$$\underline{x} = \underline{\chi}_\tau(\underline{X},t)$$

$\underline{V}$ velocity function; related to deformation function as

$$\underline{V}(\underline{\chi}_\tau(\underline{X},t),t) = \dot{\underline{\chi}}_\tau(\underline{X},t)$$

$\underset{\sim}{F}_\tau \equiv (\nabla_X \underline{\chi}_\tau(\underline{X},t))^T$ deformation gradient

$J_\tau = \det \underset{\sim}{F}_\tau$

$\underset{\sim}{L} = (\nabla \underline{V}(\underline{x},t))^T$ velocity gradient

$\dot{J} = \nabla . \underline{V}(\underline{x},t)$ dilitation

$\underset{\sim}{\varepsilon} = \frac{1}{2}(\underset{\sim}{L}+\underset{\sim}{L}^T)$ stretching

$\underset{\sim}{\omega} = \frac{1}{2}(\underset{\sim}{L}-\underset{\sim}{L}^T)$ spin

$\underline{T}$ true traction; $\underline{T}_\tau$ nominal traction relative to $C(\tau)$

$\underset{\sim}{\tau}$ true stress; $\underset{\sim}{\sigma}_\tau = J_\tau \underset{\sim}{\tau}$ Kirchhoff stress relative to $C(\tau)$

$\underset{\sim}{t}_\tau = \underset{\sim}{F}_\tau^{-1} \underset{\sim}{\sigma}_\tau$ nominal stress relative to $C(\tau)$

$\dot{\underline{T}}$ true traction rate; $\dot{\underline{T}}_\tau$ nominal traction rate

$\dot{\underset{\sim}{\sigma}} = \dot{J}\underset{\sim}{\tau} + \dot{\underset{\sim}{\tau}}$ Kirchhoff stress rate

$\dot{\underset{\sim}{t}} = -(\underset{\sim}{\varepsilon}+\underset{\sim}{\omega}) \cdot \underset{\sim}{\tau} + \dot{\underset{\sim}{\sigma}}$ nominal stress rate

$\dot{\underset{\sim}{\sigma}}^* = \dot{\underset{\sim}{\sigma}} - \underset{\sim}{\omega} \cdot \underset{\sim}{\tau} + \underset{\sim}{\tau} \cdot \underset{\sim}{\omega}$ 'corotational' stress rate

Introduction:

The research which produced the present hybrid stress fintie element algorithm was motivated by the observation that hybrid stress algorithms consistently outperform those using velocity (or displacement) as the sole variable. Hybrid stress models for infinitesimal deformation of shells and incompressible solids have been topics of intense research since Pian's first presentation of such a model in [1]. However, hybrid stress models for finite deformations have only been researched since de Veubeke's [2] presentation of a complementary energy principle for finite elastic deformations, and Atluri's [3], [4] generalization of that principle for inelastic solids. A hybrid stress model for finite elastic deformation was presented by Murakawa [5]. In this report a hybrid stress model for finite inelastic deformation is detailed.

The Boundary Value Problem:

Compatibility

$$\nabla X(\underset{\sim}{\varepsilon}-\underset{\sim}{\omega}) = 0; \tag{I.1}$$

Linear Momentum Balance (LMB)

$$\nabla.\dot{\underset{\sim}{t}} + \rho\dot{\underline{b}} = \underline{0}; \tag{I.2}$$

Angular Momentum Balance (AMB)

$$[(\underset{\sim}{\varepsilon}+\underset{\sim}{\omega}) \cdot \underset{\sim}{\tau} + \dot{\underset{\sim}{t}}] - [(\underset{\sim}{\varepsilon}+\underset{\sim}{\omega}) \cdot \underset{\sim}{\tau} + \dot{\underset{\sim}{t}}]^T = \underset{\sim}{0} \tag{I.3}$$

Constitutive Equations

$$\underset{\sim}{\varepsilon} = \partial R/\partial\dot{\underset{\sim}{t}}; \quad \dot{\underset{\sim}{\tau}} = \frac{1}{2}(\dot{\underset{\sim}{t}}+\underset{\sim}{\tau}.\underset{\sim}{\omega}-\underset{\sim}{\omega}.\underset{\sim}{\tau}+\dot{\underset{\sim}{t}}^T); \tag{I.4}$$

Velocity Boundary Condition (VBC)

$$\delta\underline{s}.(-\underset{\sim}{\varepsilon}+\underset{\sim}{\omega}+\nabla\overline{\underline{V}}) = 0 \text{ on } S_v \ (\delta\underline{s} \text{ is any tangent on } S_v) \tag{I.5}$$

Traction Boundary Condition (TBC)

$$\underline{n} \cdot \dot{\underset{\sim}{t}} = \dot{\overline{\underline{T}}}_t \text{ on } S_\sigma \tag{I.6}$$

Above are listed the equations of the general boundary value problem associated with quasistatic deformations of inelastic solids. From (I.1) through (I.4) one may obtain 18 scalar equations for the 9 unknown stress rate components $\dot{t}^{ij}$, 3 unknown spin components ω^{ij}, and 6 unknown stretching components ε^{ij}. It is possible to reset (I.1) through (I.6) so that only velocity components V^i appear as variables. Alternatively one may use (I.4) to eliminate $\underset{\sim}{\varepsilon}$ as a variable in (I.1) and (I.3), thus obtaining a boundary value problem for the components of stress rate and spin. Any solution of this latter boundary value problem is a stationary point of the functional

$$\pi_{mc}(\underline{V},\underset{\sim}{\omega},\dot{\underset{\sim}{t}}) = \int_V \{-R - \frac{1}{2}\,\tau:(\underset{\sim}{\omega}.\underset{\sim}{\omega}) + \dot{\underset{\sim}{t}}:\underset{\sim}{\omega}\}dV$$

$$+ \int_{S_V} \underline{n} \cdot \dot{\underset{\sim}{t}} \cdot \overline{\underline{V}}dS + \int_{S_\sigma} (\underline{n}.\dot{\underset{\sim}{t}}-\dot{\overline{\underline{T}}}_t).\underline{V}dS \tag{I.7}$$

provided that only stress rate variations $\delta\dot{\underset{\sim}{t}}$ such that

$$\nabla \cdot \delta\dot{\underset{\sim}{t}} = \underline{0} \tag{I.8}$$

and spin variations $\delta\underset{\sim}{\omega}$ such that

$$\delta\underset{\sim}{\omega} + \delta\underset{\sim}{\omega}^{T} = \underset{\sim}{0} \tag{I.9}$$

are admitted to $\delta\pi_{mc}$. The velocity in $\delta\pi_{mc}$ plays the role of a Lagrange multiplier.

We replace the boundary value problem for $\dot{\underset{\sim}{t}}$ and $\underset{\sim}{\omega}$ by the generalized b.v.p.:

$$\delta\pi_{mc}(\underline{V},\underset{\sim}{\omega},\dot{\underset{\sim}{t}}) = 0 \tag{I.10}$$

with subsidiary conditions:

$$\omega + \underset{\sim}{\omega}^{T} = \underset{\sim}{0} \tag{I.11}$$

$$\nabla \cdot \dot{\underset{\sim}{t}} + \rho\dot{\underline{b}} = \underline{0} \tag{I.12}*$$

The stationary conditions of π_{mc}, when (I.11) and (I.12) decide admissible $\underset{\sim}{\omega}$ and $\dot{\underset{\sim}{t}}$, are

$$\int_V \{[(\underset{\sim}{\varepsilon}+\underset{\sim}{\omega}) \cdot \underset{\sim}{\tau} + \dot{\underset{\sim}{t}}]:\delta\underset{\sim}{\omega}\} = 0 \tag{I.13}$$

$$\int_V \{[-\underset{\sim}{\varepsilon}+\underset{\sim}{\omega}]:\delta\dot{\underset{\sim}{t}}\}dV + \int_{S_V} \underline{n}.\delta\dot{\underset{\sim}{t}}.\overline{\underline{V}}dS = 0 \tag{I.14}$$

$$\int_{S_\sigma} (\underline{n}.\dot{\underset{\sim}{t}}-\dot{\overline{\underline{T}}}_t) \cdot \delta\underline{V}dS = 0 \tag{I.15}$$

where $\underset{\sim}{\varepsilon}$ is written for $\partial R/\partial\dot{\underset{\sim}{\tau}}$. Equations (I.13), (I.14), and (I.15) are variational statements of AMB (I.3), compatibility (I.1) and VBC (I.5), and TBC (I.6), respectively.

---

* the general solution of this equation is known as $\dot{\underset{\sim}{t}}=\dot{\underset{\sim}{t}}^{o}+\dot{\underset{\sim}{t}}^{b}$, where $\dot{\underset{\sim}{t}}^{o}=\nabla X\underset{\sim}{\Phi}$ and $\nabla.\dot{\underset{\sim}{t}}^{b}=-\rho\dot{\underline{b}}$.

Reformulation of the Constitutive Equation:

As may be surmised from the development above, the present approach necessitates reformulation of the constitutive equation. In applications one typically is given or may find a constitutive equation of the form

$$\overset{\nabla}{\underset{\sim}{\sigma}}{}^{*} = \underset{\approx}{V} : \underset{\sim}{\varepsilon} + \underset{\sim}{\Sigma} \tag{I.16}$$

where $\underset{\approx}{V}$ and $\underset{\sim}{\Sigma}$ generally depend upon $\underset{\sim}{\varepsilon}$, $\underset{\sim}{\tau}$, and scalar invariants*. If $\underset{\approx}{V}$ and $\underset{\sim}{\Sigma}$ do not depend on $\underset{\sim}{\varepsilon}$ then we say (I.16) is <u>affine</u> with respect to $\underset{\sim}{\varepsilon}$. This includes most material models found in the engineering literature. If (I.16) is also an isotropic function then $\underset{\approx}{V}$ and $\underset{\sim}{\Sigma}$ may be set in the forms

$$\begin{aligned} V_{ijkl} = {} & \lambda^{11}(\delta_{ij}\delta_{kl}) + \lambda^{12}(\delta_{ij}\tau'_{kl}) + \lambda^{13}(\delta_{ij}s_{kl}) \\ & \lambda^{21}(\tau'_{ij}\delta_{kl}) + \lambda^{22}(\tau'_{ij}\tau_{kl}) + \lambda^{23}(\tau'_{ij}s_{kl}) \\ & \lambda^{31}(s_{ij}\delta_{kl}) + \lambda^{32}(s_{ij}\tau'_{kl}) + \lambda^{33}(s_{ij}s_{kl}) \\ & + 2\mu'(\delta_{ik\ jl}) + \mu^{2}(\delta_{ik}\tau'_{lj}+\tau'_{ik}\delta_{lj}) + \mu^{3}(\delta_{ik}s_{lj}+s_{ik}\delta_{lj}) \end{aligned} \tag{I.17}$$

and $$\Sigma_{ij} = \eta^{1}\delta_{ij} + \eta^{2}\tau'_{ij} + \nu^{3}s_{ij} \tag{I.18}$$

where $\underset{\sim}{\tau}'$ is the stress deviator and $\underset{\sim}{s}=\underset{\sim}{\tau}'.\underset{\sim}{\tau}'$. The λ^{IJ}, μ^{I}, and η^{I} are functions of the scalar invariants of the deformation.

This form still includes most material models found in the engineering literature. Notable exceptions are models for materials with anisotropy in the stress free state, where the present model reduces to

$$\overset{\nabla}{\underset{\sim}{\sigma}}{}^{*} = 2\mu^{1}\underset{\sim}{\varepsilon} + \lambda^{11}(\underset{\sim}{I}:\underset{\sim}{\varepsilon})\underset{\sim}{I} \tag{I.19}$$

By retaining the constitutive equation in the general form (I.16), (I.17), (I.18) in our development we are led naturally to a 'unified numerical procedure' for problems of large strain elasticity, plasticity, viscoplasticity, and creep.

* temperature, strain histories, as well as joint invariants of $\underset{\sim}{\tau}$ and $\underset{\sim}{\varepsilon}$.

The desired form for the constitutive equation may be found by noting the relation between the stress rates $\overset{\circ}{\underset{\sim}{\sigma}}{}^*$ and $\dot{\underset{\sim}{r}}$:

$$\dot{\underset{\sim}{r}} = \overset{\circ}{\underset{\sim}{\sigma}}{}^* - \frac{1}{2}(\underset{\sim}{\tau}\cdot\underset{\sim}{\varepsilon}+\underset{\sim}{\varepsilon}\cdot\underset{\sim}{\tau}) \tag{I.20}$$

Using (I.16) to eliminate $\overset{\circ}{\underset{\sim}{\sigma}}{}^*$ from (I.20) gives

$$\dot{\underset{\sim}{r}} = (\underset{\approx}{V}:\underset{\sim}{\varepsilon}+\underset{\sim}{\Sigma}) - \frac{1}{2}(\underset{\sim}{\tau}\cdot\underset{\sim}{\varepsilon}+\underset{\sim}{\varepsilon}\cdot\underset{\sim}{\tau}) = \underset{\approx}{W}:\underset{\sim}{\varepsilon} + \underset{\sim}{\Sigma} \tag{I.21}$$

where $\underset{\approx}{W}$ is defined by

$$W_{ijkl} = V_{ijkl} - \frac{1}{2}(\tau_{ik}\delta_{lj}+\delta_{ik}\tau_{lj}) \tag{I.22}$$

Inversion of the relation (I.21) yields

$$\underset{\sim}{\varepsilon} = \underset{\approx}{W}^{-1}:(\dot{\underset{\sim}{r}}-\underset{\sim}{\Sigma}) \tag{I.23}$$

If $\underset{\approx}{W}^{-1}$ is symmetric (i.e., $W^{-1}_{ijkl}=W^{-1}_{klij}$) then a potential R exists for $\underset{\sim}{\varepsilon}$:

$$\underset{\sim}{\varepsilon} = \partial R/\partial\dot{\underset{\sim}{r}};\ R = \frac{1}{2}(\dot{\underset{\sim}{r}}-\underset{\sim}{\Sigma}):\underset{\approx}{W}^{-1}:(\dot{\underset{\sim}{r}}-\underset{\sim}{\Sigma}) \tag{I.24}$$

The condition necessary and sufficient for W^{-1} to be symmetric is $\lambda^{IJ}=\lambda^{JI}$. This condition is satisfied by most engineering materials*.

In practice one must construct $\underset{\approx}{W}$ from $\underset{\approx}{V}$, then invert $\underset{\approx}{W}$ (if possible) to achieve the form (I.24). This is a major undertaking from a computational point of view since $\underset{\approx}{W}$ is generally different at each point of a stressed body. Therefore special attention is given to practical methods for construction of $\underset{\approx}{W}^{-1}$. For plane problems $\underset{\approx}{W}^{-1}$ can be found analytically. For general problems in which $\underset{\approx}{V}^{-1}$ is known a simple approximation for $\underset{\approx}{W}^{-1}$ is often of acceptable accuracy. The details of the two special cases are discussed in Appendix B of [6].

The Finite Element Algorithm:

Equations (I.13), (I.14), and (I.15) are the basis for the finite element algorithm presented in this report. The finite element equations are obtained

* Flow laws using the corotational rate of the true stress are an exception.

by introduction of polynomial representations for $\underset{\sim}{V}$, $\underset{\sim}{\omega}$, and $\dot{\underset{\sim}{t}}^*$ to (13) and (14); on the N^{th} element:

$$\underset{\sim}{V} = \sum_{i=1}^{NQ} \underline{N}_i \, \tilde{q}_N^i \qquad \underline{N}_i: \text{ isoparametric shape functions} \tag{I.25}$$

$$\underset{\sim}{\omega} = \sum_{i=1}^{NW} \underset{\sim}{QW}_i \alpha_N^i \qquad \text{where } \underset{\sim}{QW}_i + \underset{\sim}{QW}_i^T = 0 \tag{I.26}$$

$$\dot{\underset{\sim}{t}} = \sum_{i=1}^{NT} \underset{\sim}{QT}_i \beta_N^i + \dot{\underset{\sim}{t}}^b \qquad \text{where } \underset{\sim}{QT}_i = \nabla \times \underset{\sim}{\Phi}_i \tag{I.27}$$

$$\nabla . \dot{\underset{\sim}{t}}^b = -\rho \dot{\underline{b}}$$

The representations for $\underset{\sim}{\omega}$ and $\dot{\underset{\sim}{t}}$ are independent on each element, so (I.15) must be replaced by the 'interelement traction reciprocity' relation:

$$\sum_{N=1}^{NELM} \left\{ \int_{S_N - (S_N \cap S_V)} (\underline{n} . \dot{\underset{\sim}{t}} . \delta \underline{V}) \, dS - \int_{(S_N \cap S_\sigma)} \dot{\underline{\bar{T}}}_t . \delta \underline{V} \, dS \right\} = 0 \tag{I.28}$$

which includes (I.15). The finite element equations are obtained by performing the assigned integrations (Gaussian quadrature rules are used). Those equations are listed below (the element index 'N' has been suppressed on the α_N^i and β_N^i):

$$\{\delta\alpha\}^T \{ -[H^{11} \quad H^{12}] \{ {\alpha \atop \beta} \} + \{P^{\alpha,b}\} + \{P^{\alpha,\Sigma}\} \} = 0 \tag{I.29}$$

$$\{\delta\beta\}^T \{ -[H^{21} \quad H^{22}] \{ {\alpha \atop \beta} \} + \{P^{\beta,b}\} + \{P^{\beta,\Sigma}\} + [G]\{\tilde{q}_N\} \} = 0 \tag{I.30}$$

$$\sum_{N=1}^{NELM} \{ \{\delta q_N\}^T [0 \quad G_N^T] \{ {\alpha \atop \beta} \} - \{\delta q_N\}^T \{F_N\} \} = 0 \tag{I.31}$$

*Mathematical 'rank' conditions require that $NT \geq NQ-T$, where T is the number of translational degrees of freedom of an element. Moreover, the [QW] and [QT] should be of the same polynomial degree.

Henceforth we refer to (I.29) as AMB, to (I.30) as compatibility, and to (I.31) as TBC. The individual matrices are defined below:

$$H_{ij}^{11} = \int_{V_N} \{(\underset{\sim}{\tau}.\underset{\sim}{QW}_i):\underset{\approx}{D}:(\underset{\sim}{\tau}.\underset{\sim}{QW}_j) + \underset{\sim}{\tau}:(\underset{\sim}{QW}_i\ \underset{\sim}{QW}_j)\}dV \qquad ((.32)$$

$$H_{ij}^{12} = \int_{V_N} \{(\underset{\sim}{\tau}.\underset{\sim}{QW}_i):\underset{\approx}{D}:(\underset{\sim}{QT}_j) - \underset{\sim}{QW}_i:\underset{\sim}{QT}_j\}dV \qquad (I.33)$$

$$H_{ij}^{21} = \int_{V_N} \{(\underset{\sim}{QT}_i):\underset{\approx}{D}:(\underset{\sim}{\tau}.\underset{\sim}{QW}_j) - \underset{\sim}{QT}_i:\underset{\sim}{QW}_j\}dV \qquad (I.34)$$

$$H_{ij}^{22} = \int_{V_N} \{(\underset{\sim}{QT}_i):\underset{\approx}{D}:(\underset{\sim}{QT}_j)\}dV \qquad (I.35)$$

$$G_{ij} = \int_{S_N} \underline{n}.(\underset{\sim}{QT}_i).(\underline{N}_j)dS \qquad (I.36)$$

$$F_i = \int_{(S_N \cap S_\sigma)} \dot{\underline{T}}_t.(\underline{N}_i)dS \qquad (I.37)$$

$$P_i^{\alpha,b} = \int_{V_N} \{(\underset{\sim}{QW}_i):[\dot{\underset{\sim}{t}}^b + (\underset{\approx}{D}:\dot{\underset{\sim}{t}}^b).\underset{\sim}{\tau} + \frac{1}{h}\underset{\sim}{\tau}]\}dV \qquad (I.38)$$

$$P_i^{\beta,b} = \int_{V_N} \{(\underset{\sim}{QT}_i):(-\underset{\approx}{D}:\dot{\underset{\sim}{t}}^b)\}dV \qquad (I.39)$$

$$P_i^{\alpha,\Sigma} = \int_{V_N} \{(\underset{\sim}{\tau}.\underset{\sim}{QW}_i):\underset{\approx}{D}:\underset{\sim}{\Sigma}\}dV \qquad (I.40)$$

$$P_i^{\beta,\Sigma} = \int_{V_N} \{(\underset{\sim}{QT}_i):\underset{\approx}{D}:\underset{\sim}{\Sigma}\}dV \qquad (I.41)$$

and $\underset{\approx}{D}$ is obtained from $\underset{\approx}{W}^{-1}$ by symmetrization:

$$D_{ijkl} = \frac{1}{4}(W^{-1}_{ijkl} + W^{-1}_{jikl} + W^{-1}_{ijlk} + W^{-1}_{jilk}) \qquad (I.42)$$

*The last term in the integrand is a residual whose significance is explained in [6].

This symmetrization is easily done after $\underset{\approx}{W}^{-1}$ is computed, and serves to reduce by a factor of four the number of multiplications required to compute the H matrices (I.32) through (I.35), and other matrices involving $\underset{\approx}{W}^{-1}$.

The procedure which leads one from equations (I.29) and (I.30) to the element stiffness matrix is virtually identical to that of Pian [1]. We define the element 'H-matrix' as

$$[H] = \begin{bmatrix} H^{11} & H^{12} \\ H^{21} & H^{22} \end{bmatrix} \tag{I.43}$$

and loads $\{P^b\}$ and $\{P^\Sigma\}$, due to body force and fluidity, respectively, as

$$\{P^b\} = \begin{Bmatrix} P^{\alpha,b} \\ P^{\beta,b} \end{Bmatrix} : \{P^\Sigma\} = \begin{Bmatrix} P^{\alpha,\Sigma} \\ P^{\beta,\Sigma} \end{Bmatrix} \tag{I.44}$$

Then (I.29) and (I.30) may be collected into a single equation as

$$[H]\begin{Bmatrix} \alpha \\ \beta \end{Bmatrix} = \begin{bmatrix} 0 \\ G \end{bmatrix} \{\tilde{q}\} + \{P^b + P^\Sigma\} \tag{I.45}$$

If $\underset{\approx}{D}$ is symmetric, that is, if $W^{-1}_{ijkl} = W^{-1}_{klij}$, then from (I.32) through (I.35) we easily determine that [H] is symmetric.

If the H-matrix is not singular, then we solve the matrix equation (NQ+1 right hand sides)

$$[H][H^{-1}G \quad H^{-1}P] = \left[\begin{array}{c|c} 0 & \\ G & P^b + P^\Sigma \end{array}\right] \tag{I.46}$$

on each element. Explicit calculation of the inverse of [H] is not only unnecessary, but substantially increases the time required to generate the element stiffness matrix. According to (I.45), the spin and stress parameters on each element are given by

$$\begin{Bmatrix} \alpha \\ \beta \end{Bmatrix} = [H^{-1}G]\{\tilde{q}\} + \{H^{-1}P\} \tag{I.47}$$

Using (I.47) to eliminate $\{\alpha/\beta\}$ from TBC (I.31) leads to

$$\sum_{N=1}^{NELM} \{\{\delta q_N\}^T[K_N]\{\tilde{q}_N\} + \{\delta q_N\}[0 \quad G_N^T]\{H^{-1}P_N\} - \{\delta q_N\}^T\{F_N\}\} = 0 \qquad (I.48)$$

in which the element stiffness matrix has been identified as

$$[K_N] = [0 \quad G_N^T][H^{-1}G_N] \qquad (I.49)$$

and the resultant nodal 'forces' are given by

$$-[0 \quad G_N^T]\{H^{-1}P_N\} + \{F_N\} \qquad (I.50)$$

It is easily verified that the element stiffness matrix [K] is symmetric if [H] is, and so the symmetry of [K] ultimately depends upon the symmetry of the constitutive matrix $\underset{\approx}{W}$.

To this point all of the finite element equations are independent on each element. The formal assembly of the global stiffness matrix and loads is accomplished by introduction of assembly matrices $[A_N]$ through whose use the element level velocity parameters may be expressed as functions of the global velocity parameters. For $\{\tilde{q}\}$ and $\{\delta q\}$ we write

$$\{\tilde{q}_N\} = [A_N]\{Q+\overline{Q}\}: \quad \{\delta q_N\} = [A_N]\{\delta Q\};$$

and from (I.48) thus obtain

$$\{\delta Q\}^T[K_G]\{Q\} = \{\delta Q\}^T\{P_G\} - \{\delta Q\}^T[K_G]\{\overline{Q}\} \qquad (I.51)$$

In equation (I.51) the global stiffness matrix $[K_G]$ and the loads $\{P_G\}$ are defined by

$$[K_G] = \sum_{N=1}^{NELM} [A_N]^T[K_N][A_N] \qquad (I.52)$$

and $$\{P_G\} = [A_N]^T\{\{F_N\} - [0 \quad G]\{H^{-1}P_N\}\} \qquad (I.53)$$

The load matrix $\{P_G\}$ contains contributions from the prescribed body for rate $\dot{\underline{b}}$, the relaxation $\underset{\sim}{\Sigma}$, and the traction boundary condition $\dot{\underline{T}}_t$. The global stiff-

ness matrix, as defined by (I.52), will be singular for rigid translations (but not for rigid spin). In order to solve the equation (I.51) we define a modified global stiffness matrix [K*] and a modified load {P*} as follows:

$$K^*_{IJ} = \begin{cases} \delta_{IJ} \text{ if } (\tilde{Q}_I = \overline{Q}_I) \text{ or } (\tilde{Q}_J = \overline{Q}_J) \\ K_{IJ} \text{ otherwise} \end{cases} \tag{I.54}$$

$$P^*_I = \begin{cases} Q_I \text{ if } (\tilde{Q}_I = \overline{Q}_I) \\ P_I - \sum_{J=1}^{NELM} K^G_{IJ} \overline{Q}_J \text{ otherwise} \end{cases} \tag{I.55}$$

Then (I.51) may be replaced by

$$[K^*]\{\tilde{Q}\} = \{P^*\} \tag{I.56}$$

If [K*] is not singular, then we solve (I.56) for $\{\tilde{Q}\}$,

$$\{\tilde{Q}\} = [K^*]^{-1}\{P^*\} \tag{I.57}$$

By backsubstitution we obtain the velocity (on the boundary of each element), the spin and the stress rate on each element:

$$\{\tilde{q}_N\} = [A_N][K^*]^{-1}\{P^*\} \tag{I.58}$$

$$\begin{Bmatrix} \alpha_N \\ \beta_N \end{Bmatrix} = [H^{-1}G_N][A_N][K^*]^{-1}\{P^*\} + \{H^{-1}P_N\} \tag{I.59}$$

$$\underset{\sim}{v}(\underset{\sim}{x}) = [\underline{N}(\underset{\sim}{x})][A_N][K^*]^{-1}\{P^*\} \tag{I.60}$$

$$\begin{Bmatrix} \underset{\sim}{\omega}(\underset{\sim}{x}) \\ \dot{\underset{\sim}{t}}(\underset{\sim}{x}) - \underset{\sim}{t}^b(\underset{\sim}{x}) \end{Bmatrix}_N = \begin{bmatrix} \underset{\sim}{QW}(\underset{\sim}{x}) & 0 \\ 0 & \underset{\sim}{QT}(\underset{\sim}{x}) \end{bmatrix} \left\{ [H^{-1}G_N][A_N][K^*]^{-1}\{P^*\} + \{H^{-1}P_N\} \right\} \tag{I.61}$$

Equations (I.60) and (I.61) comprise the approximate solution of the boundary value probelm.

Integration of the Motion of the Body:

The finite element algorithm just described produces an approximation for the stress rate and velocity, as opposed to stress increments and displacement increments. Thus, considerably more freedom of choice of time integration

schemes is afforded by the present approach than by incremental approaches (which are predisposed to integration by the relatively inefficient Euler's method). In this section we (i) formally state the initial value problem, (ii) discuss numerical integration of that problem, and (iii) present a 'forward gradient scheme' which stabilizes integration of deformations of bodies which exhibit stress relaxation.

Let $\{\underline{x}\} = \{\underline{x}^1, \underline{x}^2, \ldots, \underline{x}^{ND}\}$ be the vector of nodal positions, and let $\{\underline{v}\} = \{\underline{v}^1, \underline{v}^2, \ldots, \underline{v}^{ND}\}$ be the vector of nodal velocities, where ND is the total number of nodes. Similarly, let $\{\underset{\sim}{\tau}\} = \{\underset{\sim}{\tau}^1, \underset{\sim}{\tau}^2, \ldots, \underset{\sim}{\tau}^G\}$ and $\{\dot{\underset{\sim}{t}}\} = \{\dot{\underset{\sim}{t}}^1, \dot{\underset{\sim}{t}}^2, \ldots, \dot{\underset{\sim}{t}}^G\}$ be the quadrature point stresses and stress rates, respectively, where G is the total number of quadrature points in the body. To indicate the dependence of $\{\underline{v}\}$ and $\{\dot{\underset{\sim}{t}}\}$ on $\{\underline{x}\}$, $\{\underset{\sim}{\tau}\}$, and the time dependent prescribed loads, we write*

$$\{\underline{v}\} = f[\{\underline{x}\}, \{\underset{\sim}{\tau}\}, t\} \tag{I.62}$$

$$\{\dot{\underset{\sim}{t}}\} = g[\{\underline{x}\}, \{\underset{\sim}{\tau}\}, t\} \tag{I.63}$$

Since each element node is associated with the same material point $\underline{X}^I$ throughout a deformation, and likewise for each quadrature point, we may write each component of $\{\underline{x}\}$, $\{\underset{\sim}{\tau}\}$, $\{\underline{v}\}$, and $\{\dot{\underset{\sim}{t}}\}$ as

$$\underline{x}^I = \underline{\chi}_\tau(\underline{X}^I, t) \tag{I.64}$$

$$\underset{\sim}{\tau}^I = (1/J_\tau^I)\underset{\sim}{F}_\tau^I \cdot \underset{\sim}{t}_\tau(\underline{X}^I, t) \tag{I.65}$$

$$\underline{V}^T = \dot{\underline{\chi}}_\tau(\underline{X}^I, t) \tag{I.66}$$

$$\dot{\underset{\sim}{t}}^I = (1/J_\tau^I)\underset{\sim}{F}^I \cdot \dot{\underset{\sim}{t}}_\tau(\underline{X}^I, t) \tag{I.67}$$

* The function f and g are introduced specifically as a 'shorthand' for the solution of the finite element equations, as given by (I.60) and (I.61). In practice integrations may be performed on one element at a time.

Introduction of (I.64) - (I.67) to (I.62) and (I.63) gives

$$\{\dot{\underset{\sim}{\chi}}_\tau\} = f_\tau[\{\underset{\sim}{\chi}_\tau\}, \{\underset{\sim}{t}_\tau\}, t] \tag{I.68}$$

$$\{\dot{\underset{\sim}{t}}_\tau\} = g_\tau[\{\underset{\sim}{\chi}_\tau\}, \{\underset{\sim}{t}_\tau\}, t] \tag{I.69}$$

the definitions of f_τ and g_τ being clear. Equations (I.68) and (I.69) and appropriate initial values comprise an initial value problem.

The initial value problem posed by (I.68) and (I.69) and appropriate initial data is dependent upon the finite element equations. From that same discussion, and from the presentation of the finite element equations, it is also clear that the finite element-initial value problem is predisposed to numerical integration. In this section we indicate the types of numerical integration schemes suitable for the present problem, and mention a few important differences between the various types.

The finite element-initial value problem may be integrated by single step explicit schemes, multistep explicit schemes, or (generally multistep) predictor-corrector schemes. Three important facts to be kept in mind when choosing a particular scheme are

(i) the solution vector $\langle\{\underset{\sim}{\chi}_\tau(t_N)\}, \{\underset{\sim}{t}_\tau(t_N)\}\rangle$ at the time $t=t_N$ is of scalar dimension NDOF+9.G, where NDOF is the number of kinematic degrees of freedom of the mesh and G is the total number of quadrature points. Storage required for implementation or different integration schemes can vary appreciably.

(2) evaluation of $\langle f_\tau, g_\tau\rangle$ is expensive on account of the complexity of the finite element equations.

(3) the functions f_τ and g_τ are generally discontinuous at points $\langle\underset{\sim}{\chi}_\tau, \underset{\sim}{t}_\tau\rangle$ which correspond to material yield surfaces.

The multistep methods (explicit and predictor-corrector) require relatively few evaluations of $\langle f_\tau, g_\tau\rangle$ per step; this is an attractive feature.

However, multistep methods are not self starting, the time step is not easily changed, they have relatively large storage requirements (since several past values of $\langle f_\tau, g_\tau \rangle$ must be carried along), and moreover, they cannot be expected to be accurate when the solution crosses a yield surface (since they are based on smooth polynomial interpolation of the solution over several time steps).

On the other hand, the single step methods (explicit and predictor-corrector) are easily started, the time step size is easily adjusted, and they have relatively small storage requirements. They can be expected to perform more favorably than the multistep methods when the solution crosses a yield surface since smoothing over several time steps is not built in. The disadvantage of the single step methods is that a relatively larger number of evaluations of $\langle f_\tau, g_\tau \rangle$ are required per step to achieve a given accuracy when a yield surface is not crossed. However, the advantage of single step methods seem to far outweigh the disadvantages.

In the example accompanying this report the Euler and classical second order Runge-Kutta methods were used. Details of these methods may be found in many textbooks. Errors of the Euler method were gauged (qualitatively) by step-halving and by comparison to results of second order integration for randomly selected time steps. Full details are given in the description of the example problem.

It is worthy of special note that complementary work and energy principles provide no means whatever for checking the satisfaction of LMB, so it is of crucial importance that the numerical integration scheme not introduce errors which tend to unbalance the stress. This maintenance of balanced stress, necessary in stress-based finite element algorithms is the counterpart of maintenance of compatible deformation, necessary in velocity - based algorithms. It can be shown that LMB is maintained when the stress $\underset{\sim}{t}_\tau$ is integrated explicitly, but not when other stresses (such as $\underset{\sim}{\tau}$) are integrated ex-

plicitly. Thus, we integrate $\underset{\sim}{t}_\tau$ explicitly, and find $\underset{\sim}{\tau}$ (afterwards) by the formula

$$\underset{\sim}{\tau} = 1/J_\tau \underset{\sim}{F}_\tau \cdot \underset{\sim}{t}_\tau \tag{I.70}$$

Stability of Numerical Integration of the Initial Value Problem:

It is possible that the difference between two supposed numerical solutions of a given initial value problem is much larger than would be expected to arise from discretization error alone. As an example, consider integration of the stress in a material of the type (I.16) by the Euler method. We suppose, for the sake of simplicity, that $\underset{\sim}{\varepsilon}(t)$ is given and $\underset{\sim}{\Sigma}(\underset{\sim}{\tau}) = -2\mu(\frac{3}{2}\gamma\underset{\sim}{\tau}')$, so that the difference between two solutions satisfies

$$\Delta\dot{\underset{\sim}{\sigma}}^* = [\underset{\approx}{V}(\underset{\sim}{\tau} + \Delta\underset{\sim}{\tau}) - \underset{\approx}{V}(\tau)]:\underset{\sim}{\varepsilon}(t) - (3\mu\gamma)\Delta\underset{\sim}{\tau}' \tag{I.71}$$

If the elastic matrix and stretching are such that, in the Euclidean norm,

$$||[\underset{\approx}{V}(\tau+\Delta\underset{\sim}{\tau}) - \underset{\approx}{V}(\underset{\sim}{\tau})]:\underset{\sim}{\varepsilon}(t)||/||\Delta\underset{\sim}{\tau}|| \to 0 \tag{I.72}$$

as $||\Delta\underset{\sim}{\tau}|| \to 0$, then for sufficiently small $||\Delta\underset{\sim}{\tau}||$, equation (I.71) may be replaced by

$$\Delta\dot{\underset{\sim}{\sigma}}^* = -(3\mu\gamma)\Delta\underset{\sim}{\tau}' \tag{I.73}$$

Defining $\Delta\sigma$ as $\Delta\sigma = J_o\sqrt{\frac{3}{2}\Delta\underset{\sim}{\tau}':\Delta\underset{\sim}{\tau}'}$, we may reduce (I.73) to a scalar equation in the invariant $\Delta\sigma$:

$$\frac{d}{dt}(\Delta\sigma) = -(3\mu\gamma)\Delta\sigma \tag{I.74}$$

For an initial value $\Delta\sigma(0)$ (small), the analytic solution of (I.74) is

$$\Delta\sigma(t) = \Delta\sigma(0)e^{-(3\mu\gamma)t} \tag{I.75}$$

Euler's method yields

$$\Delta\sigma_N = \Delta\sigma(0)(1-3\mu\gamma h)^N \tag{I.76}$$

It is clear from (I.75) that $\Delta\sigma$ decays to zero as time passes. This means that the analytic solution of the equation

$$\dot{\underset{\sim}{\sigma}}^* = \underset{\approx}{V}:\underset{\sim}{\varepsilon}(t) + \underset{\sim}{\Sigma};\ \underset{\sim}{\tau}(0) = \underset{\sim}{\tau}_o \tag{I.77}$$

is stable with respect to sufficiently small perturbations of the deviatoric part of $\underset{\sim}{\tau}$. On the other hand, the numerical solution (I.76) attenuates as time passes only if

$$|(1 - 3\mu\gamma h)| < 1 \tag{I.78}$$

This means that the numerical solution of (I.77) is stable with respect to small perturbations of the deviatoric part of $\underset{\sim}{\tau}'$ only so long as the time step h is bounded above as

$$|h| < 2/(3\mu\gamma) \tag{I.79}$$

This bound is identical to the bound given by Cormeau [7] (see equations 16 and 54 in this reference).

Time steps such as (I.79) are found to be necessary for stability of numerical solutions of the finite element-initial value problem presented in this report. Argyris et al [8] remark that this time step restriction amounts to limiting the inelastic strain increment to be smaller than the elastic strain. Since the elastic strain is usually very small in metals such as those used in structures, this implies that a finite deformation analysis would entail an impractically large number of steps.

The work of Kanchi et al [9] and Atluri and Murakawa [4] suggests the modification we now describe. To improve the estimate of the inelastic strain increment in a time step, we replace $\underset{\sim}{\varepsilon}^p(\underset{\sim}{\tau}_N)$ by an estimate of the mean value of the inelastic stretching in that time step:

$$\underset{\sim}{\varepsilon}^p(\underset{\sim}{\tau}(t_N+\theta h)) \doteq \underset{\sim}{\varepsilon}^p(\underset{\sim}{\tau}(t_N)) + \theta h \left.\frac{d\underset{\sim}{\varepsilon}^p}{d\underset{\sim}{\tau}}\right|_{\underset{\sim}{\tau}=\underset{\sim}{\tau}_N} : \dot{\underset{\sim}{\sigma}}^* \tag{I.80}$$

where the parameter θ, $0 \leq \theta \leq 1$, serves to locate the time at which the mean value is achieved. As θ goes from zero to one, the estimate of the creep-stretch becomes increasingly more conservative.

Equation (I.80) may be introduced to the finite element algorithm through the constitutive equation; (I.16) becomes

$$\overset{\nabla}{\underset{\sim}{\sigma}}{}^{*} = \underset{\approx}{V}_{\theta} : \underset{\sim}{\varepsilon} + \underset{\sim}{\Sigma}_{\theta}$$

where

$$\underset{\approx}{V}_{\theta} = \left[\underset{\approx}{V}^{-1} + \theta h \frac{d\underset{\sim}{\varepsilon}^{p}}{d\underset{\sim}{\tau}}\right]^{-1} ; \quad \underset{\sim}{\Sigma}_{\theta} = -\underset{\approx}{V}_{\theta} : \underset{\sim}{\varepsilon}^{p} \tag{I.81}$$

From $\underset{\approx}{V}_{\theta}$ (I.81) we derive $\underset{\approx}{W}_{\theta}$ just as we derived $\underset{\approx}{W}$ from $\underset{\approx}{V}$:

$$\underset{\approx}{\dot{W}}_{\theta} = \underset{\approx}{V}_{\theta} - \underset{\approx}{T}; \quad T_{ijkl} = \frac{1}{2}(\tau_{ik}\delta_{lj} + \delta_{ik}\tau_{lj});$$

$$\underset{\sim}{\Sigma}_{\theta} = -\underset{\approx}{V}_{\theta} : \underset{\sim}{\varepsilon}^{p} = -(\underset{\approx}{W}_{\theta} + \underset{\approx}{T}) : \underset{\sim}{\varepsilon}^{p} \tag{I.82}$$

When a material which exhibits relaxation is to be analyzed, $\underset{\approx}{W}_{\theta}$ and $\underset{\sim}{\Sigma}_{\theta}$ are introduced to the finite element algorithm for $\underset{\approx}{W}$ and $\underset{\sim}{\Sigma}$.

Example: Growth of a Void in a Viscoplastic Medium:

In this example we examine the growth of a void in a hypoelastic/viscoplastic medium. This problem has been studied (numerically) by Burke and Nix [10], who treated the material as rigid/viscoplastic. We present the problem as a demonstration of the performance of the finite element algorithim. The material exhibits stress relaxation, so the forward gradient scheme must be used to stabilize the time integration. The present results agree quite closely with those of Burke and Nix.

The motion is assumed to be plane strain, and throughout the body is a doubly periodic array of cylinderical voids. Due to the symmetry we need analyse only one quadrant of one rectangular cell of the body. The finite element mesh and boundary conditions are described in Figure 1.

Burke and Nix motivate their study by explaining that certain theories for the initiation of creep fracture supose that the growth of voids can be "attributed to the inhomogeneous plastic deformation of the surrouding grains." Furthermore, "finite fracture strains can be predicted only when a void lies

in the neighborhood of another void." Such a study necessarily involves a number of special cases. For our purposes, that of demonstration, only one case is taken.

The problem has been analysed in three parts. In the first part the cell is brought rapidly from the virgin state (stress-free) to a state of purely elastic strain. This is accomplished by a single RK2 step. In the second part, relatively small time steps are taken while the stress relaxes from the elastic distribution to a nearly steady creep distribution. In the third part, time steps are taken which produce 1% nominal elongation of the cell in each step. To stabilize time integration in the second and third parts the forward gradient scheme is used, the stability parameter θ set as $\theta = 1/2$ and $3/4$. Only the Euler time stepping scheme has been used in the second and third parts of the problem.

The material model is a special case of (I.16):

$$\underset{\sim}{\varepsilon} = \underset{\sim}{\varepsilon}^{e} + \underset{\sim}{\varepsilon}^{p}$$

$$\underset{\sim}{\varepsilon}^{e} = \left(\frac{1+\nu}{E}\right)\overset{\nabla}{\underset{\sim}{\sigma}}{}^{*} - \left(\frac{\nu}{E}\right)(\underset{\sim}{I}:\overset{\nabla}{\underset{\sim}{\sigma}}{}^{*})\underset{\sim}{I}$$

$$\underset{\sim}{\varepsilon}^{p} = \frac{3}{2}\gamma\underset{\sim}{T}'$$

This model corresponds to that of Burke and Nix with (their) creep exponent n=1. The fluidity γ is set as $\gamma=1\text{x}10^{-19}$ $(\text{psi-sec})^{-1}$. The velocity at the top of the cell (see Figure 1) was adjusted so that a specimen with no void would experience a homogeneous constant stretching $\bar{\varepsilon}^{11}$ of $\dot{\bar{\varepsilon}}^{11}=0.25\text{x}10^{-14}$ sec.^{-1}. Since the material was treated as rigid/viscoplastic by Burke and Nix, our choice of elastic constants is somewhat arbitrary. We have taken Young's modulus $E=3\text{x}10^{7}$ psi and Poisson ratio $\nu=0.4$, so the material is somewhat like steel in its elastic response.

In Figures 2, 3, and 4 the contours of stress τ^{11}, stress τ^{33} and mean stress, have been plotted for L (the elongation of the cell) L=1.01. The stress concentration where the hole edge crosses the x^3 axis is approximately 2.7*. This is quite reasonable since the theoretical value for an isolated void in a purely elastic medium is 3.0. In Reference 10 an approximate value of 2.66 was found for the rigid plastic material. In Figure 5 the contours of effective strain rate $\sqrt{\frac{2}{3}\underset{\sim}{\varepsilon}^p : \underset{\sim}{\varepsilon}^p}$ are plotted for L=1.01. Qualitatively this compares very well to Figure 7 in [10].

In Figure 6 the deformation is traced from L=1.0 to L=1.5. These deformations are physically tenable. We remark that no indication of any numerical instability was observed in the course of integrating this deformation.

In Figures 7, 8, and 9 the contours of stress τ^{11}, τ^{33}, and mean stress, have been plotted for L=1.50. They compare very well to the stresses found in [10] (see Figure 8 there). We note that the stress concentration has dropped to 1.71. The stress concentration depends strongly on the geometry of the specimen; as such, it was observed to decline steadily throughout the deformation. In Figure 10 the contours of effective strain rate are plotted for L=1.5. Again, the qualitative agreement with the results of Burke and Nix [10] is noted (see Figure 9 there).

We conclude by noting that in the present analysis only 56 four noded elements were used, as compared to 56 eight noded elements used in the analysis of Burke and Nix. Considering the agreement between their results and our own, the present method appears to have performed very well, in spite of the large disparity in the degrees of freedom of the finite element mesh.

* A stress concentration of approximately 2.59 was observed for the elastically stressed medium.

Part II: Fracture Analyses Under Creep

Numerous experimental studies have been undertaken with the purpose of finding a parameter which correlates with creep crack propagation rate. Most of these investigations consider as candidate parameters, K_I, some form of net section (or reference) stress or in more recent studies C*. See, for example, the review article [11] and [12-14]. Since the introduction of C*, there appears to be less emphasis on K_I as a parameter, however, there are apparently real materials and conditions for which either net section stress or K_I provide better correlation with crack growth rate than C*.

As illustrated in Fig. 11, the above three parameters might be expected to correlate three distinctly different creep crack growth situations. In Fig. 11a, a crack and its associated ligament are shown for a material and geometry which results in negligible creep strains everywhere except in the vicinity of the crack-tip. This condition is analogous to that of small scale yielding in elastic-plastic fracture.

Fig. 11b represents a situation in which C* might be considered an appropriate parameter. This situation is characterized (i) by the body being essentially at steady-state creep conditions (which implies very slow crack propagation) and (ii) by the creep-damage process-zone being local to and therefore controlled by the crack-tip field. Fig. 11c illustrates the type of situation for which net section stress might be expected to control crack growth. In this case, the main feature is the widespread creep damage zone.

It is seen from Fig. 11 that intermediate situations can occur. For example, suppose a particular material and geometry results in a crack propagation rate such that elastic strain rates are not negligible compared to creep rates (i.e., non-steady creep) and at the same time, creep strains are no longer localized to the crack-tip region. While neither K_I nor C* could

be valid parameters for this case, it appears reasonable to expect that crack growth rate is still determined by the local crack-tip field since the creep damage process zone is still assumed to be local to the crack-tip.

In the present study, we are concerned primarily with behavior bounded by at illustrated in Fig. 11a and Fig. 11b. That is, we consider conditions in which the creep damage zone and presumably crack propagation speed are controlled by the crack-tip field. Therefore, if we have a parameter which characterizes the crack-tip fields during such behavior we presumably have a parameter which will characterize creep crack propagation rate. A parameter which spans the gap between K_I controlled growth and C* controlled growth has been introduced in [15] and subjected to initial scrutiny in [16]. This parameter is referred to as $(\Delta \underline{T})_c$ and is defined by a path-independent, vector integral. For stationary cracks, it has been shown [15,16] that the related quantity $(\dot{\underline{T}})_c$ is a measure of the amplitude of the HRR crack-tip field which presumably exists for both non-steady and steady-state creep. It has also been shown that $(\dot{T}_1)_c$ has the energy interpretation $(\dot{T}_1)_c = -\frac{\dot{dU}}{da}$ for non-steady as well as steady-state creep.

In the process of exploring this new parameter, it has been found [16] that despite C* being a valid crack-tip parameter for strictly steady-state creep conditions, it is not equivalent to the $(\dot{T}_1)_c$ parameter under any conditions and therefore does not have the energy interpretation commonly attributed to it. Since experimentalists use the energy interpretation as a means of "measuring" C* it seems more appropriate to refer to these experimental results as $(\dot{T}_1)_c$.

To start with, we define $(\Delta \underline{T})_c$ and a generalized vector integral $\underline{C}^*$ and also summarize the properties and the relationship of these parameters. The remainder of the paper discusses several finite element calculations for both stationary cracks and propagating cracks. The crack propagation study

uses a combination of analytical, numerical and experimental results to show that creep crack growth in 304 stainless steel at 650°C occurs under essentially steady-state creep conditions. Finally, based on this observation, a simple crack growth prediction methodology is outline.

Constitutive Equations:

In this study we assume strains are infinitesimal and the deformations small. Furthermore, we assume material behavior of the type:

$$\dot{\epsilon}_{ij} = \dot{\epsilon}^{e}_{ij} + \dot{\epsilon}^{c}_{ij} = C_{ijk\ell}\dot{\tau}_{k\ell} + \frac{3}{2}\gamma(\bar{\sigma})^{n-1}\tau'_{ij} \qquad \text{(II.1)}$$

where $\dot{\epsilon}^{e}_{ij}$ and $\dot{\epsilon}^{c}_{ij}$ are the elastic and creep strain rates, respectively, $C_{ijk\ell}$ is the tensor of elastic moduli, $\dot{\tau}_{k\ell}$ is the stress rate, τ'_{ij} is the deviatoric stress ($\tau'_{ij}=\tau_{ij}-\frac{1}{3}\tau_{kk}\delta_{ij}$), and $\bar{\sigma}$ is the equivalent stress given by $\bar{\sigma}=(3/2)(\tau'_{ij}\tau'_{ij})^{1/2}$. The parameters γ and n are those of the familiar Norton power law:

$$\dot{\bar{\epsilon}} = \gamma(\bar{\sigma})^{n} \qquad \text{(II.2)}$$

where

$$\dot{\bar{\epsilon}} = [(2/3)\dot{\epsilon}_{ij}\dot{\epsilon}_{ij}]^{1/2}$$

The constitutive law (II.1) can result in steady-state creep response (i.e., $\dot{\tau}_{ij} \equiv 0$) after some period of time provided the boundary conditions are some combination of time invariant tractions or time invariant displacement rates.

Fracture Parameters $(\Delta\underline{T})_c$ and $\underline{C}^*$:

We now define two vector quantities which have applications to fracture analysis under creep conditions. The first quantity is $(\Delta\underline{T})_c$ as recently defined by Atluri [15] and subsequently examined in greater detail in [16]. In [15] $(\Delta\underline{T})_c$ is defined in the context of finite strains and large deformations. Here we give the corresponding definition for infinitesimal strains and small deformations.

$$(\Delta T_i)_c \equiv \lim_{\epsilon \to 0} \int_{\Gamma_\epsilon} [n_i \Delta W - n_j(\tau_{jk}+\Delta\tau_{jk}) \frac{\partial \Delta u_k}{\partial x_i}] dS$$

$$= \int_{\Gamma_{234}} [n_i \Delta W - n_j(\tau_{jk}+\Delta\tau_{jk}) \frac{\partial \Delta u_k}{\partial x_i}] dS$$

$$+ \lim_{\epsilon \to 0} \left\{ \int_{V-V_\epsilon} [\rho(a_k - f_k) \frac{\partial \Delta u_k}{\partial x_i} - \frac{\partial \tau_{jk}}{\partial x_i} \Delta\epsilon_{jk}] dV \right.$$

$$+ \int_{\Gamma_{12}} n_i \Delta W dS + \int_{\Gamma_{45}} n_i \Delta W dS - \int_{S_t} \bar{t}_k \frac{\partial \Delta u_k}{\partial x_i} dS$$

$$\left. - \int_{S_e} n_j(\tau_{jk}+\Delta\tau_{jk}) \frac{\partial \Delta \bar{u}_k}{\partial x_i} dS \right\} \qquad \text{(II.3)}$$

The various contour integral paths and their outward unit normals $\underline{n}$ as well as V and V_ϵ are illustrated in Fig.12 for a two-dimensional, cracked body. In writing (II.3) it has been assumed that $S_e+S_t=\Gamma_{12}+\Gamma_{45}$ where S_e and S_t are the portions of the crack surfaces with applied incremental displacements, $\Delta\bar{u}_k$, and applied tractions $\bar{t}_k$, respectively. The initial stress for the increment is denoted τ_{jk}. The mass density is ρ and the acceleration and body force components at the end of the increment are a_k and f_k, respectively. The quantity ΔW is the incremental stress-working density and is given by

$$\Delta W = (\tau_{ij} + \frac{1}{2}\Delta\tau_{ij})\Delta\epsilon_{ij} \qquad \text{(II.4)}$$

The right equality of (II.3) shows that $(\Delta T_i)_c$ is independent of the selection of Γ_{234} (provided the fields within $V-V_\epsilon$ are sufficiently well behaved for the divergence theorem to be applicable). It is important to note that this path-independence exists during non-steady as well as steady-state creep.

In the present study we consider cracks along the x_1 axis and symmetrical, Mode I type deformations. Furthermore, we consider traction-free crack sur-

faces and assume body forces and accelerations are negligible. Under these conditions, only $(\Delta T_1)_c$ is of interest and we have

$$(\Delta T_1)_c = \int_{\Gamma_{234}} [n_1 \Delta W - n_j(\tau_{jk}+\Delta\tau_{jk}) \frac{\partial \Delta u_k}{\partial x_1}]dS - \int_V \frac{\partial \tau_{jk}}{\partial x_1} \Delta\epsilon_{jk} dV \qquad (II.5)$$

where we have now taken the limit of the volume integral.

It has been shown in [15] that $(\Delta T_1)_c$ has the physical meaning*

$$(\Delta T_1)_c = -\left(\frac{\Delta U_2 - \Delta U_1}{dc_1}\right) \qquad (II.6)$$

where ΔU_2 and ΔU_1 are the incremental potential energies for two cracked bodies which are indentical in loading history and geometry except that the second body has an incrementally longer crack by the amount dc_1. In creep applications, it is convenient to define the quantity

$$(\dot{T}_1)_c \equiv \underset{\Delta t \to 0}{Lt} \frac{(\Delta T_1)_c}{\Delta t} \simeq \frac{(\Delta T_1)_c}{\Delta t} \qquad (II.7)$$

where Δt is the time increment. Comparing (II.7) and (II.6) it can be seen that $(\dot{T}_1)_c$ has the physical meaning which is commonly attributed to C_1^*, i.e.

$$(\dot{T}_1)_c = -\frac{d\dot{U}}{dc_1} \qquad (II.8)$$

We now state a generalized definition for the C* parameter which has been derived in [16].

*The sign convention for ΔU_1 and ΔU_2 is reversed from that of [15,16] to reflect the conventional definition of potential energy.

$$C_i^* \equiv \lim_{\epsilon \to 0} \int_{\Gamma_\epsilon} [n_i W^* - n_j \tau_{jk} \frac{\partial \dot{u}_k}{\partial x_i}] dS$$

$$= \int_{\Gamma_{234}} [n_i W^* - n_j \tau_{jk} \frac{\partial \dot{u}_k}{\partial x_i}] dS \qquad \text{(II.9)}$$

$$+ \lim_{\epsilon \to 0} \left\{ \int_{V-V_\epsilon} \rho(a_k - f_k) \frac{\partial \dot{u}_k}{\partial x_i} dV + \int_{\Gamma_{12}} n_i W^* dS + \int_{\Gamma_{45}} n_i W^* dS \right.$$

$$\left. - \int_{S_t} \bar{t}_k \frac{\partial \dot{u}_k}{\partial x_i} dS - \int_{S_e} n_j \tau_{jk} \frac{\partial \bar{\dot{u}}_k}{\partial x_i} dS \right\}$$

Based on the same simplifying conditions used in obtaining (II.5) we have

$$C_1^* = \int_{\Gamma_{234}} [n_1 W^* - n_j \tau_{jk} \frac{\partial \dot{u}_k}{\partial x_1}] dS \qquad \text{(II.10)}$$

where it is seen that the volume integral no longer is present.

The quantity W* which appears in (II.9) and (II.10) is usually defined as

$$W^* = \int_0^{\dot{\epsilon}_{ij}} \tau_{ij} d\dot{\epsilon}_{ij} \qquad \text{(II.11)}$$

Using the steady-state case of (II.1) and the associated incompressibility condition, the following more useful expressions can be derived [16]:

$$W^* = \frac{n}{1+n} (\bar{\gamma})^{1/n} (\dot{\bar{\epsilon}})^{\frac{1+n}{n}} \qquad \text{(II.12)}$$

$$W^* = \frac{n}{1+n} \gamma (\bar{\sigma})^{1+n} \qquad \text{(II.13)}$$

As noted previously, C_1^* is often stated to have the energy interpretation which was given for $(\dot{T}_1)_c$ in (II.8). It has been shown in [16] that this incorrect. The relationship of the steady-state value of $(\dot{T}_1)_c$ (i.e. $(\dot{T}_1)_{css}$) and C_1^* is given in [16] as:

$$(\dot{T}_1)_{css} = C_1^* + (\frac{\gamma}{n+1}) \lim_{\epsilon \to 0} \int_{\Gamma_\epsilon} n_1 (\bar{\sigma})^{n+1} dS \qquad \text{(II.14)}$$

Approximate numerical evaluation of (II.14) in [16] has shown that $(\dot{T}_1)_{css}$ and C_1^* agree to within 2% for plane strain and differ by as much as 14% for plane stress.

From the above discussion it is clear that $\underline{C}^*$ and $(\dot{\underline{T}})_c$ are not equivalent quantities under any condition despite their being derivable from the same conservation law. The quantity $(\dot{\underline{T}})_c$ follows more directly from the conservation law and is the more general quantity not only in that it is applicable to non-steady as well as steady-state creep but also in that it is applicable to constitutive laws which are more general than (II.1) [15]. The quantity $\underline{C}^*$ relies on the special property of (II.1) which allows the existance of a potential W* for the deviatoric stresses, τ'_{ij}. Furthermore, since W* does not have a physical meaning whereas $\dot{W}$ has the meaning of rate of stress-working density, it is understandable that $(\dot{\underline{T}})_c$ has an energy interpretation whereas $\underline{C}^*$ does not. In light of this conclusion, it seems more appropriate to refer to experimental measurements of "$-\frac{d\dot{U}}{da}$" as measurements of $(\dot{T}_1)_c$ as opposed to measurements of C_1^* or $\dot{J}_1$ etc.

Finite Element Equations:

The following summarizes the finite element model. For a more complete description see [16]. The model is based on the principle of virtual work:

$$\int_V \tau_{ij}\delta\epsilon_{ij}dV - \int_{S_t} \bar{t}_i\delta u_i dS = 0 \qquad \text{(II.15)}$$

By substituting the following incremental stress-strain relation

$$\{\tau\}_I = \{\tau\}_{I-1} + [E]\{\Delta\epsilon\}_I - [E]\{\Delta\epsilon^c\}_I \qquad \text{(II.16)}$$

into (15) and applying customary procedures we have the final equation:

$$[K]\{\Delta Q\}_I = \{T\}_I + \{S_c\}_I - \{R\}_{I-1} \qquad \text{(II.17)}$$

In the above, $\{(\ )\}_I$ indicates the quantity at the end of the Ith increment and $\{\Delta(\ )\}_I$ the increment in the quantity for the Ith increment. The incremental node displacements are denoted $\{\Delta Q\}_I$. The remaining terms of (II.17) as follows:

$$[K] = \sum_e \int_{V_e} [B]^T[E][B]dV \tag{II.18}$$

$$\{T\}_I = \sum_e \int_{S_{t_e}} [N]^T\{\bar{t}\}_I dS \tag{II.19}$$

$$\{S_c\}_I = \sum_e \int_{V_e} [B]^T[E]\{\Delta\epsilon^c\}_I dV \tag{II.20}$$

$$\{R\}_{I-1} = \sum_e \int_{V_e} [B]^T\{\tau\}_{I-1} dV \tag{II.21}$$

The form of (II.17) makes this an initial strain formulation. It can be seen that [K] is the elastic stiffness matrix and remains unchanged throughout the time incrementing process. The quantities $\{\Delta\epsilon^c\}_I$ in (20) are predicted prior to the solution of (II.17) using (II.1) and $\{\tau\}_{I-1}$. Having sovled (II.17), and thus obtained $\{\Delta\epsilon\}_I$, the actual values of $\{\Delta\epsilon^c\}_I$ and $\{\Delta\tau\}_I$ are obtained by subdividing the time step and performing an Eulerian integration based on subincrements of $\{\Delta\epsilon\}_I$. As a result of this integration procedure, better adherence to the postulated constitutive law (II.1) is achieved but at the price of introducing some disequilibrium (i.e. $\{R\}_I \neq \{T\}_I$). This disequilibrium is corrected, however, in the next time step as a consequence of $\{R\}_{I-1}$ appearing in (II.17).

The time step size for the calculations is automatically regulated based on two criteria. The first criteria is the maximum error in the predicted creep strain increments used in solving (II.17) as compared to the creep strain

increments from the subsequent integration procedure. The second criteria is the maximum creep strain increment compared to the total elastic strain. In the present study, the criterion for maximum error in predicted creep strain is 20% and the criterion for maximum creep strain increment is 100%. For problems which have been considered, it appears that the above model and criteria give accurate transient solutions and converged steady-state solutions with time step size comparable to those used with more expensive tangent stiffness methods.

Verification of Model:

A compact specimen has been chosen for verifying the model. The particular geometry and materials were chosen to coincide with those used by Ehlers and Riedel [17] and are illustrated in Fig. 13 along with the two finite element meshes used in the verification. Both meshes consist entirely of eight-noded isoparametric elements, assume plane strain conditions and use collapsed (i.e. triangular) elements at the crack-tip. For the 102 element model these crack-tip elements are given a singular strain field ($r^{-1/2}$) by shifting the appropriate midside nodes to their quarter-points. The 300 element model uses a non-singular crack-tip.

The elastic J_1 for the 300 and 102 element meshes are 24.1 and 24.3 N/mm, respectively and agree with the value 24.2 N/mm from Srawley [18] to well within 1%. The steady-state (t=600hr) values of C_1^* for the 300 and 102 element meshes are 131 and 130 N/m·hr, respectively, and agree well with 134 N/m·hr from Shih and Kumar [19] and 137 N/m.hr (t 300hr) from Ehlers and Riedel [17]. Based on these results it is concluded that the numerical procedure in general and the quarter-point crack-tip elements in particular, are accurate and efficient tools for creep fracture analysis.

Calculations of $(\dot{T}_1)_c$ and $(\dot{T}_1)_c^{\delta}$:

Now we consider calculations of $(\dot{T}_1)_c$ (i.e. $(\Delta T_1)_c/\Delta t$). The 300 element mesh results for $(\dot{T}_1)_c$, as computed from (II.5), are shown in Fig. 14 as the solid curve. This curve shows the time dependence of $(\dot{T}_1)_c$ during the non-steady portion of the creep calculation. The steady-state value of $(\dot{T}_1)_c$ is 130 N/m·hr and thus is in agreement with the previously mentioned relationship between $(\dot{T}_1)_{css}$ and C_1^*. In [16] it was found that the evaluation of (II.5) using the 102 element mesh gave values of $(\dot{T}_1)_c$ which were generally in poor agreement with those of the 300 element mesh. The volume integral of (II.5) was determined to be the cause of this behavior and it was supposed that the origin of the problem was the use of the $r^{-1/2}$ strain singularity as opposed to the HRR type singularity (i.e. $r^{-n/(1+n)}$). However, several calculations with special conforming elements which impose the HRR type radial dependence of strain [20], have shown that this is not the case.

It now seems that the difficulty experienced in computing $(\dot{T}_1)_c$ when using singular crack-tip elements is related to the existence argument for the limit of the volume integral in (II.3). For the case when the asymptotic field has singular radial dependence but does not identically satisfy the following condition on angular behavior,

$$\lim_{\epsilon \to 0} \int_{-\pi}^{\pi} \frac{\partial \tau_{ij}(\epsilon,\theta)}{\partial x_1} \Delta\epsilon_{ij}(\epsilon,\theta) d\theta = 0 \qquad \text{(II.22)}$$

the subject limit in (II.3) does not exist (as discussed in Appendix A of [16]). The condition (II.22) need not be satisfied exactly if one does not ahve a singular radial dependence as is demonstrated by the results from the 300 element mesh.

The efficiency, simplicity and general accuracy of the quarter-point element procedure makes it a very attractive alternative to the use of very re-

fined nonsingular meshes or the derivation of singular crack-tip elements which satisfy (II.22) a priori. Therefore, a practical solution to this problem is sought. As noted above, the difficulty is associated with the volume integral over the singular elements. Therefore, calculations were made in which the volume integral over the crack-tip elements was omitted. The resulting quantity, which we call $(\dot{T}_1)_c^{\delta}$, can be written

$$(\dot{T}_1)_c^{\delta} = \int_{\Gamma_{234}} [n_1 \Delta W - n_j(\tau_{jk}+\Delta\tau_{jk}) \frac{\partial \Delta u_k}{\partial x_1}] dS - \int_{V-V_{\delta}} \frac{\partial \tau_{jk}}{\partial x_1} \Delta\epsilon_{jk} dV \qquad \text{(II.23)}$$

where V_{δ} consists of the singular crack-tip elements. The dashed curve of Fig. 14 is $(\dot{T}_1)_c^{\delta}$ from the 102 element mesh. It can be seen that $(\dot{T}_1)_c^{\delta}$ coincides with the solid curve for times after about 30 hours. For this mesh and problem it can therefore be said that $(\dot{T}_1)_c^{\delta}$ is a valid path-independent, crack-tip parameter for times after 30 hours and for values of $(\dot{T}_1)_c$ beginning at approximately 1.6 of the steady-state value. The steady-state parameter C_1^* is still significantly path-dependent at 30 hours.

For the 102 element mesh, the crack-tip elements are 5% of the ligament size. We therefore assign δ a value of 0.05. A quantity similar to $(\dot{T}_1)_c^{\delta}$ was computed using the 300 element mesh. In this case, a semi-circular region of radius approximately 3% of the ligament was omitted from the evaluation of the volume integral of (II.5). This result which we deonte $(\dot{T}_1)_c^{\epsilon}$ with ϵ=3% is also shown in Fig. 14. This curve seems to indicate that the validity of $(\dot{T}_1)_c^{\delta}$ can be expanded to earlier times with rather moderate reductions in the crack-tip, quarter-point element size. For example, the results of Fig. 14 indicate that a δ of 3% of the ligament would result in $(\dot{T}_1)_c^{\delta}$ being valid as early as seven hours and for $(\dot{T}_1)_c$ as large as 4.3 its steady-state value.

Creep Crack Growth in a Strip:

We now consider the problem of a finite height (2h) infinitely wide strip, with a semi-infinite crack. Loading consists of uniformly applied displace-

ment rates ($\dot{\delta}$) at the top and bottom edges ($y=\pm h$) such that Mode I behavior results. This problem has been chosen for two reasons. First, since the strip is infinitely wide and the boundary conditions do not change with time, the propagating crack-tip fields can be expected to reach a "convecting steady-state" creep condition. Here we use the phrase "convecting steady-state" to mean that the field remains unchanged in time with respect to a coordinate system which is centered at and moving with the crack-tip. This terminology is used so as not to confuse this condition with the usual steady-state creep condition in which material stress rates are zero.

The second reason for choosing this problem is that C_1^* can be evaluated analytically for the special case of steady-state creep (stationary crack). The analytical evaluation of (II.L0) follows easily if one chooses a rectangular contour in which the horizontal portions coincide with the top and bottom edges of the strip (i.e. $y=\pm h$) and the vertical portions are at $x=\pm\infty$. In such a contour one finds only the vertical portion at $x=+\infty$ is non-zero and therefore

$$C_1^* = 2hW_\infty^* \tag{II.24}$$

For the corresponding elastic problem with applied displacement δ, one finds a similar relation.

$$J_1 = 2hW_\infty \tag{II.25}$$

It has been noted that $(\dot{T}_1)_{css}$ and C_1^* are related and therefore it is possible to obtain $(\dot{T}_1)_{css}$ from (II.14) and (II.24). The direct evaluation of $(\dot{T}_1)_c$ in terms of either its integral representation (II.5) or its energy representation II.6) requires knowledge of the stresses in the region of the strip adjacent to the crack-tip and therefore is not a trivial task.

The material properties used in this problem are representative of 304 stainless steel at 650°C. These material properties and the finite element

Table 1. Summary of Analysis Parameters for Creep Crack Growth in the Plane Strain Strip of Fig. 15

Analytical Results					Computed Results		$\frac{da}{dt}$ from (6.4) (mm/hr)	
C_1^* (N/mm·hr)	remote τ_{yy} (MPa)	$\dot{\delta}$ (mm/hr)	δ (elastic) (mm)	J_1 (N/mm)	C_1^* (N/mm·hr)	J_1 (N/mm)	average	upper bound
0.05	83	3.44×10^{-4}	5.04×10^{-2}	4.18	4.99×10^{-2}	4.19	1.00×10^{-4}	5.00×10^{-4}
5.0	148	1.94×10^{-2}	8.95×10^{-2}	13.2	4.99	13.2	2.22×10^{-2}	1.11×10^{-1}
50	197	1.45×10^{-1}	1.19×10^{-1}	23.5	49.8	23.5	3.30×10^{-1}	1.65

discretization are given in Fig. (15). Note that collapsed, eight-noded, quarter-point elements are used at the crack-tip.

The mesh for this problem may at first appear rather coarse; however, elastic and steady-state creep solutions obtained with this mesh are sufficiently accurate to justify its use for the study at hand. The comparison of computed elastic J_1 values and steady-state C_1^* values with their analytic values is given in Table 1.

The first step in this numerical study is to select three values of C_1^* which span the range of values reported in the literature for 304 stainless steel at 650°C.† The values which have been chosen are 0.05, 5.0 and 50.0 N/mm·hr. Having these values, the remote ($x=\infty$) steady-state τ_{yy} are determined as well as the edge displacement which results in the same remote elastic τ_{yy}. These displacements are applied to the model elastically at $t=0$. Next, the steady-state edge displacement rates are determined analytically. Using the elastic solution as an initial state, the displacement rate, $\dot{\delta}$, is applied until the model reaches steady-state.

The next step in this study involves the selection of upper bound crack velocities for the three chosen values of C_1^*. The following formula is based on the experimental data reported in [13,14] and represents data from center-crack, double-edge-crack, compact, and round bar specimen types.

$$\frac{da}{dt} = \alpha [C_1^*]^{1.173} \qquad \text{(II.26)}$$

$$\text{where } \alpha = \begin{cases} 1.68 \times 10^{-2} & \text{(upper bound)} \\ 3.36 \times 10^{-3} & \text{(average)} \end{cases}$$

†The use of C_1^* rather than $(\dot{T}_1)_c$ is due to the existence of the analytical expression (24) and is justified by the numerical similarity to $(\dot{T}_1)_c$ for plane strain conditions.

Having reached steady-state, the crack is propagated at the upper bound velocity of (II.26) until it is determined that a convecting steady-state has been reached.

The crack growth simulation is accomplished through a combination of mesh shifting and periodic remeshing as illustrated in Fig. (16). The region A represents the quarter-point elements which remain centered about the crack-tip. The B type elements are standard eight-noded isoparametric elements which distort during mesh shifting so as to keep the region A centered at the crack-tip. The procedure is to shift the region A (and thus the crack-tip) by shifting appropriate nodes of the region A and type B elements. This shifting is done without altering element connectivity. Eventually the type B elements become overly distorted at which time the element connectivities are redefined in the vicinity of the crack-tip so that additional shifting is possible.

Each occurance of shifting or remeshing requires that shifted nodes have their displacements interpolated and that shifted elements have their 2x2 Gauss point stresses interpolated. The displacement interpolation is by the usual isoparametric shape functions. The stress interpolation uses linear, two-dimensional Lagrangian polynomials in element local coordinates. In the following calculations, the nominal size of the crack growth increments is 0.4 mm or 2% of the crack-tip element width. For the highest velocity case (C_1^*=50 N/mm·hr), this results in crack growth at approximately every fifth solution step.

Results for a Plane Strain Strip:

The results of the plane strain strip calculation with C_1^*=50 N/mm·hr and $\frac{da}{dt}$ =1.65 mm/hr are given in Fig. 17. The values of $(\dot{T}_1)_c^{\delta}$ and C_1^* are given for the portion of the calculation prior to steady-state as well as during the crack propagation portion. The band represents the range of values obtained from the four contours illustrated in Fig. 15. Both $(\dot{T}_1)_c^{\delta}$ and C_1^* converge

to the 50 N/mm·hr value at steady-state. During the crack propagation, it is seen that $(\dot{T}_1)_c^\delta$ and C_1^* do not depart significantly from their steady-state value. This means that this combination of loading and crack-speed results in the crack-tip fields being essentially at steady-state conditions. This in turn means that both $(\dot{T}_1)_c^\delta$ (or $(\dot{T}_1)_c$) and C_1^* are valid crack-tip field parameters during crack growth.

A closer view of the crack propagation portion of these curves is given in Fig. 18. The dashed curves bracketing the initial portion of the solid curves represent the degree of path-independence and continue to be representative of the path-independence observed during the crack propagation steps. For both $(\dot{T}_1)_c^\delta$ and C_1^*, it is seen that the strip has essentially returned to its steady-state condition prior to each crack growth increment. It is thought that the larger departure of $(\dot{T}_1)_c^\delta$ from steady-state (as compared to C_1^*) is more representative of the non-steadiness of the crack-tip field since the validity of C_1^* in general and the numerical evaluation of W* (II.13) in particular, are based on the existence of steady-state conditions.

The effect of remeshing is seen at approximately eight hours. The first two steps after the remeshing were found to result in rather erratic contour integral values and are not indicated in these figures. The equilibrium correction feature of the present model and the automatic time step regulation procedure both act to quickly restore equilibrium at the crack-tip.

The propagation portion of the calculation with C_1^*=5 N/mm·hr and $\frac{da}{dt}$ =0.111 mm/hr is given in Fig. 19. Here again it is seen that both $(\dot{T}_1)_c^\delta$ and C_1^* have converged to the analytical value of C_1^* (to within two percent, which is also about the degree of path-independence). Comparing these results with those in Fig.18 for the higher C_1^* and crack speed it is seen that steady-state creep conditions were not reached until 12 hours as opposed to approximately two

hours in previous cases. Also, the return to the steady-state value after mesh shifting takes more time (two hours compared to 0.25 hours). However, when compared to the time between crack growth steps (both use·0.4 mm) it is seen that the lower velocity case returns to steady-state well before the next growth step occurs. This result indicates that lower load levels and crack speeds are inherently closer to steady-state conditions. While this behavior seems intuitively correct, it should be kept in mind that these results depend on the empirical formula (II.26) which is valid only for 304 stainless steel. It remains to be seen if similar behavior occurs in other materials.

A calculation has also been done for the case of C_1^*=0.05 N/mm·hr. As a result of the large number of solution steps between crack growth steps, when using the maximum velocity of 5×10^{-4} mm/hr, the calculations used a higher velocity (5×10^{-3} mm/hr). Even at this unrealistically high velocity (for this level of loading), the behavior is more steady-state-like than the case of C_1^*=5.0 N/mm.hr described above.

Creep Crack Growth in Double-Edge-Crack Specimens:

The purpose of considering this problem is to apply the model to a problem for which experimental data exists. While much experimental data has been reported in the literature, most authors do not include sufficient information to allow a numerical simulation of their experiments. The current problem is based on the experiments of Koterazawa and Iwatwa [21]. The primary reasons for selecting this work for study are the crack length versus time histories were given and that the experiments were performed on 304 stainless steel for which high temperature elastic and creep properties were already available.

The geometry of the experimental specimens is given in Fig. 20. The finite element mesh for the calculations is shown in Fig. 21 with contour

integral paths being indicated by dashed lines. It can be seen that the mesh takes advantage of the two planes of symmetry for the specimen and does not model the 60^{o} notch. The initial crack length indicated in Fig. 21 corresponds to the notch depth in the specimen. All calculations for this specimen assume plane stress conditions and use the material properties given in Fig. 15. Elastic J_1 results for two crack lengths are compared in Table 2 with those (based on formulas for K_I) from [22] and are seen to be in good agreement.

The material properties are those of 304 stainless steel at $650^{o}C$ and are assumed to be the same as those used in the strip analyses. (See Fig. 15). Calculations have been made for remote applied stresses of 157 and 176 MPa. The experimental crack growth histories for these two stress levels are reproduced from [21] in Fig. 22. It is seen from these curves that the first two-thirds of the specimen lives are characterized by crack velocities of less than 0.01 mm/hr compared to nearly 0.5 mm/hr as rupture is approached.

The primary purpose of the following calculations is to verify the conclusions which were reached in the previously described strip calculations; that is, that the crack-tip fields are essentially creep-steady fields even for the most rapid creep crack velocities. These calculations will be a valid check because the input to the calculations is only the remote applied stress and the measured crack velocity history, and does not in any way depend on experimental determination of C_1^* or $(\dot{T}_1)_c$ as did the strip calculations. In fact, Koterazawa and Iwata do not report such measurements in [21].

Analysis of Initial, Low Velocity Crack Growth:

This section describes the simulation of the initial portion of the crack velocity histories given in Fig. 22. In all of these calculations, the entire load is applied elastically at t = 0 and held constant throughout the subsequent creep solution steps. The convergence of $(\dot{T}_1)_c$ and C_1^* to their

steady-state values is shown in Fig. 23, with the dashed lines in the C_1^* plots denoting the degree of path-independentce. It is seen that steady-state conditions are reached between a half and one hour after the load is applied. (Table 2 summarizes the computational aspects of this portion of the calculation.) Therefore, it is seen by refering to Fig. 22 that crack growth does not begin in the two specimens until well after steady-state conditions are reached. Since the current calculations assume small displacements and infinitesimal strains, and since only the strain and displacement magnitudes depend on time once steady-state is reached, there is no reason to continue the numerical calculations to the crack initiation times indicated by the experimental results. Therefore, the initial crack propagation is simulated at times after steady-state conditions are reached but much earlier indicated by the experiments.

The crack growth simulation results are shown in Fig. 23. The crack increment size for this study was approximately 0.01 mm which is nominally 2.4 percent of the crack-tip element size. It can be seen that only one mesh shift (i.e., crack growth step) was modeled. It is clear from this figure that the time it takes for the specimen to return to steady-state is significantly less than the time to the next crack growth increment (indicated by dashed lines). Therefore, the initial portion of the crack growth histories of Fig. 22 are clearly occurring under essentially steady-state conditions and thus C_1^* as well as $(\dot{T}_1)_c$ are valid crack-tip parameters. Since an increase in C_1^* results in a more rapid return to steady-state conditions, the above conclusion will remain valid for the initial constant velocity portions of the curves of Fig. 22.

When crack growth occurs so slowly that the crack-tip is essentially at steady-state, the crack-tip field does not depend on the history of the specimen. Therefore, assuming steady-state conditions continue to exist, it is

possible to skip to the final stages of crack growth without modeling the intermediate crack growth. If it is found that crack growth is still slow enough for steady-state conditions to exist, then it seems reasonable to expect that the behavior at intermediate crack lengths is also of a steady-state type. The following describes the results of this procedure when applied to the two double-edge-crack specimens.

Analysis of Final Stage of Crack Growth:

To analyze the final stage of crack growth, the crack length is increased to 2.75 mm and the process of applying the load elastically and creeping to steady-state is repeated. Table 2 summarizes the computational aspects of this process. The convergence of $(\dot{T}_1)_c^{\delta}$ and C_1^* is their steady-state values is shown in Fig. 24. Having reached steady-state, the cracks are grown at the rate suggested by the last portion of the crack histories (Fig. 22)as shown in Fig. 24 . The significant increase in the frequency of mesh shifting (compared to that in Fig. 23 due to the velocity increase makes the details of the curve difficult to distinguish in this figure. However, the time step size is such that six or seven steps occur between each crack growth increment. Unlike the strip problem, the values of $(\dot{T}_1)_c^{\delta}$ and C_1^* are clearly increasing during this crack propagation process.

It is necessary to determine whether this increase in the crack-tip parameters is due to the crack-tip no longer being at steady-state conditions or whether it is due to the crack-tip no longer being at steady-state conditions or whether it is due to the incraese in crack length. This is accomplished by continuing the calculation without further crack extension. If the value of the parameters do not change significantly with time, this means the increase was largely due to the crack length increase and that crack growth is still occuring under essentially steady-state conditions. Examination of the final portions of the curves of Fig. 24 shows that this is the case.

Table 2. Computational Aspects of the Elastic and Non-Steady Creep Portion of the Double-Edge-Crack Calculations

applied stress (MPa)	crack length (mm)	Elastic Solution J_1 (N/mm)	difference from [2] (%)	CP time* (sec)	Creep Solution Δt (hr) initial/final	steps to steady-state†	total CP time (sec)
157	1.75	1.12	(-2.1)	38	$8 \cdot 10^{-8}/1.9 \cdot 10^{-2}$	90	795
176	1.75	1.40	(-2.6)	38	$8 \cdot 10^{-8}/9.5 \cdot 10^{-3}$	100	880
157	2.75	1.79	(-3.3)	38	$4 \cdot 10^{-8}/8.6 \cdot 10^{-3}$	211	1820
176	2.75	2.25	(-3.2)	38	$2 \cdot 10^{-8}/4.4 \cdot 10^{-3}$	205	1770

*Control Data CYBER 74

†Solutions are stopped at times indicated in Figs. 5.19 and 5.20

Based on this analysis; it appears that the conclusions reached as a result of the strip calculations are still valid. Since, (i) the strip analyses are much less expensive than this analysis of the double-edge-crack geometry, (ii) the steady-state C_1^* for the strip is easily obtained analytically and (iii) the crack-tip parameters do not depend on crack length for the strip geometry, it seems that similar studies for other materials and/or other temperatures could most effectively be accomplished through the use of the strip geometry. The need for such studies follows from the vast simplification of fracture analysis and prediction which results if crack growth occurs under steady-state conditions. More will be said about this point in the conclusions.

Summary and Conclusions:

It has been noted that despite the fact that C_1^* characterizes the crack-tip field under steady-state creep conditions, it does not have an energy or energy rate interpretation. A related path-independence integral parameter $(\dot{T}_1)_c$, however, does have the energy rate interpretation commonly attributed to C_1^*. The derivation of $(\dot{T}_1)_c$ does not rely on the existence of steady-state creep conditions and thus is a valid crack-tip parameter for non-steady creep conditions as well as for steady-state creep.

An initial strain finite element approach provides for improved adherence to postulated constitutive behavior and for equilibrium correction has been summarized. The accuracy and efficiency of this model with eight-node isoparametric elements and the quarter-point crack-tip element approach have been verified through several calculations for a compact specimen geometry and a strip geometry. Also, a method of simulating crack growth through shifting of the quarter-point singularity elements and periodic remeshing has been described and demonstrated.

A creep crack growth simulation for 304 stainless steel has shown that for realistic load levels and corresponding crack speeds the crack-tip field

is essentially at a steady-state creep condition. This means that for this material the propagating crack-tip field is largely unaffected by the history of crack-growth or the history of loading. This feature can greatly reduce the analysis requried for predicting creep crack growth behavior in a component as can be seen from the following suggested methodology.

We assume that the crack propagation speed $\frac{da}{dt}$ is related to $(\dot{T}_1)_{css}$ (i.e., $-\frac{d\dot{U}}{dt}$) through the poer law suggested by experimental data [13,14]

$$\frac{da}{dt} = \alpha[(\dot{T}_1)_{css}]^{\beta} \tag{II.27}$$

Next we determine (eg. by steady-state creep finite element analysis) $(\dot{T}_1)_{css}$ as a function of crack length. Because of the assumed steady-state crack-tip behavior, this can be accomplished by considering several discrete crack lengths and then fitting a curve. No crack growth simulation procedures are necessary. Combining (II.27) with this result provides the followng relationship between time and crack length

$$t = \int_{a_o}^{a(t)} \frac{[(\dot{T}_1)_{css}]^{-\beta}}{\alpha}\, da + t_i \tag{II.28}$$

where a_o is the initial crack length and t_i is the time when crack growth initiates. The only unknown quantity in (II.28) is the initiation time t_i.

Vitek [23] has simulated several experiments (compact and double-edge-crack specimens) on two CrMoV steels using a dislocation model and has concluded that COD correlated well with the initiation of crack growth in these experiments. If the same conclusion is valid for 304 stainless steel, then one can presumably predict t_i based on a transient finite element analysis of the initial flawed configuration and a critical value of COD. If initiation occurs long after steady-state conditions are reached, it is then reasonable to estimate t_i using the rate of COD obtained from a steady-state finite ele-

ment solution. At this time, the validity of (II.28) and of the critical COD concept has not been investigated by the authors.

Acknowledgements:

The final support for this work provided through NASA grant NAG-3-38 from NASA-Lewis Research Center to Georgia Institute of Technology is gratefully acknowledged. The timely encouragement of Drs. M. Hischberg, B. Gross, and J. Srawley of NASA-Lewis Research Center is sincerely appreciated. Thanks are expressed to Ms. M. Eiteman for her careful assistance in the preparation of this manuscript.

References:

[1] Pian, T.H.H., "Derivation of Element Stiffness Matrices by Assumed Stress Distributions", AIAA Journal, Vol. 2, No. 7, pp. 1333-1336, 1964.

[2] de Veubeke, B.F., A New Variational Principle for Finite Elastic Deformations", International Journal of Engineering Science, Vol. 10, pp. 745-763, 1972.

[3] Atluri, S.N., "On Some New General and Complementary Energy Theorems for the Rate Problems of Finite Strain, Classical Elasto-Plasticity", Journal of Structural Mechanics, Vol. 8, No. 1, 1980, pp. 61-92.

[4] Atluri, S.N. and Murakawa, H., "New General and Complementary Energy Theorems, Finite Strain, Rate Sensitive Inelasticity and Finite Elements: Some Computational Studies," in Nonlinear Finite Element Analysis in Structural Mechanics, Wunderlich, W., Stein, E., and Bathe, K.-J., Editors, Springer-Verlag, 1981.

[5] Murakawa, H., "Incremental Hybrid Finite Element Methods for Finite Deformation Problems (with Special Emphasis on the Complementary Energy Principle)", Ph.D. Dissertation, Georgia Inst. of Technology, Aug., 1978.

[6] Reed, K.W., "Analysis of Large Quasistatic Deformations of Inelastic Solids by a New Stress-Based Finite Element Method", Ph.D. Dissertation, Center for the Advancement of Computational Mechanics, Georgia Institute of Technology, April, 1982.

[7] Cormeau, I., "Numerical Stability in Quasistatic Elasto-Viscoplasticity", Int. J. Numer. Methds. in Eng., Vol. 9, 1975, pp. 109-127.

[8] Argyris, J.H., Vaz, L.E. and Willam, K.J., "Improved Solution Methods for Inelastic Rate Problems", Computer Methods in Applied Mechanics and Engineering, Vol. 16, 1978, pp. 231-277.

[9] Kanchi, M.B., Zienkiewicz, O.C. and Owen, R.J., "The Visco-Plastic Approach to Problems of Plasticity and Creep Involving Geometric Non-linear Effects", Int. J. Numer. Meths. Eng., Vol. 12, 1978, pp. 169-181.

[10] Burke, M.A. and Nix, W.D., "A Numerical Analysis of Void Growth in Tension Creep", Int. J. Solids Structures, Vol. 15, 1979, pp. 55-71.

[11] Fu, L.S., "Creep Crack Growth in Technical Alloys at Elevated Temperature-a Review", Engng. Fracture Mech., Vol. 13, 1980, pp. 307-330.

[12] Landes, J.D. and Begley, J.A., "A Fracture Mechanics Approach to Creep Crack Growth", Mechanics of Crack Growth, ASTM STP 590, 1976, pp. 128-148.

[13] Ohji, J., Ogura, K. and Kubo, S., "The Application of Modified J-Integral to Creep Crack Growth in Austenitic Stainless Steel and Cr-Mo-V Steel", Engng. Aspects of Creep, Proc. Conf. at Univ. Sheffield, I. Mech. E., 1980, pp. 9-16.

[14] Koterazawa, R., Mori, T., "Applicability of Fracture Mechanics Parameters to Crack Propagation Under Creep Conditions", J. Engng. Materials and Technology, Vol. 99, Series H, No. 4, 1977, pp. 298-305.

[15] Atluri, S.N., "Path-Independent Integrals in Finite Elasticity and In-Elasticity, with Body Forces, Inertia, and Arbitrary Crack-Face Conditions", Report No. GIT-CACM-SNA-81-8, Georgia Institute of Technology, March, 1981, also Engng. Fracture Mech., Vol. 13, No. 2, 1982.

[16] Stonesifer, R.B. and Atluri, S.N., "On a Study of the $(\Delta \underline{T})_c$ and C* Integrals for Fracture Analysis Under Non-Steady Creep", Report No. GIT-CACM-SNA-81-21, Georgia Institute of Technology, July 1981, also Engng. Fracture Mechanics (in press).

[17] Ehlers, R. and Riedel, H., "A Finite Element Analysis of Creep Deformation in a Specimen Containing a Macroscopic Crack", Advances in Fracture Research Vol. 2, Francois, D., (Ed.), Fifth Intl. Conf. on Fracture, Ca-nes, 1981, 691-698.

[18] Srawley, J.F., "Wide Range Stress Intensity Factor Expressions for ASTM E399 Standard Fracture Toughness Specimens", Intl. J. Fracture, 12, 1976, pp. 475-476.

[19] Shih, C.F. and Kumar, V., "Estimation Technique for the Prediction of Elastic-Plastic Fracture of Structural Components of Nuclear Systems", Contract RP 1237-1, First Semiannual Report for Electric Power Research Institute, General Electric Co., Report, 1979.

[20] Stonesifer, R.B., Fast Brittle Fracture and Creep Crack Growth: Moving Singularity Finite Element Analysis, Ph.D. Dissertation, Dept. of Civil Engineering, Georgia Institute of Technology, 1981.

[21] Koterazawa, R. and Iwata, Y., "Fracture Mechanics and Fractography of Creep and Fatigue Crack Propagation at Elevated Temperature", J. of Engng. Mat. and Technology, 98, 1976, pp. 296-304.

[22] Tada, H., Paris, P.C. and Irwin, G.R., The Stress Analysis of Cracks Handbook, Del Research Corp., Hellertown, PA, 1973.

[23] Vitek, V., "A Theory of the Initiation of Creep Crack Growth", Int. J. of Fracture, Vol. 13, No. 1, 1977, pp. 39-50.

APPENDIX A

Plane Strain:

The deformation studied in the example accompanying Part I of this report is plane strain in the character. Just as for formulations using ordinary stresses, a number of the components of the velocity, spin, and stress rate vanish if a Cartesian coordiante system is chosen with one axis normal to the plane of deformation. We have chosen the x^2 coordinate line to be normal to the plane of deformation, so that the velocity, spin, stress rate, and stress are of the forms

$$\underset{\sim}{v} = v^1 \underline{e}_1 + v^3 \underline{e}_3$$

$$\underset{\sim}{\omega} = \omega^{13} \underline{e}_1 \underline{e}_3 + \omega^{31} \underline{e}_3 \underline{e}_1$$

$$\dot{\underset{\sim}{t}} = \dot{t}^{11} \underline{e}_1 \underline{e}_1 + \dot{t}^{13} \underline{e}_1 \underline{e}_3 + \dot{t}^{22} \underline{e}_2 \underline{e}_2 + \dot{t}^{31} \underline{e}_3 \underline{e}_1 + \dot{t}^{13} \underline{e}_3 \underline{e}_3$$

$$\underset{\sim}{\tau} = \tau^{11} \underline{e}_1 \underline{e}_1 + \tau^{13} \underline{e}_1 \underline{e}_3 + \tau^{22} \underline{e}_2 \underline{e}_2 + \tau^{31} \underline{e}_3 \underline{e}_1 + \tau^{33} \underline{e}_3 \underline{e}_3$$

None of the components depends upon x^2. The velocity is represented on each element as

$$\underline{v} = \sum_{i=1}^{NQ} N_i q^i$$

The shape functions $\underline{N}_i$ are described below. Similarly the spin and stress rate are represented as

$$\underset{\sim}{\omega} = \sum_{i=1}^{NW} \underset{\sim}{QW}_i \alpha^i; \quad \overset{\cdot}{\underset{\sim}{t}} = \sum_{i=1}^{NT} \underset{\sim}{QT}_i \beta^i$$

We note that this approach requries minimal specialization in programming for the particular case of plane strain. The plane strain condition is not satisfied a priori; that is

$$\delta\varepsilon_{22} = (\underline{e}_2\underline{e}_2):\underset{\approx}{W}^{-1}:\delta\overset{\cdot}{\underset{\sim}{r}} \neq 0$$

for arbitrary $\delta\overset{\cdot}{\underset{\sim}{r}}$. Rather, $\varepsilon_{22}=0$ follows from the stationary condition (a component of 7.1):

$$\int_V [-\varepsilon_{22}(\overset{\cdot}{\underset{\sim}{t}},\underset{\sim}{\omega})]\delta\overset{\cdot}{t}^{22}dV = 0$$

In using the finite element algorithm the plane strain condition is only satisfied approximately. In practice a qulitative check for satisfaction of the plane strain condition can be made by seeing that the stress component τ^{22} and the mean stress are nearly equal. This method for checking $\tau_{22}=0$ works so long as the inelastic stretching is proportional to the stress deviator (in the constitutive equation).

SHAPE FUNCTIONS FOR VELOCITY, STRESS RATE, AND SPIN

Shape Functions for Plane Strain

$$x^i=X \qquad x^3=z$$

VELOCITY SHAPE FUNCTIONS

$$\underline{N}_i = N_{1,i}\underline{e}_1 + N_{3,i}\underline{e}_3$$

FOUR NODED ELEMENT:

$$N_{1,i} = \begin{cases} \frac{1}{4}(1+\xi\xi_i)(1+\eta\eta_i) & i=1,2,3,4. \\ 0 & i=5,6,7,8. \end{cases}$$

$$N_{3,i} = \begin{cases} 0 & i=1,2,3,4. \\ \frac{1}{4}(1+\xi\xi_{i-4})(1+\eta\eta_{i-4}) & i=5,6,7,8. \end{cases}$$

$|\xi|\leq 1,\ |\eta|\leq 1,$

$\xi_1 = -1,\ \xi_2=1,\ \xi_3=1,\ \xi_4=-1$

$\eta_i = -1,\ \eta_2=-1,\ \eta_3=1,\ \eta_4=1$

SHAPE FUNCTIONS FOR SPIN:

$QW(1,3,1) = C_1$

$QW(3,1,1) = -C_1$

$QW(1,3,2)=X\ C_2$

$QW(1,3,3)=Z\ C_3$

$QW(3,1,2) = -X\ C_2$

$QW(3,1,3)=-Z\ C_3$

$\underset{\sim}{QW}_i = \underset{\sim}{QW}_{13,i}\underline{e}_1\underline{e}_3 + \underset{\sim}{QW}_{31,i}\underline{e}_3\underline{e}_1$

The constants were used to improve the condition of [H].

STRESS SHAPE FUNCTIONS:

$QT(1,1,1)=1$

$QT(3,1,2)=-1$

$QT(2,2,3)=1$

$QT(1,3,4)=-1$

$QT(3,3,5)=1$

$QT(1,1,6)=X$

$QT(3,1,6)=-Z$

$QT(3,1,7)=-X$

$QT(2,2,8)=X$

$QT(1,3,9)=-X$

$QT(3,3,9)=Z$

$QT(3,3,1)=X$

$QT_i = QT_{11,i}\underline{e}_1\underline{e}_1 + 0 + QT_{13,i}\underline{e}_1\underline{e}_3 + 0 + QT_{22,i}\underline{e}_2\underline{e}_2 + QT_{31,i}\underline{e}_3\underline{e}_1 + 0 + QT_{33,i}\underline{e}_3\underline{e}_3$

```
QT(1,1,11)=Z

QT(1,3,12)=-Z

QT(2,2,13)=Z
```

3x3 Gauss Quadrature on this Element.

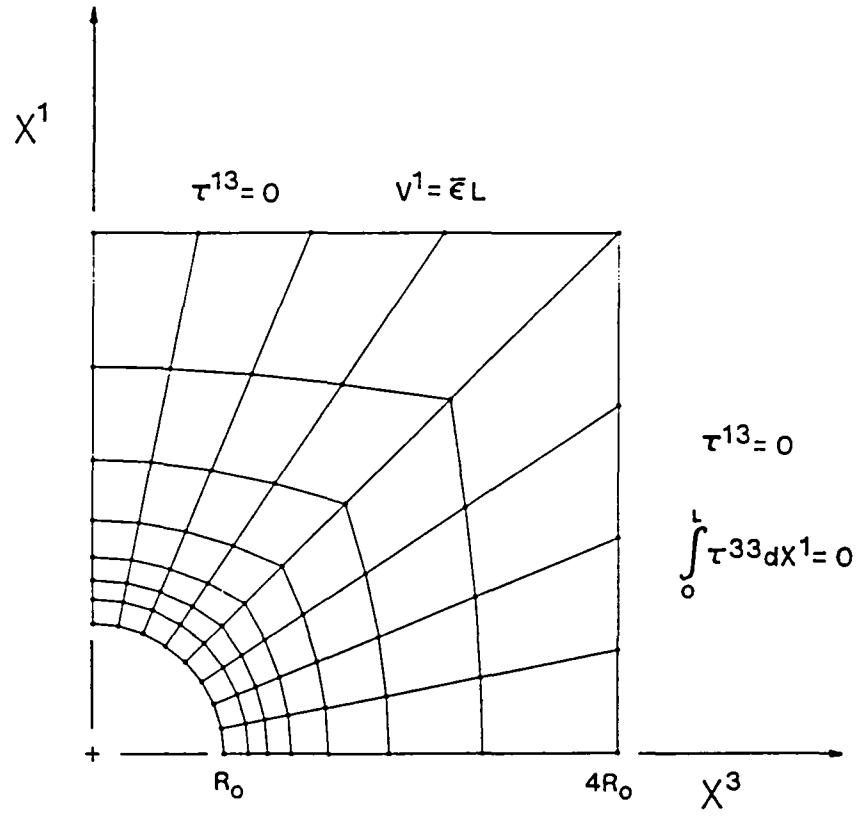

Figure 1. Finite Element Mesh and Boundary Conditions for the Problem of Growth of a Void.

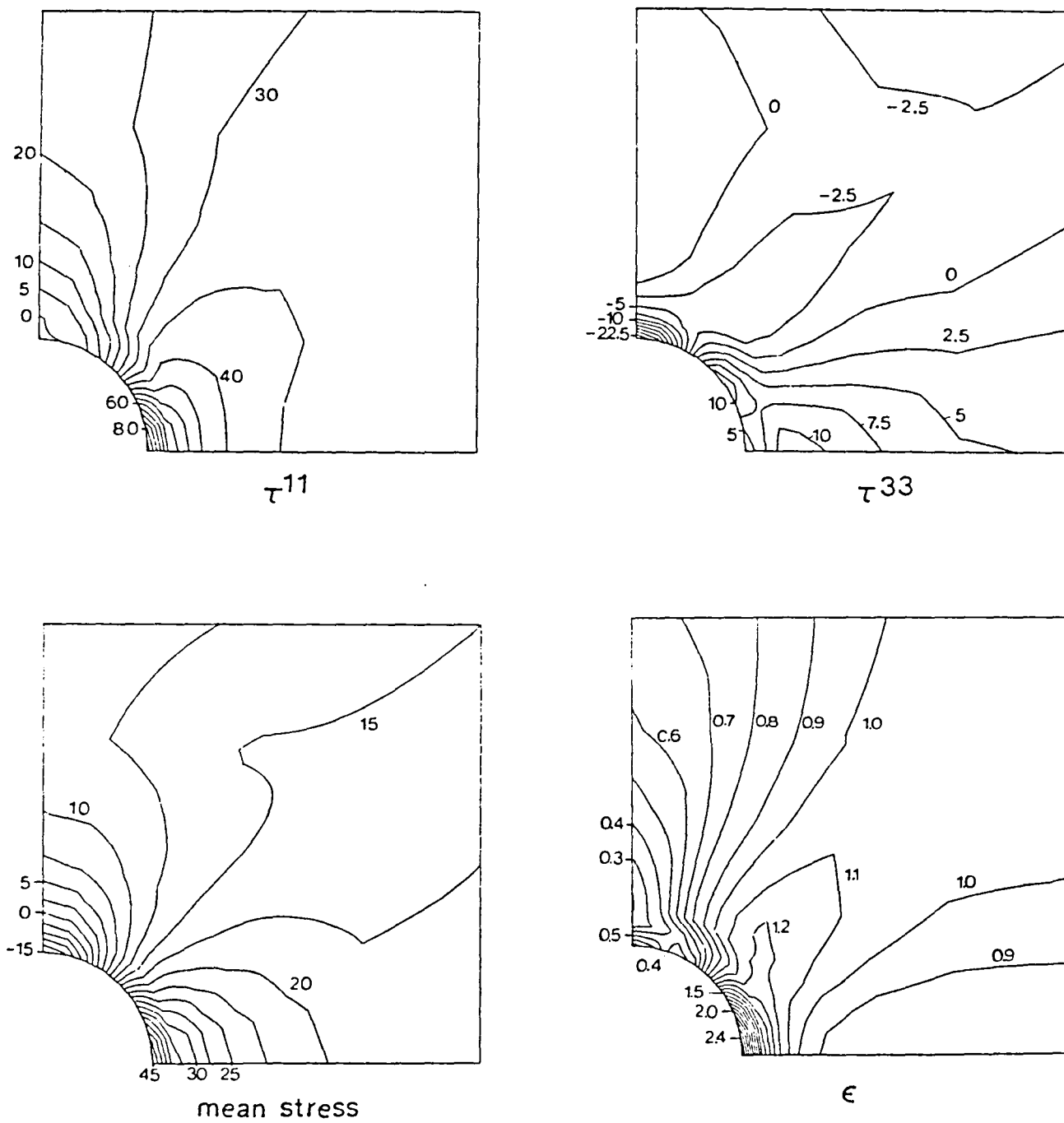

Figure 2-5. Stresses and Mean Strain Rate at Elongation Ratio L=1.01.

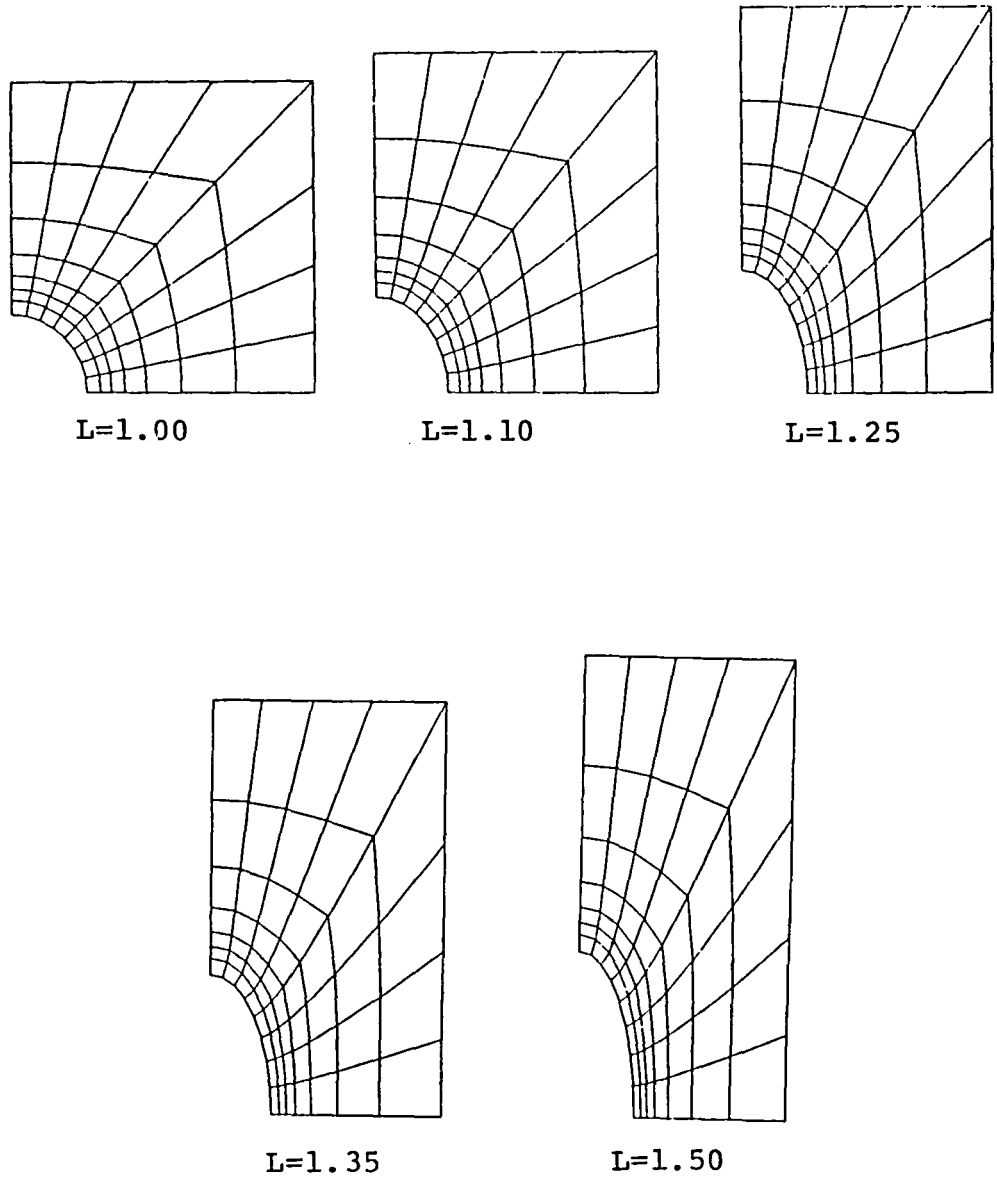

Figure 6. Deformation of Cell.

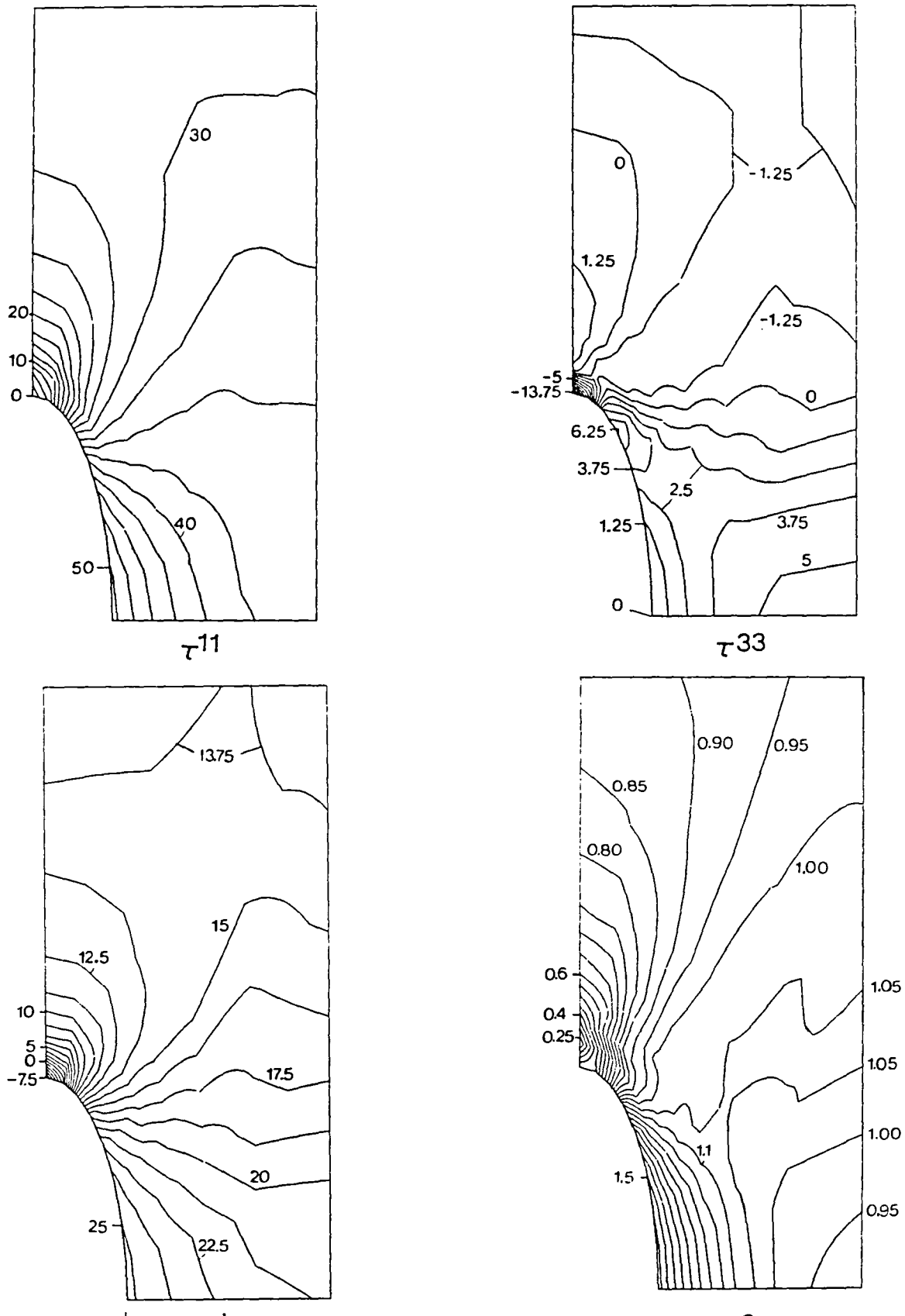

Figure 7-10. Stresses and Mean Strain at Elongation Ratio L=1.50.

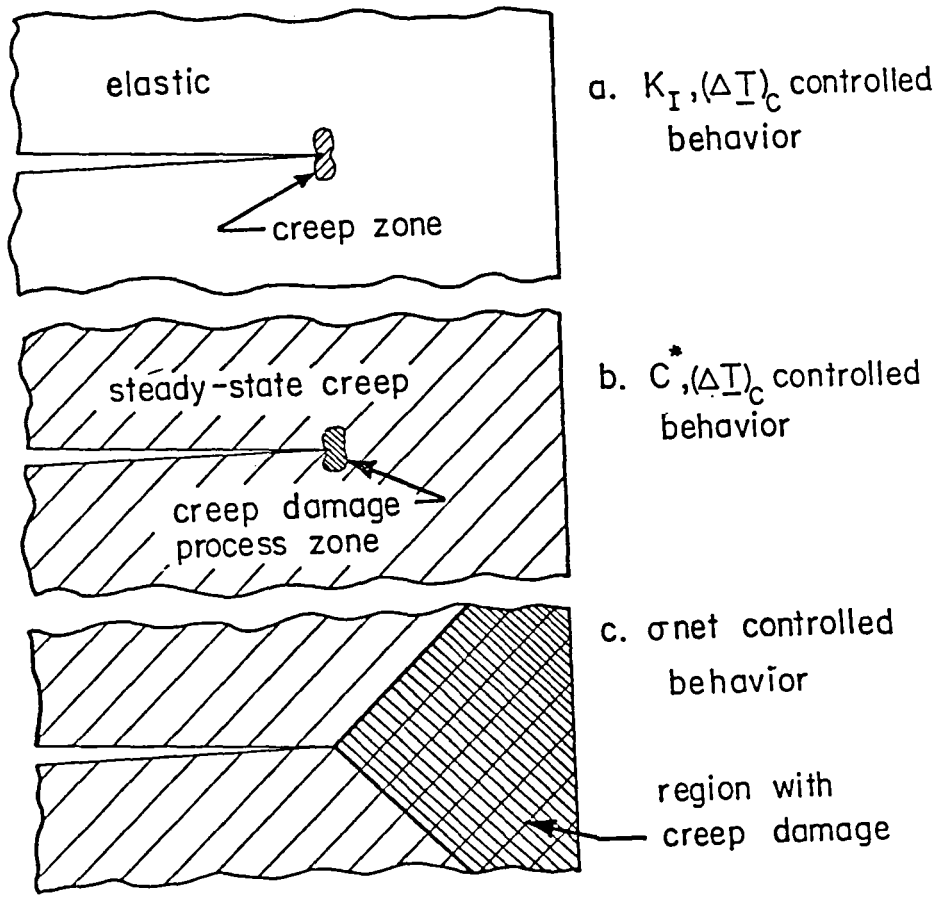

Figure 11. Conditions for which Creep Crack Growth Parameters are Expected to be Valid.

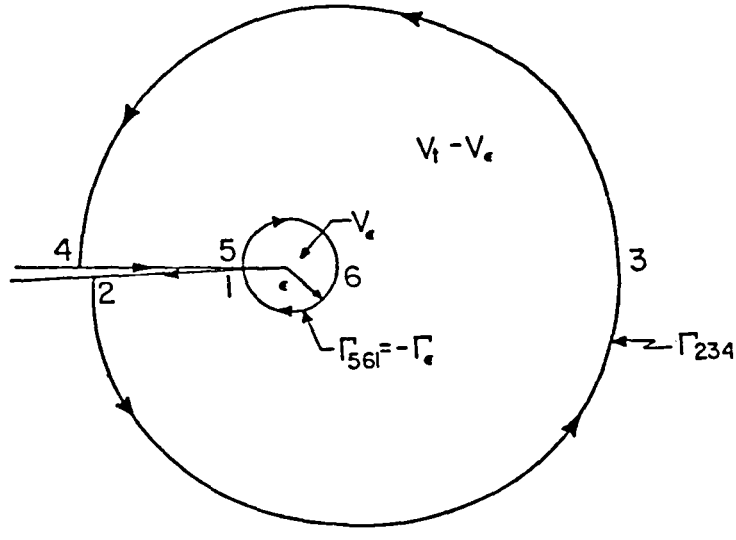

Figure 12. Contours for Applying the Conservation Law to a Two-Dimensional, Cracked Body.

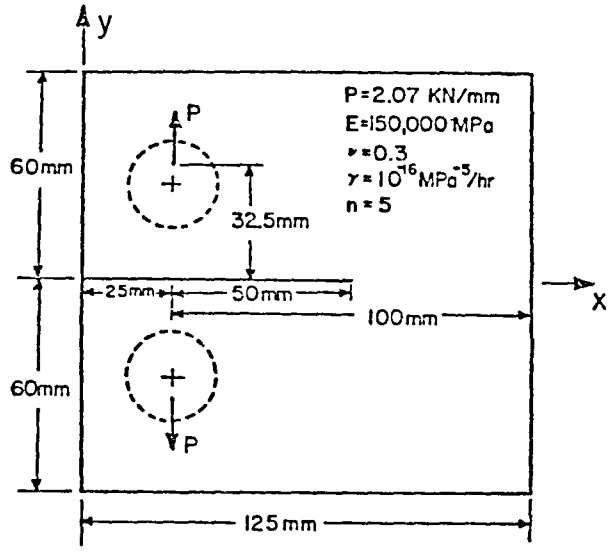

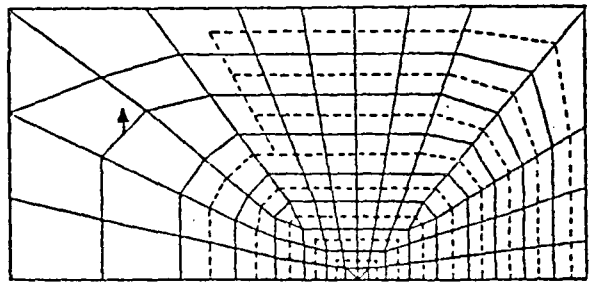

The 102 element mesh (331 nodes; 642 d.o.f.)

The 300 element mesh (941 nodes; 1840 d.o.f.)

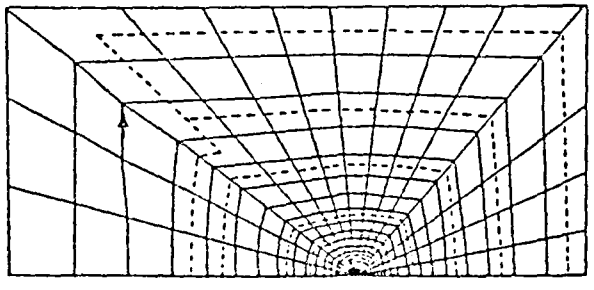

Figure 13. Summary of Geometry, Loading, Material Properties and Finite Element Meshes for the Compact Specimen.

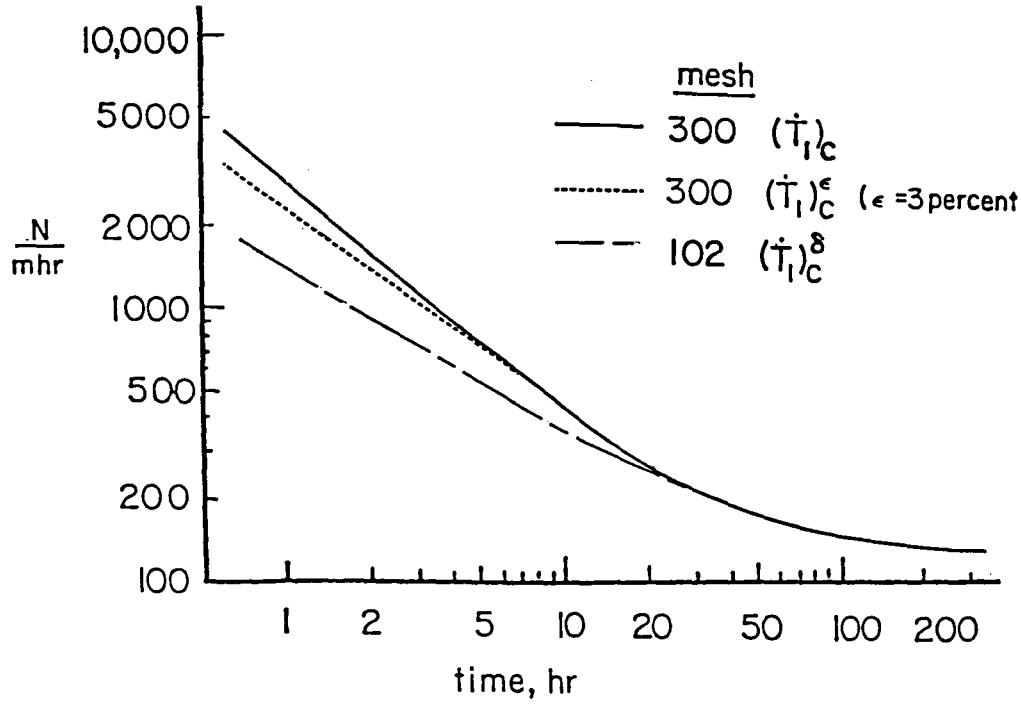

Figure 14. Comparison of $(\dot{T}_1)_c$ and $(\dot{T}_1)_c^{\delta}$ for the compact specimen.

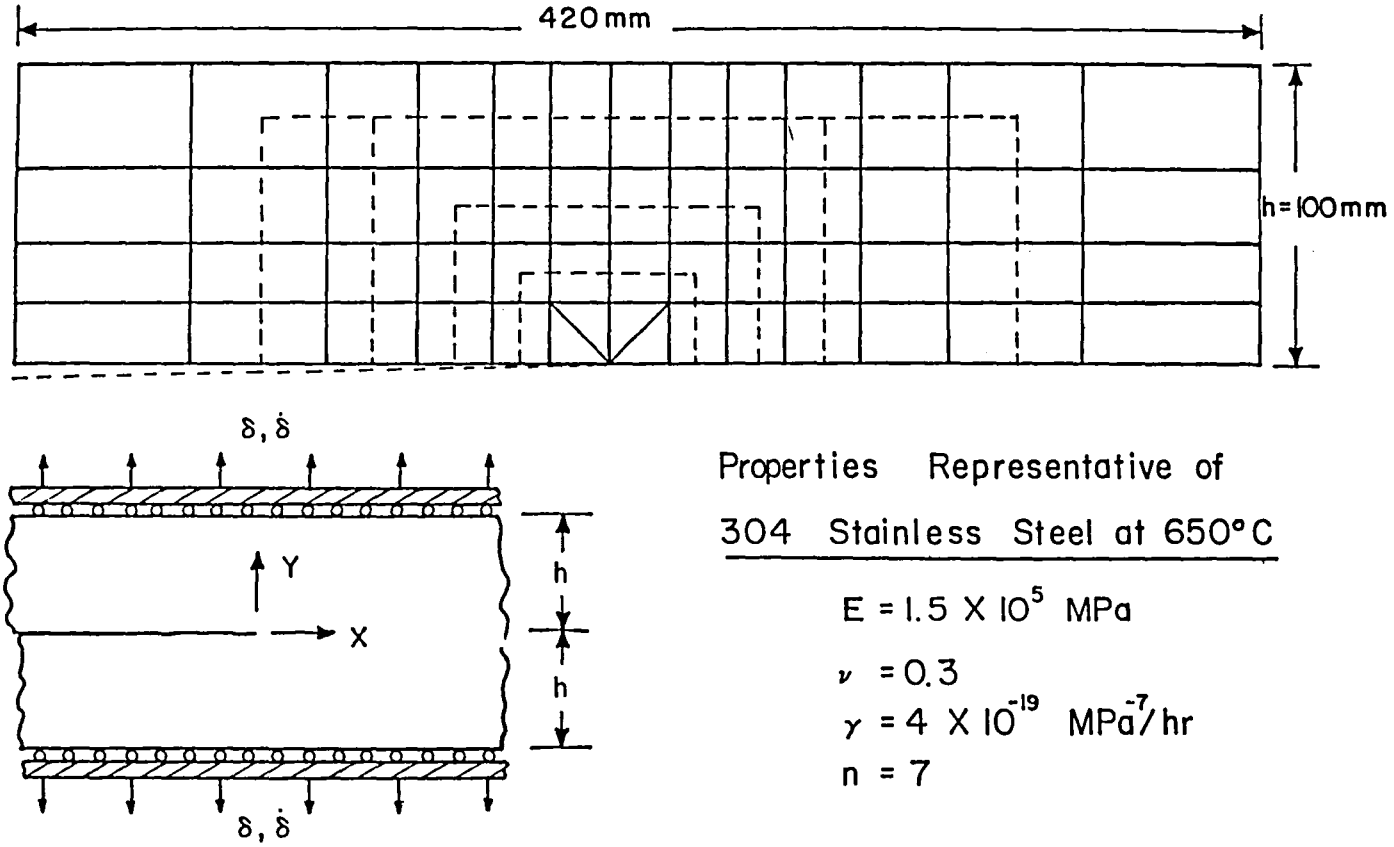

Figure 15. Summary of Geometry, Loading, Material Properties and Finite Element Meshes for the Compact Specimen.

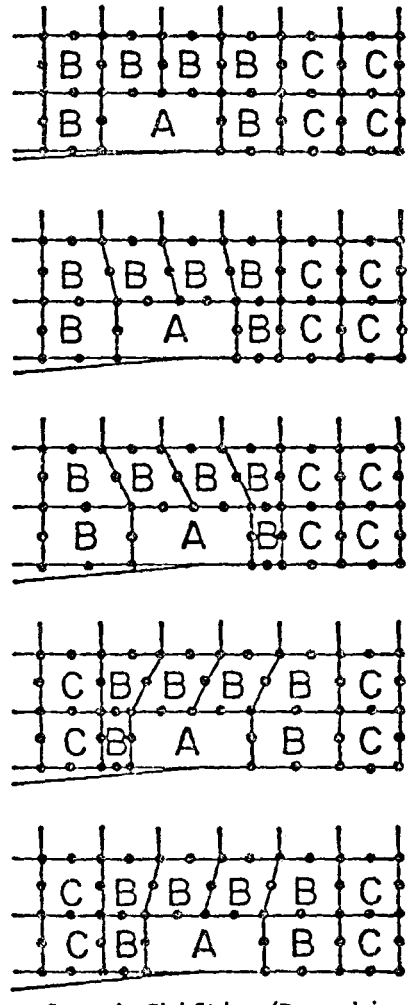

Figure 16. Illustration of Mesh Shifting/Remeshing Procedure for Simulation of Crack Growth.

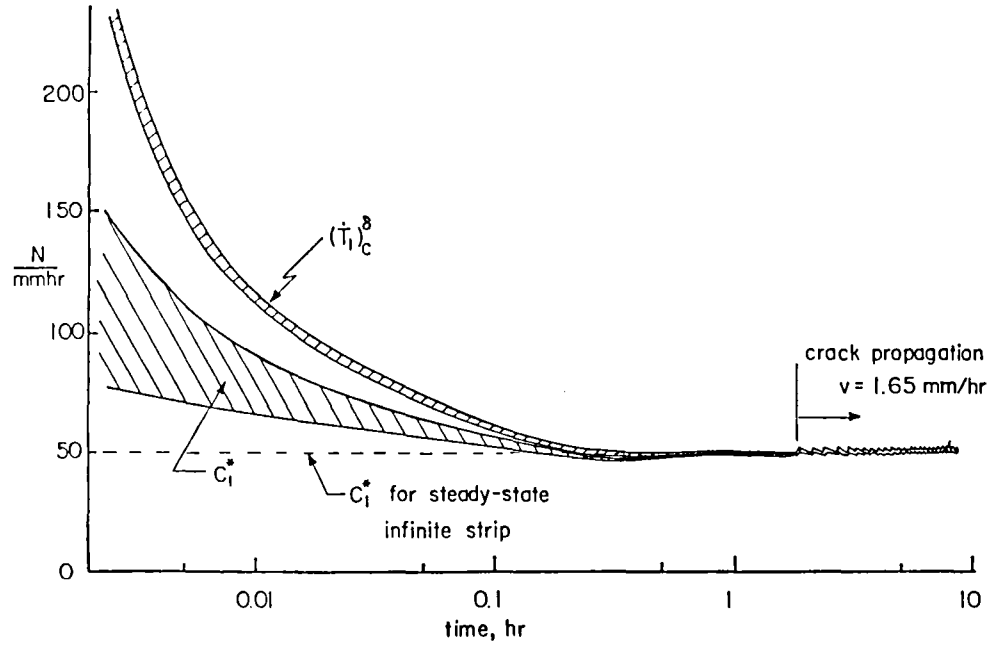

Figure 17. History of $(\dot{T}_1)_c^\delta$ and C_1^* for Creep Crack Growth in a Plane Strip (Steady-State C_1^*=50 N/mm.hr, da/dt=1.65 mm/hr).

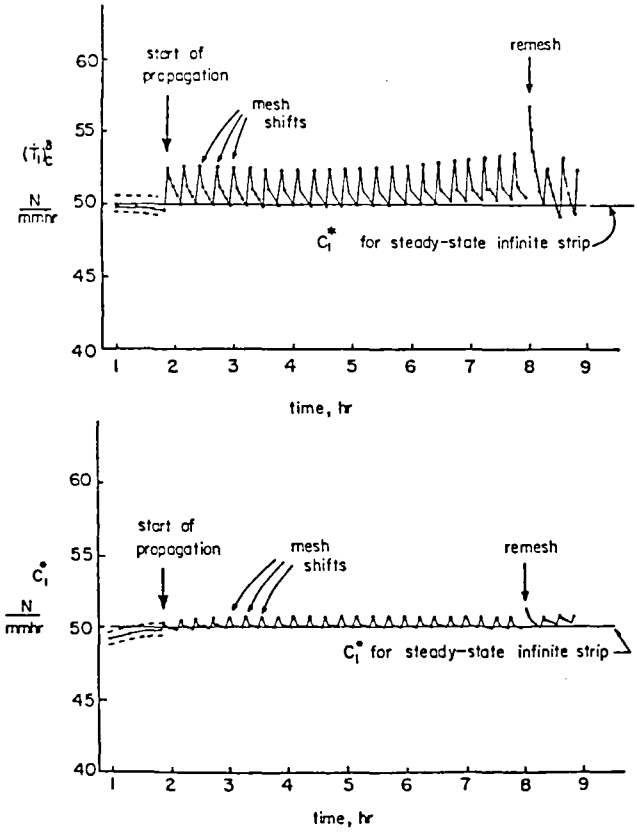

Figure 18. Behavior of $(\dot{T}_1)_c^\delta$ and C_1^* During Simulated Creep Crack Growth in a Plane-Strain Strip (Steady-State C_1^*=50 N/mm.hr da/dt=0.11 mm/hr).

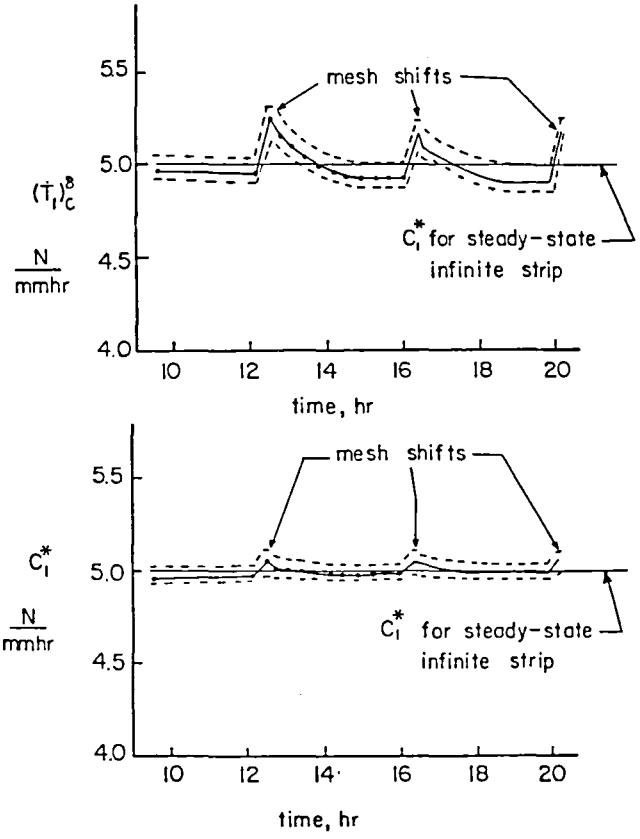

Figure 19. (Behavior of $(\dot{T}_1)_c^\delta$ and During Simulated Creep Crack Growth in a Plane Strain Stip (Steady-State C_1^*=5 N/mm.hr, da/dt=0.111 mm/hr).

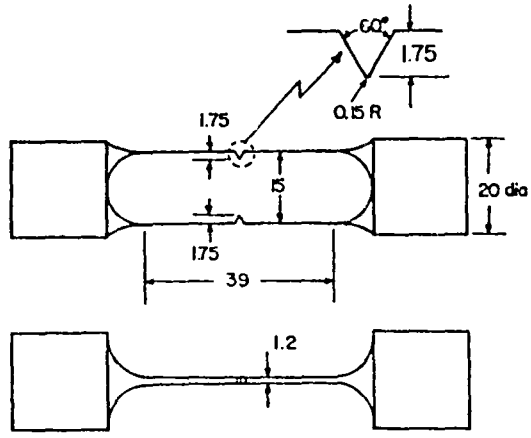

Figure 20. Geometry of Double-Edge Crack Specimen.

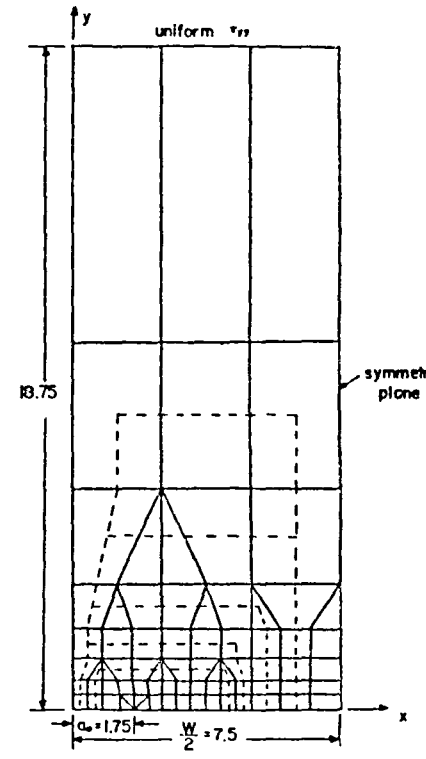

Figure. 21. Finite Element Model and ($\dot{T}$) Integral Path for the DEC Specimen.

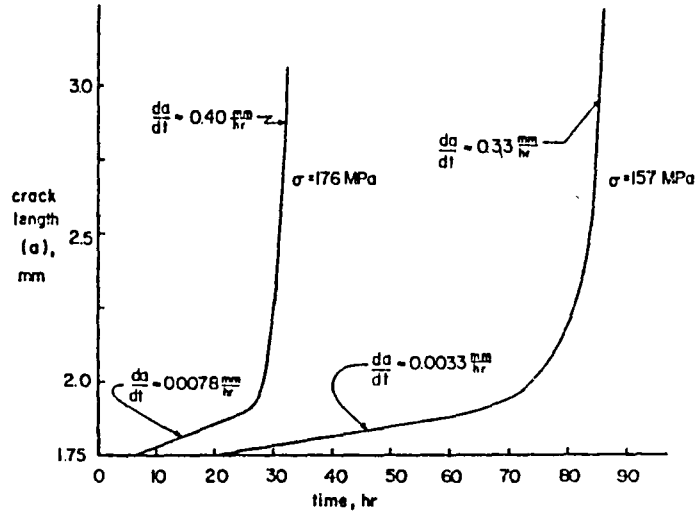

Figure 22. Experimentally Determined Crack Growth Histories (From Koterazawa and Iwata).

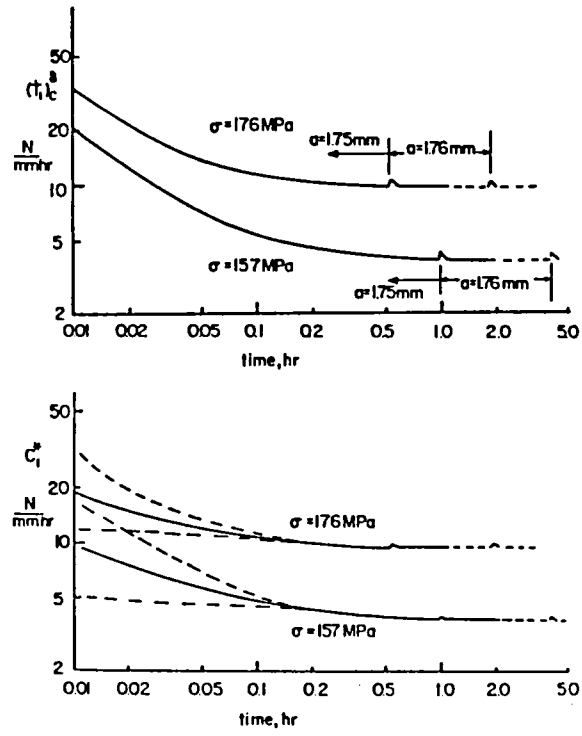

Figure. 23. Values of ($\dot{T}$) and C* During Earlier Phases of Creep Crack Growth.

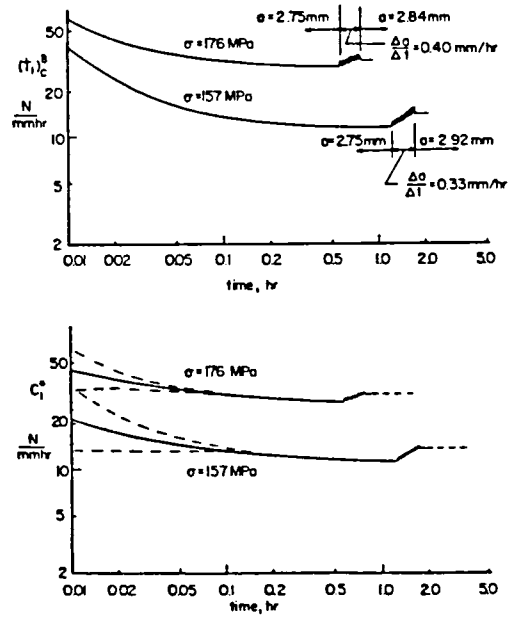

Figure 24. Values of ($\dot{T}$) and C* During Latter Phases of Creep Crack Growth.

PANEL DISCUSSION AND RECOMMENDATIONS

L. Berke, NASA Lewis Research Center, Moderator

An effective participation of the Symposium attendees was complete with the following individual recommendations on:

Where should development effort in constitutive relations for high temperature applications be concentrated in the 1980's

E. Krempl (RPI)

1. Systematic uniaxial and biaxial experiments under constant and variable temperature (extensometers needed for biaxial testing)

2. Modeling of specific material phenomena, such as:

   - o Aging
   - o Metallurgical changes by environment
   - o Strain aging
   - o Metallurgical changes by deformation
   - o Metallurgical instability
   - o Anisotropy

3. Computational tools (variational principles, minimum principle, efficiency)

4. Link with life prediction effort

5. Dissemination and education, with the goal of obtaining a unified approach

W. Haisler (Texas A&M University)

1. Updating of material property data base

2. Better understanding of actual material environment under service conditions

3. Constitutive models designed with specific objectives (prediction capabilities) in mind

4. Closer definition of capabilities of current models

5. Education of nonlinear code users

6. Mutual working relationships among code developers, material specialists and experimenters

R. L. McKnight (General Electric Company)

1. Anisotropic materials

2. Powder materials

3. Higher temperatures

4. Coatings

5. Historical variation

6. Practical accuracy requirements

7. Verification and validation

V. Moreno (Pratt and Whitney, United Technologies)
Directions for Future Constitutive Model Development

1. Current models

   Improve rate sensitive response
   Multiaxial applications

2. Numerical efficiency

   Reduce loading steps
   User independent

3. Model development-metallurgical examination

   Guidelines for solution/development

D. Robinson (Oak Ridge National Laboratory)

1. The primary limitation on large scale inelastic analysis is economic. Need simplified and approximate methods of inelastic analysis (e.g. bounding techniques, shakedown theorems. . .) Constitutive relations must lend themselves to approximate methods.

2. To do boundary value problems one wants the simplest representation that can give a reasonable approximate solution.

3. Emphasis placed on basic physical aspects in simple mathematical terms rather than on simple physical idealizations in-complex mathematical form.

4. Need improved capability of measuring multiaxial strains at elevated temperature. Experimental effort must be thought of as only a check on theory. Its major contribution should be to guide the development of theory.

5. The fast breeder industry has adopted the philosophy of developing a constitutive equation framework based on the virgin, fully-annealed state. Should fully-aged material be used?

6. Many non-isothermal constitutive formulations are based solely on isothermal testing. Approximate non-isothermal tests should be part of the data base.

7. Constitutive relations should be based on a data base that is reasonably obtainable. Testing should be largely phenomenological.

8. Continuum properties: uniqueness, convergence, etc.

1. Report No.	2. Government Accession No.	3. Recipient's Catalog No.
NASA CP-2271		

4. Title and Subtitle	5. Report Date
NONLINEAR CONSTITUTIVE RELATIONS FOR HIGH TEMPERATURE APPLICATIONS	March 1983
	6. Performing Organization Code
7. Author(s)	8. Performing Organization Report No. E-1541
	10. Work Unit No.
9. Performing Organization Name and Address National Aeronautics and Space Administration Lewis Research Center Cleveland, Ohio 44135	11. Contract or Grant No.
	13. Type of Report and Period Covered Conference Publication
12. Sponsoring Agency Name and Address University of Akron Akron, Ohio 44304	14. Sponsoring Agency Code

15. Supplementary Notes

16. Abstract

A Symposium on Nonlinear Constitutive Relations for High Temperature Applications, under the joint sponsorship of the NASA Lewis Research Center and the University of Akron, was held at the University of Akron on May 19-20, 1982. The purpose of this symposium was to review the state-of-the-art in nonlinear constitutive modeling of high temperature materials and to identify the need for future research and development efforts in this area. Through this symposium, it was recognized that considerable research efforts are urgently needed in the development of nonlinear constitutive relations for high temperature applications. This need is further prompted by recent advances in high temperature materials technology and new demands on material and component performance. The demands for better material performance have come from the aerospace, stationary power and automotive industries. Papers presented at this symposium are contained in the Conference Proceedings.

17. Key Words (Suggested by Author(s))	18. Distribution Statement
Viscoplastic theory; Unified theory; Constitutive theory; Nonlinear; Creep; Plasticity; Inelastic; Constitutive modeling; Material behavior; High temperature; Numerical predictions	Unclassified - unlimited STAR Category 39

19. Security Classif. (of this report)	20. Security Classif. (of this page)	21. No. of Pages	22. Price*
Unclassified	Unclassified	378	A17

* For sale by the National Technical Information Service, Springfield, Virginia 22161

☆USGPO: 1983 — 659-094/333